UNIVERSITY OF SOUTHERN QUEENSLAND

MULTISCALE STOCHASTIC SIMULATION OF TRANSIENT COMPLEX FLOWS

A thesis submitted by

HUNG QUOC NGUYEN

B.Eng., Ho Chi Minh City University of Technology, Vietnam, 2009

M.Eng., Ho Chi Minh City University of Technology, Vietnam, 2011

For the award of the degree of

Doctor of Philosophy

2016

Dedication

To my parents

and my wife

Abstract

The thesis reports new multiscale simulation methods to predict rheological properties of complex fluids. Dilute polymer solutions, polymer melts and fibre suspensions with a Newtonian matrix are the main interests of this study. In the present multiscale approach, the stress contributed by polymers or suspended fibres is determined by the Brownian configuration field (BCF) method using kinetic models whereas integrated radial basis function (IRBF) based numerical methods are used to approximate field variables and their derivatives and to discretise governing equations. The macro-micro multiscale system is linked together by a stress formula by kinetic models.

The IRBF-BCF based multiscale method is first applied to simulate dilute polymer solutions modelled by bead-spring chains (BSCs), incorporating finitely extensible nonlinear elastic springs, hydrodynamic interaction and excluded volume effects. Then, the simulation method is further developed for polymer melt systems, in which the entanglement of polymer molecules is described by Doi-Edwards, Curtiss-Bird, reptating rope and double reptation models. The numerical stability of the method, which is generally known as a challenging problem in the simulation of polymer melts, is enhanced owing to the combination of the IRBF method and the BCF idea. As an illustration of the method, the start-up Couette flow and the flow over a cylinder in a channel are investigated for both dilute polymer solutions and polymer melts.

A new multiscale approach is also developed to simulate the rheological characteristics of fibre suspensions in both dilute and non-dilute regimes. The approach is a combination of the IRBF scheme, the discrete adaptive viscoelastic stress splitting (DAVSS) formulation and the BCF idea. The macroscopic conservation equations described in stream function-vorticity formulation are solved using the 1D-IRBF scheme combined with the DAVSS technique. The evolution equation for fibre configuration fields governed by the Jeffery equation for dilute fibre suspensions or the Folgar-Tucker equation for non-dilute fibre suspensions is explicitly advanced in time using the BCF approach. The fibre stress is determined based one fibre configuration fields using the Lipscomb and Phan-Thien–Graham models for dilute and non-dilute fibre suspensions, respectively. The method is verified with the simulation of flows of fibre suspensions between two parallel plates, flows through a circular tube, the 4:1 and 4.5:1 axisymmetric contraction flows, and the 1:4 axisymmetric expansion flows.

Numerical experiments confirm the present method efficiency based on both the enhanced convergence rate of the solution and the stability of a stochastic process.

Certification of Thesis

I certify that the idea, experimental work, results and analyses, software and conclusions reported in this thesis are entirely my own effort, except where otherwise acknowledged. I also certify that the work is original and has not been previously submitted for any other award.

Hung Quoc NGUYEN — Date

ENDORSEMENT

Dr. Canh–Dung TRAN, Principal supervisor — Date

Prof. Thanh TRAN–CONG, Co-supervisor — Date

Acknowledgements

I would like to express my deepest gratitude to my supervisors, Dr. Canh-Dung Tran and Prof. Thanh Tran-Cong, who have given me an opportunity and motivation to pursue my research career. Without their dedicated guidance and enormous support, this thesis would not have been possible.

I gratefully acknowledge the University of Southern Queensland (USQ) for the Postgraduate Research Scholarship; the Faculty of Health, Engineering and Science (FoHES) for the top-up scholarship; and the Computational Engineering and Science Research Centre (CESRC) for the financial supplement. The administrative support from the HES Research Office and the Office of Research and Graduate Studies and the technical support in using USQ High Performance Computing (HPC) system from the HPC Admin team are highly appreciated.

I would also like to thank Prof. Nam Mai-Duy, Dr. Duc Ngo-Cong and other friends and colleagues at CESRC for their friendship, useful advice and necessary assistance in the course of my study.

I am also appreciative of the supports, which I have received before my PhD candidature at USQ, from the Institute for Computational Science and Technology (Ho Chi Minh City, Vietnam).

I am deeply indebted to my family including my parents in law and my wife for their silent sacrifice, unconditional love, extraordinary support and constant encouragement.

Publications resulting from the Thesis

Journal papers

1. **Nguyen, H.Q.**, Tran, C.-D., Pham-Sy, N., and Tran-Cong, T. (2014). A numerical solution based on the Fokker-Planck equation for dilute polymer solutions using high order RBF methods. *Applied Mechanics and Materials*, 553: 187-192. DOI:10.4028/www.scientific.net/AMM.553.187

2. **Nguyen, H.Q.**, Tran, C.-D., and Tran-Cong, T. (2015). RBFN stochastic coarse-grained simulation method: Part I - Dilute polymer solutions using Bead-Spring Chain models. *CMES: Computer Modeling in Engineering & Sciences*, 105(5): 399-439. DOI:10.3970/cmes.2015.105.399

3. **Nguyen, H.Q.**, Tran, C.-D., and Tran-Cong, T. (2015). A multiscale method based on the fibre configuration field, IRBF and DAVSS for the simulation of fibre suspension flows. *CMES: Computer Modeling in Engineering & Sciences*, 109-110(4): 361-403. DOI:10.3970/cmes.2015.109.361

4. **Nguyen, H.Q.**, Tran, C.-D., and Tran-Cong, T. (2016). RBFN stochastic coarse-grained simulation method: Part II - Polymer melts using reptation models. *CMES: Computer Modeling in Engineering & Sciences.* (Under review)

5. **Nguyen, H.Q.**, Tran, C.-D., Ngo-Cong, D. and Tran-Cong, T. (2016). Simulation of non-dilute fibre suspension flows using the high-order IRBF-

BCF based multiscale method. *CMES: Computer Modeling in Engineering & Sciences*. (In press)

Conference papers

6. **Nguyen, H.Q.**, Tran, C.-D., Pham-Sy, N., and Tran-Cong, T. (2013). A numerical solution based on the Fokker-Planck equation for dilute polymer solutions using high order RBF methods. CD Proceedings: the 1st Australian Conference Computational Mechanics (ACCM 2013), University of Sydney, Australia.
7. **Nguyen, H.Q.**, Tran, C.-D., and Tran-Cong, T. (2015). Simulation of flow of fibre suspensions using an IRBF-BCF based multiscale approach, Eleventh International Conference on CFD in the Minerals & Process Industries 11-12 December, 2015, CSIRO, Melbourne, Australia.

Table of Contents

List of Figures

List of Tables

Chapter 1

Introduction

1.1 Motivation, significance and objectives

Simulation of transient non-Newtonian fluid flows, e.g. flows of viscoelastic fluid or fibre suspensions, plays a very important role in several manufacturing industries, for example, processing of polymer liquids (dilute or concentrated solutions and melts) (Barone and Tucker, 1989) and fibre-reinforced composite materials (Folkes, 1982). The simulation in these fields is practically interesting but computationally challenging. Although the macroscopic simulation for the evolution of non-Newtonian flows has achieved significant progresses over the last five decades, the approach is deficient in solving several real flow problems in terms of both geometry and materials, for example, moving boundary and free surface for complex geometry and lack of closed-form constitutive equation for complex fluid. Hence, any computational achievement in solving such problems will advance the simulation method and bring enormous benefits to industry.

Recently, various multiscale methods for the modelling and simulation of polymeric fluid flows have been developed (Laso and Ottinger, 1993; Hulsen et al., 1997; Van den Brule, 1993; Weinan and Engquist, 2003) and attracted significant attention. In the multiscale approaches, different physical laws are often required to describe the system at different scales. For example, at the macro-scale, complex fluids are accurately described by the velocity, pressure, and temperature fields which satisfy the physical conservation equations while on the micro-scale, it is necessary to use kinetic theory to get a more detailed material description in terms of the probability distribution function of particles (Bird et al., 1987b). This approach is known as the continuum-microscopic multiscale method and does not require closed-form constitutive equations (Ottinger, 1996). More recently, the Computational Engineering and Science Research Centre, University of Southern Queensland, has developed radial basis function networks (RBFNs) based numerical methods for the simulation of stochastic multiscale macro-micro models of fluids (Tran-Canh and Tran-Cong, 2002b, 2004; Tran et al., 2011, 2012a). Our research is a further development of this approach with the main objectives as follows.

1. To devise multiscale simulation approaches, incorporating the IRBF approximation scheme, which will be both accurate and efficient, for the simulation of a system of hybrid governing equations of non-Newtonian flows;
2. To apply the new methods for the solution of complex fluid flows using various kinetic models such as the Bead Spring Chain (BSC) models for dilute polymer solutions and reptation models for concentrated polymer solutions and polymer melts; and
3. To develop efficient computational procedures based on the BCF coarse grained method and RBF schemes for the simulation of fibre suspension flows in both dilute and non-dilute regimes.

1.2 Governing equations

This section is to briefly review the conservation equations of mass, momentum and energy and the constitutive equations for Newtonian fluids, polymeric fluids and fibre suspensions.

1.2.1 Conservation equations

It is known from continuum fluid mechanics that the physical behaviour of a fluid is completely governed by a set of conservation equations of mass, momentum and energy as follows (Bird et al., 1987a).

- **Equation of continuity**

$$\frac{D\rho}{Dt} + \rho(\nabla \cdot \mathbf{u}) = \mathbf{0}, \tag{1.1}$$

- **Equation of motion**

$$\rho\frac{D\mathbf{u}}{Dt} = (\nabla \cdot \boldsymbol{\sigma}) + \rho\mathbf{b}, \tag{1.2}$$

- **Equation of energy**

$$\rho\frac{De}{Dt} = -(\nabla \cdot \mathbf{q}) - (\boldsymbol{\sigma} : \nabla\mathbf{u}), \tag{1.3}$$

where $\mathbf{u}$ is the velocity vector; t the time; ρ the density of the fluid; $\boldsymbol{\sigma}$ the total stress tensor; $\mathbf{b}$ and e the body force and the internal energy per unit mass, respectively; and $\mathbf{q}$ the heat flux vector. D/Dt is the substantial or material time derivative associated with a specific fluid element $(\bullet)$ and defined as

$$\frac{D}{Dt}(\bullet) = \partial(\bullet)/\partial t + \mathbf{u} \cdot \nabla(\bullet). \tag{1.4}$$

The total stress tensor $\boldsymbol{\sigma}$ for a given fluid can be decomposed as

$$\boldsymbol{\sigma} = -p\mathbf{I} + \boldsymbol{\tau}_e, \tag{1.5}$$

where p is the hydrostatic pressure; $\mathbf{I}$ the identity tensor; and $\boldsymbol{\tau}_e$ the extra stress tensor which is defined by means such as constitutive relations.

For an isothermal and incompressible fluid whose ρ is a constant, the conservation equation of energy (1.3) is neglected. So the conservation equations of mass and momentum (1.1)-(1.2) with no body force ($\mathbf{b} = 0$) are rewritten as follows.

$$\nabla \cdot \mathbf{u} = \mathbf{0}, \tag{1.6}$$

$$\rho \left(\frac{\partial \mathbf{u}}{\partial t} + \mathbf{u} \cdot \nabla \mathbf{u} \right) = -\nabla p + \nabla \cdot \boldsymbol{\tau}_e. \tag{1.7}$$

1.2.2 Constitutive equations

The constitutive equation derived from experimental observations or theoretical principles describes the relation between the stress tensor and the flow kinematics. Several constitutive equations are summarised as follows.

Newtonian fluids

For a Newtonian fluid, the extra stress tensor $\boldsymbol{\tau}_e$ in Eq. (1.5) is replaced by the Newtonian stress tensor $\boldsymbol{\tau}_s$, which is defined by the stress-strain relation of the fluid as

$$\boldsymbol{\tau}_s = 2\eta_s \mathbf{D}, \tag{1.8}$$

where η_s is the fluid constant viscosity; $\mathbf{D} = \frac{1}{2}(\nabla \mathbf{u} + (\nabla \mathbf{u})^T)$ the fluid deformation rate tensor; and $\nabla \mathbf{u}$ and $(\nabla \mathbf{u})^T$ the velocity gradient and its transpose, respectively.

Polymeric fluids (solutions and melts)

For a polymeric fluid, the extra stress tensor $\boldsymbol{\tau}_e$ consists of two components, one contributed by the polymer and the other by a Newtonian matrix. Therefore, the total stress tensor in Eq. (1.5) is rewritten as follows.

$$\boldsymbol{\sigma} = -p\mathbf{I} + \boldsymbol{\tau}_s + \boldsymbol{\tau}_p, \tag{1.9}$$

where $\boldsymbol{\tau}_p$ is the polymer contributed stress caused by the evolution of configurations of polymer molecules in the fluid. Thus, the momentum conservation equation for a polymeric fluid is given by

$$\rho\left(\frac{\partial \mathbf{u}}{\partial t}+\mathbf{u}\cdot\nabla\mathbf{u}\right)=-\nabla p+\nabla\cdot\left(\boldsymbol{\tau}_s+\boldsymbol{\tau}_p\right). \tag{1.10}$$

Several common constitutive equations, which are listed below, are used to determine the polymer-contributed stress $\boldsymbol{\tau}_p$.

- **Upper-convected Maxwell (UCM) model**

  The linear UCM model was derived by Oldroyd (1950) as follows.

  $$\boldsymbol{\tau}_p+\lambda\overset{\triangle}{\boldsymbol{\tau}_p}=2\eta_p\mathbf{D}, \tag{1.11}$$

  where λ is the relaxation time; η_p the polymer-contributed viscosity; and $\overset{\triangle}{\boldsymbol{\tau}_p}$ the upper-convected derivative of the polymer stress tensor. In general, the upper-convected derivative for any second-order tensor $\mathbf{A}$ is defined by (Oldroyd, 1950)

  $$\overset{\triangle}{\mathbf{A}}=\frac{\partial\mathbf{A}}{\partial t}+\mathbf{u}\cdot\nabla\mathbf{A}-(\nabla\mathbf{u})^T\cdot\mathbf{A}-\mathbf{A}\cdot\nabla\mathbf{u}. \tag{1.12}$$

- **Oldroyd-B model**

  A combination of the Newtonian solvent stress and the polymer stress in the UCM model yields the Oldroyd-B model (Bird et al., 1987a)

  $$\boldsymbol{\tau}_e+\lambda_1\overset{\triangle}{\boldsymbol{\tau}_e}=2\eta_0\left(\mathbf{D}+\lambda_2\overset{\triangle}{\mathbf{D}}\right), \tag{1.13}$$

  where λ_1 is the relaxation time; $\lambda_2=\lambda_1\frac{\eta_s}{\eta_0}$ the retardation time; and $\eta_0=\eta_s+\eta_p$ the total viscosity. It should be noted that the Oldroyd-B model reduces to the Newtonian fluid for $\lambda_2=\lambda_1$ and the UCM model for $\lambda_2=0$.

- **Phan-Thien–Tanner (PTT) models**

  The PTT models derived from the network theory have been introduced by Phan-Thien and Tanner (1977) and Phan-Thien (1978) for polymer melts and concentrated polymer solutions. The PTT models are expressed in the following two forms

- The linear PTT model (Phan-Thien and Tanner, 1977)

  $$\left(1+\frac{\lambda_1\epsilon}{\eta_p}\mathrm{tr}\left(\boldsymbol{\tau}_p\right)\right)\boldsymbol{\tau}_p+\lambda_1\overset{\triangle}{\boldsymbol{\tau}_p}+\xi\lambda_1\left(\boldsymbol{\tau}_p\cdot\mathbf{D}+\mathbf{D}\cdot\boldsymbol{\tau}_p\right)=2\eta_p\mathbf{D}, \quad (1.14)$$

  where ϵ and ξ are the adjustable parameters of the model and determined from experiments; and tr($*$) the trace of (*).

- The exponential PTT model (Phan-Thien, 1978)

  $$\exp\left(\frac{\lambda_1\epsilon}{\eta_p}\mathrm{tr}\left(\boldsymbol{\tau}_p\right)\right)\boldsymbol{\tau}_p+\lambda_1\overset{\triangle}{\boldsymbol{\tau}_p}+\xi\lambda_1\left(\boldsymbol{\tau}_p\cdot\mathbf{D}+\mathbf{D}\cdot\boldsymbol{\tau}_p\right)=2\eta_p\mathbf{D}. \quad (1.15)$$

Other constitutive equations in the literature such as the differential Pom-Pom model for branched polymer melt systems and the integral K-BKZ model for polymer melts can be found in Bird et al. (1987b); Aksel (2002); McLeish and Ball (1986) and Tanner (1988).

Fibre suspensions

For fibre suspensions with a Newtonian solvent, the extra stress tensor $\boldsymbol{\tau}_e$ is decomposed into two components: the Newtonian solvent stress $\boldsymbol{\tau}_s$ and the fibre-contributed stress $\boldsymbol{\tau}_f$. As a result, the total stress formulation (1.5) and the momentum equation (1.7) are rewritten for fibre suspensions as follows.

$$\boldsymbol{\sigma}=-p\mathbf{I}+\boldsymbol{\tau}_s+\boldsymbol{\tau}_f, \quad (1.16)$$

$$\rho\left(\frac{\partial\mathbf{u}}{\partial t}+\mathbf{u}\cdot\nabla\mathbf{u}\right)=-\nabla p+\nabla\cdot\boldsymbol{\tau}_s+\nabla\cdot\boldsymbol{\tau}_f. \quad (1.17)$$

It is worth noting that there is no closed-form constitutive equation for fibre suspensions without using closure approximations (Fan, 2006; Lu et al., 2006; Chinesta and Ausias, 2015). Therefore, most fibre stress formulations were derived in terms of the orientation of fibre configurations, which is basically characterised by a unit vector $\mathbf{P}$ along the fibre's axis.

Fibres are considered as unique, rigid and cylindrical particles whose length and diameter are l_f and d_f, respectively. Several constitutive equations for fibre suspensions are briefly described as follows.

- **Transversely isotropic fluid (TIF) model for dilute suspensions**

  The TIF model of an anisotropic fluid was first proposed by Ericksen (1960) and then derived by Hinch and Leal (1975) for dilute suspensions from the theory of microstructures. The particle/fibre-contributed stress by the TIF model is determined as follows (Hinch and Leal, 1976).

  $$\begin{aligned}\boldsymbol{\tau}_f = 2\eta_s\phi \Big\{ A\left\langle \mathbf{PPPP}\right\rangle : \mathbf{D} + B\big(\mathbf{D}\cdot\left\langle\mathbf{PP}\right\rangle + \left\langle\mathbf{PP}\right\rangle\cdot\mathbf{D}\big) \\ + C\mathbf{D} + D_r F\left\langle\mathbf{PP}\right\rangle\Big\},\end{aligned} \tag{1.18}$$

  where $\mathbf{P}$ is the unit vector directed along a suspended particle; $\mathbf{PPPP}$ and $\mathbf{PP}$ the fourth-order and second-order orientation tensors of $\mathbf{P}$, respectively; $\big\langle(*)\big\rangle$ the statistical average of $(*)$; ϕ the fibre volume fraction of the suspension; D_r the rotational diffusivity coefficient; $a_r = \frac{l_f}{d_f}$ the aspect ratio of the fibre; and A, B, C and F functions of a_r. For a suspension of high aspect ratio fibres, these coefficients are given by (Phan-Thien and Graham, 1991)

  $$\begin{aligned} A &= \frac{a_r^2}{2\left(\ln 2a_r - 1.5\right)}, \qquad & B &= \frac{6\ln 2a_r - 11}{a_r^2}, \\ C &= 2, \qquad & F &= \frac{3a_r^2}{\ln 2a_r - 0.5}. \end{aligned} \tag{1.19}$$

- **Lipscomb model for dilute suspensions**

  Lipscomb et al. (1988) has transformed the TIF constitutive equation into a coordinate system which instantaneously coincides with the major axes of the ellipsoid particle. The corresponding fibre-contributed stress for non-Brownian suspensions of high aspect ratio fibres is determined as (Lipscomb et al., 1988)

  $$\boldsymbol{\tau}_f = \frac{\phi\mu}{\eta_s}\left\langle\mathbf{PPPP}\right\rangle : \mathbf{D}, \tag{1.20}$$

  where μ is the material constant defined as $\mu = \eta_s a_r^2/\ln a_r$ with a sufficiently high aspect ratio of fibres. The Lipscomb model is used to simulate dilute fibre suspensions in this research.

- **Dinh-Armstrong model for semi-concentrated suspensions**

  The model was developed to approximate the fibre stress for semi-concentrated stiff fibre suspensions with a Newtonian solvent whose volume fraction is in the range $\left[1/a_r^2, 1/a_r\right]$ (Dinh and Armstrong, 1984). The fibre stress formulation of this model is given by

$$\boldsymbol{\tau}_f = 2\eta_s \mathbf{D} \left[\frac{1}{48} \frac{n_f l_f^3}{\ln(2h_f/d_f)} : \int \frac{\mathbf{PPPP}}{\left(1 + \boldsymbol{\gamma}^0 : \mathbf{PP}\right)^{1.5}} d\mathbf{P} \right], \tag{1.21}$$

  where n_f is the fibres density; $\boldsymbol{\gamma}^0$ the infinite strain tensor; and h_f the parameter representing the average distance from a fibre to its nearest neighbour. Other parameters was defined as above. More details of the model can be found in Dinh and Armstrong (1984).

- **Phan-Thien–Graham model for concentrated suspensions**

  A constitutive equation for suspensions with rod-like particles whose aspect ratio is in the range $[5, 30]$ has been proposed by Phan-Thien and Graham (1991). The equation neglects the Brownian motion of fibres and only considers the dominant term related to the fourth-order orientation tensor **PPPP** in the TIF model. The fibre-contributed stress tensor is determined as (Phan-Thien and Graham, 1991)

$$\boldsymbol{\tau}_f = 2\eta_s f(\phi, a_r) \mathbf{D} : \langle \mathbf{PPPP} \rangle \,. \tag{1.22}$$

  The function $f(\phi, a_r)$ in Eq. (1.22) is given by

$$f(\phi, a_r) = \frac{a_r^2 \phi (2 - \phi/\phi_m)}{4(\ln 2a_r - 1.5)(1 - \phi/\phi_m)^2}, \tag{1.23}$$

  where ϕ_m is the maximum volume fraction of the suspension and approximated based on the experimental results of Kitano et al. (1981) as

$$\phi_m = 0.53 - 0.013 a_r, \qquad 5 < a_r < 30. \tag{1.24}$$

  Introducing the rotational diffusivity of fibres D_r into Eq. (1.22) yields a modified Phan-Thien–Graham model (Fan et al., 1999)

$$\boldsymbol{\tau}_f = \eta_s f(\phi) \left(A\mathbf{D} : \langle \mathbf{PPPP} \rangle + D_r F \langle \mathbf{PP} \rangle \right), \tag{1.25}$$

where A and F are the parameters as defined in Eq. (1.19); and $f(\phi)$ is now given by

$$f(\phi) = \frac{\phi(2 - \phi/\phi_m)}{2(1 - \phi/\phi_m)^2}. \tag{1.26}$$

In this research project, the Phan-Thien–Graham model is used to approximate fibre stress in the simulation of concentrated fibre suspension flows.

1.3 Simulation of polymeric fluids

Generally, there are two common approaches for simulations of flows of polymeric fluid: the purely macroscopic approach and the macro-micro multiscale approach. The two simulation approaches are similar in integrating the effect of polymer phase in the motion equation of the flow but distinctively different in the manner of calculating the polymer stress. Indeed, the polymer-contributed stress is obtained by solving the constitutive equation in the macroscopic approach whereas it is computed from the information of micro-structures, which represent the real polymer molecules, in the macro-micro approach.

1.3.1 Macroscopic approach

In the macroscopic method, the conservation equations are closed by a constitutive equation for polymeric fluids. The constitutive equation can be expressed in either the differential form (Maxwell, Oldroyd-B and PTT models) or the integral form (K-BKZ model). The two models have been investigated extensively in the literature. However, the main difficulty in both models is how to find a suitable closed-form constitutive equation for a specific fluid investigated in the problem. In addition, it is known from the literature that the constitutive equations of several complex fluids are not able to be derived in a closed form (Owens and

Phillips, 2002; Engquist et al., 2009).

1.3.2 Macro-micro multiscale approach

In the macro-micro multiscale approach or the coarse-grained (CG) simulation, there are two separate procedures which need to be carried out at each time step: the macro and micro procedures. In the macro procedure, the kinetic behaviour of the flow is governed by the conservation equations for mass and momentum. Meanwhile, in the micro procedure, the dynamic behaviour of polymeric liquids is described based on the micro-configuration/structure of polymers using kinetic CG models. The governing equations in the two procedures are then linked together by the Kramers expression, which is used to calculate the polymer stress from the configurations of polymer models in the micro procedure.

One of the potential techniques in the CG simulation is the Brownian dynamics simulation (BDS) technique in which the evolution of polymer configurations can be captured by either a diffusion equation, known as the Fokker-Planck equation (FPE), or the corresponding stochastic differential equations (SDEs) (Ottinger, 1996; Lozinski et al., 2011). The FPE is generally a deterministic PDE of a probability density function whereas SDEs are differential equations whose independent variables are stochastic processes. This yields the two main directions of the BDS for viscoelastic fluid flows, namely the FPE-based and SDE-based methods. While the macro component can be discretised by either the conventional numerical methods such as FEM (Laso and Ottinger, 1993) or the RBFN-based mesh-free methods (Tran-Canh and Tran-Cong, 2002b; Tran et al., 2011), the manner of processing of the micro component gives rise to the basic difference between the two methods. The main advantage of the FPE-based method over the SDE scheme is that the obtained solution is not disturbed by statistical noise (Chauviere and Lozinski, 2004b; Tran et al., 2012b). However, the FPE-based simulation is far less attractive to researchers than the stochastic ones due to (i) the mathematical complexity in solving the FPE (Keunings, 2004), and (ii) the instability caused by high Weissenberg numbers, especially, in complex flows of viscoelastic fluids (Chauviere and Lozinski, 2004a). While both of the two methods are studied in this thesis, the SDE-based method is the main focus of our research project. The SDE simulation method can be classified into two main groups: the Lagrangian BDS and the Eulerian BDS.

The Lagrangian BDS was developed by Ottinger and Laso (Laso and Ottinger, 1993) (named as the Calculation Of Non-Newtonian Flows: Finite Elements & Stochastic Simulation Techniques (CONNFFESSIT)). The main idea of the CONNFFESSIT is that the polymer-contributed stress is averagely calculated from the configurations of a large ensemble of microstructures, which describe polymer chains existing in the polymer solution (Bird et al., 1987b; Ottinger, 1996). Thus, there is no need for a closed form constitutive equation. However, there are several challenges for the method, including: (i) the stochastic noise in the solution of the fibre stress and (ii) particle tracking of a huge number of particles at each time step.

Hulsen et al. (1997) have later proposed the Eulerian BDS scheme, also known as the Brownian configuration field (BCF) technique. The BCF's main idea is that the collection of discrete particles in the CONNFFESSIT is replaced by an ensemble of continuous configuration fields. These configuration fields are convected and deformed by the drift components (the velocity gradient of flow and elastic forces) and the Brownian diffusion motion during the simulation. Owing to the Eulerian nature, the variance reduction techniques and parallel processing simulations can be set up easily in the BCF-based algorithm (Ottinger et al., 1997).

In the macro-micro multiscale approach, polymer liquids are described by kinetic CG models. Some of them are presented in this chapter including the bead-rod-spring (BRS) and reptation models, which are commonly used for the modelling of dilute polymer solutions and polymer melts, respectively. A complete description of kinetic CG models can be found in Bird et al. (1987b).

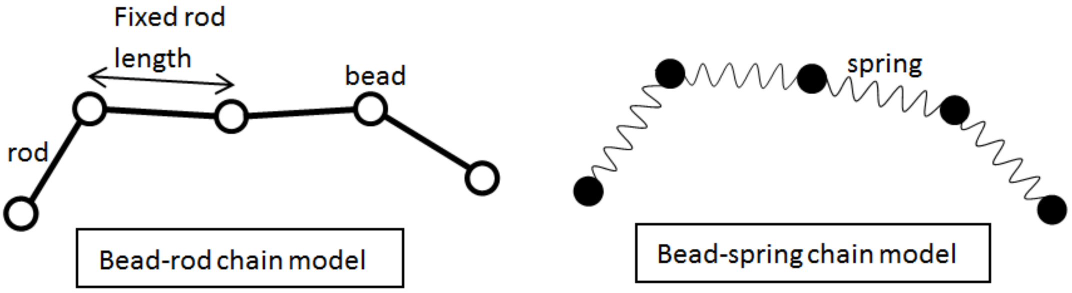

Figure 1.1: An illustration of 5-bead chain of multi BRS models.

Bead-rod-spring (BRS) models for dilute polymer solutions

For these kinetic models, beads are considered as mass points, rods are massless and have a fixed length, and the pendant hydrogen atoms are reduced for simplicity. Generally, BRS models are divided into two basic subclasses. The first group consists of the freely rotating chain model and the freely jointed multi-bead-rod chain model (or the Kramers chain) (Fig. 1.1 - left figure). In the second group, beads are connected by springs, forming the freely jointed bead-spring chain model (Fig. 1.1 - right figure). The model offers some advantages over the corresponding bead-rod model, e.g. the internal constraints are not considered in the bead-spring model. However, it also suffers from some disadvantages. For example, the chain length is not bounded, especially if the extension of spring is governed by the Hookean law, the polymer chain can be stretched unlimitedly in shear flow. The simplest form of the BRS models is the dumbbell model with 2 beads. More details of BRS models can be found in Bird et al. (1987b); Cruz et al. (2012).

In order to enhance the ability of BRS models in expressing the properties of viscoelastic fluid flows, the intramolecular interactions in a polymer system, including the hydrodynamic interaction (HI) and the excluded volume (EV) effects were introduced into the BRS models (Zimm, 1956; Verdier and Stockmayer, 1962). These models predict very well some properties of dilute polymer solutions, for instance, the dependence of the viscometric functions, the diffusion coefficient and the relaxation time on the molecular weight. By incorporating HI and EV effects into the simulation, the rheological characteristics such as the existence of the second normal stress difference or the shear dependence of viscometric functions are forecasted accurately (Zimm, 1956). Thus, the obtained results by the simulation now are able to be compared with those achieved by experiments. Recently, a number of significant advancements of the BRS models have been developed to fully examine the effects of the intramolecular forces on the motion of molecular chains (Ottinger, 1987b, 1989b; Zylka, 1991; Prakash, 2002).

Reptation models for concentrated polymer solutions and polymer melts

Polymer melts and concentrated polymer solutions are extremely complex systems due to the very high density of polymer molecules. Thus, the motion of a molecule is restricted by neighbouring ones. In addition, a polymer chain can move mainly along its backbone and the motion in the direction perpendicular to the backbone is mostly limited by surrounding polymers (Bird et al., 1987b). As a result, the motion of a molecule in an undiluted polymer system is assigned to so-called reptational motion (de Gennes, 1971). The reptation theory was firstly proposed by Doi and Edwards (Doi and Edwards, 1978a,b,c). In the Doi-Edwards (DE) model, each polymer chain reptates in a fictitious tube created by its neighbouring ones. A transformation of the DE model based on a different interpretation of reptation theory is the Curtiss-Bird (CB) model (Curtiss and Bird, 1981a,b; Bird et al., 1982a,b). In this model, an anisotropic friction tensor is employed to describe the limitation of the sideway motion instead of using the "tube" constraint in the DE model. Ottinger (1990) proposed a stochastic version for the reptation models in which the diffusion equation is transformed into an SDE.

1.4 Simulation of fibre suspensions

In this thesis, fibre suspension flows are simulated with the assumptions as follows. (i) fibres are rigid, rod-like particles, and (ii) the fluid is homogeneous because of a constant volume fraction on the whole investigated domain. Two characteristic parameters of the fibres are the aspect ratio a_r and the volume fraction ϕ, which is defined as the total volume of fibres as a fraction of the total volume of suspension. The constitutive equations for fibre suspensions (Section 1.2.2) are formed in terms of statistical averages of the orientation tensors (**PPPP** and **PP**) and it is not easy to derive deterministic closed-form constitutive equations in terms of material properties and standard kinematic quantities. Therefore, in order to close the system, it is necessary to establish an evolution equation for fibres' orientation **P**'s and a formulation to determine the orientation tensors. A discussion on these issues is as follows.

1.4.1 Evolution equation

Jeffery (1922) has introduced the motion equation of a single ellipsoidal particle as

$$\frac{d\mathbf{P}}{dt} = \mathbf{\Omega} \cdot \mathbf{P} + \lambda \left(\mathbf{D} - \mathbf{D} : \mathbf{PPI} \right) \cdot \mathbf{P}, \tag{1.27}$$

where $\mathbf{\Omega} = \frac{1}{2}\left((\nabla \mathbf{u})^T - \nabla \mathbf{u} \right)$ is the vorticity tensor; and λ is a parameter dependent on the ellipsoidal aspect ratio and given by $\lambda = (a_r^2 - 1)/(a_r^2 + 1)$.

This equation has been later used extensively by rheologists to simulate fibre suspensions in dilute regime (Goettler et al., 1979, 1981; Givler, 1981; Givler et al., 1983; Lipscomb et al., 1988; Chiba et al., 1990).

For dilute fibre suspensions, each fibre can rotate freely without any hindrance by its neighbours, and the hydrodynamic interactions between fibres are small and neglected. However, the assumption is not valid for suspensions in 'non-dilute' regimes. In such regimes, the motion of a fibre is restricted by neighbouring ones, therefore, fibre-fibre interactions need to be introduced into the evolution equation. By experimental observations, Folgar and Tucker (1984) proposed an evolution equation with the effect of fibre-fibre interactions for the description of non-dilute suspensions as follows.

$$\frac{d\mathbf{P}}{dt} = \mathbf{\Omega} \cdot \mathbf{P} + \lambda \left(\mathbf{D} - \mathbf{D} : \mathbf{PPI} \right) \cdot \mathbf{P} - \frac{D_r}{\psi} \nabla_{\mathbf{P}} \psi, \tag{1.28}$$

where ψ is the probability distribution function of $\mathbf{P}$ ($\psi = \psi(\mathbf{P}, t)$ for the homogeneous suspensions); and $\nabla_{\mathbf{P}}$ the gradient operator associated with $\mathbf{P}$. D_r is the rotational diffusivity coefficient and approximated by (Folgar and Tucker, 1984).

$$D_r = C_i \dot{\gamma}, \tag{1.29}$$

where $\dot{\gamma} = \sqrt{2 \left(\mathbf{D} : \mathbf{D} \right)}$ is the general strain rate; and C_i the interaction coefficient, namely the Folgar-Tucker constant.

The diffusion equation or the FPE derived from Eq. (1.28) for fibre suspensions is given by (Folgar and Tucker, 1984)

$$\frac{\partial \psi}{\partial t} = \frac{\partial}{\partial \mathbf{P}} \Big\{ \psi \left[\mathbf{\Omega} \cdot \mathbf{P} + \lambda \left(\mathbf{D} - \mathbf{D} : \mathbf{PPI} \right) \cdot \mathbf{P} \right] \Big\} + C_i \dot{\gamma} \frac{\partial^2 \psi}{\partial \mathbf{P}^2}. \tag{1.30}$$

The stochastic version of the FPE (1.30) is written as follows (Fan et al., 1999)

$$\frac{d\mathbf{P}}{dt} = \boldsymbol{L} \cdot \mathbf{P} - \boldsymbol{L} : \mathbf{PPP} + \left(\mathbf{I} - \mathbf{PP} \right) \cdot \mathbf{F}^{(b)} (t), \tag{1.31}$$

where $\boldsymbol{L}$ is the effective velocity gradient tensor and given by $\boldsymbol{L} = (\nabla \mathbf{u})^T - \zeta \mathbf{D}$ with $\zeta = 2/(a_r^2 + 1)$ and $\zeta = 1 - \lambda$. The Brwonian force $\mathbf{F}^{(b)}(t)$ possesses the properties $\left\langle \mathbf{F}^{(b)}(t) \right\rangle = 0$ and $\left\langle \mathbf{F}^{(b)}(t+s) \, \mathbf{F}^{(b)}(t) \right\rangle = 2D_r \delta(s) \mathbf{I}$ where $\delta(s)$ is the Dirac delta function. The Brownian force is a function of white noise and given by (Ottinger, 1996).

$$\mathbf{F}^{(b)}(t) = \sqrt{2C_i \dot{\gamma}} \frac{d\mathbf{W}}{dt}, \tag{1.32}$$

where $\mathbf{W}$ is a Wiener process. Substituting Eq. (1.32) into Eq. (1.31) yields the evolution equation for non-dilute fibre suspensions as follows.

$$\frac{d\mathbf{P}}{dt} = \boldsymbol{L} \cdot \mathbf{P} - \boldsymbol{L} : \mathbf{PPP} + \sqrt{2C_i \dot{\gamma}} \left(\mathbf{I} - \mathbf{PP} \right) \cdot \frac{d\mathbf{W}}{dt}, \tag{1.33}$$

where the interaction coefficient $C_i \neq 0$. Eq. (1.33) becomes the Jeffery equation (1.27) for dilute fibre suspensions with $C_i = 0$ (Phan-Thien and Graham, 1991)

1.4.2 Simulation methods

The general procedure for the simulation of fibre suspensions consists of three steps as follows: Firstly, solve the conservation equations with a known fibre stress to update the velocity and pressure fields; Secondly, solve the evolution equation with the updated pressure and velocity fields to determine the fibres' configuration of the current time step; Lastly, calculate the fibre stress field from the updated configuration of fibres. Follow this procedure, several simulation methods have been devised to predict dynamic behaviours of fibre suspension flows. The methods differ mainly in the way to proceed the last two steps in the procedure. Generally, these methods can be classified into several main approaches as follows.

Closure approximation

In this approach, instead of solving the evolution equation for the unit orientation vector $\mathbf{P}$, ones solve the evolution equation for either the second-order or fourth-order tensors of $\mathbf{P}$. The evolution equation for the second-order tensor of $\mathbf{P}$ is given by

$$\begin{aligned}\frac{d\left\langle \mathbf{PP}\right\rangle}{dt} &= \boldsymbol{L}\cdot\left\langle \mathbf{PP}\right\rangle + \left\langle \mathbf{PP}\right\rangle\cdot\boldsymbol{L}^T - 2\boldsymbol{L} : \left\langle \mathbf{PPPP}\right\rangle \\ &\quad + 2C_i\dot{\gamma}\left(\mathbf{I} - \alpha_d\left\langle \mathbf{PP}\right\rangle\right),\end{aligned} \tag{1.34}$$

where α_d is the number of dimension of fibre, i.e. $\alpha_d = 2$ for 2-D orientation and $\alpha_d = 3$ for 3-D orientation. Since Eq. (1.34) also includes the unknown fourth-order orientation tensor $\langle \mathbf{PPPP}\rangle$, it is not a closed form. Therefore, many closure approximations have been proposed to approximate the fourth-order orientation tensor from the second-order one.

Let $P_{ijkl} = \langle \mathbf{PPPP}\rangle$ and $P_{ij} = \langle \mathbf{PP}\rangle$ be the fourth-order and the second-order orientation tensors, respectively. Several common closure approximations were developed as follows.

- The linear closure approximation (Hand, 1962),

$$\begin{aligned}\hat{P}_{ijkl} \simeq \frac{1}{4+\alpha_d}&\left(P_{ij}\delta_{kl}+P_{ik}\delta_{jl}+P_{il}\delta_{jk}+P_{kl}\delta_{ij}+P_{jl}\delta_{ik}+P_{jk}\delta_{il}\right)\\ &-\frac{1}{(4+\alpha_d)(2+\alpha_d)}\left(\delta_{ij}\delta_{kl}+\delta_{ik}\delta_{jl}+\delta_{il}\delta_{jk}\right);\end{aligned} \tag{1.35}$$

- The quadratic closure approximation (Lipscomb et al., 1988),

$$\tilde{P}_{ijkl} \simeq P_{ij}P_{kl} \tag{1.36}$$

- The hybrid closure approximation (Advani and Tucker III, 1987, 1990), which is a combination of the quadratic and linear approximations, is given by

$$\bar{P}_{ijkl} \simeq (1-f)\hat{P}_{ijkl} + f\tilde{P}_{ijkl}, \tag{1.37}$$

  where f is the scalar measure of orientation and given as $f = 1-N\det\langle\mathbf{PP}\rangle$ (Advani and Tucker III, 1990) with $N = 4$ for 2-D and $N = 27$ for 3-D fibre's orientation .

Other advanced closure approximations can be found in several publications by Verleye et al. (1993); Dupret et al. (1997); Cintra Jr and Tucker III (1995); Chung and Kwon (2001, 2002) and Jack et al. (2010).

Statistical scheme

For this approach, the Jeffery equation is integrated along streamlines and the fourth-order orientation tensor at a particular point on the streamlines is directly calculated from the orientation of N_f fibres surrounding that point as follows.

$$\langle\mathbf{PPPP}\rangle = \frac{1}{N_f}\sum_{i=1}^{N_f}\mathbf{P}_i\mathbf{P}_i\mathbf{P}_i\mathbf{P}_i. \tag{1.38}$$

Eq. (1.38) depicts that there is no need of any closure approximation. The approach were used to successfully simulate several dilute fibre suspension flows such as flow past 1:4 backward-facing step channels and flow between two parallel plates (Chiba and Nakamura, 1998; Chiba et al., 2001)

FPE-based simulation

In this approach, the FPE (1.30) is solved for the probability distribution function $\psi(\mathbf{P}, t)$ and the orientation tensors are then calculated using the following formulae (Advani and Tucker III, 1987)

$$\langle \mathbf{PP} \rangle = \int_{\mathbf{P}} \mathbf{PP}\psi d\mathbf{P}, \tag{1.39}$$

$$\langle \mathbf{PPPP} \rangle = \int_{\mathbf{P}} \mathbf{PPPP}\psi d\mathbf{P}. \tag{1.40}$$

The application of this scheme for complex flows is very challenging because of the complexity in solving PDEs in multidimensional spaces (Ammar et al., 2006, 2007).

BCF-based simulation

This approach is based on the principle of the BCF approach, which was proposed by Hulsen et al. (1997) for the multiscale simulation of viscoelastic fluids. Following the approach, a set of N_f fibre configuration fields is used to replace all individual fibres on the whole domain. Each configuration field is evolved by Eq. (1.33), which is now rewritten under the Eulerian view as follows.

$$\frac{\partial \mathbf{P}\left(\mathbf{x}, t\right)}{\partial t} + \mathbf{u} \cdot \nabla \mathbf{P} = \boldsymbol{L} \cdot \mathbf{P} - \boldsymbol{L} : \mathbf{PPP} + \sqrt{2C_i \dot{\gamma}} \left(\mathbf{I} - \mathbf{PP}\right) \cdot \frac{d\mathbf{W}}{dt}, \tag{1.41}$$

Eq. (1.41) is solved by the BCF approach. This approach has been used to successfully simulate many complex flows of non-dilute fibre suspensions with a wide range of volume fractions, e.g. flow past a sphere in a tube (Phan-Thien and Fan, 1999; Fan et al., 1999) and axisymmetric contraction and expansion flows

(Lu et al., 2006).

1.5 Numerical methods for deterministic PDEs

From the classical mechanics, most physical phenomena can be described by a set of deterministic partial differential equations (PDEs). The conventional methods such as finite difference method (FDM), finite element method (FEM), boundary element method (BEM) and finite volume method (FVM) had been thoroughly developed and had demonstrated their superior ability in finding the numerical solution of PDEs for various problems in sciences and engineering. Recently, RBFN-based methods have emerged as a powerful tool and have been successfully applied in several research areas.

1.5.1 Finite difference method

FDM is probably considered as the oldest and simplest method, especially for uniform grids, applied to find numerical solutions of differential equations (Hirsch, 2007). The method is based on the Taylor series expansion of an unknown function for a set of nodal points generated by a Cartesian grid. The derivatives of the function are approximated from the function's value at nodal points. These approximations together with their truncated Taylor series are used to transform the PDEs into a set of algebraic equations, which can be then solved by iterative techniques such as the Newton-Raphson scheme. Owing to its simple implementation and the banded system matrix obtained from the set of linearised equations, FDM has been widely used in various problems in continuum mechanics including the simulation of viscoelastic fluids (Perera and Walters, 1977; Olsson, 1994; Griebel and Ruttgers, 2014) and fibre suspensions (Chiba and Nakamura, 1998; Dou et al., 2007). However, the difficulty of handling complex geometry and the significant truncation error for non-linear problems limit the range of its applications.

1.5.2 Finite element method

The method was first introduced by Turner et al. (1956) for the solution of structural problems and then applied to solve the Navier-Stokes equations for fluid flow problems in the late 1970s by several authors, including Temam (1977); Chung (1978); Girault and Raviart (1979). In this method, the investigated domain is divided into unstructured finite elements, which are interconnected at points called nodes. The approximate solution of an unknown variable at each node is defined as a linear superposition of known basis functions or shape functions, usually polynomials, and the numerical values of the unknown at all nodes (Hirsch, 2007). In general, an FEM-based discretisation process can be done through two steps: (i) Transform the original differential equations into integral equations, or their weak formulation, using the variational principle or the methods of weighted residual; (ii) Discretise the weak form equations based on the chosen shape functions to obtain a set of algebraic equations for unknowns. The FEMs have been used extensively for the simulation of viscoelastic fluids in both the macroscopic approach (Crochet et al., 1984; Baaijens, 1998; Sandri, 2004; Ganvir et al., 2007; Mu et al., 2010) and the multiscale macro-micro methods (Laso and Ottinger, 1993; Hulsen et al., 1997; Van Heel et al., 1999; Jourdain et al., 2002; Le Bris and Lelievre, 2012; Lipscomb et al., 1988). An advantage of FEM in solving viscous and viscoelastic flows is its capacity in handling complex geometries. However, generating a mesh of elements may be very time-consuming especially for moving boundary or three-dimensional problems. In addition, the method becomes unstable for highly nonlinear problems due to intrinsic errors produced from Galerkin-based approximations (Osswald and Gramann, 2001).

1.5.3 Boundary element method

Unlike the FDM and FEM where the discretisation is required on the entire domain as well as the boundary of the problem, the discretisation in BEM is only processed on the boundary for certain class of problems. Therefore, the dimensionality of the problem in BEM is reduced by one, which offers a typical advantage of BEM over the element-type methods for problems with complex geometries and in 3D space (Brebbia et al., 1984; Hunter and Pullan, 2001). In this method, an integral equation related to only boundary values needs to be formulated from the original PDE using several mechanisms such as the reciprocal theorems combined with the Green function and the method of weighted residual. The approximate solution at the boundary nodes is then obtained from solving the integral equation. The numerical values of the interior nodes can be approximated from the boundary data if required. The BEM has been rapidly developed and broadly applied to various complex engineering problems (Brebbia et al., 1984). In computational rheology, the method has been used successfully to solve several complex flow problems such as the squeeze-film flow (Phan-Thien et al., 1987a), the flagellar hydrodynamics problems (Phan-Thien et al., 1987b), the 3-D extrusion processes (Tran-Cong and Phan-Thien, 1988), the Stokes problems of multiparticle systems (Tran-Cong and Phan-Thien, 1989; Tran-Cong et al., 1990), and the suspension problems (Phan-Thien et al., 1991; Fan et al., 1998). However, while BEM works successfully for linear and mildly nonlinear problems, it is less effective in solving highly non-linear viscoelastic problems (Tanner and Xue, 2002).

1.5.4 Finite volume method

FVM is one of the most popular discretisation techniques used in CFD. The computational domain is partitioned into a number of non-overlapping control volumes (CVs). Generally, both structured and unstructured meshes are also available in the FVM, which offers an advantage in handling problems with complex geometry. There are two common approaches for the selection of the finite volume, namely the cell-centred approach and the cell-vertex approach (Hirsch, 2007). The basic difference between the two is that the unknowns are defined at the CV's centre for the former approach whereas they are determined at the corners of each CV for the latter. The original governing equation is transformed into an integral equation, in which the surface integral term is approximated by calculating the sum of fluxes passing all individual faces of each CV. The physical balance laws are strictly obeyed on each CV, therefore, the governing conservation equations are automatically satisfied on the whole domain in the FVM-based discretisation. The FVM has also been applied extensively to several problems in computational rheology (Mompean and Deville, 1997; Xue et al., 1998; Wachs and Clermont, 2000; Sahin and Wilson, 2008; Fu et al., 2009). However, like the other element based methods (e.g. FDM, FEM, and BEM), FVM is also considered as a low-order interpolation scheme, therefore a huge number of elements are necessary to obtain an accurate solution. This leads to difficulties in solving large-scale problems.

1.5.5 Spectral method

Like in FEM, the discretisation process in spectral method (SM) is also based on the method of weighted residuals, whose two key elements are the trial functions (or basis functions or shape functions in FEM) and the test functions (or weight functions) (Canuto et al., 1988). The trigonometric, Chebyshev and Legendre polynomials are usually used as the trial functions in SM. Unlike FEM where the trial functions are locally defined on each element, these functions in SM are valid on the whole computational domain. As a result, SM outperforms FEM and FDM in terms of solution accuracy and high-order convergence rate but is very limited in handling problems with complex geometry (Gheorghiu, 2007; Canuto et al., 1988). Therefore, there are just a few applications of SM in solving complex fluid flow problems in the literature such as Beris et al. (1992); Avgousti et al. (1993); Sureshkumar and Beris (1995); Bell et al. (1997).

The spectral element method which is the combination of SM and FEM has been first introduced by Patera (1984) for fluid dynamics. The method still maintains the accuracy of high-order approximation polynomials in SM but also improves its ability in handling problems with complicated geometries like the original FEM. Owing to this characteristic, the method has been used widely for computations of non-Newtonian fluids in complex geometries using both the macroscopic approach (Jafari, 2011; Lozinski et al., 2002; Van Os and Phillips, 2004, 2005) and the multiscale macro-micro approach (Chauviere and Owens, 2002; Lozinski and Chauviere, 2003).

1.5.6 Radial basis function (RBF) methods

Basically, a RBF network can be considered as a universal approximator. In RBF-based methods, the considered domain is discretised by a set of data points which are distributed regularly or randomly and the unknown function and its derivatives are approximated by a linear combination of RBFs. The RBF-based methods offer some advantages over some traditional methods. Firstly, the method can be referred to as a truly meshless method in the context of the point collocation formulation (Kansa, 1990). Consequently, the time-consuming meshing process in the element-based methods is reduced significantly. Secondly, owing to the use of RBF-based approximations instead of polynomial functions in other methods, the RBFN-based methods can achieve higher order approximation and fast convergence rate for the solution of PDEs (Fasshauer, 2007).

The RBF-based methods for the solution of PDEs can be classified into two main branches: differentiated RBF (DRBF) (Kansa, 1990) and integrated RBF (i.e. IRBF) (Mai-Duy and Tran-Cong, 2001). In the former method, the original unknown function is first approximated by RBFs and then its first and second derivatives are calculated by differentiation. On the other hand, the IRBF methods begin RBF-based approximation at the highest order derivative of the original function. The lower order derivatives and the unknown function are obtained by integration. Several strong points of the IRBF methods over the DRBF counterparts can be listed as follows. (i) a superior accuracy for the approximation of a function and its derivatives, even with a relatively coarse discretisation (Mai-Duy and Tran-Cong, 2003); and (ii) high convergence rate, good accuracy and easy implementation in solving high-order ordinary differential equations and PDEs (Mai-Duy, 2005; Mai-Duy and Tran-Cong, 2005). Multiquadric (MQ) or thin-plate spline (TPS) functions are usually chosen for their superior performance over other functions (Franke, 1982; Hardy, 1971).

The IRBF methods can be global, local or compact local and their implementation is based on both collocation points or control volume techniques. Generally, a global scheme uses all grid nodes to approximate the dependent variable and its derivatives at a specific point, whereas only a small number of neighbouring nodes is needed for the approximation process in local schemes (Mai-Duy and Tran-Cong, 2009a; An-Vo et al., 2011; Ngo-Cong et al., 2012). For large scale problems, the global scheme becomes severely limited as the system matrix becomes too large and ill-conditioned. Local schemes can overcome these drawbacks, however, these schemes produce less accurate solutions than the global ones because of the limitation of the number of nodes used in the approximation process. The accuracy of the local IRBF methods can be recovered by incorporating compact schemes into the approximation process, which is now based on not only the function values of local grid nodes but also more information from the governing equation and/or the function derivatives (Mai-Duy and Tran-Cong, 2011; Hoang-Trieu et al., 2012; Thai-Quang et al., 2012; Pham-Sy et al., 2013; Tien et al., 2015).

Recently, the RBF-based methods have been widely used for the simulation of non-Newtonian fluid flows in both the macroscopic approach (Tran-Cong et al., 2001; Tran-Canh and Tran-Cong, 2002a; Mai-Duy and Tanner, 2005; Bernal and Kindelan, 2007; Lopez-Gomez et al., 2007; Mai-Duy and Tran-Cong, 2009b; Le-Cao et al., 2010; Ho-Minh et al., 2010) and the multiscale macro-micro approach (Tran-Canh and Tran-Cong, 2002b, 2004; Tran et al., 2009, 2011, 2012a; Nguyen et al., 2015a,b,c).

In this thesis, the IRBF scheme in our present multiscale methods is used not only to solve the macro governing equations of polymeric liquid and fibre suspension flows but also to approximate the field variables and their derivatives in the micro procedure.

1.6 Numerical methods for Stochastic differential equations (SDEs)

Recently, the stochastic theory has significantly contributed to the development of many disciplines such as applied mathematics, quantum physics, engineering mechanics, communication process and economics (Gardiner, 2004; Henderson and Plaschko, 2006). In particular, the incorporation of stochastic processes into polymer kinetic theory yields extraordinary successes in the simulation of polymer dynamics (Ottinger, 1996). Basically, a stochastic process can be interpreted in two approaches: Ito and Stratonovich SDE (Kloeden and Platen, 1992). Since the first one is more practical in the computation, a brief review of the Ito SDE and its numerical integration schemes are presented in this section. Other extension of the Ito SDEs related to this research will be presented in relevant chapters.

1.6.1 Introduction

Consider the multi-component SDE of an Ito process as follows.

$$d\mathbf{Q}\left(t\right)=\mathbf{A}\big(\mathbf{Q}\left(t\right),t\big)\,dt+\mathbf{B}\big(\mathbf{Q}\left(t\right),t\big)\,d\mathbf{W}\left(t\right), \tag{1.42}$$

where $\mathbf{A}$ is a d-dimensional column vector; $\mathbf{B}$ a $[d \times d]$ matrix; $\mathbf{A}\big(\mathbf{Q}(t), t\big)\,dt$ and $\mathbf{B}\big(\mathbf{Q}(t), t\big)\,d\mathbf{W}(t)$ the drift and the diffusion terms, respectively; and $\mathbf{W}(t)$ a d-dimensional Wiener process. In the case of $\mathbf{B} = \mathbf{0}$, Eq. (1.42) becomes a deterministic differential equation. In addition, if $\mathbf{B}$ is a function of $\mathbf{Q}(t)$, the SDE is a multiplicative random process, otherwise it is an additive random one. It is worth noting that the existence and uniqueness conditions of a SDE's solution, which are accepted in many applications of the kinetic theory (Ottinger, 1996), are also assumed in this thesis.

1.6.2 Numerical integration schemes

Several numerical integration schemes for the solution of SDEs can be classified into two main approaches: the stochastic theta (θ) method and the predictor-corrector method.

- **The stochastic theta method (STM):**

  Applying the STM with fixed step size Δt to Eq. (1.42) yields the following temporal discretisation

  $$\mathbf{Q}_{i+1} = \mathbf{Q}_i + (1-\theta)\,\mathbf{A}\left(\mathbf{Q}_i, t_i\right)\Delta t + \theta\mathbf{A}\left(\mathbf{Q}_{i+1}, t_{i+1}\right)\Delta t + \mathbf{B}\left(\mathbf{Q}_i, t_i\right)\Delta\mathbf{W}_i, \tag{1.43}$$

  where $t_i = i\Delta t$ and $t_{i+1} = (i+1)\Delta t$ are the times at step i and $i+1$, respectively; $\mathbf{Q}_i = \mathbf{Q}\left(t_i\right)$ and $\mathbf{Q}_{i+1} = \mathbf{Q}\left(t_{i+1}\right)$; $\Delta\mathbf{W}_i = \mathbf{W}_{i+1} - \mathbf{W}_i$ the increment of the Wiener process at two successive time steps; and θ a parameter in $[0,1]$. There are several numerical integration schemes corresponding to different values of θ as follows.

  - For $\theta = 0$, we have the explicit Euler-Maruyama method and Eq.(1.43) is given by

    $$\mathbf{Q}_{i+1} = \mathbf{Q}_i + \mathbf{A}\left(\mathbf{Q}_i, t_i\right)\Delta t + \mathbf{B}\left(\mathbf{Q}_i, t_i\right)\Delta\mathbf{W}_i; \tag{1.44}$$

  - For $\theta > 0$, the scheme is implicit. Especially, the scheme is fully implicit for the case of $\theta = 1$ and Eq.(1.43) is rewritten as follows.

    $$\mathbf{Q}_{i+1} = \mathbf{Q}_i + \mathbf{A}\left(\mathbf{Q}_{i+1}, t_{i+1}\right)\Delta t + \mathbf{B}\left(\mathbf{Q}_i, t_i\right)\Delta\mathbf{W}_i. \tag{1.45}$$

  It can be seen that the implicit method is applied only in the drift term but not in the diffusion one. For the Euler-Maruyama explicit scheme, the size of time step needs to be sufficiently small to ensure the numerical stability. Furthermore, the convergence order of the this method for SDEs is only 0.5 whereas it is of the order 1 for deterministic differential equations (Kloeden and Platen, 1992). The other methods with higher order Taylor approximation for SDEs can be found in Kloeden and Platen (1992); Ottinger (1996).

- **Predictor-corrector methods (PCMs):**

  PCMs are employed to enhance the stability in solving SDEs without the demand of a small time step. The methods consist of the following two steps:

  1. The predictor step uses the explicit scheme for (1.42) as follows.

     $$\mathbf{Q}^{*}_{i+1} = \mathbf{Q}_i + \mathbf{A}\left(\mathbf{Q}_i, t_i\right)\Delta t + \mathbf{B}\left(\mathbf{Q}_i, t_i\right)\Delta\mathbf{W}_i, \tag{1.46}$$

     where $\mathbf{Q}^{*}_{i+1}$ is a predicted solution of $\mathbf{Q}_{i+1}$;

  2. The corrector step uses the implicit scheme, in which the predicted value $\mathbf{Q}^{*}_{i+1}$ is employed instead of $\mathbf{Q}_{i+1}$ on the right-hand side of the corrector step. The corrected value is given by

     $$\begin{aligned}\mathbf{Q}_{i+1} = \mathbf{Q}_i &+ \Big\{\theta\mathbf{A}\left(\mathbf{Q}^{*}_{i+1}, t_{i+1}\right) + (1-\theta)\,\mathbf{A}\left(\mathbf{Q}_i\right), t_i\Big\}\Delta t_i \\ &+ \Big\{\theta'\mathbf{B}\left(\mathbf{Q}^{*}_{i+1}, t_{i+1}\right) + \left(1-\theta'\right)\mathbf{B}\left(\mathbf{Q}_i\right), t_i\Big\}\Delta\mathbf{W}_i,\end{aligned} \tag{1.47}$$

  where θ and θ' are parameters defined in $[0,1]$. Owing to the presence of the corrector step which is implicit in nature, the stability of the method is enhanced. In addition, the difference between $\mathbf{Q}^{*}_{i+1}$ and $\mathbf{Q}_{i+1}$ from the two steps can be used to assess the local error at each time step.

1.7 Outline of the Thesis

The present thesis is organised as follows.

- Chapter 2 presents an efficient CG method for the simulation of dilute polymer solution flows. The method is based on the combination of high-order IRBF schemes and the Brownian configuration field approach, namely the IRBF-BCF multiscale method. In this chapter, the polymer solutions are modelled by complex bead-spring chain models with the presence of all nonlinear properties such as the finitely extensible nonlinear elastic spring force, the hydrodynamic interaction, and the excluded volume. The method efficiency is verified by comparing the obtained results for the creeping flow and several transient flows with a range of Weissenberg numbers with those in the literature (Nguyen et al., 2015b).

- Chapter 3 reports the simulation of polymer melt systems using the IRBF-BCF multiscale method presented in Chapter 2. In this chapter, a damping parameter is introduced into the macro governing equations to improve the stability of the solutions of primitive variables (**u**-p). These transformed equations are then solved by the IRBF based projection method. In the microscopic procedure, the classical reptation models are used to predict the dynamic behaviours of polymer melts. Some test and benchmark problems, namely the start-up Couette flow and the flow over a cylinder in a channel, are carried out to demonstrate the efficiency of the method (Nguyen et al., 2016a).

- Chapter 4 is to develop a new multiscale simulation method for dilute fibre suspension flows. The method is based on the marriage of the 1D-IRBF scheme, the discrete adaptive viscoelastic stress splitting (DAVSS) technique and the BCF idea. In the work, the macro governing equations are expressed by the vorticity-stream function ($\omega-\Psi$) formulation. The DAVSS transformation is introduced into the momentum equation to maintain the stability of the solution. In the micro procedure, the evolution equation for fibre configuration fields governed by the Jeffery equation and the Lipscomb model are used to determine the fibre stress using the BCF approach. Some test and benchmark problems, namely the flow between two parallel plates, the flow through a circular tube, and the 4.5:1 and 4:1 contraction flows, are simulated to demonstrate the method efficiency (Nguyen et al., 2015a).

- Chapter 5 is to report the application of the method introduced in Chapter 4 to simulate 'non-dilute' fibre suspension flows. In this chapter, the contraction and expansion flow problems are investigated with a range of volume fractions and fibre aspect ratios covering the semi-dilute and concentrated regimes. In addition, the dynamic behaviours of the flows and the orientation of fibres are also studied with different values of Reynolds numbers and fibre parameters. Some test and benchmark problems, namely the flow through a circular tube, the 4:1 axisymmetric contraction flow and the 1:4 axisymmetric expansion flow, are carried out to demonstrate the working of the method (Nguyen et al., 2016b).

- Chapter 6 presents a numerical solution based on the Fokker-Planck equation for polymer solutions. In this chapter, the FPE based macro-micro multiscale models for dilute polymer solution are simulated by the high-order IRBF collocation scheme. In this approach, both the macro governing equations and the FPE are discretised using the 1D-IRBF approach. The method is verified through the solution of several test problems including the startup Couette flow with the Hookean and FENE dumbbell models (Nguyen et al., 2014).

- Chapter 7 gives some concluding remarks on the contributions and achievements of this research, and some recommendations for future works.

Chapter 2

RBFN stochastic coarse-grained method for the simulation of dilute polymer solutions using nonlinear BSC models

In this chapter, dynamic behaviours of dilute polymer solutions of various bead-spring chain (BSC) models in shear flows are studied using a coarse-grained (CG) method based on the integrated radial basis function networks (IRBFNs) and stochastic technique (Nguyen et al., 2015b). The velocity field governed by the macroscopic conservation equations is determined by the IRBFN-based method, whereas the evolution of configurations of polymer chains governed by the stochastic differential equations (SDEs) is captured by the Brownian configuration field (BCF) approach. The system of micro-macro equations is closed by the Kramers expression, which allows for the determination of the polymer stresses in terms of BCF configurations. In this work, all nonlinear effects in a BSC model such as the finitely extensible nonlinear elastic (FENE) spring force, the hydrodynamic interaction (HI) and the excluded volume (EV) effects between beads in the same chain, are considered. Since the simulation requires a considerable computational effort, parallel calculations are performed where possible. As an illustration of the method, the start-up planar Couette flow is examined, in which the evolution of viscometric functions such as shear stress, the first and the second normal stress differences is assessed with various BSC models.

2.1 Introduction

A polymer solution may be modelled as polymer chains suspended in a solvent. Polymer chains are represented by particles connected by some connector force laws. Several kinds of polymer chains have been used in polymer rheology as CG models of macromolecules, for example, the bead-rod chain, the BSC, and the worm-like chain. The BSC is a simple CG model of a polymer molecule, which can capture most of the important nonlinear rheological properties of polymer solution (Bird et al., 1987b). Recently, the CG simulation methods have been developed and applied in several scientific and engineering areas because of their advantages in the simulation of soft matters, including complex viscoelastic fluids (Phan-Thien, 2012). Stochastic multiscale methods have also been introduced to model the constitutive relations and mechanical behaviour of concretes (Liu et al., 2013, 2014a,b). For polymeric fluids, the main idea of this approach is that the polymer-contributed stress is calculated averagely from a large ensemble of configurations of microstructures, which describe the real molecules existing in the polymer solutions. Meanwhile, the velocity field is determined by discretising the conservation equations. One scheme of this approach, namely the CONNFFESSIT (Laso and Ottinger, 1993; Ottinger, 1996), is a stochastic macro-micro multiscale simulation method. Another scheme, known as the BCF approach (Hulsen et al., 1997), is based on the idea of an ensemble of configuration fields instead of using a collection of individual micro elements as in the CONNFFESSIT. In an alternative approach, the combination of the radial basis function networks (RBFN) and the stochastic CG method has been suggested by Tran-Canh and Tran-Cong (2002b). The method overcame the difficulties of complex meshing task by discretising the conservation equations on a set of collocation points using the high-order RBFN approximation. As a result, the computed global stress tensor and velocity field with respect to time are very smooth. Furthermore, with a rather coarse set of collocation points, the method showed a stable and accurate solution for a range of problems, including planar Couette flow, Poiseuille flow, lid-driven cavity flow and 10 : 1 planar contraction flow (Tran-Canh and Tran-Cong, 2002b, 2004; Tran et al., 2009). Recently, the method was further improved by introducing the IRBF-based approximation instead of the differentiated/original RBF-based techniques to decrease the white noise in the stochastic simulation and increase the convergence rate of numerical solutions (Tran et al., 2011, 2012a). In this chapter, more complex BSC models are used to investigate the efficiency and adaptability of the IRBF-based stochastic CG method in the simulation of polymer solutions.

In the context of polymer kinetic theory, the simplest BSC model is the Rouse one, which represents the real polymer chain by a set of identical dumbbells, each of which consists of two beads linked by a Hookean spring (Rouse and Prince, 1953). This model is very straightforward and is set up easily in Brownian dynamic simulations. However, the ability of the Rouse model to capture the properties of viscoelastic fluids or polymer solutions is very limited. There are only a few basic features of the dilute solution able to be predicted through the Rouse model, for example, the existence of a constant nonzero value of the first normal stress difference. However, other features, for example, the appearance of the nonzero second normal stress difference and the shear rate dependence of the viscometric functions cannot be predicted by the Rouse model (Bird et al., 1987b; Prakash, 2001). These limitations are due to (i) the existence of the Hookean law for the springs in the Rouse model, which can make the chain become infinitely extensible in shear/elongational flows and (ii) the neglect of intramolecular interactions of beads in a polymer chain such as HI and EV effects. In order to improve the performance of the Rouse model, HI effect has been included in computational models in the equilibrium averaged form by Zimm (1956). As a result, the Zimm model has given better predictions of several properties of a polymer solution such as the diffusion coefficient and the relaxation time which are dependent on the molecular weight. Since both the Rouse and Zimm models are not successful in predicting the nonvanishing second normal stress difference as well as the dependence of viscometric functions on shear rate, the FENE spring-force law has been developed to resolve the limits of the Hookean-based BSC models (Wedgewood et al., 1991; Herrchen and Ottinger, 1997). A number of significant advancements of the BSC model have been recently achieved to relevantly examine the effects of the intramolecular forces on the motion of molecular chains (Ottinger, 1987b, 1989b; Magda et al., 1988). These improvements are very useful to predict the material properties of viscoelastic fluid flows and polymer solutions. By incorporating HI and EV into the simulation, the rheological characteristics including the existence of the second normal stress difference or the shear dependence of viscometric functions are accurately forecast (Ottinger, 1989b; Zylka, 1991; Prakash, 2001). Thus, the obtained results from the simulation are now able to be compared directly with those achieved from experiments. However, the considerable consumption of time and computer resources is a major hindrance in this simulation approach because the nonlinear intramolecular forces of each pair of beads in a chain need to be calculated successively at each time step. This barrier can be overcome by introducing a parallel calculation into the simulation. Hence, the aim of this chapter is to predict some rheological properties of polymer solutions in start-up shear flows, in which all nonlinear effects such as spring force laws, HI and EV are included using the IRBF-based stochastic CG method, taking advantage of parallel computation where possible.

The chapter is organised as follows. Section 2.2 gives a short review of the governing equations of incompressible polymeric fluid flows using the CG approach. In Section 2.3, a stochastic CG simulation method is described in which the BCF technique for the computation of the polymer contributed stress is presented using different BSC models with/without nonlinear effects such as the HI and the EV. Specifically, the coupled macro-micro multiscale system for the BSC model is introduced together with its dimensionless forms in Section 2.4. In Section 2.5, the IRBF-based discretisation of governing macroscopic equations is introduced in details, followed by the explicit integration scheme for microscopic equations. A parallel computation for the microscopic simulation is also presented in this section. Numerical examples and obtained results are discussed in Section 2.6. Finally, the chapter is closed by several concluding remarks in Section 2.7.

2.2 Coarse-grained (CG) models based simulation approach

As introduced in Section 1.2.2, the mass and momentum conservation equations of an isothermal and incompressible dilute polymer solution are written as follows.

$$\nabla \cdot \mathbf{u} = 0, \tag{2.1}$$

$$\rho \left(\frac{\partial \mathbf{u}}{\partial t} + \mathbf{u} \cdot \nabla \mathbf{u} \right) = \nabla \cdot \boldsymbol{\sigma}, \tag{2.2}$$

where ρ is the fluid density; $\mathbf{u}$ the velocity field; t the time; and $\boldsymbol{\sigma}$ is the total stress tensor and given by

$$\boldsymbol{\sigma} = -p\mathbf{I} + \boldsymbol{\tau}_s + \boldsymbol{\tau}_p, \tag{2.3}$$

where $\boldsymbol{\tau}_s = 2\eta_s\mathbf{D}$ and $\boldsymbol{\tau}_p$ are stress components contributed by Newtonian solvent and polymer, respectively; η_s the solvent viscosity; $\mathbf{D} = \frac{1}{2}\left(\nabla\mathbf{u} + (\nabla\mathbf{u})^T\right)$ the rate of strain tensor; p the hydrostatic pressure; and $\mathbf{I}$ the unit tensor.

In a stochastic CG simulation method, the polymer-contributed stress ($\boldsymbol{\tau}_p$) can be calculated by directly solving the Fokker-Planck equation or the corresponding SDEs. The coupling of the conservation equations (Eqs. (2.1)-(2.2)) and the equations expressing the evolution of grain configurations forms the basis for stochastic CG methods (Ottinger, 1996). In this work, the BCF-based stochastic CG method is used to describe the evolution of CG structures, and the non-Newtonian contribution to the stress is deduced from the evolution of CG configurations. This chapter focuses on considering BSC models (Fig. 2.1) with the effects of EV and HI.

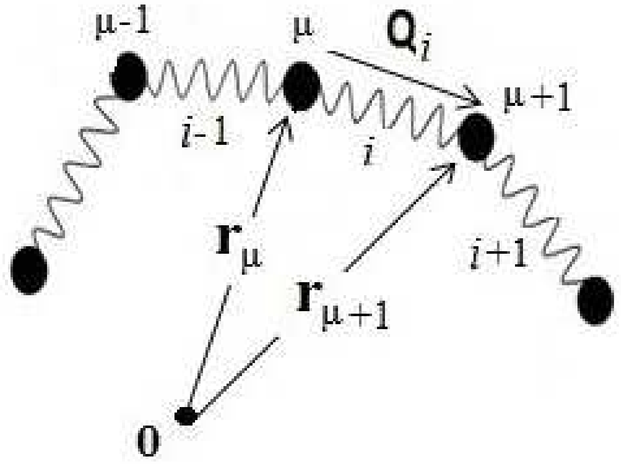

Figure 2.1: Schema of a BSC model. The Latin subscripts (i, j, k, ...) of a tensor/vector denote springs while the Greek ones (μ, ν, ...) denote beads in a polymer chain; $\mathbf{Q}_i = \mathbf{r}_{\mu+1} - \mathbf{r}_\mu$.

2.3 A BCF-based stochastic CG method for BSC models

In the BCF approach, the general BSC model with all nonlinear effects, including HI and EV for the evolution of a connector vector $\mathbf{Q}_i$, is given as follows. (Prabhakar and Prakash, 2004).

$$\begin{aligned} d\mathbf{Q}_i = &\left[-\mathbf{u} \cdot \nabla \mathbf{Q}_i + (\nabla \mathbf{u})^T \cdot \mathbf{Q}_i + \frac{1}{\zeta} \sum_{\nu=1}^{N_b} \left(\boldsymbol{\Upsilon}_{(\mu+1)\nu} - \boldsymbol{\Upsilon}_{\mu\nu} \right) \cdot \mathbf{F}_\nu^\phi \right] dt + \\ &\sqrt{\frac{2k_BT}{\zeta}} \sum_{\nu=1}^{N_b} \left(\mathbf{B}_{(\mu+1)\nu} - \mathbf{B}_{\mu\nu} \right) \cdot d\mathbf{W}_\nu, \end{aligned} \tag{2.4}$$

where subscript i denotes the index of connecting vectors ($i = 1, \ldots, N_s$); subscript μ indicates the index of beads ($\mu = 1, \ldots, N_b$), $\mu = i$; N_s and $N_b = N_s + 1$ are the numbers of springs and beads, respectively, in a polymer chain; $\mathbf{u}$ the velocity field; ζ the friction coefficient of the solvent; k_B the Boltzmann constant; T the absolute temperature of the solution; and $\mathbf{W}_\nu$ is the Wiener process defined by an independent Gaussian variable with zero mean and dt variance. $\boldsymbol{\Upsilon}_{\mu\nu}$ is the diffusion tensor and given by

$$\boldsymbol{\Upsilon}_{\mu\nu} = \delta_{\mu\nu} \mathbf{I} + \zeta \boldsymbol{\Omega}_{\mu\nu}, \tag{2.5}$$

where $\mathbf{\Omega}_{\mu\nu}$ and $\delta_{\mu\nu}$ are the hydrodynamic interaction tensor and the Kronecker delta, respectively. $\mathbf{\Omega}_{\mu\nu}$ is a function of vector $\mathbf{r}_{\mu\nu}$ ($\mathbf{r}_{\mu\nu} = \mathbf{r}_\nu - \mathbf{r}_\mu$) of the two beads μ and ν. It is worth noting that if μ and ν are two adjacent beads then $\mathbf{r}_{\mu\nu}$ is the connector vector of spring ($\mathbf{Q}$) between the two beads (Fig. 2.1). $\mathbf{B}_{\mu\nu}$ is a second-order tensor and determined by $\mathbf{\Upsilon}_{\mu\nu} = \mathbf{B}_{\mu\nu} \cdot \mathbf{B}^T_{\mu\nu}$. In the SDE (2.4), $\mathbf{F}^\phi_\nu$ is the intramolecular interaction force, defined as $\mathbf{F}^\phi_\nu = -\frac{\partial \phi}{\partial \mathbf{r}_\nu}$ and includes two components written as follows.

$$\mathbf{F}^\phi_\nu = \mathbf{F}^S_\nu + \mathbf{F}^E_\nu, \tag{2.6}$$

where ϕ is the potential energy; $\mathbf{F}^E_\nu$ is the excluded volume force on bead ν by other beads in a chain; and $\mathbf{F}^S_\nu$ is the spring force by springs connected to bead ν and given by

$$\mathbf{F}^S_\nu = \begin{cases} \mathbf{F}^D_1 & \text{if } \nu = 1, \\ \mathbf{F}^D_k - \mathbf{F}^D_{k-1} & \text{if } 1 < \nu < N_b, \\ -\mathbf{F}^D_{N_s} & \text{if } \nu = N_b, \end{cases} \tag{2.7}$$

where $\mathbf{F}^D_k$ is the force of spring k on bead ν and depends on the kinetic model of polymer used. For example, the spring forces of the Hookean and FENE dumbbells are given, respectively, as follows.

$$\mathbf{F}^D_k = H\mathbf{Q}_k, \qquad \mathbf{F}^D_k = \frac{H\mathbf{Q}_k}{1 - \frac{Q_k^2}{b_0}}, \tag{2.8}$$

where H is the spring constant; $\mathbf{Q}_k$ ($\mathbf{Q}_k = \mathbf{r}_{\nu+1} - \mathbf{r}_\nu$) the connector vector of the k^{th} spring (see Fig. 2.1); Q_k the norm of $\mathbf{Q}_k$; and b_0 the square of dimensional maximum length/extension of the k^{th} spring for the FENE dumbbell.

The system of multiscale governing equations Eqs. (2.1), (2.2) and (2.4) are closed by a connecting equation which determines the polymer stress contribution. For a CG model with intramolecular forces, the connecting equation known as Kramers expression is given by (Bird et al., 1987b; Prakash, 2002)

$$\boldsymbol{\tau}_p = (N_b - 1)\, n_p k_B T \mathbf{I} - n_p \sum_{k=1}^{N_s} \left\langle \mathbf{Q}_k \mathbf{F}^D_k \right\rangle + \mathbf{Z}, \tag{2.9}$$

where n_p is the number of polymer chains in a unit volume and the other parameters were defined as before. On the right-hand side of Eq. (2.9), the first term is the stress caused by the motion of beads in a polymer chain (Ottinger, 1996), the second term results from spring forces and the last term is produced by excluded volume interaction forces and given by (Prakash, 2002)

$$\mathbf{Z} = n_p \sum_{\nu=1}^{N_b} \sum_{k=1}^{N_s} D_{\nu k} \left\langle \mathbf{Q}_k \mathbf{F}_{\nu}^{E} \right\rangle , \tag{2.10}$$

where $D_{\nu k}$ are the entries of matrix $\mathbf{D}_{\nu k}$ of dimension $N_b \times N_s$ and defined as $D_{\nu k} = \left(k/N_b\right) - \Theta\left(k - \nu\right)$ where $\Theta\left(k - \nu\right)$ is the Heaviside function.

2.3.1 Nonlinear properties of bead-spring chain (BSC) model

Hydrodynamic interaction (HI) effect

HI is an indirect influence by the motion of beads through a solvent. Indeed, a bead moving in the solvent causes perturbations in the flow, which will influence the motions of remaining beads in the chain. The HI effect is incorporated into BSC models by introducing a hydrodynamic tensor $\mathbf{\Omega}_{\mu\nu}$ into the equation of motion of beads. This tensor expresses the relationship between the force $\mathbf{F}_\nu$ exerted on bead ν and the velocity perturbation by other beads μ's in a polymer chain $\Delta\mathbf{u}\left(\mathbf{r}_\mu\right)$ $(\mu = 1, \cdots, N_b$ and $\mu \neq \nu)$ as follows.

$$\Delta\mathbf{u}\left(\mathbf{r}_\mu\right) = \mathbf{\Omega}_{\mu\nu} \cdot \mathbf{F}_\nu\left(\mathbf{r}_\nu\right) . \tag{2.11}$$

A hydrodynamic tensor proposed by Rotne-Prager-Yamakawa (RPY) is given by (Rotne and Prager, 1969; Yamakawa, 1971)

$$\mathbf{\Omega}_{\mu\nu} = \frac{1}{8\pi\eta_s r_{\mu\nu}} \mathbf{C}\left(\mathbf{r}_{\mu\nu}\right) , \tag{2.12}$$

with

$$\mathbf{C}\left(\mathbf{r}_{\mu\nu}\right)=\begin{cases}\left(1+\frac{2}{3}\frac{a_b^2}{r_{\mu\nu}^2}\right)\mathbf{I}+\left(1-\frac{2a_b^2}{r_{\mu\nu}^2}\right)\frac{\mathbf{r}_{\mu\nu}\mathbf{r}_{\mu\nu}}{r_{\mu\nu}^2} & \text{if } r_{\mu\nu}\geq 2a_b,\\ \frac{r_{\mu\nu}}{2a_b}\left[\left(\frac{8}{3}-\frac{3r_{\mu\nu}}{4a_b}\right)\mathbf{I}+\frac{r_{\mu\nu}^2}{4a_b}\frac{\mathbf{r}_{\mu\nu}\mathbf{r}_{\mu\nu}}{r_{\mu\nu}^2}\right] & \text{if } r_{\mu\nu}<2a_b,\end{cases}\tag{2.13}$$

where a_b is the bead radius defined by the Stokes law as $\zeta = 6\pi\eta_s a_b$; $\mathbf{r}_{\mu\nu}$ is the connecting vector between two beads μ and ν and $r_{\mu\nu}$ is the length/norm of vector $\mathbf{r}_{\mu\nu}$. An alternative formula of the hydrodynamic tensor $\mathbf{\Omega}_{\mu\nu}$ is established by Zimm (1956) as follows.

$$\mathbf{\Omega}_{\mu\nu}=\begin{cases}\frac{1}{6\pi\eta_s}\sqrt{\frac{2H}{\pi k_B T|\mu-\nu|}}\mathbf{I} & \text{if } \mu\neq\nu,\\ 0 & \text{if } \mu=\nu,\end{cases}\tag{2.14}$$

where all parameters were defined as before.

Excluded volume (EV) effect

The EV presence allows for an accurate prediction of the non-vanishing second normal stress difference and the shear rate dependence of viscometric functions of dilute polymer solutions. The EV effect can be incorporated into the simulation by introducing a force $\mathbf{F}_\nu^E$ in the convective term of Eq. (2.4). The force exerted on bead ν by the repulsive interactions from other beads μ's in the chain is written by (Prakash, 2001)

$$\mathbf{F}_\nu^E=-\frac{\partial E}{\partial \mathbf{r}_\nu}=-\sum_{\substack{\mu=1\\ \mu\neq\nu}}^{N_b}\frac{\partial}{\partial \mathbf{r}_\nu}E_{\mu\nu}\left(\mathbf{r}_{\mu\nu}\right),\tag{2.15}$$

where E is the EV potential energy; and $E_{\mu\nu}$ is the short-range function and given by (Prakash, 2002)

$$E_{\mu\nu}=\left(\frac{\overline{z}}{\overline{d}^{\,3}}\right)k_B T\exp\left(-\frac{H}{2k_B T}\frac{\mathbf{r}_{\mu\nu}^2}{\overline{d}^{\,2}}\right),\tag{2.16}$$

where $\bar{z}$ and $\bar{d}$ are the quantities characterizing the strength and the range of the EV interactions, respectively. For the FENE BSC model, the strength $\bar{z}$ and range $\bar{d}$ of EV interaction are given by

$$\bar{z} = \frac{z\chi^3}{\sqrt{N_b}}, \tag{2.17}$$

$$\bar{d} = K\bar{z}^{\ 1/5}, \tag{2.18}$$

where z is the solvent quality; K an arbitrary constant; and χ a known function of b_{BSC} and given spring force law. For example, $\chi = 1$ for the Hookean BSC model and $\chi = \left(\frac{b_{BSC}}{b_{BSC}+5}\right)$ for the FENE BSC model (Sunthar and Prakash, 2005).

2.3.2 A coupled stochastic multiscale system

Collecting the conservation equations (2.1)-(2.2), the total stress formula Eq. (2.3), the stochastic BCF equation (2.4) and the Kramers expression Eq. (2.9) yields a stochastic multiscale system as follows.

$$\nabla \cdot \mathbf{u} = 0, \tag{2.19}$$

$$\rho\frac{\partial \mathbf{u}}{\partial t} + \rho\left(\mathbf{u}\cdot\nabla\mathbf{u}\right) - \eta_s\Delta\mathbf{u} + \nabla p = \nabla\cdot\boldsymbol{\tau}_p, \tag{2.20}$$

$$\begin{aligned} d\mathbf{Q}_i = &\left[-\mathbf{u}\cdot\nabla\mathbf{Q}_i + (\nabla\mathbf{u})^T\cdot\mathbf{Q}_i + \frac{1}{\zeta}\sum_{\nu=1}^{N_b}\left(\boldsymbol{\Upsilon}_{(\mu+1)\nu} - \boldsymbol{\Upsilon}_{\mu\nu}\right)\cdot\mathbf{F}^{\phi}_{\nu}\right]dt+ \\ &\sqrt{\frac{2k_BT}{\zeta}}\sum_{\nu=1}^{N_b}\left(\mathbf{B}_{(\mu+1)\nu} - \mathbf{B}_{\mu\nu}\right)\cdot d\mathbf{W}_{\nu}, \end{aligned} \tag{2.21}$$

$$\boldsymbol{\tau}_p = \left(N_b - 1\right)n_pk_BT\mathbf{I} - n_p\sum_{k=1}^{N_s}\left\langle\mathbf{Q}_k\mathbf{F}^D_k\right\rangle + \mathbf{Z}, \tag{2.22}$$

where all parameters were defined as before.

2.4 Non-dimensionalisation

Let U be a characteristic velocity; $\eta_p = n_pk_BT\lambda_H$ the viscosity associated with the polymers; λ_H and $L = \sqrt{k_BT/H}$ the time scale and the characteristic length scale of the BSC polymer, respectively. Dimensionless variables are given as follows.

$$\mathbf{Q}_k^* = \frac{\mathbf{Q}_k}{L}, \quad \mathbf{u}^* = \frac{\mathbf{u}}{U}, \quad t^* = \frac{t}{\lambda_H}, \quad \boldsymbol{\tau}_p^* = \boldsymbol{\tau}_p \frac{L}{\eta_o U}, \tag{2.23}$$

where η_o ($\eta_o = \eta_s + \eta_p$) is the total viscosity of the solution.

The dimensionless numbers Re, We, and ε are defined respectively as follows (Ottinger, 1996; Laso and Ottinger, 1993).

$$Re = \frac{\rho U L}{\eta_o} \,(\text{Reynolds number}), \quad We = \frac{\lambda_H U}{L} \,(\text{Weissenberg number}), \quad \varepsilon = \frac{\eta_p}{\eta_o}.$$

The stochastic multiscale system Eqs. (2.19)-(2.22) is rewritten in the dimensionless form as follows.

$$\nabla^* \cdot \mathbf{u}^* = 0, \tag{2.24}$$

$$Re\frac{\partial \mathbf{u}^*}{\partial t^*} + Re\,(\mathbf{u}^* \cdot \nabla^* \mathbf{u}^*) - (1-\varepsilon)\Delta^* \mathbf{u}^* + \nabla^* p^* = \nabla^* \cdot \boldsymbol{\tau}_p^*, \tag{2.25}$$

$$\begin{aligned} d\mathbf{Q}_i^* = &\Bigg[-\mathbf{u}^* \cdot \nabla^* \mathbf{Q}_i^* + (\nabla^* \mathbf{u}^*)^T \cdot \mathbf{Q}_i^* + \frac{1}{4We} \sum_{\nu=1}^{N_b} \Big(\boldsymbol{\Upsilon}^*_{(\mu+1)\nu} - \\ &\boldsymbol{\Upsilon}^*_{\mu\nu} \Big) \cdot \mathbf{F}_\nu^{\phi *} \Bigg] dt^* + \sqrt{\frac{1}{2We}} \sum_{\nu=1}^{N_b} \Big(\mathbf{B}^*_{(\mu+1)\nu} - \mathbf{B}^*_{\mu\nu} \Big) \cdot d\mathbf{W}_\nu^*, \end{aligned} \tag{2.26}$$

$$\boldsymbol{\tau}_p^* = \frac{\epsilon}{\widetilde{We}} \left[(N_b - 1)\,\mathbf{I} - \sum_{k=1}^{N_s} \left\langle \mathbf{Q}_k^* \mathbf{F}_k^{D*} \right\rangle + \mathbf{Z}^* \right], \tag{2.27}$$

where $\widetilde{We}$ is defined as $We\frac{(N_s+1)^2-1}{3+15/b_{BSC}}$; and $b_{BSC} = \frac{Hb_0}{k_B T}$ the square of maximum dimensionless extension of each spring in the chain (Wiest and Tanner, 1989). The other dimensionless quantities associated with the dimensional ones including $\boldsymbol{\Upsilon}_{\mu\nu}$, $\mathbf{B}_{\mu\nu}$ and $\mathbf{W}_\nu$ were defined as before. It is worth noting that $\lambda_H = \frac{\lambda_H^D}{d}$ where $\lambda_H^D = \zeta/4H$ is the Hookean/FENE dumbbell relaxation time and coefficient d is given by

$$d = \left[\frac{b_{BSC}(b_D + 7)}{15 b_D (b_{BSC} + 5)} \right] \left[2\,(N_s + 1)^2 + 7 - \frac{12\left((N_s+1)^2 + 1\right)}{(N_s+1)(b_{BSC}+7)} \right],$$

where b_D is the square of dimensionless maximum extension of FENE dumbbell model and defined as $b_D = b_{BSC} N_s$ (Koppol et al., 2007).

The dimensionless form of Hookean and FENE spring forces $\mathbf{F}_k^D$ (Eq. (2.8)) and the EV-contributed stress component $\mathbf{Z}$ (Eq. (2.10)) are respectively rewritten as follows.

$$\mathbf{F}_k^{D*} = \mathbf{Q}_k^*, \tag{2.28}$$

$$\mathbf{F}_k^{D*} = \frac{\mathbf{Q}_k^*}{1 - \frac{\mathbf{Q}_k^{*2}}{b_{BSC}}}, \tag{2.29}$$

$$\mathbf{Z}^* = \sum_{\nu=1}^{N_b} \sum_{k=1}^{N_s} D_{\nu k} \left\langle \mathbf{Q}_k^* \mathbf{F}_\nu^{E*} \right\rangle, \tag{2.30}$$

where the dimensionless form of the volume force $\mathbf{F}_\nu^{E*}$ is given by

$$\mathbf{F}_\nu^{E*} = - \sum_{\substack{\mu=1 \\ \mu \neq \nu}}^{N_b} \frac{\partial}{\partial \mathbf{r}_\nu^*} E_{\mu\nu}^* \left(\mathbf{r}_{\mu\nu}^* \right), \tag{2.31}$$

with

$$E_{\mu\nu}^* = \left(\frac{\bar{z}}{\bar{d}^3} \right) \exp \left(- \frac{1}{2} \frac{\mathbf{r}_{\mu\nu}^{*2}}{\bar{d}^2} \right). \tag{2.32}$$

The RPY hydrodynamic tensor in Eq. (2.12) is expressed in the dimensionless form as follows (Prabhakar and Prakash, 2004).

$$\zeta \boldsymbol{\Omega}_{\mu\nu}^* = \frac{3\sqrt{\pi}\bar{h}}{4 r_{\mu\nu}^*} \mathbf{C}^* \left(\mathbf{r}_{\mu\nu}^* \right), \tag{2.33}$$

with

$$\mathbf{C}^* \left(\mathbf{r}_{\mu\nu}^* \right) = \begin{cases} \left(1 + \frac{2\pi}{3} \frac{\bar{h}^2}{r_{\mu\nu}^{*2}} \right) \mathbf{I} + \left(1 - \frac{2\pi \bar{h}^2}{r_{\mu\nu}^{*2}} \right) \mathbf{pp}, & \text{if } r_{\mu\nu}^* \geq 2\sqrt{\pi}\bar{h}, \\ \frac{r_{\mu\nu}^*}{2\sqrt{\pi}\bar{h}} \left(\frac{8}{3} - \frac{3}{4} \frac{r_{\mu\nu}^*}{\sqrt{\pi}\bar{h}} \right) \mathbf{I} + \frac{r_{\mu\nu}^{*2}}{8\pi\bar{h}} \mathbf{pp}, & \text{if } r_{\mu\nu}^* < 2\sqrt{\pi}\bar{h}, \end{cases} \tag{2.34}$$

where $\bar{h}$ is the HI parameter and chosen within $[0.1, 0.3]$ (Ottinger, 1987a); $\mathbf{p}$ the unit vector ($\mathbf{p} = \mathbf{r}_{\mu\nu}^* / r_{\mu\nu}^*$); and $r_{\mu\nu}^*$ the norm of $\mathbf{r}_{\mu\nu}^*$. Other parameters were defined as before.

Henceforth, all variables will be written in the dimensionless form and the asterisk symbol will be removed for simplicity.

2.5 Numerical discretisation schemes

In this section, numerical schemes for the solution of the macro-micro system of differential equations are presented. Specifically, the deterministic PDEs (continuity and momentum equations) are approximated by a semi-implicit method based on IRBFNs while the evolution of the SDEs is determined using the Euler-Maruyama explicit scheme.

2.5.1 IRBF-based method for solution of the macroscopic governing equations

Consider the conservation equations (2.24)-(2.25). In order to solve this system, the problem domain is discretised using a set of nodal points, called the macro-scale grid. Here, instead of using the continuity equation (2.24), the incompressibility condition is enforced via the penalty method as follows (Laso et al., 1997; Tran-Canh and Tran-Cong, 2004).

$$p = -p_e \nabla \cdot \mathbf{u}, \tag{2.35}$$

where p_e is a sufficiently large penalty parameter. Eqs. (2.24)-(2.25) and Eq. (2.35) yield the following equation

$$Re \frac{\partial \mathbf{u}}{\partial t} + Re\left(\mathbf{u} \cdot \nabla \mathbf{u}\right) - (1-\varepsilon)\Delta \mathbf{u} - p_e \nabla \left(\nabla \cdot \mathbf{u}\right) = \nabla \cdot \boldsymbol{\tau}_p. \tag{2.36}$$

In this work, the one-dimensional IRBFN (1D-IRBFN) based semi-implicit scheme is employed to discretise the governing equation and presented in the next subsections.

Spatial discretisation

Consider a two-dimensional (2-D) rectangular domain which is discretised by a uniform $N_x \times N_y$ Cartesian grid, where N_x and N_y are the number of grid points on x-direction and y-direction, respectively. All grid points are assumed to be numbered from bottom to top and from left to right.

At a time t, the second-order derivative of a dependent variable $u\left(x,t\right)$ along an x-gridline is decomposed as follows (Mai-Duy and Tanner, 2007).

$$\frac{\partial^2 u}{\partial x^2} = \sum_{j=1}^{N_x} w_j\left(t\right) g_j\left(x\right) = \sum_{j=1}^{N_x} w_j\left(t\right) G_j^{[2]}\left(x\right), \tag{2.37}$$

where $\left\{w_j\left(t\right)\right\}_{j=1}^{N_x}$ and $\left\{g_j\left(x\right)\right\}_{j=1}^{N_x}$ are the set of RBF weights and the set of RBFs, respectively. In this research, the multiquadric RBFs (MQ-RBFs) is employed to approximate (i) the velocity field in the macroscopic conservation equations and (ii) gradient of the stress field, and given by

$$g_j\left(x\right) = \sqrt{(x-c_j)^2 + a_j^2}, \tag{2.38}$$

where $\left\{c_j\right\}_{j=1}^{N_x}$ and $\left\{a_j\right\}_{j=1}^{N_x}$ are RBF centres and widths, respectively. The centres are chosen to be the same as the data points x_j in this work.

The corresponding first-order derivative and function itself are then determined through the direct integration as follows.

$$\frac{\partial u}{\partial x} = \sum_{j=1}^{N_x} w_j\left(t\right) G_j^{[1]}\left(x\right) + C_1\left(t\right), \tag{2.39}$$

$$u\left(x,t\right) = \sum_{j=1}^{N_x} w_j\left(t\right) G_j^{[0]}\left(x\right) + C_1\left(t\right)x + C_2\left(t\right), \tag{2.40}$$

where $G_j^{[1]}\left(x\right) = \int G_j^{[2]}\left(x\right)dx$, $G_j^{[0]}\left(x\right) = \int G_j^{[1]}\left(x\right)dx$; and C_1 and C_2 are unknown integration constants at time t.

Collocating Eqs. (2.37), (2.39) and (2.40) at every grid point $\left\{x_j\right\}_{j=1}^{N_x}$ yields the following set of algebraic equations

$$\widehat{\frac{\partial^2 \mathbf{u}}{\partial x^2}} = \widehat{\mathbf{G}}^{[2]}\left(x\right)\widehat{\mathbf{w}}\left(t\right), \tag{2.41}$$

$$\widehat{\frac{\partial \mathbf{u}}{\partial x}} = \widehat{\mathbf{G}}^{[1]}\left(x\right)\widehat{\mathbf{w}}\left(t\right), \tag{2.42}$$

$$\widehat{\mathbf{u}} = \widehat{\mathbf{G}}^{[0]}(x)\,\widehat{\mathbf{w}}(t), \tag{2.43}$$

where

$$\widehat{\mathbf{G}}^{[i]} = \begin{bmatrix} G_1^{[i]}(x_1) & \cdots & G_{N_x}^{[i]}(x_1) & a_1^{[i]} & b_1^{[i]} \\ \vdots & \ddots & \vdots & \vdots & \vdots \\ G_1^{[i]}(x_{N_x}) & \cdots & G_{N_x}^{[i]}(x_{N_x}) & a_{N_x}^{[i]} & b_{N_x}^{[i]} \end{bmatrix}, \ i = 0, 1, 2 \tag{2.44}$$

with

$$\left(a_1^{[i]}, a_2^{[i]}, \ldots, a_{N_x}^{[i]}\right)^T = \begin{cases} (0 \ \cdots \ 0)^T, i = 2 \\ (1 \ \cdots \ 1)^T, i = 1 \\ (x_1 \ \cdots \ x_{N_x})^T, i = 0 \end{cases},$$

$$\left(b_1^{[i]}, b_2^{[i]}, \ldots, b_{N_x}^{[i]}\right)^T = \begin{cases} (0 \ \cdots \ 0)^T, i = 1, 2 \\ (1 \ \cdots \ 1)^T, i = 0 \end{cases},$$

$$\widehat{\mathbf{w}} = \begin{pmatrix} w_1(t) & w_2(t) & \cdots & w_{N_x}(t) & C_1(t) & C_2(t) \end{pmatrix}^T,$$

$$\widehat{\mathbf{u}} = \begin{pmatrix} u_1(t) & u_2(t) & \cdots & u_{N_x}(t) \end{pmatrix}^T,$$

$$\frac{\widehat{\partial^k \mathbf{u}}}{\partial x^k} = \begin{pmatrix} \frac{\partial^k u_1(x,t)}{\partial x^k} & \frac{\partial^k u_2(x,t)}{\partial x^k} & \cdots & \frac{\partial^k u_{N_x}(x,t)}{\partial x^k} \end{pmatrix}^T,$$

where $u_i = u(x_i)$ with $i = (1, 2, \ldots, N_x)$.

The presence of integration constants in the IRBFN based approximation yields beneficial mechanism for the incorporation of additional constraints such as nodal derivative values into the algebraic equation system. Thus, the algebraic equation system Eq. (2.43) can be reformulated as follows.

$$\begin{pmatrix} \widehat{\mathbf{u}} \\ \widehat{\mathbf{f}} \end{pmatrix} = \begin{bmatrix} \widehat{\mathbf{G}^{[0]}} \\ \widehat{\mathbf{L}} \end{bmatrix} \widehat{\mathbf{w}} = \widehat{\mathbf{C}}\widehat{\mathbf{w}},$$

where $\widehat{\mathbf{f}} = \widehat{\mathbf{L}}\widehat{\mathbf{w}}$ are additional constraints. The conversion of the network-weight space into the physical space yields

$$\widehat{\mathbf{w}} = \widehat{\mathbf{C}}^{-1} \begin{pmatrix} \widehat{\mathbf{u}} \\ \widehat{\mathbf{f}} \end{pmatrix}, \tag{2.45}$$

where $\widehat{\mathbf{C}}^{-1}$ is the conversion matrix. By substituting Eq. (2.45) into Eqs. (2.37) and (2.39), the second- and first-order derivatives of u will be expressed in terms of nodal variable values as follows.

$$\frac{\partial^2 u}{\partial x^2} = \mathcal{D}_{2x}\widehat{\mathbf{u}} + k_{2x}, \qquad \frac{\partial u}{\partial x} = \mathcal{D}_{1x}\widehat{\mathbf{u}} + k_{1x}, \tag{2.46}$$

where $\mathcal{D}_{1x}$ and $\mathcal{D}_{2x}$ are known vectors of length N_x; and k_{2x} and k_{1x} scalars determined by $\widehat{\mathbf{f}}$. Applying Eq. (2.46) at every collocation point on the gridline yields

$$\widehat{\frac{\partial^2 \mathbf{u}}{\partial x^2}} = \widehat{\mathcal{D}}_{2x}\widehat{\mathbf{u}} + \widehat{\mathbf{k}}_{2x}, \qquad \widehat{\frac{\partial \mathbf{u}}{\partial x}} = \widehat{\mathcal{D}}_{1x}\widehat{\mathbf{u}} + \widehat{\mathbf{k}}_{1x}, \tag{2.47}$$

where $\widehat{\mathcal{D}}_{2x}$ and $\widehat{\mathcal{D}}_{1x}$ are known matrices of dimension $N_x \times N_x$; and $\widehat{\mathbf{k}}_{2x}$ and $\widehat{\mathbf{k}}_{1x}$ known vectors of length N_x.

The values of the second- and first-order derivatives of u with respect to y along a vertical line can be expressed similarly as follows.

$$\widehat{\frac{\partial^2 \mathbf{u}}{\partial y^2}} = \widehat{\mathcal{D}}_{2y}\widehat{\mathbf{u}} + \widehat{\mathbf{k}}_{2y}, \qquad \widehat{\frac{\partial \mathbf{u}}{\partial y}} = \widehat{\mathcal{D}}_{1y}\widehat{\mathbf{u}} + \widehat{\mathbf{k}}_{1y}, \tag{2.48}$$

where $\widehat{\mathcal{D}}_{2y}$ and $\widehat{\mathcal{D}}_{1y}$ are known matrices of dimension $N_y \times N_y$; $\widehat{\mathbf{k}}_{2y}$ and $\widehat{\mathbf{k}}_{1y}$ known vectors of length N_y; and N_y the number of grid points on a vertical line as defined above.

For 2-D formulations, the values of the derivatives of u on the whole domain can be produced by using Kronecker tensor products as follows.

$$\begin{aligned}
\widetilde{\frac{\partial^2 \mathbf{u}}{\partial x^2}} &= \left(\widehat{\mathcal{D}}_{2x} \otimes \mathbf{I}_y\right)\widetilde{\mathbf{u}} + \widetilde{\mathbf{k}}_{2x} = \widetilde{\mathcal{D}}_{2x}\widetilde{\mathbf{u}} + \widetilde{\mathbf{k}}_{2x}, && (2.49)\\
\widetilde{\frac{\partial \mathbf{u}}{\partial x}} &= \left(\widehat{\mathcal{D}}_{1x} \otimes \mathbf{I}_y\right)\widetilde{\mathbf{u}} + \widetilde{\mathbf{k}}_{1x} = \widetilde{\mathcal{D}}_{1x}\widetilde{\mathbf{u}} + \widetilde{\mathbf{k}}_{1x}, && (2.50)\\
\widetilde{\frac{\partial^2 \mathbf{u}}{\partial y^2}} &= \left(\mathbf{I}_x \otimes \widehat{\mathcal{D}}_{2y}\right)\widetilde{\mathbf{u}} + \widetilde{\mathbf{k}}_{2y} = \widetilde{\mathcal{D}}_{2y}\widetilde{\mathbf{u}} + \widetilde{\mathbf{k}}_{2y}, && (2.51)
\end{aligned}$$

$$\widetilde{\frac{\partial \mathbf{u}}{\partial y}} = \left(\mathbf{I}_x \otimes \widehat{\mathcal{D}}_{1y}\right)\widetilde{\mathbf{u}} + \widetilde{\mathbf{k}}_{1y} = \widetilde{\mathcal{D}}_{1y}\widetilde{\mathbf{u}} + \widetilde{\mathbf{k}}_{1y}, \tag{2.52}$$

where $\mathbf{I}_x$ and $\mathbf{I}_y$ are the identity matrices of dimension $N_x \times N_x$ and $N_y \times N_y$, respectively; $\widetilde{\mathbf{k}}_{2x}$, $\widetilde{\mathbf{k}}_{1x}$, $\widetilde{\mathbf{k}}_{2y}$ and $\widetilde{\mathbf{k}}_{1y}$ known vectors of length N_xN_y; $\widetilde{\mathcal{D}}_{2x}$, $\widetilde{\mathcal{D}}_{1x}$, $\widetilde{\mathcal{D}}_{2y}$ and $\widetilde{\mathcal{D}}_{1y}$ known matrices of dimension $N_xN_y \times N_xN_y$; and $\widehat{\mathbf{u}} = \begin{pmatrix} u_1 & u_2 & \cdots & u_{N_xN_y}\end{pmatrix}^T$.

Time discretisation

A semi-implicit scheme (Crank-Nicolson) is employed to temporally discretise the momentum equation, which is solved for the velocity field u at each time step where the polymer contributed stress $\boldsymbol{\tau}_p$ is considered as a known variable from the microscopic procedure. Details will be presented in numerical examples in Section 2.6.

2.5.2 Euler-Maruyama explicit scheme for solving microscopic SDEs

The evolution of the configuration of polymer chains in Eq. (2.26) using the Euler-Maruyama explicit scheme is given by (Ottinger, 1996)

$$\begin{aligned} \mathbf{Q}_i^{n+1} = \mathbf{Q}_i^n + & \Bigg[(\nabla \mathbf{u}^{n+1})^T \cdot \mathbf{Q}_i^n - \mathbf{u}^{n+1} \cdot \nabla \mathbf{Q}_i^n + \\ & \frac{1}{4We} \sum_{\nu=1}^{N_b} \left(\boldsymbol{\Upsilon}^n_{(\mu+1)\nu} - \boldsymbol{\Upsilon}^n_{\mu\nu} \right) \cdot \mathbf{F}^{\phi}_{\nu} \Bigg] \Delta t + \\ & \sqrt{\frac{\Delta t}{2We}} \sum_{\nu=1}^{N_b} \left[\mathbf{B}^n_{(\mu+1)\nu} - \mathbf{B}^n_{\mu\nu} \right] \cdot \mathbf{W}_{\nu}, \end{aligned} \tag{2.53}$$

where superscripts n and $n+1$ denote two successive time steps at $t_n = n\Delta t$ and $t_{n+1} = (n+1)\Delta t$, respectively; Δt the time step size; $(\nabla \mathbf{u}^{n+1})^T$ the gradient of the known velocity field computed in the macroscopic procedure at the time step t_{n+1}; $\boldsymbol{\Upsilon}_{(\mu+1)\nu}$ and $\boldsymbol{\Upsilon}_{\mu\nu}$ the diffusion tensors; $\mathbf{F}^{\phi}_{\nu}$ the intramolecular forces; and $\mathbf{W}_{\nu}$ the three-dimensional (3-D) Wiener process at bead ν. The diffusion tensors and intramolecular forces are calculated based on the configuration of all BSCs at time step t_n. After a new configuration is obtained, the new polymer stress tensor is determined by Eq. (2.27) and its first-order derivative is approximated using MQ-RBF as presented in Section 2.5.1.

2.5.3 Parallel implementation

The stochastic macro-micro simulation requires considerable numerical computation. Furthermore, since the processing of tasks in the microscopic procedure dominates the throughput (Table 2.2), a parallel algorithm for the stochastic microscale simulation is incorporated into the present method to speed-up the computation. The stochastic tasks consist of: (i) solving SDEs and (ii) computing average stresses at collocation points. In general, these tasks are carried out independently for all configurations generated at each and every collocation point in the considered domain of a problem.

The parallel implementation of the algorithm is based on the message passing interface for parallel communication in Matlab environment. The implementation is carried out on the High Performance Computing system of the University of Southern Queensland whose details can be found in $http://hpc.usq.edu.au$. The parallelisation is established in regard to stochastic tasks at collocation points. In the framework of this chapter, several results on the efficiency and speed-up are presented for the FENE-based BSC model, taking into account the HI and EV effects and discussed in Section 2.6.4.

2.5.4 Algorithm of the present approach

The present simulation method can now be described in a more detailed algorithm as follows and the implementation will be expressed in the illustrative examples.

(a) Generate a set of collocation points. Start with a given initial condition for the first iteration (velocity field, BSC configurations) together with the given boundary conditions of the problem. In the present work, the initial conditions are zero initial velocity field, and initial BSC configurations sampled from equilibrium Gaussian distribution.

(b) Assign N_f BSCs of N_s springs to each collocation point. All BSCs having the same index constitute a configuration field. Hence, there is an ensemble of N_f configuration fields. Since all the BSCs having the same index receive the same random number, there is a strong correlation between BSCs in a configuration field.

(c) Solving the macro PDEs for the velocity field using the 1D-IRBFN collocation method described in Section 2.5.1.

(d) Solving the micro SDEs for the polymer configuration fields using the method presented in Section 2.5.2. As mentioned in step (a), in order to ensure strong correlation within a configuration field, all the BSCs of the same index have the same random number.

(e) Determine the polymer contributed stress by taking the ensemble average of the polymer BSC configurations at each collocation point $\mathbf{x}_i$, using Eq. (2.27). The tasks include the computation of the HI tensor (the RPY tensor in this work) and the EV interaction forces with regard to HI and EV effects, respectively.

Note: A parallel algorithm is installed within steps (d)-(e), see Section 2.5.3 for details.

(f) With the stress field just obtained, approximate the gradient of stress field using the IRBFNs and then solve the macroscopic governing equation (2.36) for the new velocity field by the 1D-IRBFN method described in Section 2.5.1;

(g) Terminate the simulation when either the desired time or convergence is reached. The latter is determined by a convergence measure (CM) for the velocity field, defined by

$$CM(\mathbf{u}) = \sqrt{\frac{\sum_1^N \sum_{i=1}^{d_s} \left(u_i^n - u_i^{n-1}\right)^2}{\sum_1^N \sum_{i=1}^{d_s} (u_i^n)^2}} \leq tol \tag{2.54}$$

where d_s is the number of dimensions; tol a preset tolerance; u_i the i-component of the velocity at a collocation point; N the total number of collocation points; and n the iteration number.

(h) Return to step (d) for the next time step of the microscopic procedure until a steady state or a given time is reached.

2.6 Numerical examples

The present method is employed to simulate the planar Couette flow described in Fig. 2.2 using several BSC models. This problem with simpler polymer models was earlier studied by Laso and Ottinger (1993); Mochimaru (1983); Tran-Canh and Tran-Cong (2002b, 2004). Koppol et al. (2007) studied the same problem using a finite element-based method.

Firstly, a creeping flow of viscoelastic fluid using FENE-BSC model which was considered in Koppol et al. (2007) is simulated to assess the validity of the present method. The problem is then further investigated with the Rouse and Zimm models to study the HI effect on the rheological properties of the flow. Finally, the start-up problem is solved using general BSC models with fully nonlinear effects.

The problem is defined as follows. For time $t < 0$, the fluid is at rest. At $t = 0$, the lower plate starts to move with a constant velocity $V = 1$. No-slip condition is assumed at the walls. The fluid parameters of each considered BSC model mentioned above are presented in the next subsections. A set of collocation points is initialised uniformly along the y direction. Then the same number of BSC configurations is initiated randomly on each and every collocation point (see Section 2.5.4, item a).

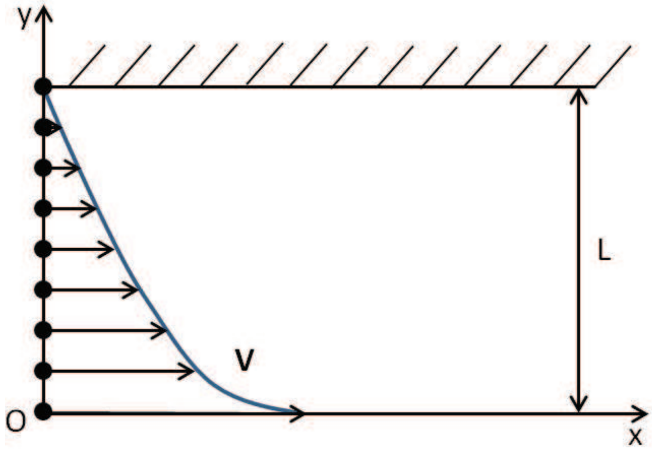

Figure 2.2: The start-up planar Couette flow problem. The collocation points and the velocity profile are only presented schematically.

The polymer stress field is calculated by Eq. (2.27) based on the initial BSC configurations. The obtained values by the microscopic procedure are located on the collocation points (i.e. micro-structural properties are transferred to a bulk property). These values at the grid points along with the boundary and initial conditions are used to start the simulation in the macroscopic procedure. The macroscopic governing equation is solved for the velocity field, and afterwards, the transpose of velocity gradient $(\nabla \mathbf{u})^T$ in the SDE (2.26) is defined by the IRBF-based approximation. All above calculations are repeated at each time step until the numerical convergence is satisfied.

2.6.1 Governing equations

From the characteristics of the start-up Couette flow of dilute polymer solution using the general BSC model, the system of stochastic multiscale equations (2.25)-(2.27) is developed as follows.

$$Re\frac{\partial u}{\partial t}(y,t) - (1-\varepsilon)\frac{\partial^2 u}{\partial y^2}(y,t) = \frac{\partial \tau_{p,xy}}{\partial y}(y,t), \tag{2.55}$$

$$\begin{aligned} dQ_{i,x}(y,t) = & \left[\frac{\partial u}{\partial y}(y,t)\, Q_{i,y}(y,t) + \frac{1}{4We}\sum_{\nu=1}^{N_b} \Delta \boldsymbol{\Upsilon}^{\nu,[1]}_{(\mu+1)\mu} \cdot \right. \\ & \left. \mathbf{F}^{\phi}_{\nu}\left(\mathbf{Q}_i(y,t)\right) \right] dt + \sqrt{\frac{1}{2We}} \sum_{\nu=1}^{N_b} \Delta \mathbf{B}^{\nu,[1]}_{(\mu+1)\mu} \cdot d\mathbf{W}_{\nu}, \end{aligned} \tag{2.56}$$

$$dQ_{i,y}\left(y,t\right)=\frac{1}{4We}\sum_{\nu=1}^{N_b}\Delta\boldsymbol{\Upsilon}^{\nu,[2]}_{(\mu+1)\mu}\cdot\mathbf{F}^{\phi}_{\nu}\left(\mathbf{Q}_i\left(y,t\right)\right)dt+ \sqrt{\frac{1}{2We}}\sum_{\nu=1}^{N_b}\Delta\mathbf{B}^{\nu,[2]}_{(\mu+1)\mu}\cdot d\mathbf{W}_{\nu}, \tag{2.57}$$

$$dQ_{i,z}\left(y,t\right)=\frac{1}{4We}\sum_{\nu=1}^{N_b}\Delta\boldsymbol{\Upsilon}^{\nu,[3]}_{(\mu+1)\mu}\cdot\mathbf{F}^{\phi}_{\nu}\left(\mathbf{Q}_i\left(y,t\right)\right)dt+ \sqrt{\frac{1}{2We}}\sum_{\nu=1}^{N_b}\Delta\mathbf{B}^{\nu,[3]}_{(\mu+1)\mu}\cdot d\mathbf{W}_{\nu}, \tag{2.58}$$

$$\boldsymbol{\tau}_{\mathrm{p}}=\frac{\epsilon}{\widetilde{We}}\left[\left(N_b-1\right)\mathbf{I}-\sum_{k=1}^{N_s}\left\langle\mathbf{Q}_k\mathbf{F}^{D}_{k}\right\rangle+\mathbf{Z}\right], \tag{2.59}$$

where u is the x-component of the velocity; $\boldsymbol{\tau}_p$ the polymer stress tensor including the shear stress $\tau_{p,xy}$; and $Q_{i,x}$, $Q_{i,y}$ and $Q_{i,z}$ the components of connector vector $\mathbf{Q}_i$ at location y. $\Delta\mathbf{H}^{\nu,[k]}_{(\mu+1)\mu}$ is row k ($k=1,2,3$) of matrix $\Delta\mathbf{H}^{\nu}_{(\mu+1)\mu}$ ($\mathbf{H}=\boldsymbol{\Upsilon}$ or $\mathbf{B}$) with $\Delta\mathbf{H}^{\nu}_{(\mu+1)\mu}=\mathbf{H}_{(\mu+1)\nu}-\mathbf{H}_{\mu\nu}$, $\mathbf{F}^{\phi}_{\nu}=\left(F^{\phi}_{\nu,x},F^{\phi}_{\nu,y},F^{\phi}_{\nu,z}\right)^T$; and $d\mathbf{W}_{\nu}=\left(dW_{\nu,x},dW_{\nu,y},dW_{\nu,z}\right)^T$.

Other parameters are defined as before. The discretisation of equations (2.55)-(2.58) are carried out through two interlaced procedures of different scales as presented in Section 2.5.4.

Discretisation of the macro-scale governing equation

Applying the Crank-Nicolson scheme for time discretisation of the macroscopic governing equation (2.55) yields

$$Re\frac{u^{n+1}-u^n}{\Delta t}-\frac{(1-\varepsilon)}{2}\frac{d^2u^{n+1}}{dy^2}=\frac{(1-\varepsilon)}{2}\frac{d^2u^n}{dy^2}+\frac{d\tau^n_{p,xy}}{dy},$$

or

$$\beta u^{n+1}-\alpha\frac{d^2u^{n+1}}{dy^2}=\alpha\frac{d^2u^n}{dy^2}+\frac{d\tau^n_{p,xy}}{dy}+\beta u^n, \tag{2.60}$$

where $\beta=Re/\Delta t$; $\alpha=0.5(1-\varepsilon)$; and other parameters as defined above.

Discretisation of the micro-scale stochastic governing equation

The equations (2.56)-(2.58) are discretised using the Euler explicit scheme with $N_f = 1024$ realizations of each random process as follows.

$$
\begin{aligned}
Q_{i,x}^{n+1} = Q_{i,x}^{n} + \frac{du^{n+1}}{dy} Q_{i,y}^{k,n} \Delta t + \frac{\Delta t}{4We} \sum_{\nu=1}^{N_b} \Delta \mathbf{\Upsilon}_{(\mu+1)\mu}^{\nu,[1]} \cdot \mathbf{F}_{\nu}^{\phi,n} + \\
\sqrt{\frac{\Delta t}{2We}} \sum_{\nu=1}^{N_b} \Delta \mathbf{B}_{(\mu+1)\mu}^{\nu,[1]} \cdot \mathbf{W}_{\nu}^{k,n},
\end{aligned} \tag{2.61}
$$

$$
Q_{i,y}^{n+1} = Q_{i,y}^{n} + \frac{\Delta t}{4We} \sum_{\nu=1}^{N_b} \Delta \mathbf{\Upsilon}_{(\mu+1)\mu}^{\nu,[2]} \cdot \mathbf{F}_{\nu}^{\phi,n} + \sqrt{\frac{\Delta t}{2We}} \sum_{\nu=1}^{N_b} \Delta \mathbf{B}_{(\mu+1)\mu}^{\nu,[2]} \cdot \mathbf{W}_{\nu}^{n}, \tag{2.62}
$$

$$
Q_{i,z}^{n+1} = Q_{i,z}^{n} + \frac{\Delta t}{4We} \sum_{\nu=1}^{N_b} \Delta \mathbf{\Upsilon}_{(\mu+1)\mu}^{\nu,[3]} \cdot \mathbf{F}_{\nu}^{\phi,n} + \sqrt{\frac{\Delta t}{2We}} \sum_{\nu=1}^{N_b} \Delta \mathbf{B}_{(\mu+1)\mu}^{\nu,[3]} \cdot \mathbf{W}_{\nu}^{n}, \tag{2.63}
$$

where all parameters were defined as above. The velocity field of the flow at the time t_{n+1} is given by either the initial conditions or the solution of the macro-scale procedure which was previously determined using the 1D-IRBFN method. The stress $\boldsymbol{\tau}_p$ is then calculated using the coupling equation (2.59).

2.6.2 Creeping flows of viscoelastic fluid using FENE-based BSC models

This problem was solved by Koppol et al. (2007) with the Reynolds number $Re = 0$ using the FENE-BSC model of $N_S = 1, 3, 6$-dumbbell chains and neglecting HI and EV effects. The parameters of the BSC model fluid include: the ratio of polymer viscosity and total viscosity of the fluid $\epsilon = 0.5$, the square of maximum extensibility of the FENE dumbbell model $b_D = 900$ and thus the square of maximum extension of each spring in the chain $b_{BSC} = b_D/N_s$, and the Weissenberg number of the flow $We = 5$. The SDE equation is developed for each dumbbell in a configuration of the 3-dumbbell BSC model as follows.

$$
d\mathbf{Q}_1 = \left[(\nabla \mathbf{u})^T \cdot \mathbf{Q}_1 - \frac{1}{4We} \left(2\mathbf{F}_1^D - \mathbf{F}_2^D \right) \right] dt + \frac{1}{\sqrt{2We}} \left(d\mathbf{W}_2 - d\mathbf{W}_1 \right), \tag{2.64}
$$

$$d\mathbf{Q}_2 = \left[(\nabla\mathbf{u})^T \cdot \mathbf{Q}_2 - \frac{1}{4We}\left(-\mathbf{F}_1^D + 2\mathbf{F}_2^D - \mathbf{F}_3^D\right)\right] dt + \frac{1}{\sqrt{2We}}\left(d\mathbf{W}_3 - d\mathbf{W}_2\right), \tag{2.65}$$

$$d\mathbf{Q}_3 = \left[(\nabla\mathbf{u})^T \cdot \mathbf{Q}_3 - \frac{1}{4We}\left(-\mathbf{F}_2^D + 2\mathbf{F}_3^D\right)\right] dt + \frac{1}{\sqrt{2We}}\left(d\mathbf{W}_4 - d\mathbf{W}_3\right), \tag{2.66}$$

where $\mathbf{F}_k^D$ $(k = 1, 2, 3)$ is given by Eq. (2.29) for a FENE dumbbell. The 3-D development of the equation (2.64) for dumbbell 1 is given by

$$dQ_{1,x} = \left[-\frac{1}{4We}\left(\frac{2Q_{1,x}}{C_1} - \frac{Q_{2,x}}{C_2}\right) + \frac{\partial u}{\partial y}Q_{1,y}\right] dt + \frac{1}{\sqrt{2We}}\left(dW_{2,x} - dW_{1,x}\right), \tag{2.67}$$

$$dQ_{1,y} = -\frac{1}{4We}\left(\frac{2Q_{1,y}}{C_1} - \frac{Q_{2,y}}{C_2}\right) dt + \frac{1}{\sqrt{2We}}\left(dW_{2,y} - dW_{1,y}\right), \tag{2.68}$$

$$dQ_{1,z} = -\frac{1}{4We}\left(\frac{2Q_{1,z}}{C_1} - \frac{Q_{2,z}}{C_2}\right) dt + \frac{1}{\sqrt{2We}}\left(dW_{2,z} - dW_{1,z}\right), \tag{2.69}$$

where $C_k = 1 - \frac{\|\mathbf{Q}_k\|^2}{b_{BSC}}$; and $\| \mathbf{Q}_k \|^2 = Q_{k,x}^2 + Q_{k,y}^2 + Q_{k,z}^2$ $(k = 1, 2)$.

Temporal discretisation scheme

For microscopic procedure, the use of Euler integration scheme to discretise the SDEs (2.64)-(2.66) yields

$$\begin{aligned}\mathbf{Q}_1^{n+1} = \mathbf{Q}_1^n + \left[(\nabla\mathbf{u}^{n+1})^T \cdot \mathbf{Q}_1^n - \frac{1}{4We}\left(2\mathbf{F}_1^D - \mathbf{F}_2^D\right)^n\right] \Delta t + \\ \sqrt{\frac{\Delta t}{2We}}\left(\mathbf{W}_2^n - \mathbf{W}_1^n\right),\end{aligned} \tag{2.70}$$

$$\begin{aligned}\mathbf{Q}_2^{n+1} = \mathbf{Q}_2^n + \left[(\nabla\mathbf{u}^{n+1})^T \cdot \mathbf{Q}_2^n - \frac{1}{4We}\left(-\mathbf{F}_1^D + 2\mathbf{F}_2^D - \mathbf{F}_3^D\right)^n\right] \Delta t + \\ \sqrt{\frac{\Delta t}{2We}}\left(\mathbf{W}_3^n - \mathbf{W}_2^n\right),\end{aligned} \tag{2.71}$$

$$\begin{aligned}\mathbf{Q}_3^{n+1} = \mathbf{Q}_3^n + \left[(\nabla\mathbf{u}^{n+1})^T \cdot \mathbf{Q}_3^n - \frac{1}{4We}\left(-\mathbf{F}_2^D + 2\mathbf{F}_3^D\right)^n\right] \Delta t + \\ \sqrt{\frac{\Delta t}{2We}}\left(\mathbf{W}_4^n - \mathbf{W}_3^n\right).\end{aligned} \tag{2.72}$$

Based on the Euler explicit scheme, the time discretisation of Eqs. (2.67) -(2.69) for dumbbell 1 is written as follows.

$$Q_{1,x}^{n+1} = \left(1 - \frac{\Delta t}{2WeC_1}\right) Q_{1,x}^{n} + \frac{\Delta t}{4WeC_2} Q_{2,x}^{n} + \frac{du^{n+1}}{dy} Q_{1,y}^{n} \Delta t + \sqrt{\frac{\Delta t}{2We}} \left(W_{2,x}^{n} - W_{1,x}^{n}\right), \tag{2.73}$$

$$Q_{1,y}^{n+1} = \left(1 - \frac{\Delta t}{2WeC_1}\right) Q_{1,y}^{n} + \frac{\Delta t}{4WeC_2} Q_{2,y}^{n} + \sqrt{\frac{\Delta t}{2We}} \left(W_{2,y}^{n} - W_{1,y}^{n}\right), \tag{2.74}$$

$$Q_{1,z}^{n+1} = \left(1 - \frac{\Delta t}{2WeC_1}\right) Q_{1,z}^{n} + \frac{\Delta t}{4WeC_2} Q_{2,z}^{n} + \sqrt{\frac{\Delta t}{2We}} \left(W_{2,z}^{n} - W_{1,z}^{n}\right). \tag{2.75}$$

A study for the convergence of time step for the case of $N_s = 6$ and $N_f = 1024$ is done with a range of values of $\Delta t = \{0.01, 0.005, 0.001, 0.0005, 0.0001\}$ using the number of grid nodes $N_y = 11$ and parameters presented above. The evolution of the shear stress (τ_{xy}) and the velocity field (u) with different Δt's are introduced in Figs. 2.3 and 2.4, respectively. For τ_{xy}, the results produced from $\Delta t = \{0.001, 0.0005, 0.0001\}$ are nearly identical and only show a minor difference to the results using coarser time steps $\Delta t = \{0.01, 0.005\}$. Meanwhile, the solutions of the velocity field are mostly unchanged with Δt's examined. Therefore, the value of $\Delta t = 0.001$ is sufficiently small to obtain converged solutions and is chosen for this problem.

For the creeping problem ($Re = 0$), the pseudo-time scheme is used to discretise the momentum conservation equation with time step size $\Delta t = 0.001$ for both the micro and macro procedures. With a coarse spatial discretisation $\Delta y = 0.1$ ($N_y = 11$) and number of chains $N_f = 1024$ at each collocation point, the numerical solutions obtained by the present method confirm a very good agreement with the results where finer meshes were used in Koppol et al. (2007), evidenced by the following

- Fig. 2.5 describes evolutions of the velocity at four locations $y = 0.2$, 0.4, 0.6 and 0.8 of the BSC models of 1, 3 and 6 dumbbells. The evolution of the velocity profile indicates that the overshoots before reaching the steady state are not significant. The results show that the method is able to achieve a very high accuracy using a coarse grid ($N_y = 11$, $\Delta t = 0.001$);

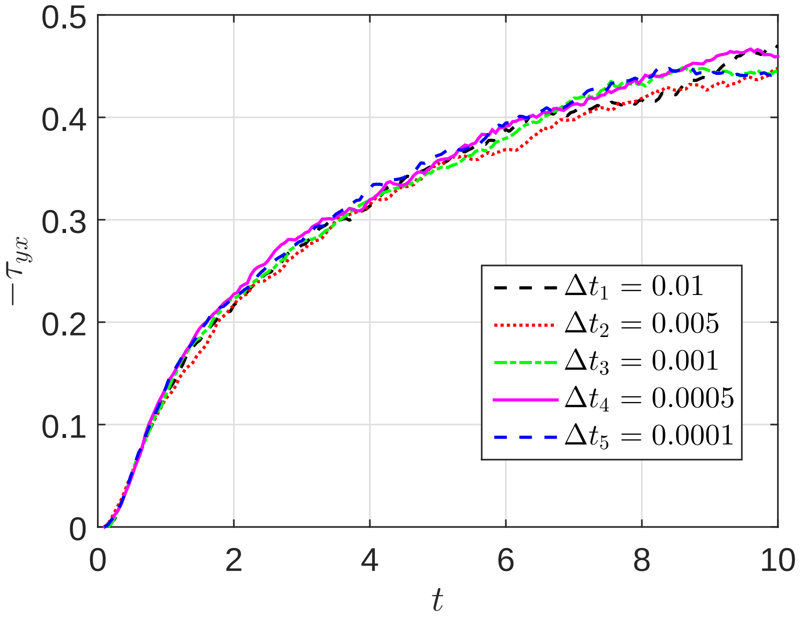

Figure 2.3: The creeping planar Couette flow problem using the FENE-based BSC model. A convergence study for the time step size Δt with $N_s = 6$, $N_f = 1024$, $Re = 0$, $\epsilon = 0.5$, $b_D = 900$ and $We = 5$. The evolution of the shear stress at $y = 0.2$ for a range of values of Δt.

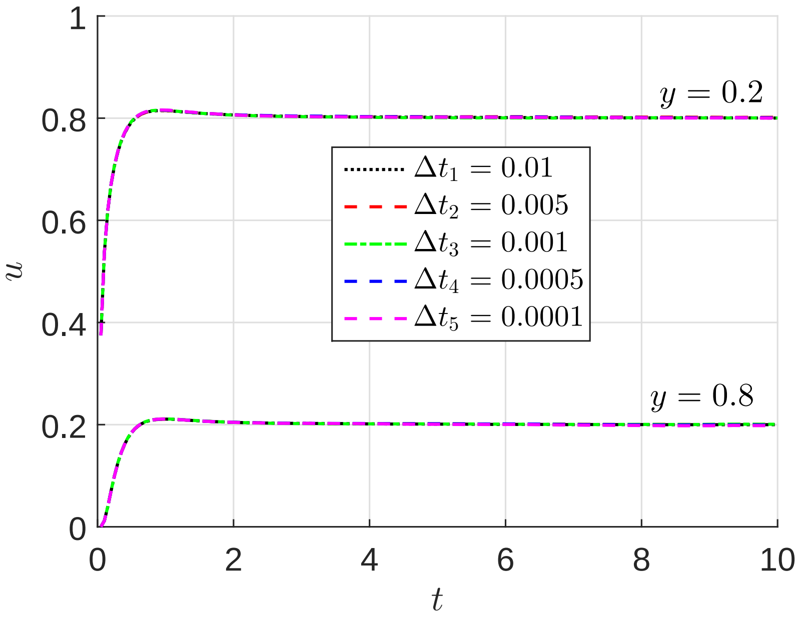

Figure 2.4: The creeping planar Couette flow problem using the FENE-based BSC model. A convergence study for the time step size Δt with parameters mentioned in Fig. 2.3. The evolution of the velocity at $y = 0.2$ and $y = 0.8$ for a range of values of Δt.

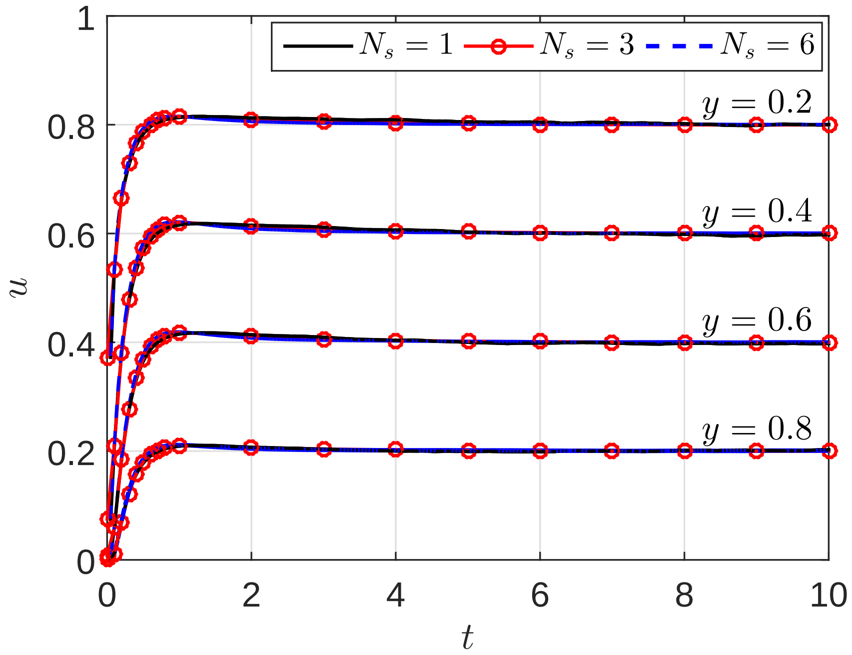

Figure 2.5: The creeping planar Couette flow problem using FENE-based BSC models of 1, 3 and 6 dumbbells. The parameters of the problem: number of collocation points $N_y = 11$, $N_f = 1024$, $b_D = 900$, $We = 5$, $\epsilon = 0.5$, $Re = 0$ and $\Delta t = 0.001$. The evolution of the velocity at four locations $y = 0.2$, $y = 0.4$, $y = 0.6$ and $y = 0.8$.

- Figs. 2.6 depict the evolution of the first normal stress (Fig. 2.6(a)) and the shear stress (Fig. 2.6(b)) at the location $y = 0.8$ for several BSC models of 1, 3 and 6 dumbbells using 1024 and 2048 configurations at each collocation point. The absolute values of shear stresses reach a stable stage around 0.42 to 0.48 while the stable first normal stresses cover a range from 3.2 to 4. Theses results are in very good agreement with ones in Fig. 3 presented in Koppol et al. (2007);

- Figs. 2.7 show the evolution of the first normal stress difference (Fig. 2.7(a)) and the square of end-to-end distance of chain configuration (Fig. 2.7(b)) at the location $y = 0.8$ for the different BSC models of 1, 3 and 6 dumbbells. Several interesting points by the results for this case include: (i) the number of configurations $N_f = 1024$ is sufficient for a reliable stochastic simulation and (ii) the more number of springs/dumbbells in a BSC model is, the higher extensibility of the BSC is.

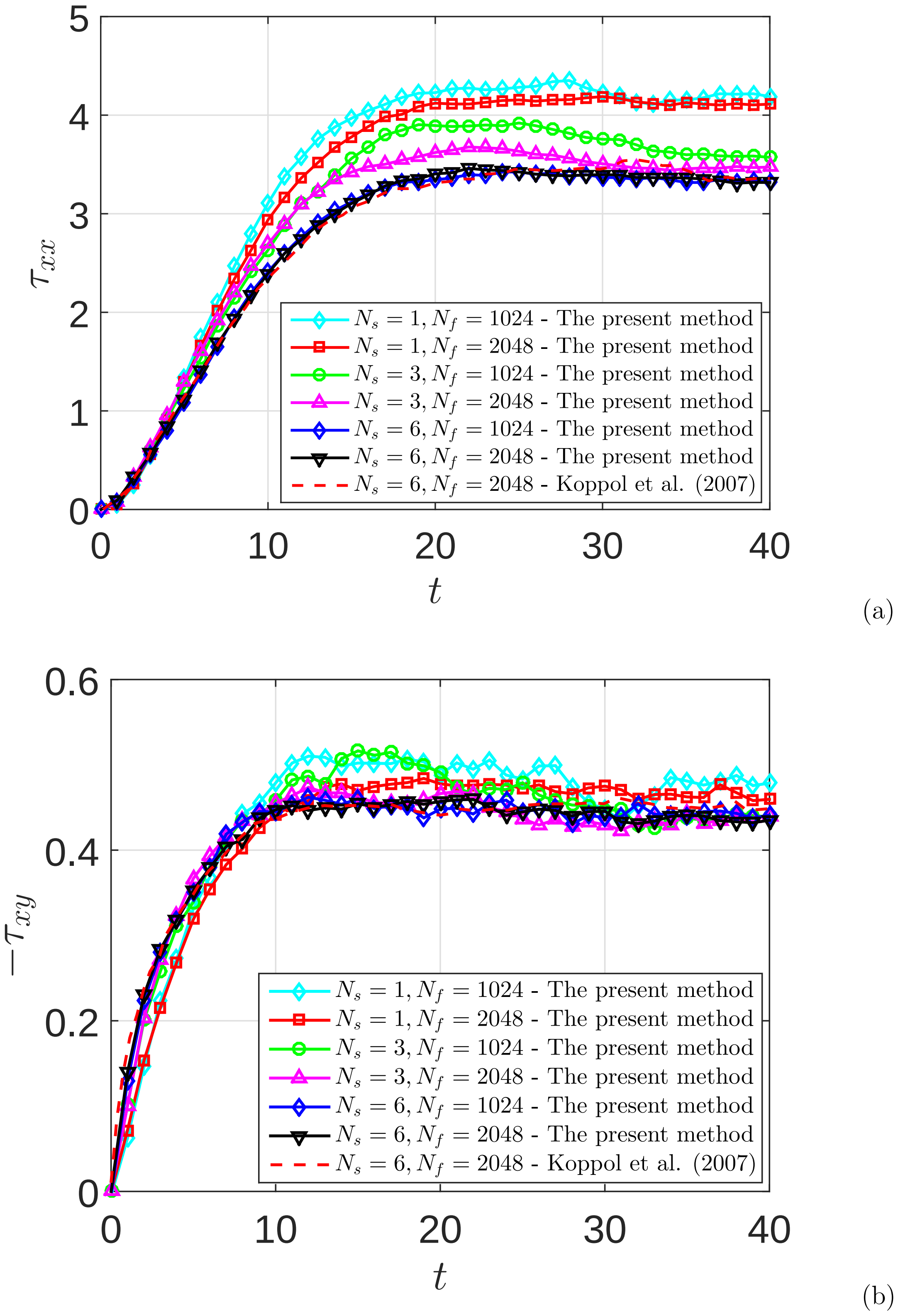

Figure 2.6: The creeping planar Couette flow problem using the FENE-based BSC model of 1, 3 and 6 dumbbells. The parameters of the problem are given in Fig. 2.5. The evolution of the first normal stress (figure (a)) and the shear stress (figure (b)) at location $y = 0.8$.

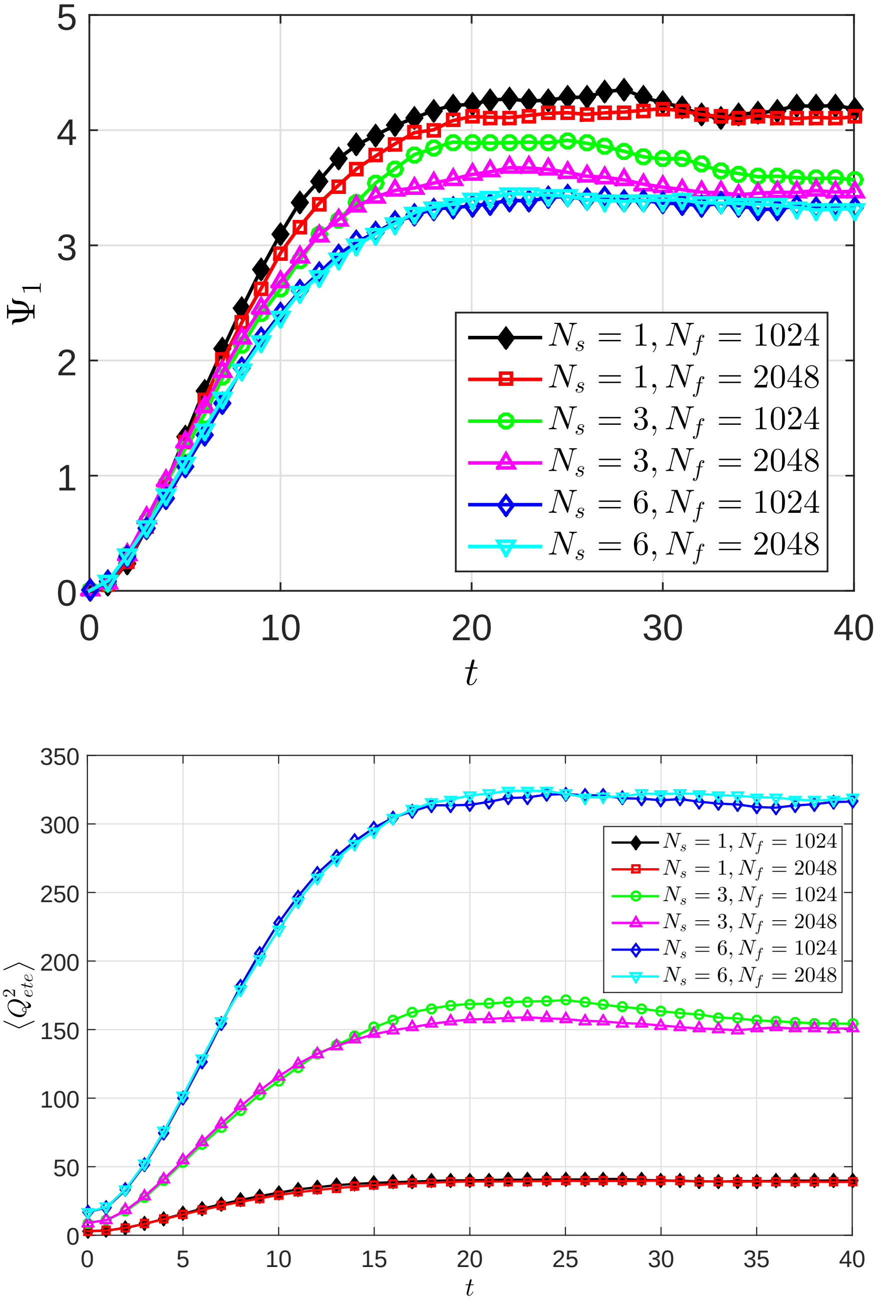

(a)

(b)

Figure 2.7: The creeping planar Couette flow problem using the FENE-based BSC model of 1, 3 and 6 dumbbells. The parameters of the problem are given in Fig. 2.5. The the evolution of first normal stress difference (figure (a)) and the square of end-to-end distance of the BSC configuration (figure (b)) at location $y = 0.8$.

Fig. 2.8 depicts the evolution of the convergence measure of the velocity field using the FENE-based BSC model of 1, 3 and 6 dumbbells by the present IRBF-BCF collocation method. While most published results confirmed that convergence measures obtained for a stochastic approach are not high (from $1E-2$ to $1E-3$ for velocity and stress (Laso and Ottinger, 1993; Tran et al., 2012a)), the results in Fig. 2.8 show that the convergence measure has been significantly enhanced by the present method. Furthermore, the statistical errors obtained at the steady state show a significant improvement by the present method as described in Table 2.1. Indeed, in most of the cases, except $N_s = 3$ with $N_f = 1024$, the statistical errors by the present method are smaller than those of Koppol et al. (2007).

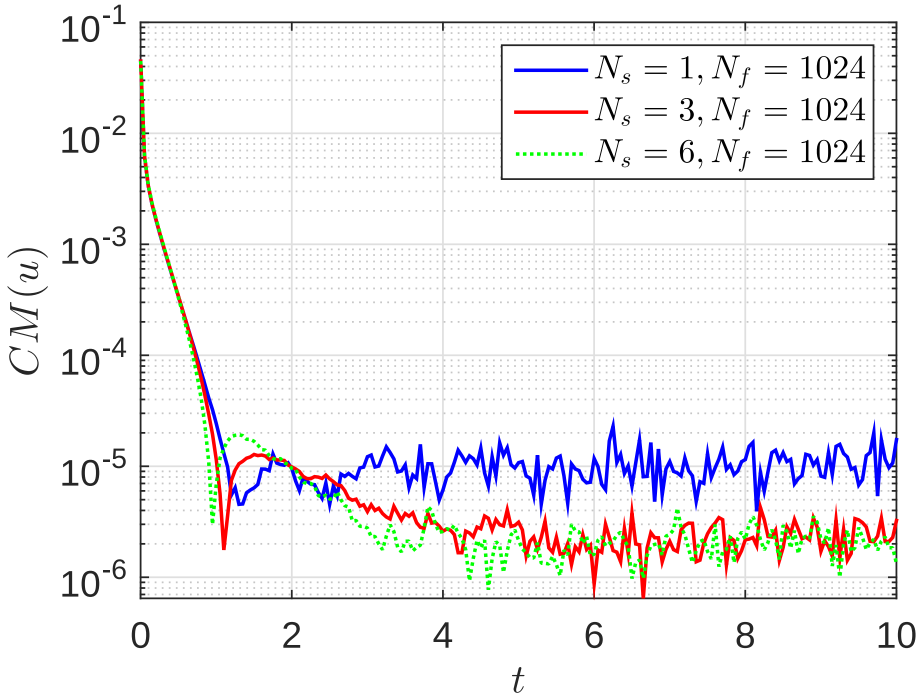

Figure 2.8: The creeping planar Couette flow problem using the FENE-based BSC model of 1, 3 and 6 dumbbells. The parameters of the problem are given in Fig. 2.5. The convergence measures for the velocity field are significantly enhanced in comparison with other published results.

Table 2.1: The creeping planar Couette flow problem using the FENE-based BSC model of 1, 3 and 6 dumbbells. The parameters of the problem are given in Fig. 2.5. An evaluation of the numerical stability of the present method: the statistical errors of the shear stress and the first normal stress of the present method are compared with those of Koppol et al. (2007). $S[\tau_{xy}]$ and $S[\tau_{xx}]$ are the statistical errors of the shear stress and the first normal stress, respectively.

		Koppol et al.(2007)		The present method	
N_s	N_f	$S[\tau_{xy}]$	$S[\tau_{xx}]$	$S[\tau_{xy}]$	$S[\tau_{xx}]$
1	1024	0.025	0.172	0.024	0.167
1	2048	0.018	0.120	0.017	0.112
3	1024	0.016	0.123	0.018	0.137
3	2048	0.012	0.091	0.012	0.085
6	1024	0.015	0.117	0.015	0.117
6	2048	0.011	0.088	0.011	0.077

2.6.3 Comparisons between the Rouse and Zimm models

In this section, the difference in dynamic behaviour of dilute polymer solution in shear flow using the Rouse and Zimm models is discussed. While both of them are Hookean dumbbell-based BSC models, only the Zimm model takes into account the effect of HI. The SDE (2.26), describing the evolution of the configuration in dimensionless form, is rewritten for the Rouse model as

$$d\mathbf{Q}_i = \left[(\nabla \mathbf{u})^T \cdot \mathbf{Q}_i - \frac{1}{4We} \sum_{k=1}^{N_s} A_{ik}^R \mathbf{F}_k^D \right] dt + \sqrt{\frac{1}{2We}} \left(d\mathbf{W}_{\mu+1} - d\mathbf{W}_{\mu} \right), \quad (2.76)$$

where $\mu = i$ and A_{ik}^R are entries of the Rouse matrix of dimension $N_s \times N_s$ and given by

$$A_{ik}^R = \begin{cases} 2 & \text{if } |i-k| = 0, \\ -1 & \text{if } |i-k| = 1, \\ 0 & \text{otherwise.} \end{cases} \quad (2.77)$$

and for the Zimm model by

$$d\mathbf{Q}_i = \left[(\nabla \mathbf{u})^T \cdot \mathbf{Q}_i - \frac{1}{4We} \sum_{k=1}^{N_s} A_{ik}^Z \mathbf{F}_k^D \right] dt + \sqrt{\frac{1}{2We}} \sum_{\nu=1}^{N_b} \left(\mathbf{B}_{(\mu+1)\nu} - \mathbf{B}_{\mu\nu} \right) \cdot d\mathbf{W}_{\nu}, \quad (2.78)$$

where A_{ik}^Z are entries of the Zimm matrix of dimension of $N_s \times N_s$ and defined as

$$A_{ik}^Z = A_{ik}^R + \sqrt{2}\bar{h} \left(\frac{2}{\sqrt{|i-k|}} - \frac{1}{\sqrt{|i-k+1|}} - \frac{1}{\sqrt{|i-k-1|}} \right), \quad (2.79)$$

where $\bar{h}$ is the HI parameter ($\bar{h} = 0.25$ is used in this work); tensor $\mathbf{B}_{\mu\nu}$ is determined by formulae (2.5) and (2.14).

The polymer stresses are given by

$$\boldsymbol{\tau}_{\mathrm{p}} = \frac{\epsilon}{\widetilde{We}} \left[(N_b - 1)\, \mathbf{I} - \sum_{k=1}^{N_s} \left\langle \mathbf{Q}_k \mathbf{F}_k^D \right\rangle \right], \quad (2.80)$$

where N_b and N_s are the numbers of beads and springs, respectively. Other parameters are defined as before.

The start-up problem of the Rouse and Zimm models is analysed using 2-dumbbell chains with the following physical parameters: $\eta_o = \eta_s + \eta_p = 1, \rho = 1.2757, \lambda_H = 49.62, \eta_s = 0.0521$ as done in Laso and Ottinger (1993); Tran-Canh and Tran-Cong (2004) where η_o, η_s, η_p, ρ, are defined above.

The corresponding Weissenberg number, Reynolds number and the ratio ε are given by

$$Re = \frac{\rho U L}{\eta_o} = 1.2757; \quad We = \frac{\lambda_H U}{L} = 49.62 \quad \text{and} \quad \varepsilon = \frac{\eta_p}{\eta_o} = 0.9479.$$

Since the Zimm model takes into account the HI effect, the mechanical behaviours are significantly different from those in the Rouse model and that is shown in numerical results by the present method. Results clearly showed that the maximum extension of BS chains of the two models increases monotonically with respect to time and the increment rate of Zimm chains is higher than the Rouse ones because of the HI effect (Fig. 2.9). Indeed, BS chain lengths reach the values of 800 and 1000 after the elapsed time $t = 25$ for the Rouse and Zimm models, respectively.

Figs. 2.10 depict the evolution of velocity field at four locations $y = 0.2$, $y = 0.4$, $y = 0.6$ and $y = 0.8$ by the Rouse and Zimm models. Since they are Hookean-based BS chains, the evolution of velocity profile and values of flow velocity are nearly identical (Fig. 2.10(a)) except a small difference during the velocity overshoot at the start-up period (Fig. 2.10(b)).

On the rheological behaviour, the comparison between the models in the Couette start-up flows is summarised in Fig. 2.11 for the evolution of stresses. Results in Figs. 2.11 show that due to the HI effect, the magnitude of shear stress (Fig. 2.11(a)) and the first normal stress difference (Fig. 2.11(b)) by the Zimm model are higher than the Rouse's ones whereas a zero-value is observed for the second normal stress differences of the two models. These results are completely in line with predictions in classical kinetic theory (Bird et al., 1987b; Ottinger, 1996).

The simulation is also carried out with a range of Weissenberg numbers ($We = 5$, 10 and 30) to investigate the present method. Results presented in Figs. 2.12 and

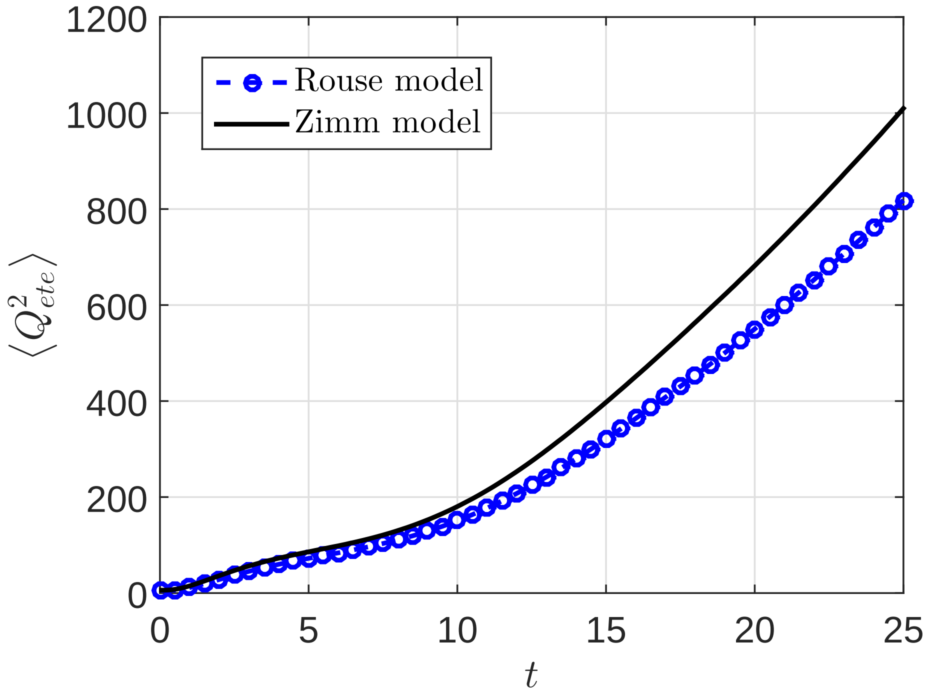

Figure 2.9: The start-up planar Couette flow problem using the Rouse and the Zimm models. The parameters of the problem: number of configurations $N_f = 1024$, number of springs $N_s = 2$, the hydrodynamic interaction parameter for Zimm model $\bar{h} = 0.25$, number of collocation points $N_y = 11$, $Re = 1.2757$, $We = 49.62$, $\epsilon = 0.9479$ and $\Delta t = 0.001$. The evolution of the square of end-to-end distance at the location $y = 0.2$.

2.13 confirm the influence of the Weissenberg number on the velocity through the start-up period, the shear stress and the first normal stress difference.

For the evolution of velocity, Fig. 2.12 shows that the maximum amplitude as well as the oscillatory frequency of the over/undershoot are higher for smaller Weissenberg numbers for both Rouse and Zimm models. Meanwhile, with a given Weissenberg number, due to the HI effect, the over/undershoot of velocity is stronger with the Zimm model.

On the polymer stresses, the higher Weissenberg number is, the lower magnitude of the shear stress (Fig. 2.13(a)) and the first normal stress difference (Fig. 2.13(b)) are for both Rouse and Zimm models. Furthermore, with a given Weissenberg number, the absolute value of shear stress and the first normal stress difference of flow by the Zimm model are higher than those by the Rouse model.

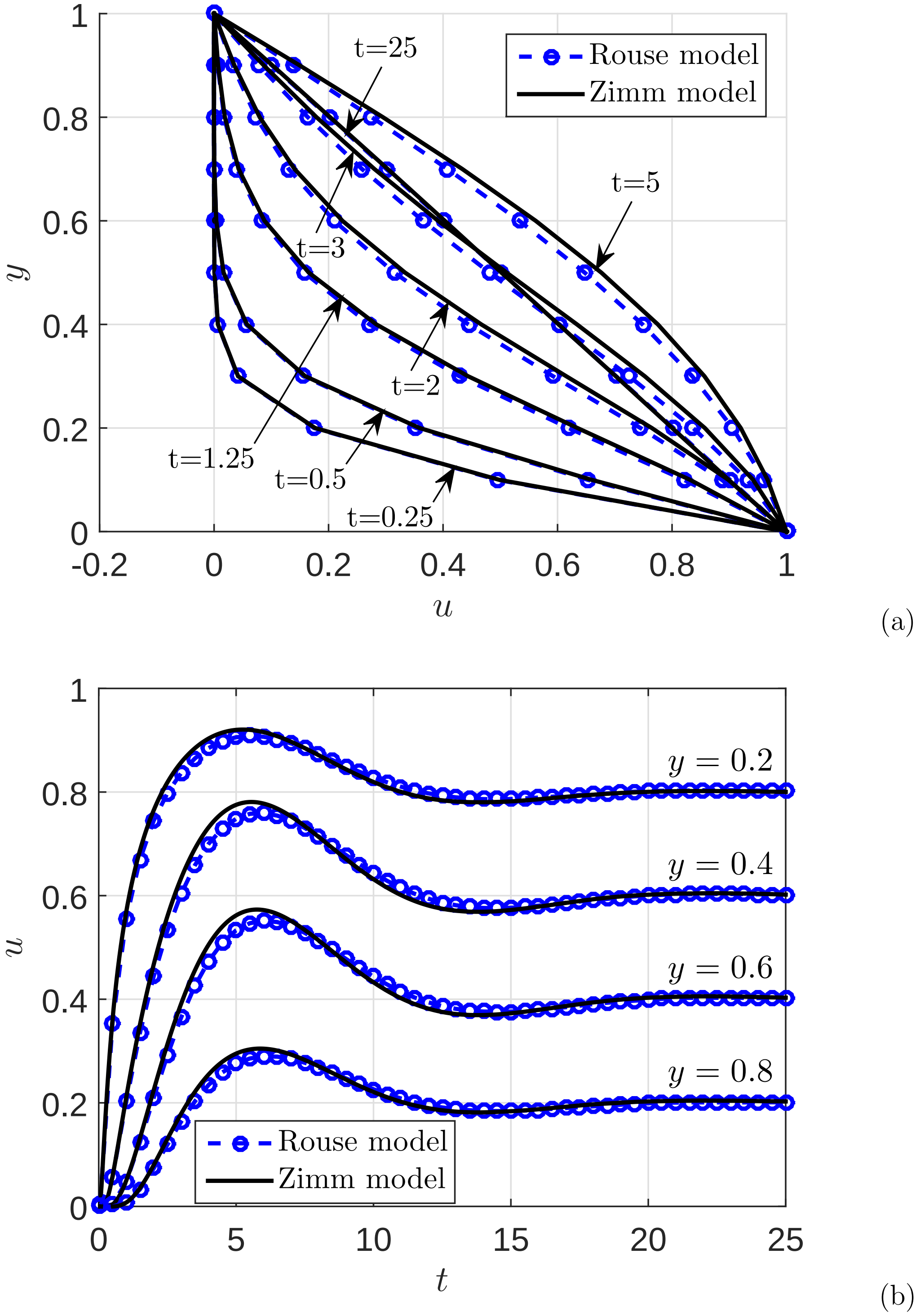

Figure 2.10: The start-up planar Couette flow problem using the Rouse and the Zimm models. The parameters are given in Fig. 2.9. The evolution of the velocity profile (figure (a)) and the comparison of the evolution of velocity (figure (b)) between Rouse and Zimm models at locations $y = 0.2$, $y = 0.4$, $y = 0.6$ and $y = 0.8$.

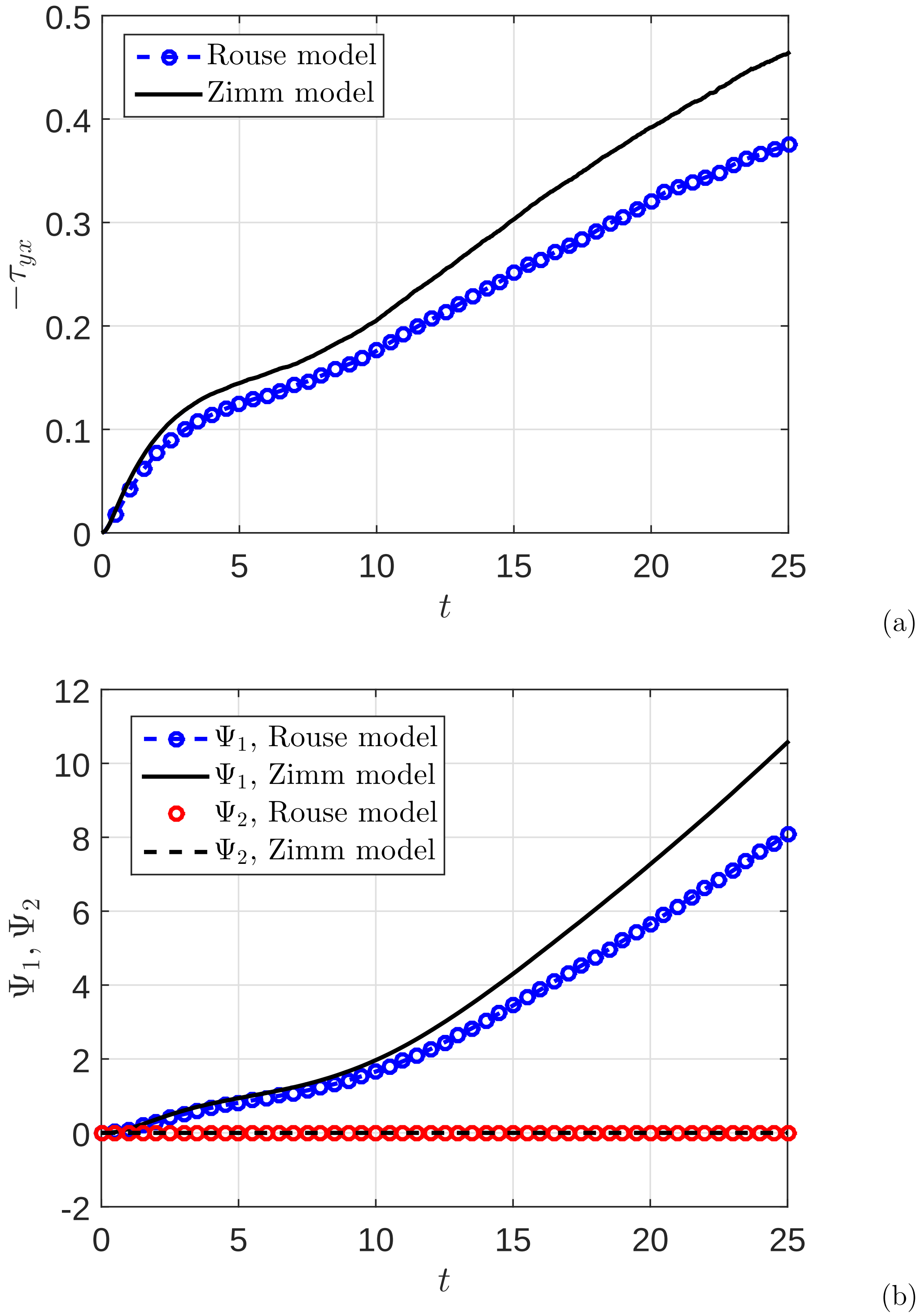

Figure 2.11: The start-up planar Couette flow problem using the Rouse and the Zimm models. The parameters are the same as in Fig. 2.9. The evolution of the shear stress (figure (a)) and the evolution of the first and the second normal stress differences (figure (b)) at location $y = 0.2$.

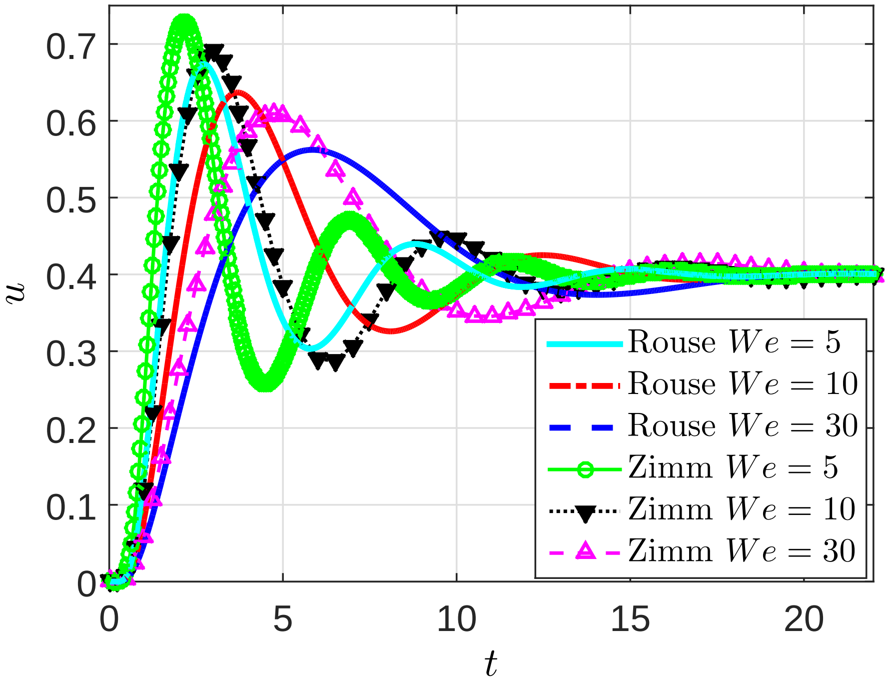

Figure 2.12: The start-up planar Couette flow problem using the Rouse and the Zimm models. The parameters are the same as in Fig. 2.9. Comparison of the fluid rheological properties using the Rouse and Zimm models for several Weissenberg numbers ($We = 5, 10$ and 30). The evolution of velocity.

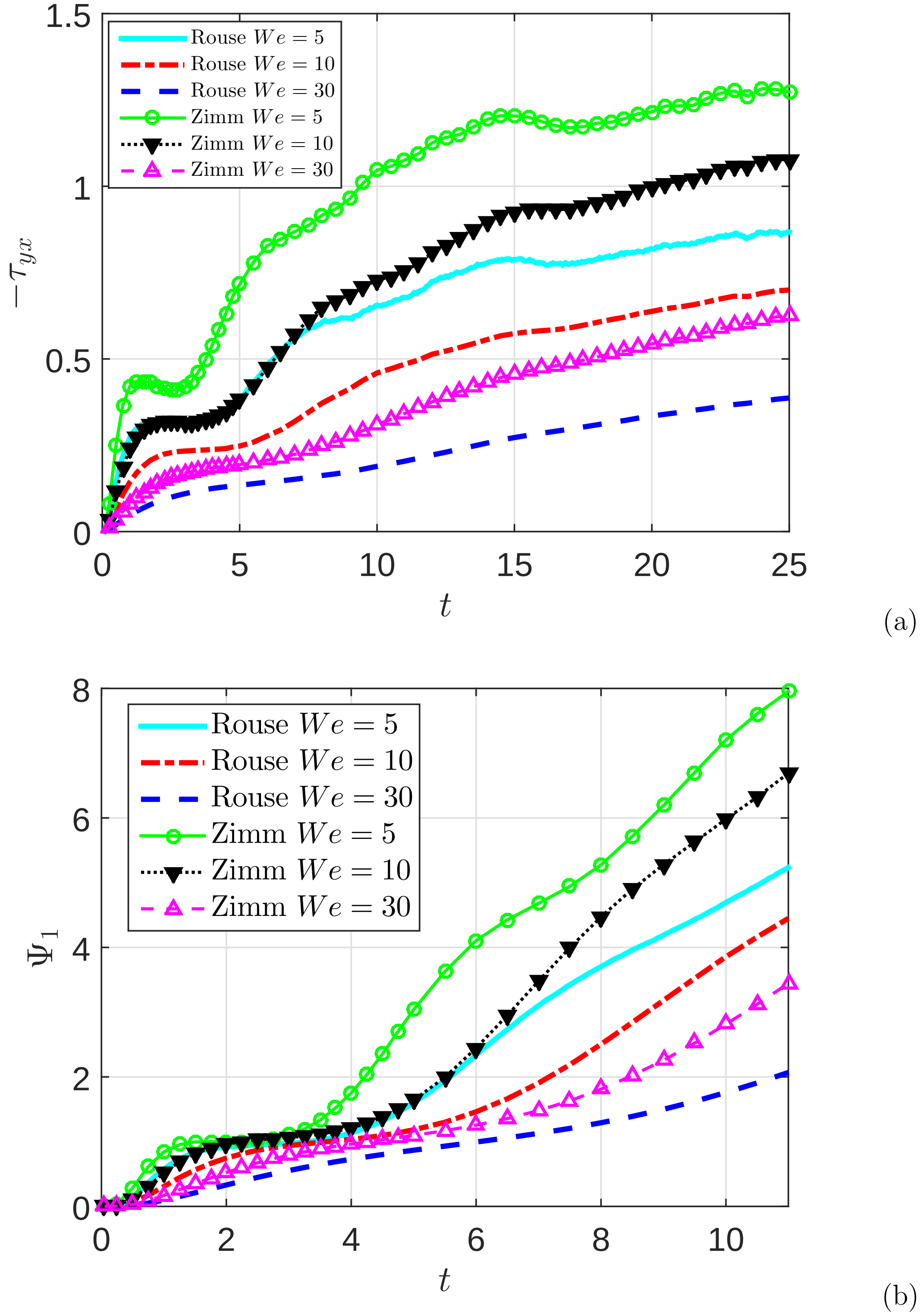

Figure 2.13: The start-up planar Couette flow problem using the Rouse and the Zimm models. The parameters are the same as in Fig. 2.9. Comparison of the fluid rheological properties using the Rouse and Zimm models for several Weissenberg numbers ($We = 5, 10$ and 30). The evolution of the shear stress (figure (a)) and the first normal stress difference at location $y = 0.2$ (figure (b)).

2.6.4 Start-up Couette flow using the FENE-based BSC models with HI and EV effects

The method is finally demonstrated with the start-up Couette flow of fully nonlinear FENE-based BSC model fluids. The HI and EV effects are included in the model with varying number of FENE dumbbells in each chain ($N_s = 1, 2, \cdots, 6$). The governing SDE (2.26) of a general BSC model with HI and EV effects and the stress formula for the polymer (2.27) are reproduced as follows.

$$d\mathbf{Q}_i = \left[(\nabla\mathbf{u})^T \cdot \mathbf{Q}_i + \frac{1}{4We}\sum_{\nu=1}^{N_b}\left(\boldsymbol{\Upsilon}_{(\mu+1)\nu} - \boldsymbol{\Upsilon}_{\mu\nu}\right)\cdot\mathbf{F}^{\phi}_{\nu}\right]dt + \sqrt{\frac{1}{2We}}\sum_{\nu=1}^{N_b}\left(\mathbf{B}_{(\mu+1)\nu} - \mathbf{B}_{\mu\nu}\right)\cdot d\mathbf{W}_{\nu}, \tag{2.81}$$

$$\boldsymbol{\tau}_{\mathrm{p}} = \frac{\epsilon}{\widetilde{We}}\left[(N_b - 1)\,\mathbf{I} - \sum_{k=1}^{N_s}\left\langle \mathbf{Q}_k\mathbf{F}^D_k\right\rangle + \mathbf{Z}\right], \tag{2.82}$$

where $\mathbf{Z}$ is determined by Eq. (2.30) and other parameters are defined as before.

The physical parameters of the fluid, including the Weissenberg number, Reynolds number and the ratio ε, are chosen as presented in Section 2.6.3. The parameters $\bar{h} = 0.25$ for the HI effect and the constants $z = 1$ (Eq. (2.17)) and $K = 1$ (Eq. (2.18)) for the EV effect are used in this section.

On the mechanical behaviour, Fig. 2.14 depicts the evolution of shear stress and Figs. 2.15 the first normal stress difference (Fig. 2.15(a)) and the second normal stress difference (Fig. 2.15(b)) at the location of $y = 0.2$. Overshoots are observed for shear stress, the first and the second normal stress differences. In particular, the existence of the non-zero second normal stress difference is very clear as compared with simulations using the BSC models without both HI and EV effects (see cases of Rouse and Zimm models in Fig. 2.11(b)). This is because the nonlinear effects of HI and EV have been included in the simulations. Results also show the influence of the number of dumbbells in a polymer chain on the dynamics properties through the start-up time before reaching stable values. For example, the overshoot of the shear stress (Fig. 2.14) and the first normal stress difference (Fig. 2.15(a)) decrease with increasing number of dumbbells in the chain configuration.

The development of velocity with respect to time at different locations ($y = 0.2$, 0.4, 0.6 and 0.8) are presented in Figs. 2.16. Generally, an overshoot at the beginning time is formed before a stable state is reached. The obtained results show a significant influence of the number of dumbbells in the chain on the initial transient behaviour. It can be seen clearly that the velocity simulated with higher number of dumbbells achieves the maximum value (or the debut position of the overshoot) sooner and thus needs less time to reach a stable state (Fig. 2.16(b)).

Last but not least, it is worth noting that with a given b_D, the HI and EV influences on the polymer stresses increase and only significantly for polymer chains having large enough number of dumbbells in chain (Figs. 2.17). For example, the difference of the shear stress (Fig. 2.17(a)) and the first normal stress difference (Fig. 2.17(b)) of the FENE-BSC models with and without HI and EV are very small for the 2-dumbbell chain model but very significant for the 6-dumbbell chain model. A similar observation can be seen for the square maximum extension of end-to-end connecting vector (Fig. 2.18). Meanwhile, these nonlinear effects are not significant for the velocity field of the flow (Figs. 2.19).

2.6.5 Performance of parallel computation

The problem is solved using 1024 BSCs at each collocation point to ensure the accuracy and stability in stochastically determining the stresses. In order to estimate the efficiency of the parallel algorithm, a range of 2, 4 and 8 CPUs is used to solve the SDEs corresponding to 1024 configurations in parallel generated at each and every collocation point and to determine the averaged stresses at the grid points. Especially, the presence of HI and EV effects makes a massive increase in the computational cost because of the bead-bead and bead-spring interactions in the fluid model. For this numerical example, the FENE-BSC model of 2 dumbbells with HI and EV effects is considered to initially evaluate the efficiency

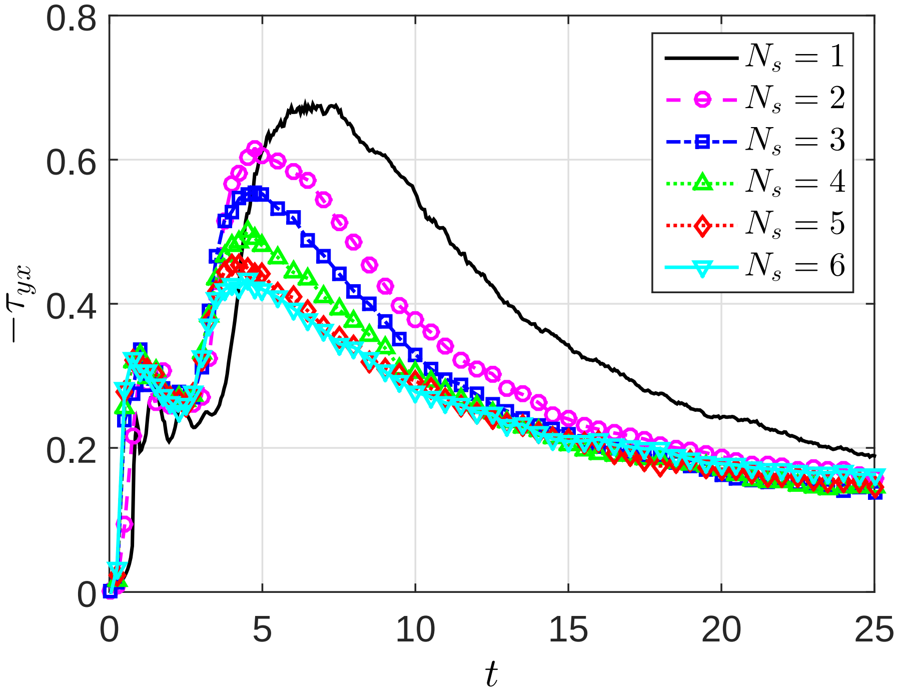

Figure 2.14: The start-up planar Couette flow problem using FENE-based BSC models of several numbers of dumbbells with HI and EV effects. The parameters of the problem: $\bar{h} = 0.25$, $z = 1$, $K = 1$, $N_y = 11$, $We = 49.62$, $\epsilon = 0.9479$, $b_D = 50$. The evolution of the shear stress at location $y = 0.2$ using $1, 2, 3, 4, 5$ and 6 dumbbells.

of the parallel algorithm.

Table 2.2 shows the effect of the number of CPUs on the speed-up as well as the efficiency of the parallel technique. A significant improvement of the throughput has been achieved. For example, the speed-up increased 1.7, 2.96 and 3.66 times when using 2, 4 and 8 CPUs, respectively. However, the efficiency of the algorithm reduces with increasing number of CPUs. The results presented in Table 2.2 and Figs. 2.20 show the effect of the number of CPUs on the speed-up and the efficiency of the present method are in agreement with several recent results reported in Tran et al. (2009); Laso et al. (1997).

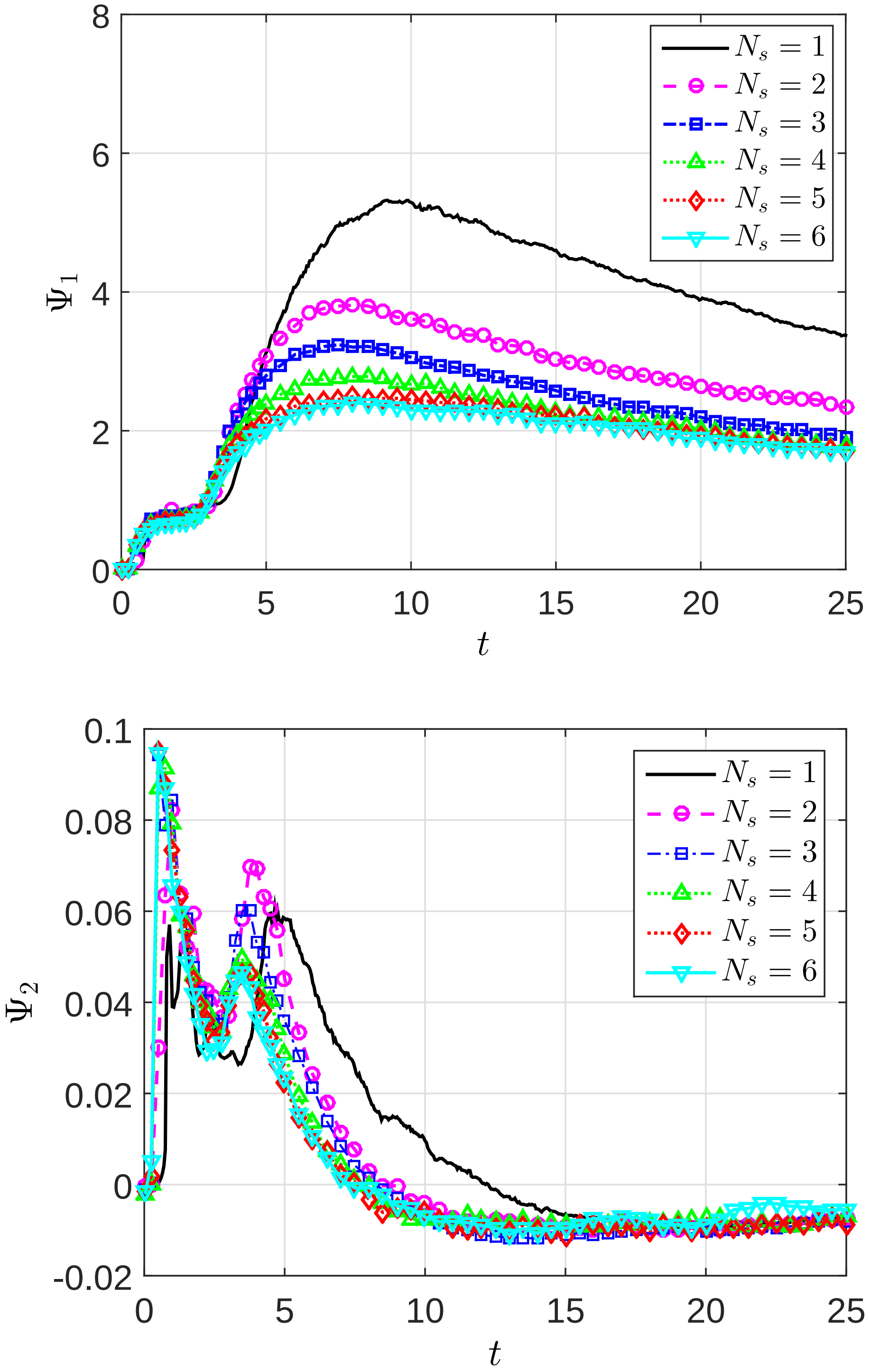

(a)

(b)

Figure 2.15: The start-up planar Couette flow problem using FENE-based BSC models of several numbers of dumbbells with HI and EV effects. The parameters are the same as in Fig. 2.14. The evolution of the first normal stress difference (figure (a)) and the second normal stress difference (figure (b)) at location $y = 0.2$ using $1, 2, 3, 4, 5$ and 6 dumbbells.

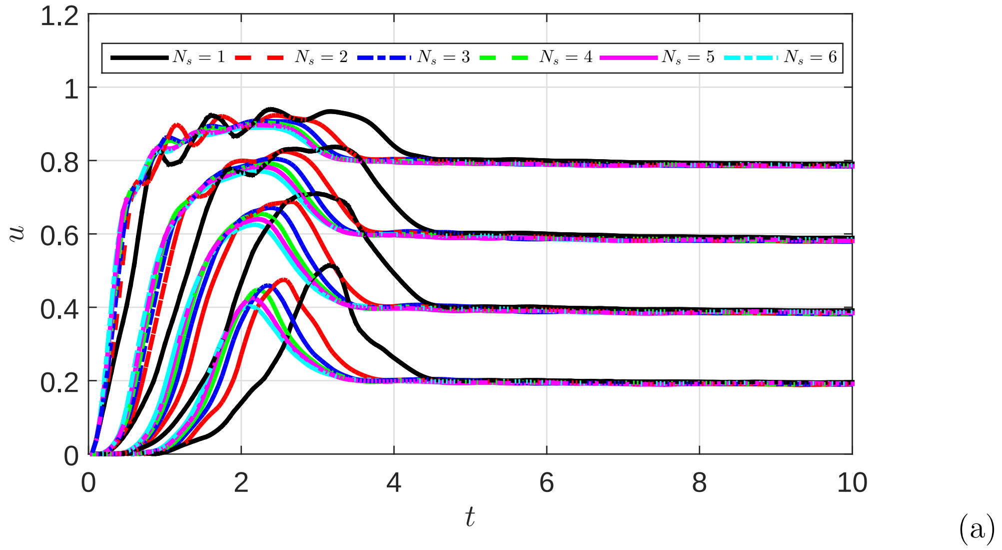

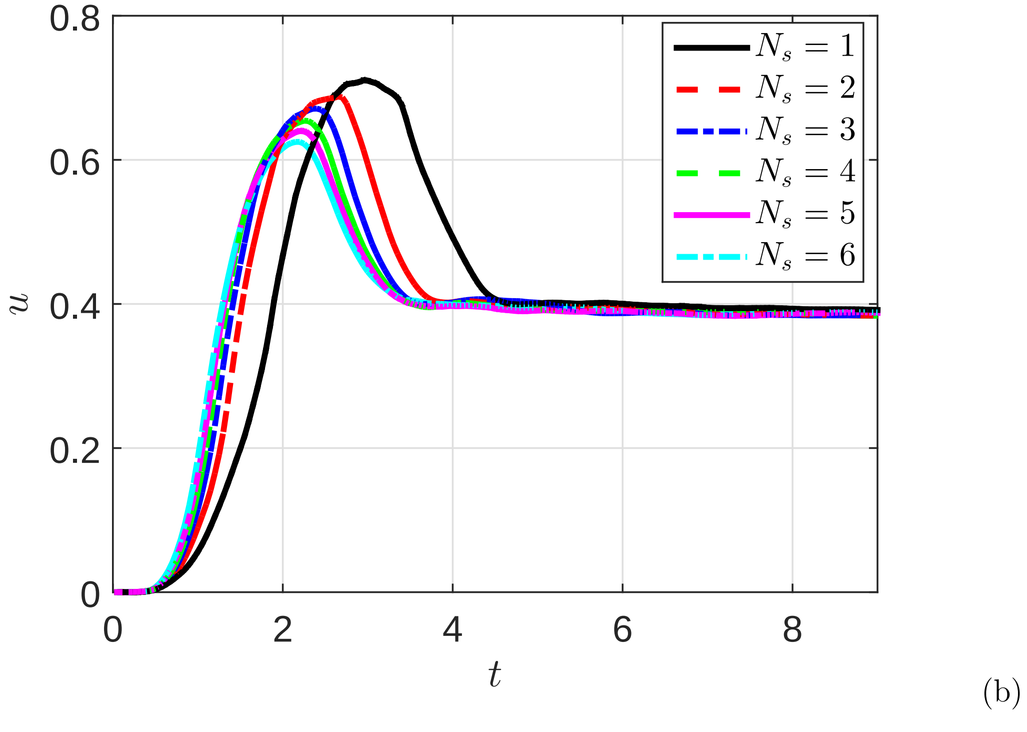

Figure 2.16: The start-up planar Couette flow problem using FENE-based BSC models of several numbers of dumbbells with HI and EV effects. The parameters are the same as in Fig. 2.14. The evolution of the velocity field at locations $y = 0.2$, $y = 0.4$, $y = 0.6$ and $y = 0.8$ (figure (a)) and an enlarged velocity profile at location $y = 0.6$ (figure (b)) using $1, 2, 3, 4, 5$ and 6 dumbbells.

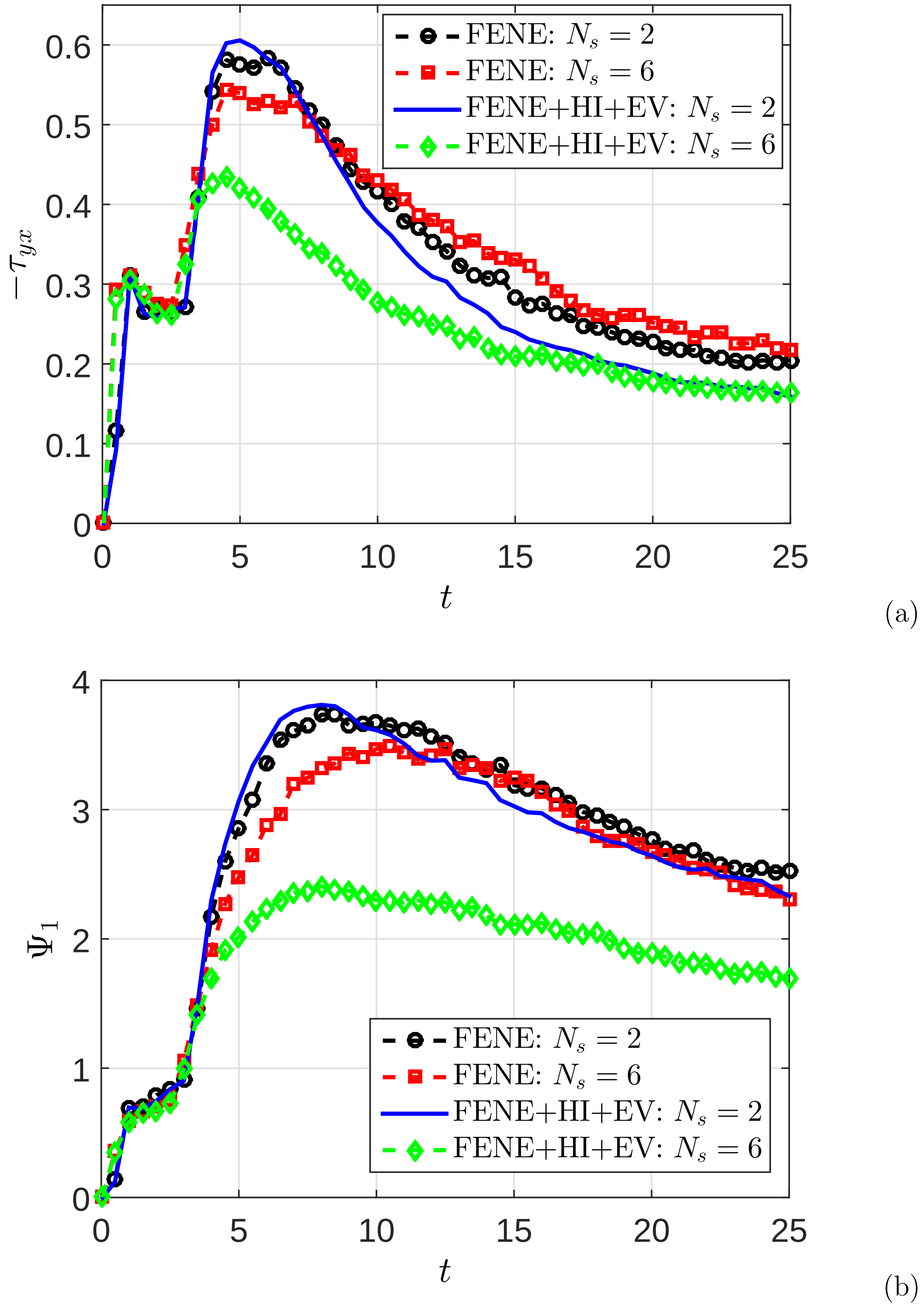

Figure 2.17: The start-up planar Couette flow problem using FENE-based BSC models of several numbers of dumbbells. The parameters are shown as in Fig. 2.14. The influence of HI and EV effects on rheological properties of the fluid. The evolution of the shear stress (figure (a)) and the first normal stress difference (figure (b)) at location $y = 0.2$.

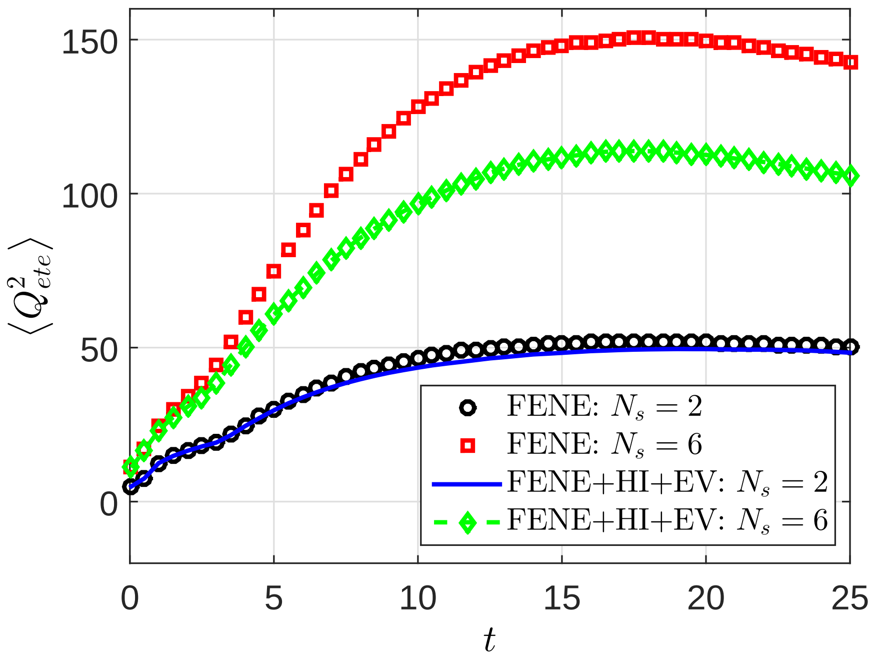

Figure 2.18: The start-up planar Couette flow problem using FENE-based BSC models of several numbers of dumbbells. The parameters are shown as in Fig. 2.14. The influence of HI and EV effects on rheological properties of the fluid. The evolution of the end-to-end connector vector at location $y = 0.2$.

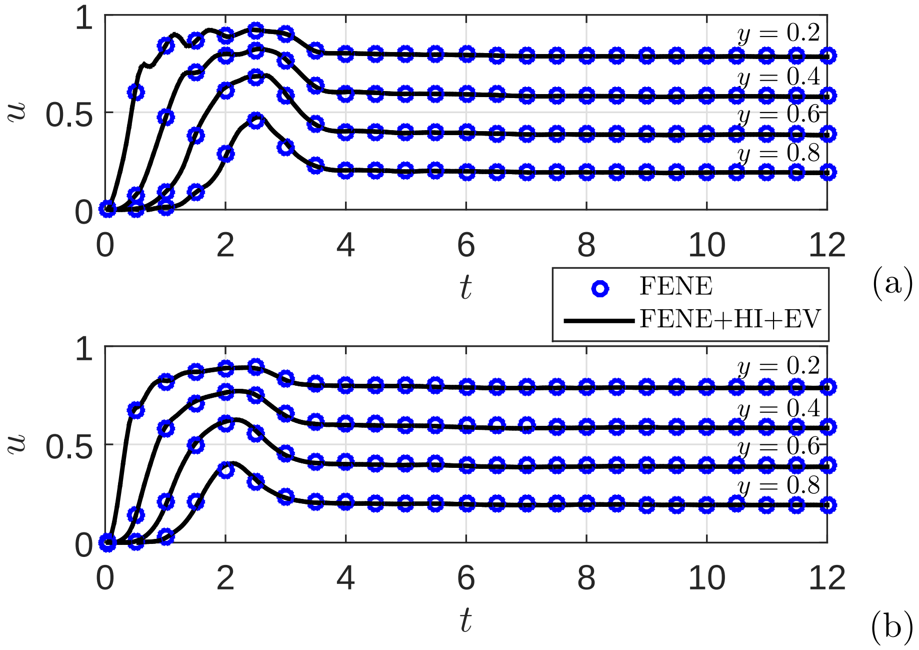

Figure 2.19: The start-up planar Couette flow problem using FENE-based BSC models of several numbers of dumbbells. The parameters are shown as in Fig. 2.14. The influence of HI and EV effects on rheological properties of the fluid. The evolution of the velocity profile with/without EV and HI effects using 2-dumbbell (figure (a)) and 6-dumbbell (figure (b)) BSC models at locations $y = 0.2$, $y = 0.4$, $y = 0.6$ and $y = 0.8$.

Table 2.2: The start-up planar Couette flow problem using FENE-BSC models with HI and EV effects. The parameters of problem: number of dumbbells in a BSC $N_s = 2$, number of BSC configurations at each collocation point $N_f = 1024$, $\Delta t = 0.001$, number of iterations $it = 2.5E + 4$. Parallel computation results are shown in the table where CPUs is number of CPUs, t_m is elapsed time for the micro procedure, t_M is elapsed time for the macro procedure, S is single mode, P is parallel mode, Spd is speed-up and Eff is efficiency.

Mode	CPUs	t_m	t_M	Spd	Eff (%)
S	1	3.02E+5	3.957267	1.00	100%
P	2	1.78E+5	4.311329	1.70	85%
P	4	1.02E+5	4.334896	2.96	74%
P	8	8.27E+4	4.333779	3.66	46%

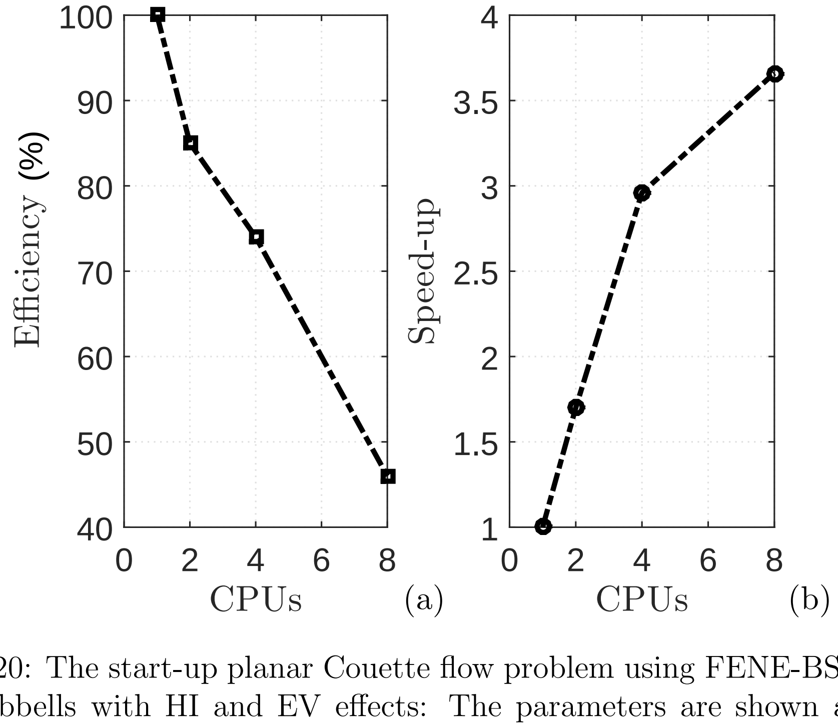

Figure 2.20: The start-up planar Couette flow problem using FENE-BSC models of 2 dumbbells with HI and EV effects: The parameters are shown as in Fig. 2.14. Parallel computation results: The efficiency (figure (a)) and the speed-up (figure (b)) with respect to the number of CPUs.

2.7 Concluding remarks

The IRBFN-BCF based CG method is employed to simulate the flow of dilute polymer solutions using complex nonlinear BSC models. The hybrid simulation method is a combination of a high-order RBFN-based approximation for the solution of macroscopic conservation equations and a BCF-based CG technique for the evolution of polymer configuration. The present method offers the advantages of a mesh-free based stochastic CG method in the simulation of viscoelastic polymer flows as presented in Tran et al. (2011). The method efficiency based on both the enhanced convergence rate of numerical solution and the stability of a stochastic process is evidenced by the successful simulation of flows using complex BSC models which take into account nonlinear interaction forces in the polymer solution, e.g. HI and EV effects. This allows the method to effectively simulate models which are realistic in comparison with experimental results. The method will be further applied for simulations of polymer melts in the next chapter.

Chapter 3

Simulation of polymer melt flows modelled by reptation models using a high-order RBF–BCF approach

The radial basis function and Brownian configuration fields (RBF-BCF) based coarse-grained method, which was reported for the flow of dilute polymer solutions in Chapter 2, is further developed to simulate the dynamic behaviours of polymer melt flows (Nguyen et al., 2016a). Macro-micro equations of a polymer melt are discretised and solved for the primitive variables, including velocity and pressure, as well as the evolution of kinetic behaviours of the polymer melt, yielding the stress in the fluid. In this chapter, a polymer melt system is modelled using "single-segment" reptation models or tube models where the polymer stress is averagely computed from an ensemble of thousands of tube segments at each grid point. The use of a Cartesian grid-based 1D-integrated RBF (1D-IRBF) approximation not only helps avoid any complex meshing process but also ensure a fast convergence rate for the solution of macro-micro governing equations. Furthermore, the use of BCF maintains the correlation of polymer stress fields in the simulation and hence enhances the numerical stability of the method. As an illustration of the method, the start-up Couette polymer melt flow and the polymer melt flow over a cylinder in a channel are examined using four classical reptation models including the Doi-Edwards, Curtiss-Bird, reptating rope, and double reptation models.

3.1 Introduction

Polymer melts and concentrated polymer solutions are extremely complex fluids due to the existence of very high density of polymer molecules. In such systems, the motion of a molecule is restricted by the neighbouring ones. Thus, a polymer chain can move mainly along its backbone and the motion in the direction perpendicular to the backbone is mostly limited by surrounding polymers (Bird et al., 1987b). Therefore, the motion of a molecule in an undiluted polymer system is assigned to a so-called reptational motion (de Gennes, 1971). In the first publication on the use of reptation theory to model undiluted polymer systems (known as the Doi and Edwards (DE) model), Doi and Edwards assumed each polymer chain in a highly concentrated system reptates in a fictitious tube created by its neighboring molecules (Doi and Edwards, 1978a,b,c). Based on the reptation concept, Curtiss and Bird (CB) model uses an anisotropic friction tensor instead of using the "tube" constraint to describe the limit of the sideways motion of polymers in the DE model (Curtiss and Bird, 1981a,b; Bird et al., 1982a,b). Furthermore, other reptation based models for the simulation of undiluted polymers such as reptating rope (RR) and double reptation (DR) models were developed. While the RR model considers the interaction between segments in each polymer chain (Jongschaap, 1988; Jongschaap and Geurts, 1988), the DR model takes into account the effect of the constraint release mechanism (des Cloizeaux, 1988). Recently, Ottinger and his coworkers developed the theory of stochastic processes which relates to theoretical kinetic models governed by a corresponding diffusion equation (Ottinger, 1989a, 1990). In this approach, the diffusion equation is transformed into a stochastic differential equation that preserves all the physical meanings while the numerical simulation method for its solution is very elegant (Ottinger, 1989a).

Over the past two decades, the stochastic macro-micro methods have been contributing significantly to the simulation of flows of viscoelastic fluids, including dilute polymer solutions, liquid crystals and polymer melts. Basically, the "macro-micro" term is based on the fact that the governing conservation equations in continuum mechanics are coupled with the coarse-grained molecular models based on kinetic theory for the solution of viscoelastic flow problems. In 1992, Ottinger and coworkers proposed the CONNFFESSIT method (Calculation of Non-Newtonian Flow: Finite Elements and Stochastic Simulation Technique) (Ottinger and Laso, 1992). One of the notable characteristics of the CONNFFESSIT is that the polymer stress field is calculated from the configuration distribution of coarse-grained molecules (dumbbells) instead of using a constitutive equation. Owing to this great advantage, the method has become a preferable choice for rheologists in finding out the dynamic characteristics of polymer flows without the need of a closed form constitutive equation (Keunings, 2004). The Eulerian approach of this method, namely Brownian configuration field (BCF) (Hulsen et al., 1997), uses an ensemble of continuous configuration fields which are convected and deformed by the drift components including the velocity gradient of the flows, elastic forces and the Brownian diffusion motion in the simulation. In an alternative approach, Tran-Canh and Tran-Cong developed an RBFN-based stochastic macro-micro meshfree method using both Lagrangian and Eulerian approaches to simulate dilute polymer solutions (Tran-Canh and Tran-Cong, 2002b, 2004). In this approach, the domain under consideration is discretised by a set of uniform or random collocation points instead of using an element-based method. Thus, it is more flexible than the CONNFFESSIT for the solution of problems with complex geometries, moving boundary and free surface. High performance computing with domain decomposition and parallel computation was also applied in the method to efficiently deal with the large-scale problems (Tran et al., 2009). The method has been further developed with the use of the integrated RBF (IRBF) (Mai-Duy et al., 2008) in discretising partial differential governing equations of the system to enhance the convergence rate as well as reduce the white noise of the multiscale method (Tran et al., 2011, 2012a; Nguyen et al., 2015b). In this chapter, the IRBF-BCF-based coarse-grained method (Nguyen et al., 2015b) is extended to simulate polymer melt systems using reptation models in a transient flow.

The chapter is organized as follows. The equations for the conservation of mass and momentum for a polymer melt flow are presented in Section 3.2. Section 3.3 is a brief introduction of the "single-segment" reptation models used in the simulation, the micro governing equations and the stress formula for each model are also shown. A general system of macro-micro governing equations is presented in Section 3.4. The numerical method is introduced in detail in Section 3.5. Section 3.6 describes the main points of the present algorithm. The numerical examples of the start-up Couette flow and the flow past a cylinder are illustrated in Section 3.7. Finally, the chapter is closed by a conclusion in Section 3.8.

3.2 Governing equations of a polymer melt flow

The flow of an incompressible and isothermal polymer melt is governed by the following equations for the conservation of mass and momentum

$$\nabla \cdot \mathbf{u} = 0, \tag{3.1}$$

$$\rho \frac{D\mathbf{u}}{Dt} = -\nabla p + \nabla \cdot \boldsymbol{\tau}_p, \tag{3.2}$$

where ρ is the polymer melt density; $\mathbf{u}$ the velocity field; t the time; $\frac{D}{Dt}(\bullet)$ the material derivative defined by $\frac{D}{Dt}(\bullet) = \frac{\partial}{\partial t}(\bullet) + (\mathbf{u} \cdot \nabla)(\bullet)$; p the hydrostatic pressure; and $\boldsymbol{\tau}_p$ the polymer stress tensor. It is worth noting that since the melt density is very high, the motion of polymer molecules is severely restricted by neighbouring ones. Thus, the behaviour of polymer melt flow is mostly dominated by the viscous component rather than inertia one and the motion equation of polymer melt flows is rewritten as

$$-\nabla p + \nabla \cdot \boldsymbol{\tau}_p = 0. \tag{3.3}$$

Polymer melt flows behave like an inertialess flow as there is no contribution from solvent viscosity. Its numerical simulation, however, faces difficulties because the macro velocity field becomes oscillating in the absence of the solvent viscosity. This instability in simulations of polymer melt system has been mentioned by

Hua and Schieber (1998) and Van Heel et al. (1999). In their work, a "numerical damping term" has been added into the inertialess momentum equation to ensure that a large change between two iterations cannot occur. The momentum equation for polymer melt flow is now modified as (Van Heel et al., 1999)

$$-\nabla p + D_P \nabla^2 (\mathbf{u} - \mathbf{u}_0) + \nabla \cdot \boldsymbol{\tau}_p = 0, \tag{3.4}$$

where D_P is a numerical damping parameter in a polymer melt flow simulation; p, $\boldsymbol{\tau}_p$ and $\mathbf{u}_0$ the known pressure, polymer stress and velocity fields, respectively, of the previous time step and $\mathbf{u}$ the unknown current velocity field. It should be noted that when the velocity field achieves a stable state, that is $\mathbf{u} \approx \mathbf{u}_0$, the "damping term" disappears and Eq. (3.4) returns to its original inertialess momentum equation for polymer melt flow (3.3).

In the macroscopic approach the system (3.1)-(3.4) is usually closed by a constitutive equation using several models of polymer melts such as the K-BKZ (Bernstein et al., 1963; Kaye, 1962), Phan-Thien–Tanner (Phan-Thien and Tanner, 1977) or Pom-Pom models (McLeish and Larson, 1998) for the polymer-contributed stress $\boldsymbol{\tau}_p$. In contrast, $\boldsymbol{\tau}_p$ is here determined numerically via a coarse-grained technique (Bird et al., 1987b; Ottinger, 1996) using reptation models. An overall microscopic procedure is described in the next section.

3.3 Stochastic mesoscopic technique for polymer melt flows using reptation models

In this approach, the determination of polymer stress tensor is carried out through two steps (Ottinger, 1996). The first step is to derive the diffusion equation or Fokker-Planck equation for the configurational distribution function which is the probability density of the polymer configuration $\mathbf{P}$ occurring at time t. The second step is to develop an expression for the stress tensor corresponding to reptation models. The stochastic simulation is based on the relationship between the diffusion equation and the stochastic differential equation (SDE). In polymer kinetic theory, polymer melts and concentrated polymer solutions are often represented in the form of tube or reptation models (Masubuchi, 2014). For the reptation concept, the evolution of tube configurations is determined and the polymer melt stress tensor is updated at each time step based on the obtained configurations of the tube model. In this work, "single-segment" tube models including the DE, CB, RR and DR models are studied using BCF based stochastic simulation technique.

In this approach, two characteristics of the segment monitored are the unit vector $\mathbf{P}$ along the segment and the position of the segment on the tube S, with $S \in [0, 1]$; and $S = 0$ and $S = 1$ are two ends of the tube. It should be emphasised that, the two characteristic quantities $\mathbf{P}$ and S of the stochastic process are governed by two separate differential equations. The stochastic and deterministic differential equations and the polymer stress formulae of reptation models are briefly presented in the forthcoming sections. The rheological aspects of the models in relation to the polymer kinetic theory were detailed in Ottinger (1996).

3.3.1 Doi-Edwards (DE) and Curtiss-Bird (CB) models

The DE and CB models are based on the diffusion equation for a probability density function $\psi(\mathbf{p}, s, t)$ as follows (Doi and Edwards, 1978a).

$$\frac{\partial \psi(\mathbf{p}, s, t)}{\partial t} = -\frac{\partial}{\partial \mathbf{u}} \cdot \left\{ \left[\left(\nabla \mathbf{u}(t)\right)^T \cdot \mathbf{p} - \left(\nabla \mathbf{u}(t)\right)^T : \mathbf{ppp} \right] \psi(\mathbf{p}, s, t) \right\} + \frac{1}{\lambda} \frac{\partial^2 \psi(\mathbf{p}, s, t)}{\partial s^2}, \tag{3.5}$$

where $\mathbf{p}$ is a unit vector describing the direction of polymer at the position s ($s \in [0, 1]$); $(\nabla \mathbf{u})^T$ the transposed velocity gradient tensor; and λ a characteristic or reptation time constant. The boundary condition for $s = 0$ and $s = 1$ is $\psi(\mathbf{p}, 0, t) = \psi(\mathbf{p}, 1, t) = \frac{1}{4\pi}\delta(|\mathbf{p}| - 1)$ where δ is the Dirac delta function.

The system of deterministic and stochastic differential equations for a stochastic process ($\mathbf{P}$,S) corresponding to the DE and CB models derived from Eq. (3.5) is given by (Van Heel et al., 1999).

$$d\mathbf{P}\left(\mathbf{x},t\right) = \left(\mathbf{I}-\mathbf{PP}\right)\cdot\left(\nabla\mathbf{u}\left(\mathbf{x},t\right)\right)^{T}\cdot\mathbf{P}\left(\mathbf{x},t\right)dt-\mathbf{u}\left(\mathbf{x},t\right)\cdot\nabla\mathbf{P}\left(\mathbf{x},t\right)dt, \tag{3.6a}$$

$$dS = \sqrt{\tfrac{2}{\lambda}}dW\left(t\right), \tag{3.6b}$$

where $\mathbf{I}$ is the identity matrix or tensor; $W\left(t\right)$ the 1-D time-dependent Wiener process; and $\mathbf{P}$ and S ($S\in[0,1]$) the unit vector and real value associated with $\mathbf{p}$ and s, respectively. Since the two characteristics $\mathbf{P}$ and S of the stochastic process are governed by two separate differential equations (3.6a)-(3.6b), respectively, when S goes beyond the limits ($S<0$ or $S>1$), a reflection needs to be done as follows: $S\rightarrow -S$ for $S<0$, and $S\rightarrow 2-S$ for $S>1$. In such cases, the configuration field $\mathbf{P}$'s is randomly re-initialised.

The polymer stress tensor associated with the DE and CB models is given by

$$\boldsymbol{\tau}_p\left(t\right) = Nn_pk_BT\left[\frac{1}{3}\mathbf{I}-\langle\mathbf{PP}\rangle-l_1\lambda(\nabla\mathbf{u})^{T}:\big\langle S\left(1-S\right)\mathbf{PPPP}\big\rangle\right] \tag{3.7}$$

where T is the absolute temperature; k_B the Boltzmann constant; n_p the density of polymers; N the number of beads of a Kramers chain; $\langle\mathbf{PP}\rangle$ the statistical average of $\mathbf{PP}$; and l_1 ($l_1\in[0,1]$) the link tension coefficient (Curtiss and Bird, 1981a). With $l_1=0$, the stress tensor in Eq. (3.7) is for the DE model.

3.3.2 Reptating rope (RR) model

In the RR model, each polymer molecule is considered as an elastic rope moving in a constraining tube and the interaction between segments within a single chain is taken into account in the simulation of polymer melt flows. Thus, two reptation processes $(\mathbf{P},S)$ and $(\mathbf{P}',S')$ governed by Eqs. (3.6a)-(3.6b) are simultaneously processed to simulate polymer melt flows (Ottinger, 1990). The stress tensor of the model is determined as follows.

$$\boldsymbol{\tau}_p\left(t\right) = Nn_pk_BT\left(\frac{1}{3}\mathbf{I}-\langle\mathbf{PP}\rangle\right)+\Delta\boldsymbol{\tau}_p, \tag{3.8}$$

where $\Delta\boldsymbol{\tau}_p\left(t\right)$ is given by

$$\Delta\boldsymbol{\tau}_p = -\frac{1}{2}n_p k_B T\lambda(\nabla\mathbf{u})^T : \left\langle \left(S + S' - \left|S - S'\right| - 2SS'\right)\mathbf{P}'\mathbf{P}'\mathbf{P}\mathbf{P}\right\rangle. \tag{3.9}$$

It should be noted that S and S' are two separate segments within the same polymer chain; $\mathbf{P}$ and $\mathbf{P}'$ denote the direction of the two segments S and S', respectively.

In order to consider the correlation between the two reptation processes, a length parameter Δ $(0 \leq \Delta \leq 1)$ is introduced into the simulation (Ottinger, 1996). If the difference $|S - S'|$ is larger than Δ, the processes have no correlation and the directions of $\mathbf{P}$ and $\mathbf{P}'$ are independent from each other. Otherwise, their directions are coincident.

3.3.3 Double reptation (DR) model

In the DR model, a constraint release mechanism is introduced into the evolution of $\mathbf{P}$. The system of deterministic and stochastic differential equations is given by (Ottinger, 1996).

$$\begin{aligned} d\mathbf{P}\left(\mathbf{x},t\right) = (\mathbf{I} - \mathbf{P}\mathbf{P}) \cdot \left[(\nabla\mathbf{u})^T \cdot \mathbf{P}dt + \frac{\pi l_2}{\sqrt{3\lambda}}d\mathbf{W}_2(t)\right] & \\ -\frac{\pi^2 {l_2}^2}{3\lambda}\mathbf{P}dt - \mathbf{u}\cdot\nabla\mathbf{P}dt, & \end{aligned} \tag{3.10a}$$

$$dS = \sqrt{\tfrac{2}{\lambda}}dW_1\left(t\right), \tag{3.10b}$$

where l_2 is a real number related to the reptation coefficient l' (Ottinger, 1996); and $\mathbf{W_2}$ the 3-D Wiener process describing the effect of constraint release which was introduced into the DE and CB models. The corresponding stress tensor for the DR model is determined as follows.

$$\begin{aligned} \boldsymbol{\tau}_p(t) = Nn_p k_B T\left[\frac{1}{3}\mathbf{I} - \langle\mathbf{P}\mathbf{P}\rangle - l_1\lambda\left(\nabla\mathbf{u}\right)^T : \left\langle S\left(1 - S\right)\mathbf{P}\mathbf{P}\mathbf{P}\mathbf{P}\right\rangle\right. & \\ \left. -l_3\lambda(\nabla\mathbf{u})^T : \langle\mathbf{P}\mathbf{P}\mathbf{P}\mathbf{P}\rangle\right] & \end{aligned} \tag{3.11}$$

where l_3 is the dimensionless parameter defined from experimental or theoretical methods; and others as defined above. It is worth emphasising that the system (3.10) can be considered as the general form for classical reptation models.

3.4 A coupled macro-micro multiscale system for polymer melt flows using the classical reptation models

Collecting the differential conservation equations (3.1)-(3.4), the BCF stochastic differential equations of tube segments, the Brownian motion of the random walker and the stress tensor using the classical reptation models yields a macro-microscopic multiscale system as follows.

$$\nabla \cdot \mathbf{u} = 0, \tag{3.12a}$$

$$D_P \nabla^2 \left(\mathbf{u} - \mathbf{u}_0\right) + \nabla \cdot \boldsymbol{\tau}_p - \nabla p = 0, \tag{3.12b}$$

$$\begin{aligned} d\mathbf{P}\left(\mathbf{x}, t\right) = \left(\mathbf{I} - \mathbf{P}\mathbf{P}\right) \cdot &\left[\left(\nabla \mathbf{u}\right)^T \cdot \mathbf{P} dt + \frac{\pi l_2}{\sqrt{3\lambda}} d\mathbf{W}_2(t) \right] \\ &- \frac{\pi^2 {l_2}^2}{3\lambda} \mathbf{P} dt - \mathbf{u} \cdot \nabla \mathbf{P} dt, \end{aligned} \tag{3.12c}$$

$$dS\left(t\right) = \sqrt{\tfrac{2}{\lambda}} dW_1\left(t\right), \tag{3.12d}$$

$$\begin{aligned} \boldsymbol{\tau}_p = N n_p k_B T \Big[&\frac{1}{3}\mathbf{I} - \langle \mathbf{P}\mathbf{P} \rangle - l_1 \lambda \left(\nabla \mathbf{u}\right)^T : \big\langle S\left(1 - S\right) \mathbf{P}\mathbf{P}\mathbf{P}\mathbf{P} \big\rangle \\ &- l_3 \lambda \left(\nabla \mathbf{u}\right)^T : \langle \mathbf{P}\mathbf{P}\mathbf{P}\mathbf{P} \rangle \Big] + l_4 \Delta \boldsymbol{\tau}_p, \end{aligned} \tag{3.12e}$$

where all parameters are defined in previous sections. It should be noted that the system of macro-micro equations (3.12) are developed in the general form for all reptation models. Specifically, with $l_1 = l_2 = l_3 = l_4 = 0$ the equations are for the DE model; $l_2 = l_3 = l_4 = 0$ for the CB model; $l_1 = l_2 = l_3 = 0$ for the RR model; and $l_4 = 0$ for the DR model.

Let U_c and L_c be the characteristic velocity and length, respectively; $t_c = \frac{L_c}{U_c}$ the macroscopic characteristic time; $\tau_d = \frac{\lambda}{\pi^2}$ the characteristic relaxation time of reptation models used in the present work. Dimensionless variables are given by (Van Heel et al., 1999).

$$p^* = p\frac{L_c}{\eta_0 U_c} \qquad \boldsymbol{\tau}_p^* = \boldsymbol{\tau}_p\frac{L_c}{\eta_0 U_c}, \qquad \mathbf{u}^* = \frac{\mathbf{u}}{U_c}, \qquad t^* = \frac{t}{t_c}, \tag{3.13}$$

where η_0 is the zero-shear-rate viscosity. Other parameters were defined as before. The dimensionless Weissenberg number We is defined as follows.

$$We = \frac{\tau_d}{t_c} = \frac{\lambda U_c}{\pi^2 L_c}.$$

The stochastic multiscale system (3.12a)-(3.12e) are rewritten in dimensionless form as

$$\nabla^* \cdot \mathbf{u}^* = 0, \tag{3.14a}$$

$$D_P^*(\nabla^*)^2\left(\mathbf{u}^* - \mathbf{u}_0^*\right) + \nabla^* \cdot \boldsymbol{\tau}_p^* - \nabla^* p^* = 0, \tag{3.14b}$$

$$\begin{aligned} d\mathbf{P} = (\mathbf{I} - \mathbf{PP}) \cdot &\left[(\nabla^* \mathbf{u}^*)^T \cdot \mathbf{P} dt^* + \frac{l_2}{\sqrt{3We}} d\mathbf{W}_2^*\right] \\ &- \frac{{l_2}^2}{3We}\mathbf{P}dt^* - \mathbf{u}^* \cdot \nabla^* \mathbf{P} dt^*, \end{aligned} \tag{3.14c}$$

$$dS = \sqrt{\tfrac{2}{\pi^2 We}}\, dW_1^*, \tag{3.14d}$$

$$\begin{aligned} \boldsymbol{\tau}_p^* = \left[N n_p k_B T\right]^* &\left[\frac{1}{3}\mathbf{I} - \langle\mathbf{PP}\rangle - l_1\pi^2 We\,(\nabla^*\mathbf{u}^*)^T : \left\langle S\,(1-S)\,\mathbf{PPPP}\right\rangle \right. \\ &\left. - l_3\pi^2 We\,(\nabla^*\mathbf{u}^*)^T : \langle\mathbf{PPPP}\rangle\right] + l_4\Delta\boldsymbol{\tau}_p^*, \end{aligned} \tag{3.14e}$$

where $\Delta\boldsymbol{\tau}_p^*$ is given by

$$\Delta\boldsymbol{\tau}_p^* = -\frac{1}{2}\left[n_p k_B T\right]^* \pi^2 We(\nabla^*\mathbf{u}^*)^T : \left\langle \left(S + S' - \left|S - S'\right| - 2SS'\right)\mathbf{P}'\mathbf{P}'\mathbf{PP}\right\rangle. \tag{3.15}$$

In Eqs. (3.14)-(3.15), the asterisk symbol ($*$) indicates the dimensionless form of variables. It should be pointed out that $\left[N n_p k_B T\right]^*$ and $\left[n_p k_B T\right]^*$ depict the dimensionless form of $N n_p k_B T$ and $n_p k_B T$ (stress dimension), respectively.

Henceforth, all variables will be written in the dimensionless form and the asterisk symbol will be removed for simplicity.

3.5 Numerical method

In this section, the spatial and temporal discretisations for the hybrid system of macro-micro governing equations are introduced in detail. In the macro procedure, the 1D-IRBF scheme is applied to spatially discretise the conservation equations (3.14a)-(3.14b). In the micro procedure, the stochastic differential equations (3.14d)-(3.14c) are advanced with respect to time using a simple Euler explicit scheme.

3.5.1 IRBF-based projection method for solution of the macroscopic governing equations

The projection method is used to solve the macroscopic governing equations (3.14a)-(3.14b) of a polymer melt flow. The process includes three steps as follows (Kim and Moin, 1985).

- Step 1: An intermediate velocity $\bar{\mathbf{u}}$ is calculated by solving Eq. (3.14b), neglecting the pressure gradient term and incompressibility.

  $$\frac{\bar{\mathbf{u}}-\mathbf{u}^n}{\Delta t}=D_P\nabla^2\left(\bar{\mathbf{u}}-\mathbf{u}^n\right)+\nabla\cdot\boldsymbol{\tau}_p^n, \tag{3.16}$$

  where Δt is the time step size; and $\mathbf{u}^n$ and $\boldsymbol{\tau}_p^n$ the known velocity vector and stress tensor, respectively, in the previous time step $t^n=n\Delta t$. The Dirichlet boundary conditions $\bar{\mathbf{u}}=\mathbf{u}^n$ are imposed on boundaries.

- Step 2: Solve the Poisson equation for the pseudo pressure ϕ,

  $$\nabla^2\phi=\frac{1}{\Delta t}\nabla\cdot\bar{\mathbf{u}}, \tag{3.17}$$

  where ϕ is related to the pressure p by the expression $p=\phi-D_P\Delta t\left(\frac{\partial^2\phi}{\partial x^2}+\frac{\partial^2\phi}{\partial y^2}\right)$. The Neumann boundary condition for the solution of Eq. (3.17) is determined by

  $$\mathbf{n}\cdot\nabla\phi=\frac{1}{\Delta t}\mathbf{n}\cdot\left(\bar{\mathbf{u}}-\mathbf{u}^n\right), \tag{3.18}$$

where $\mathbf{n}$ is the outward normal vector of the boundary. It can be seen that the mass conservation equation (3.14a) is satisfied by the introduction of Eq. (3.17).

- Step 3: Determine the velocity field $\mathbf{u}^{n+1}$ at the current time step $t^{n+1} = (n+1)\Delta t$,

$$\mathbf{u}^{n+1} = \bar{\mathbf{u}} - \Delta t \nabla \phi. \tag{3.19}$$

The boundary value problems mentioned in steps 1 and 2 of Section 3.5.1 are discretised using the 1D-IRBF approximation scheme as presented in Section 2.5.1.

3.5.2 BCF-based simulation technique for the evolution of polymer melt configurations

BCF algorithm for the simulation of a reptation process

In the present BCF-IRBFN multiscale approach, the analysis domain is discretised by a set of N collocation points instead of using a mesh of elements in the element based methods. At each collocation point, N_f tube segments $\mathbf{P}_i(t)$ $(i = 1, 2, 3, ..., N_f)$ are attached to the point in the course of simulation. Therefore, there are N sets of N_f tube segments on the whole domain. A configuration field $\mathbf{P}_i(\mathbf{x}, t)$ is defined as a set of the tube segments having the same index i on the domain or, in other words, a configuration field consists of N tube segments indexed by i on N collocation points. An illustrative example with $N = 9$ and $N_f = 2$ is presented in Fig. 3.1.

At the initial time, N_f configuration fields are uniformly initiated on all collocation points,

$$\mathbf{P}_i(\mathbf{x}, 0) = \mathbf{P}_i^0 \qquad (i = 1, 2, 3, \ldots, N_f). \tag{3.20}$$

The initialising of a uniform tube configuration field yields an identical stress field on the whole domain, which reduces the numerical instability of the stress field in the simulation. The evolution of the configuration field is governed by equation

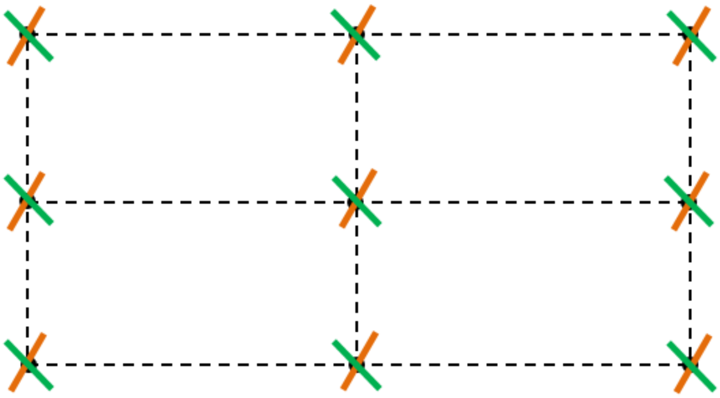

Figure 3.1: An illustrative example of configuration fields with $M = 9$ and $N_f = 2$. N: Number of collocation points; N_f: number of tube segments attached at each collocation points. Thus, there are two configuration fields: $\mathbf{P}_1(\mathbf{x}, t)$ and $\mathbf{P}_2(\mathbf{x}, t)$.

(3.14c) which is solved with the boundary condition of $S_i \in [0, 1]$. Nonetheless, since each tube segment makes a random walk S governed by Eq. (3.14d) through the reptation process, the initial correlation of the stress field is more likely to be degraded by the stochastic process. In order to fix this issue, Van Heel et al. (1999) have proposed that each configuration field $\mathbf{P}_i(\mathbf{x}, t)$ associates with only one random walk S_i. When S_i is reflected at a boundary, a random unit vector is generated and assigned to all tube segments in the configuration field $\mathbf{P}_i(\mathbf{x}, t)$.

The Euler explicit method for temporal discretisation of the stochastic differential equations

The evolution of the polymer melt configuration in Eqs. (3.14c)-(3.14d) using the Euler explicit scheme is given for the characteristic S by

$$S_i^{n+1} = S_i^{n} + \sqrt{\frac{2\Delta t}{\pi^2 We}} W_{1i}{}^{n}, \tag{3.21}$$

where Δt is the time step; S_i^{n+1} and S_i^{n} values of S at two successive time steps $t^{n+1} = (n+1)\Delta t$ and $t^n = n\Delta t$, respectively; W_{1i} a single Gaussian random number and i presents the configuration field as described in the previous subsection; and for the characteristic $\mathbf{P}$ by

$$\begin{aligned}\mathbf{P}_i^{n+1} = \mathbf{P}_i^{n} + (\mathbf{I} - \mathbf{P}_i^{n}\mathbf{P}_i^{n}) \left[(\nabla \mathbf{u}^n)^T \cdot \mathbf{P}_i^{n} \Delta t + \frac{l_2\sqrt{\Delta t}}{\sqrt{3We}} \mathbf{W}_i^{n} \right] \\ - \frac{l_2^2}{3We} \mathbf{P}_i^{n} \Delta t - \mathbf{u}^n \cdot \nabla \mathbf{P}_i^{n} \Delta t,\end{aligned} \tag{3.22}$$

where $\mathbf{u}^n$ and $\nabla\mathbf{u}^n$ are the velocity and velocity gradient at the time step n, respectively.

The Euler discretisation causes a significant error unless sufficiently small time steps are used. Indeed, at time step t^n, if S^n is out of $[0, 1]$, an observed reflection at boundaries is carried out. Otherwise, S^n could go beyond the limit $[0, 1]$ during the time period $[t^n = n\Delta t,\ t^{n+1} = (n + 1)\Delta t]$. Thus, Ottinger (1989a) has proposed a treatment at boundaries $S = 0$ and $S = 1$ in the simulation of polymer melt flows using an unobserved reflection as follows.

The conditional probability for an unobserved reflection to happen is given by

$$P_{\text{ur}} = e^{-\frac{\pi^2 We(b-S_i^n)(b-S_i^{n+1})}{\Delta t}}, \tag{3.23}$$

where b is a boundary at which an unobserved reflection happens and determined as follows.

$$\left[\begin{array}{lll} b = 0 & \text{if} & S_i^n + S_i^{n+1} \leq 1, \\ b = 1 & \text{if} & S_i^n + S_i^{n+1} > 1. \end{array}\right. \tag{3.24}$$

The unobserved reflection algorithm associated with the BCF approach for the treatment of stochastic process $(\mathbf{P}, S)$ is presented in Fig. 3.2.

3.6 Algorithm of the present procedure

The algorithm of the BCF-IRBFN based macro-micro multiscale method as reported in Section 2.5.4 is modified to incorporate the reptation concept for different polymer melt systems as follows.

(a) The simulation starts with N_f initial configurations of tube segments ($\mathbf{P}_i^0$,

$i = \big(1, 2, \ldots N_f\big))$ which are generated and uniformly distributed on every collocation points for the microscopic procedure. A set of N_f values of S_i in $[0, 1]$ is also initiated corresponding with $\mathbf{P}_i^0$.

(b) The stress tensor at every point on the considered domain is calculated from a set of N_f tube segments assigned to each collocation point. A uniform polymer stress field is obtained at the first iteration because the initial molecular configurations are identical.

(c) The projection method, presented in Section 3.5.1, is applied to solve the conservation equations (3.14a)- (3.14b) for the new velocity and pressure fields .

(d) The polymer configuration fields are processed by advancing the stochastic differential equations (3.14d)-(3.14c) of reptation models with respect to time using the improved algorithm presented in Fig. 3.2. The correlation of configurations is maintained at each time step because each configuration field associates with only one random walk S.

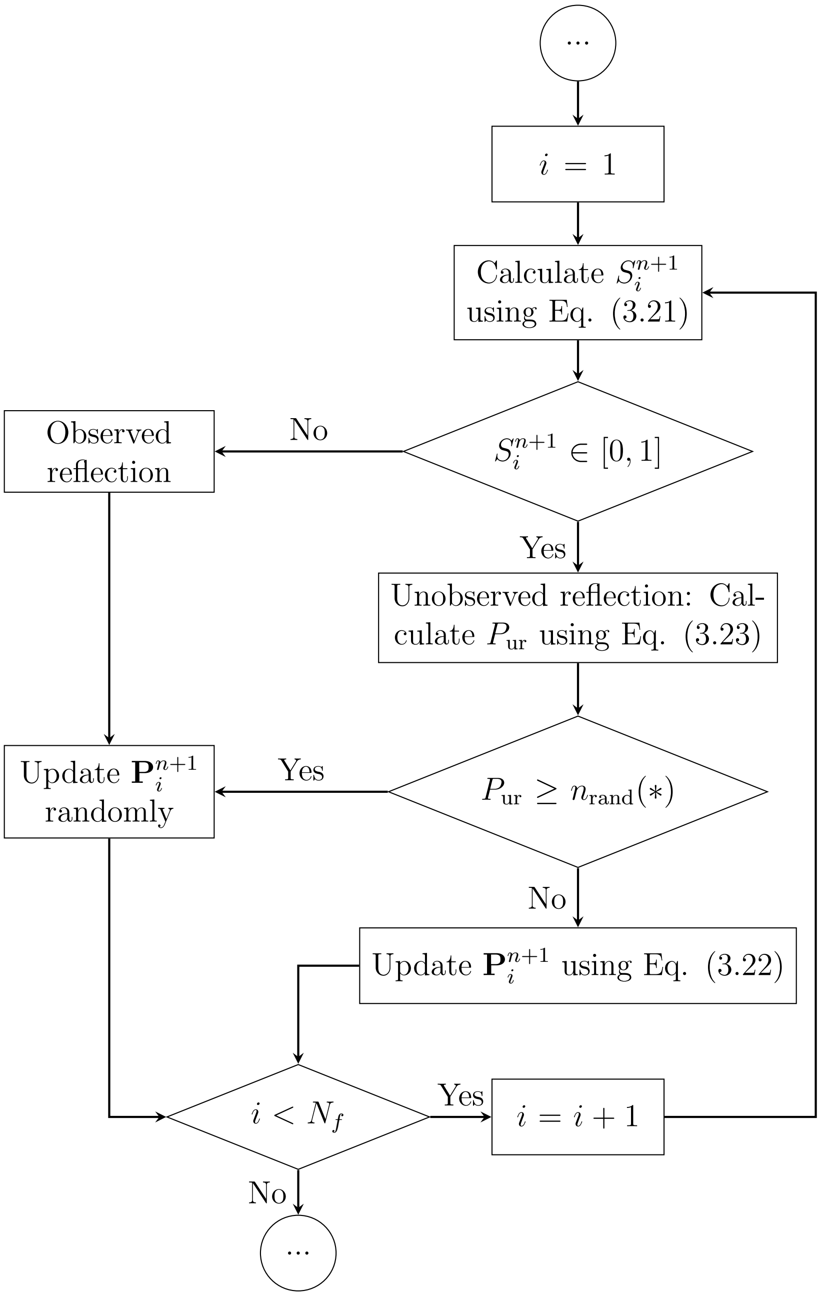

Figure 3.2: The BCF-based unobserved reflection algorithm for the treatment of stochastic process $(\mathbf{P}, S)$. $(*)$ n_{rand} is a uniformly distributed random scalar number in the interval (0,1).

3.7 Numerical examples

In this work, the start-up Couette flow and the flow past a cylinder in a long channel of polymer melt systems of different reptation models are simulated using the BCF-IRBF methods. While results obtained by the simulation of the latter problem are verified with those by Van Heel et al. (1999), the solutions of the former one are compared with those of Ottinger and Laso (1995) for the DE model.

3.7.1 Start-up Couette flow of polymer melts with reptation models

The start-up Couette flow problem is presented in Fig. 3.3. It consists of two parallel plates, where the top plate is fixed while the bottom plate constantly moves with a velocity $U_c = 1$. The distance between two plates is scaled as $L_c = 1$.

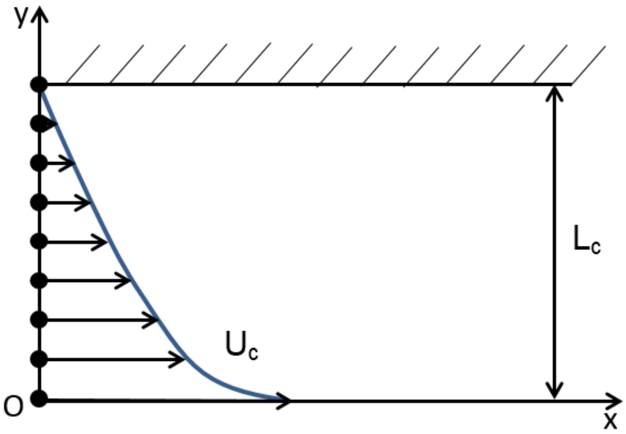

Figure 3.3: The start-up Couette flow problem. The collocation points and the velocity profile are only presented schematically.

From the characteristics of the problem of Couette flow problem of polymer melts, a system of stochastic macro-micro equations (3.12a,b,c,d,e) is developed as follows.

$$D_P\left(\frac{\partial^2 u}{\partial y^2}(y,t)-\frac{\partial^2 u_0}{\partial y^2}(y,t)\right)+\frac{\partial \tau_{p,xy}}{\partial y}(y,t)=0, \tag{3.25}$$

$$dS(t)=\sqrt{\frac{2}{\pi^2 We}}dW_1(t), \tag{3.26}$$

$$\begin{cases} dP_x(y,t)=\frac{\partial u}{\partial y}(y,t)P_y(y,t)\,dt+\frac{l_2}{\sqrt{3We}}dW_{2x}-\frac{l_2{}^2}{3We}P_x(y,t)\,dt, \\ dP_y(t)=\frac{l_2}{\sqrt{3We}}dW_{2y}-\frac{l_2{}^2}{3We}P_y(y,t)\,dt, \\ dP_z(t)=\frac{l_2}{\sqrt{3We}}dW_{2z}-\frac{l_2{}^2}{3We}P_z(y,t)\,dt, \end{cases} \tag{3.27}$$

$$\begin{cases} \tau_{p,xx}=Nn_pk_BT\Big[\frac{1}{3}-\langle P_xP_x\rangle-l_1\pi^2We\frac{\partial u}{\partial y}S(1-S)\left\langle P_xP_yP_xP_x\right\rangle \\ \qquad -l_3\pi^2We\frac{\partial u}{\partial y}\left\langle P_xP_yP_xP_x\right\rangle\Big]+\Delta\tau_{p,xx}, \\ \tau_{p,yy}=Nn_pk_BT\Big[\frac{1}{3}-\left\langle P_yP_y\right\rangle-l_1\pi^2We\frac{\partial u}{\partial y}S(1-S)\left\langle P_xP_yP_yP_y\right\rangle \\ \qquad -l_3\pi^2We\frac{\partial u}{\partial y}\left\langle P_xP_yP_yP_y\right\rangle\Big]+\Delta\tau_{p,yy}, \\ \tau_{p,zz}=Nn_pk_BT\Big[\frac{1}{3}-\langle P_zP_z\rangle-l_1\pi^2We\frac{\partial u}{\partial y}S(1-S)\left\langle P_xP_yP_zP_z\right\rangle \\ \qquad -l_3\pi^2We\frac{\partial u}{\partial y}\left\langle P_xP_yP_zP_z\right\rangle\Big]+\Delta\tau_{p,zz}, \\ \tau_{p,xy}=Nn_pk_BT\Big[-\left\langle P_xP_y\right\rangle-l_1\pi^2We\frac{\partial u}{\partial y}S(1-S)\left\langle P_xP_yP_xP_y\right\rangle \\ \qquad -l_3\pi^2We\frac{\partial u}{\partial y}\left\langle P_xP_yP_xP_y\right\rangle\Big]+\Delta\tau_{p,xy}, \end{cases} \tag{3.28}$$

where $\left(P_x,P_y,P_z\right)$ and $\left(W_{2x},W_{2y},W_{2z}\right)$ are three components of vectors $\mathbf{P}$, and $\mathbf{W}_2$, respectively; $\tau_{p,xx}$, $\tau_{p,yy}$, $\tau_{p,zz}$ and $\tau_{p,xy}$ the normal and shear stress components of $\boldsymbol{\tau}_p$. $\Delta\tau_{p,xx}$, $\Delta\tau_{p,yy}$, $\Delta\tau_{p,zz}$ and $\Delta\tau_{p,xy}$ are components of the stress contribution characterised by the RR model and given by (see Eq. (3.15))

$$\begin{cases} \Delta\tau_{p,xx}=-\frac{1}{2}n_pk_BT\pi^2We\frac{\partial u}{\partial y}\left(S+S'-|S-S'|-2SS'\right)\left\langle P'_xP'_yP_xP_x\right\rangle, \\ \Delta\tau_{p,yy}=-\frac{1}{2}n_pk_BT\pi^2We\frac{\partial u}{\partial y}\left(S+S'-|S-S'|-2SS'\right)\left\langle P'_xP'_yP_yP_y\right\rangle, \\ \Delta\tau_{p,zz}=-\frac{1}{2}n_pk_BT\pi^2We\frac{\partial u}{\partial y}\left(S+S'-|S-S'|-2SS'\right)\left\langle P'_xP'_yP_zP_z\right\rangle, \\ \Delta\tau_{p,xy}=-\frac{1}{2}n_pk_BT\pi^2We\frac{\partial u}{\partial y}\left(S+S'-|S-S'|-2SS'\right)\left\langle P'_xP'_yP_xP_y\right\rangle, \end{cases} \tag{3.29}$$

where P'_x, P'_y and P'_z are three components of the unit segment $\mathbf{P}'$; S' the position of the $\mathbf{P}'$ in a rope model; and Δ the correlation length parameter related to the link tension coefficient l_1 by $\Delta=\frac{1}{2l_1N}$ (Ottinger, 1996).

It is worth noting that while the Couette flow problem is in 1-D space, the micro configuration fields are processed in 3-D one. Hence, the time discretisation of the macro-microscopic governing equations (3.25)-(3.27) using the numerical schemes presented in Sections 3.5.1 and 3.5.2 yields

$$u^{n+1} - D_P \frac{d^2 u^{n+1}}{dy^2} \Delta t = u^n - D_P \frac{d^2 u^n}{dy^2} \Delta t + \frac{d\tau^n_{p,xy}}{dy} \Delta t, \tag{3.30}$$

$$S^{n+1} = S^n + \sqrt{\frac{2\Delta t}{\pi^2 We}} W^n_1, \tag{3.31}$$

$$\begin{cases} P^{n+1}_x = P^n_x + \left(\frac{du}{dy}\right)^{n+1} P^n_y \Delta t + \frac{l_2\sqrt{\Delta t}}{\sqrt{3We}} W^n_{2x} - \frac{l_2{}^2}{3We} P^n_x \Delta t, \\ P^{n+1}_y = P^n_y + \frac{l_2\sqrt{\Delta t}}{\sqrt{3We}} W^n_{2y} - \frac{l_2{}^2}{3We} P^n_y \Delta t, \\ P^{n+1}_z = P^n_z + \frac{l_2\sqrt{\Delta t}}{\sqrt{3We}} W^n_{2z} - \frac{l_2{}^2}{3We} P^n_z \Delta t, \end{cases} \tag{3.32}$$

where Δt is the time step size for both macro and micro procedures; the superscripts $(n+1)$ and n depict the two successive time steps $t^{n+1} = (n+1)\Delta t$ and $t^n = n\Delta t$, respectively. The numerical damping parameter D_P is defined as $D_P = G\Delta t$, where $G = N n_p k_B T$ is the modulus of rigidity of the reptation model (Van Heel et al., 1999).

Numerical results and discussion for the flow using the DE model

The polymer melt parameters used in the simulation include the fluid density $\rho = 1$, the zero-shear-rate viscosity $\eta_0^{DE} = 1$ and the relaxation time $\lambda = 50$. The Weissenberg number of the polymer melt flow is defined as $We = \frac{\lambda U_c}{\pi^2 L_c} = \frac{50}{\pi^2} \simeq 5$.

The time step size Δt for this problem is studied with the number of collocation points $N_y = 21$ and the number of configuration fields $N_f = 2500$. The results for the evolution of shear stress (τ_{yx}) and the convergence measures of velocity field ($CM(u)$) for $\Delta t = \{0.01, 0.005, 0.002, 0.001, 0.0005, 0.0001\}$ are presented in Figs. 3.4 and 3.5. It is observed that the difference of τ_{yx} with different Δt's is insignificant. However, $CM(u)$'s for large time steps $\Delta t = \{0.01, 0.005\}$ show a sudden increase after the time $t \approx 17$ (Fig. 3.5). Therefore, Δt should be chosen in the range of $\{0.002, 0.001, 0.0005, 0.0001\}$ to maintain the stability of the present method in both macro and micro procedures. In this example, $\Delta t = 0.001$ is chosen.

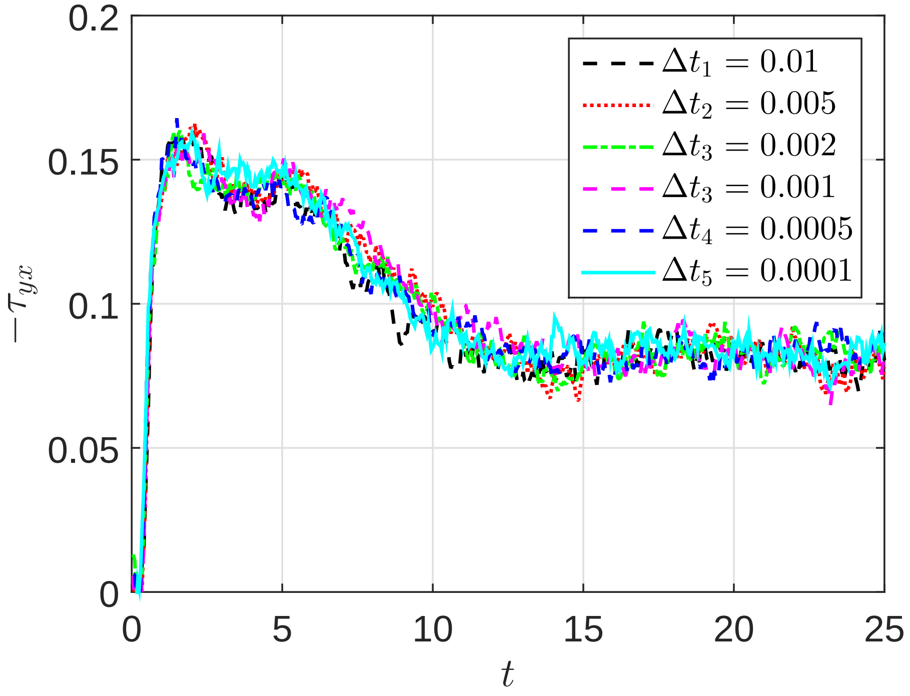

Figure 3.4: The start-up Couette flow of polymer melt using the DE model: the evolution of the shear stress at the position $y = 0.2$ for $\Delta t = \{0.01, 0.005, 0.002, 0.001, 0.0005, 0.0001\}$.

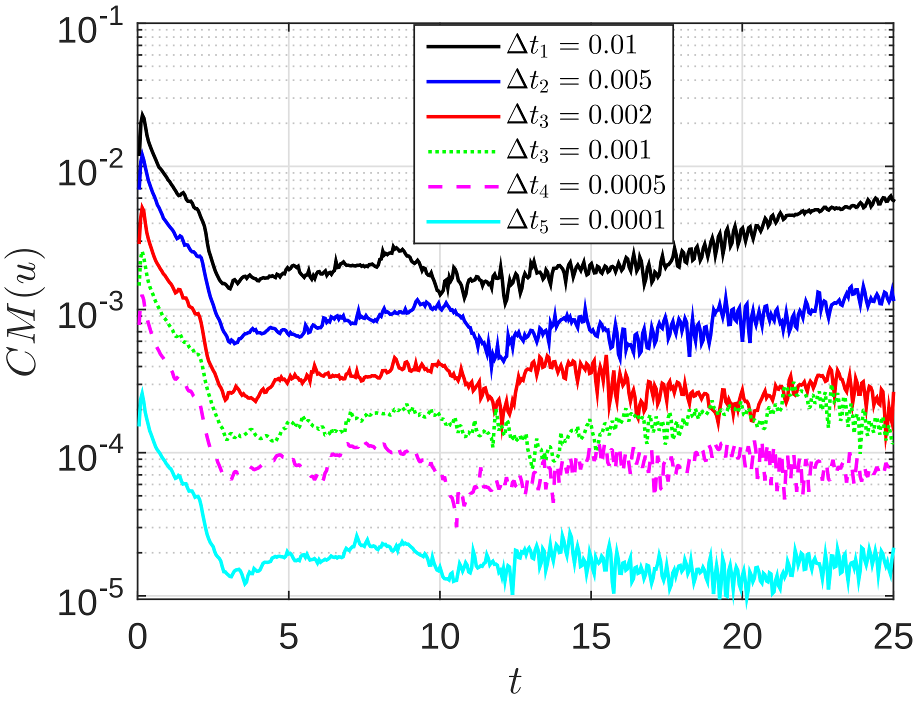

Figure 3.5: The start-up Couette flow of polymer melt using the DE model: the convergence measure of the velocity field ($CM(u)$) for $\Delta t = \{0.01, 0.005, 0.002, 0.001, 0.0005, 0.0001\}$.

The results by the present method show a very good agreement with those by Ottinger and Laso (1995) where finer meshes (40 elements) and finer time step ($\Delta t = 0.0001$) were used. A discussion of the present results and a comparison with others are as follows.

- Fig. 3.6 describes the evolution of the velocity profile in the considered domain as follows. At a very early time ($t = 0.25$), the plate motion causes a perturbation on the velocity field in the region near the plate. Then, the momentum caused by the plate motion is successively transferred to next layers of polymer melt along the y-direction with a propagating speed (c) given by (Ottinger and Laso, 1995)

  $$c^2 = \frac{12\eta_0^{DE}}{\rho\lambda}, \tag{3.33}$$

  where $\eta_0^{DE} = Nn_pk_BT\lambda/60$ is the zero-shear-rate viscosity for the DE model. Other parameters are defined as before. As a result, the polymer layer near the wall (top plate, Fig. 3.3) starts moving after $t = 2$ of the flow's start-up (see Fig. 3.6: $t = 2$) according to Eq. (3.33). The velocity then gradually decreases until reaching a stable state. Fig. 3.6 also depicts the existence of two separate shear regions at the stable state of the flow as reported in McLeish and Ball (1986); Malkus et al. (1990); Ottinger and Laso (1995); Hua and Schieber (1996). Very low velocity gradient dominates most of the flow field ($y \in [0.1, 1]$) and a narrow region near the moving plate ($y \in [0, 0.1]$) is influenced by a very high velocity gradient (see Fig. 3.7). This characteristic distinguishes polymer melt from dilute solutions in a shear flow.

- The evolution of velocity at locations $y = 0.05$, 0.1, 0.4 and 0.8 is presented in Fig. 3.8. Due to the existence of two different shear rate zones in the flow, the velocity evolution at different locations are very distinct. To be more specific, the velocity in the high-shear-rate region at location $y = 0.05$ is significantly higher than ones in the low-shear-rate zone at locations $y = 0.1$, 0.4 and 0.8. Furthermore, the overshoot of the velocity is always observed before reaching a stable value.

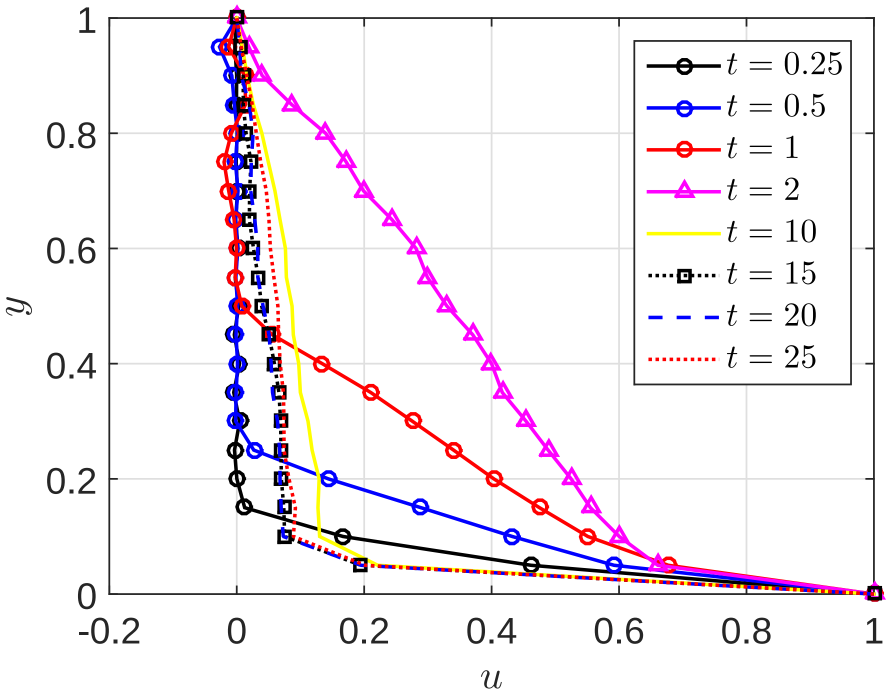

Figure 3.6: The start-up Couette flow of polymer melt using the DE model: The evolution of velocity profile on whole domain.

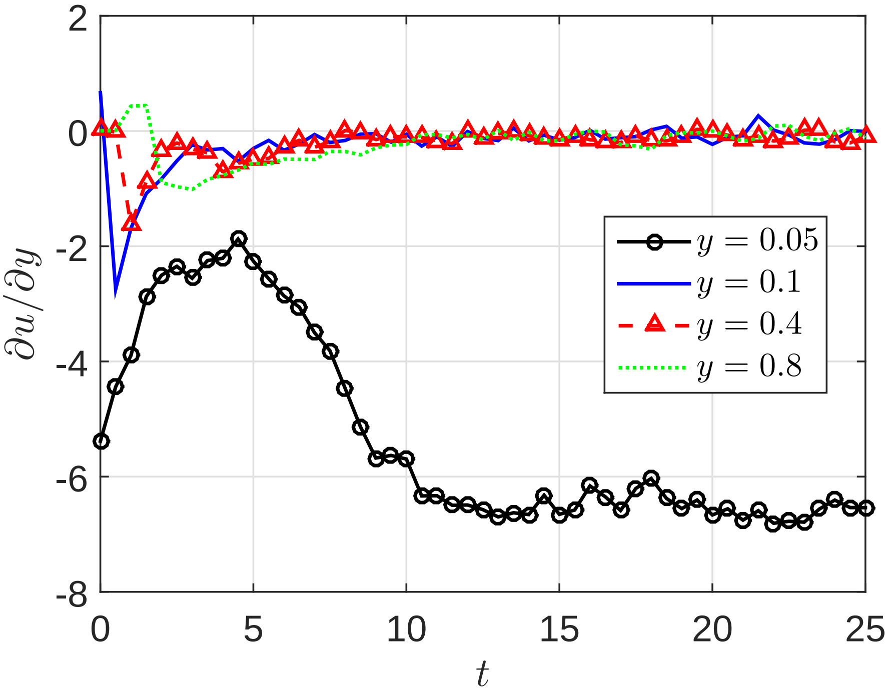

Figure 3.7: The start-up Couette flow of polymer melt using the DE model: The velocity gradient with respect to time in the high-shear-rate region at location $y = 0.05$ and the low-shear-rate region at locations $y = 0.1$, 0.4 and 0.8.

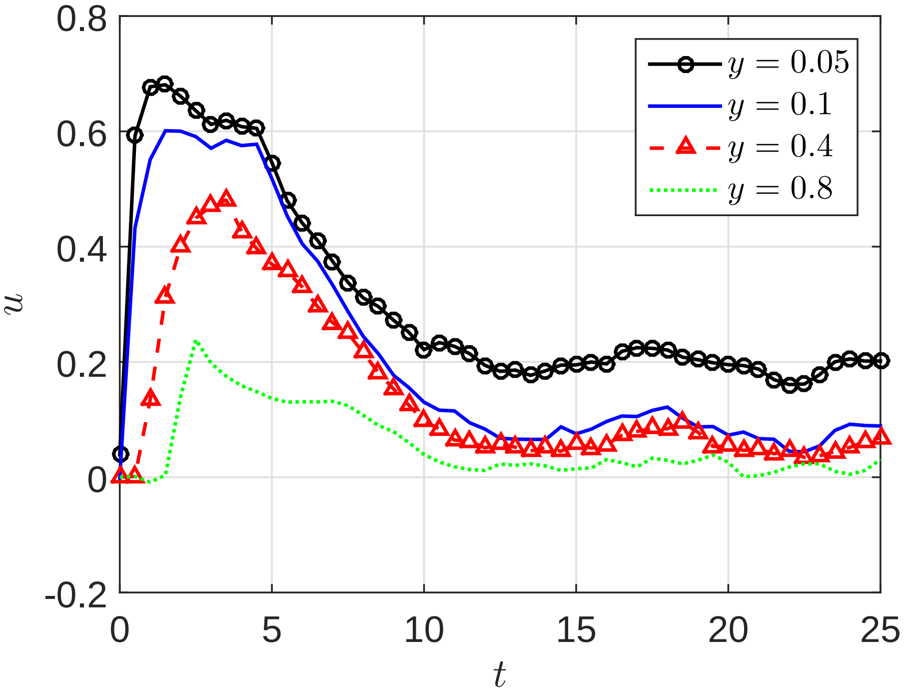

Figure 3.8: The start-up Couette flow of polymer melt using the DE model: The evolution of the velocity field at locations $y = 0.05$, 0.1, 0.4 and 0.8.

- Figs. 3.9 show the evolution of the shear stress (Fig. 3.9(a)) and the first normal stress difference (Fig. 3.9(b)) at locations $y = 0.05$, 0.1, 0.4 and 0.8. The shear stress is the same whereas the first normal stress difference is very distinct in the two shear rate areas. This typical behaviour of polymer melt in the start-up Couette flow was reported in Hua and Schieber (1996). Furthermore, the overshoot also appears in the evolution of shear stress at any location of the domain (Fig. 3.9(a)) whereas it only appears for the first normal stress difference in the low-shear-rate region (Fig. 3.9(b)). A study on the stresses' evolution in the high and low-shear-rate regions is highlighted in Figs. 3.10. The results in Figs. 3.10 show that the second normal stress difference is always negative in both high and low-shear-rate regions, which agrees with experimental observations presented in Beris et al. (1992) and Keentok et al. (1980)

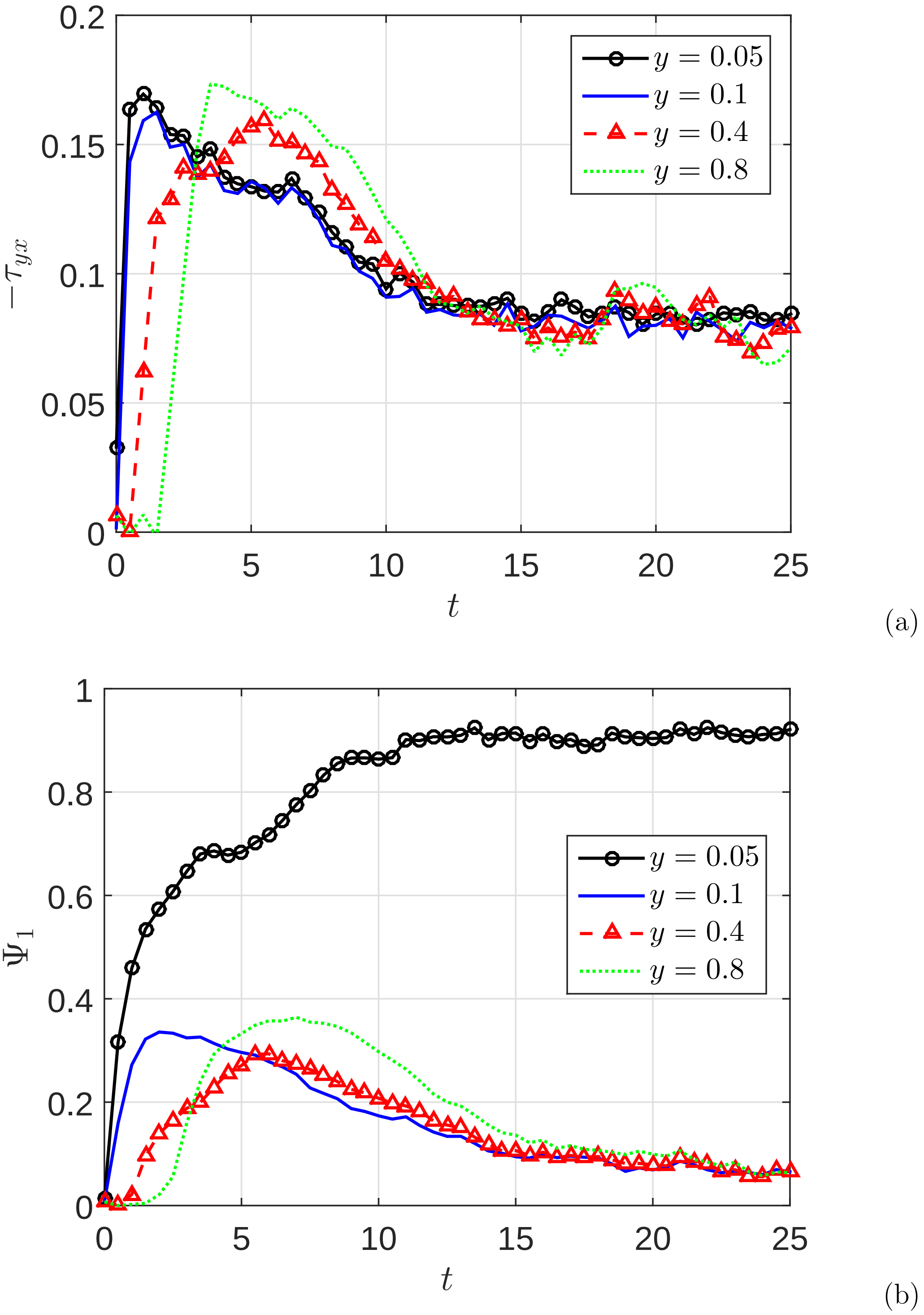

Figure 3.9: The start-up Couette flow of polymer melt using the DE model: The evolution of the shear stress (figure (a)) and the first normal stress difference (figure (b)) at locations $y = 0.05$, 0.1, 0.4 and 0.8.

Comparison of numerical simulation of the flows using the DE, CB, RR and DR models

In this section, the Couette flow of polymer melt is simulated by the present macro-micro multiscale using other reptation models including the CB, RR and

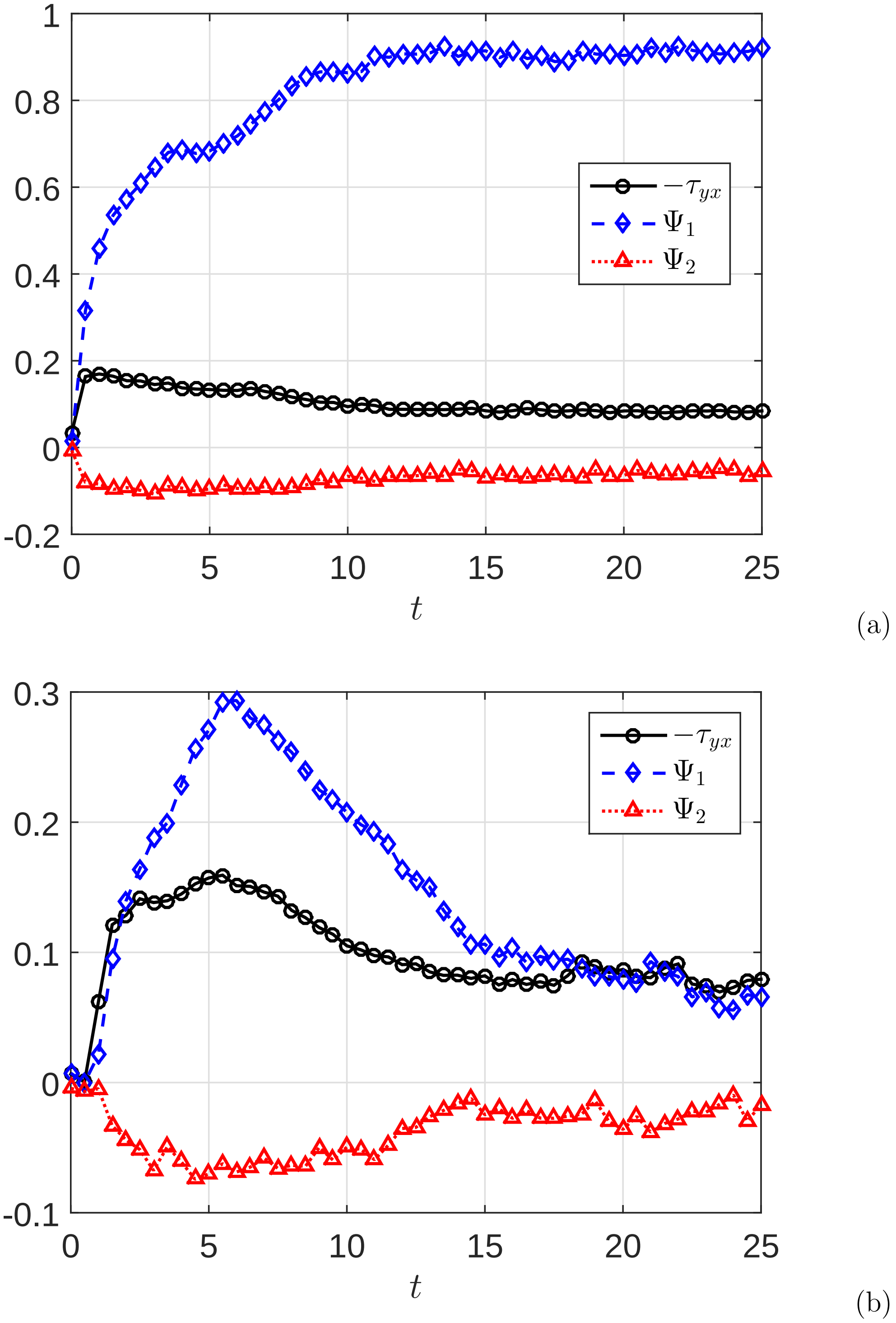

Figure 3.10: The start-up Couette flow of polymer melt using the DE model: polymer stresses (shear stress, the first and normal stress differences) in the high-shear-rate zone at location $y = 0.05$ (figure (a)) and the low-shear-rate zone at location $y = 0.4$ (figure (b)).

DR to investigate the role of several physical interactions of polymer chains. For example, the RR model considers the interaction between segments in a single chain through the correlation parameter Δ and the link tension parameter l_1 while the DR model takes into account the constraint release mechanism via the parameters l_1, l_2 and l_3.

As pointed out in Section 3.4, a polymer melt of the classical reptation models is governed by the system of macro-micro equations (3.14a)-(3.14e) with $l_1 = l_2 = l_3 = l_4 = 0$ for the DE model; $l_2 = l_3 = l_4 = 0$ for the CB model; $l_1 = l_2 = l_3 = 0$ for the RR model; and $l_4 = 0$ for the DR model. Hence, the start-up Couette flow of polymer melt is successively simulated using the CB, RR, DR models whose parameters are given and derived from those of the DE model in Section 3.7.1.

The simulated cases together with parameters are given in Table 3.1 where the modulus of rigidity G ($G = Nn_pk_BT$) in the last column is determined for the DE, CB, RR and DR models, respectively, as follows (Ottinger, 1996).

$$\eta_0^{DE} = \tfrac{1}{60} Nn_pk_BT\lambda, \tag{3.34a}$$

$$\eta_0^{CB} = \tfrac{1}{60}\left(1 + \tfrac{2}{3}l_1\right) Nn_pk_BT\lambda \tag{3.34b}$$

$$\eta_0^{RR} = \tfrac{1}{60}\left[1 + \tfrac{2}{3}l_1\Delta^2\left(4 - 6\Delta + 4\Delta^2 - \Delta^3\right)\right] Nn_pk_BT\lambda, \tag{3.34c}$$

$$\eta_0^{DR} = \tfrac{1}{60}\left\{\tfrac{12}{\pi^2 {l_2}^2}\left[1 - \tfrac{tanh(\pi l_2/2)}{\pi l_2/2}\right] + \tfrac{2}{3}l_1 + 4l_3\right\} Nn_pk_BT\lambda. \tag{3.34d}$$

Fig. 3.11 shows the velocity profiles of the Couette flow of polymer melt using the CB model by the present multiscale method for a range of values of $l_1 \in [0.01, 1]$ as presented in Table 3.1. The results confirm that the coefficient l_1 reflects the appearance of a “two different shear rate regions” which is a distinctive feature of a polymer melt system. When the value of l_1 increases, the steady velocity of polymer melt system reaches that of a Newtonian flow ($l_1 = 0.5, 1$, Fig. 3.11). Therefore, a sufficiently small value of l_1 ($l_1 = 0.01$ in this simulation) is necessary to characterise this typical behaviour of polymer melt systems as discussed in Ottinger (1996).

For the RR-modelled polymer melt, the link tension coefficient l_1 is chosen as 0.01 and the start-up Couette flow is investigated with a range of correlation parameter values Δ in $\{0, 0.1, 0.25, 0.5, 0.75, 1\}$. The velocity profile for all cases

Table 3.1: Simulation of the start-up Couette flow of polymer melt using the DE, CB, RR, DR models. Parameters of 16 different cases including six cases of the CB model (CB_{T1} - CB_{T6}), six cases of the RR model (RR_{T1} - RR_{T6}) and three cases of the DR model (DR_{T1} - DR_{T3}) are derived from the DE model with $\lambda = 50$, $\eta_o = 1$ and $l_3 = 0$; $G = Nn_pk_BT$: the rigidity modulus of models. Parameters were defined in previous sections.

Cases	Model	l_1	l_2	Δ	G
1	DE	0	0	0	1.200
2	CB$_{T1}$	0.01	0	0	1.192
3	CB$_{T2}$	0.05	0	0	1.161
4	CB$_{T3}$	0.1	0	0	1.125
5	CB$_{T4}$	0.25	0	0	1.029
6	CB$_{T5}$	0.5	0	0	0.900
7	CB$_{T6}$	1	0	0	0.720
8	RR$_{T1}$	0.01	0	0	1.200
9	RR$_{T2}$	0.01	0	0.1	1.2
10	RR$_{T3}$	0.01	0	0.25	1.199
11	RR$_{T4}$	0.01	0	0.5	1.196
12	RR$_{T5}$	0.01	0	0.75	0.194
13	RR$_{T6}$	0.01	0	1	1.192
14	DR$_{T1}$	0	0.25	0	1.274
15	DR$_{T2}$	0	0.5	0	1.495
16	DR$_{T3}$	0	0.75	0	1.862

of the flow is presented in Fig. 3.12. Results in the figure depict that for the RR modelled polymer melt, the correlation parameter only impacts the shape of the low-shear-rate zone in a shear flow.

The polymer melt flow using the DR model is governed by Eqs. (3.14a)- (3.14e) with $l_1 = l_3 = 0$. Thus, the problem is examined with a range of the parameter l_2 in $\{0.25, 0.5, 0.75\}$. The velocity profile is described in Fig. 3.13, showing that the low-shear-rate zone is enlarged with increasing l_2.

Finally, the simulation of the start-up Couette flow of polymer melt using four reptation models: DE, CB$_{T1}$, RR$_{T4}$ and DR$_{T1}$, whose parameters are given in Table 3.1, is carried out in order to compare the behaviour of these models in this particular flow.

- Fig. 3.14(a) depicts the velocity profiles at the steady state of the fluid flow using the four models. The results show that while there is not any significant change in the high-shear-rate zone, the velocity gradient is decreasing

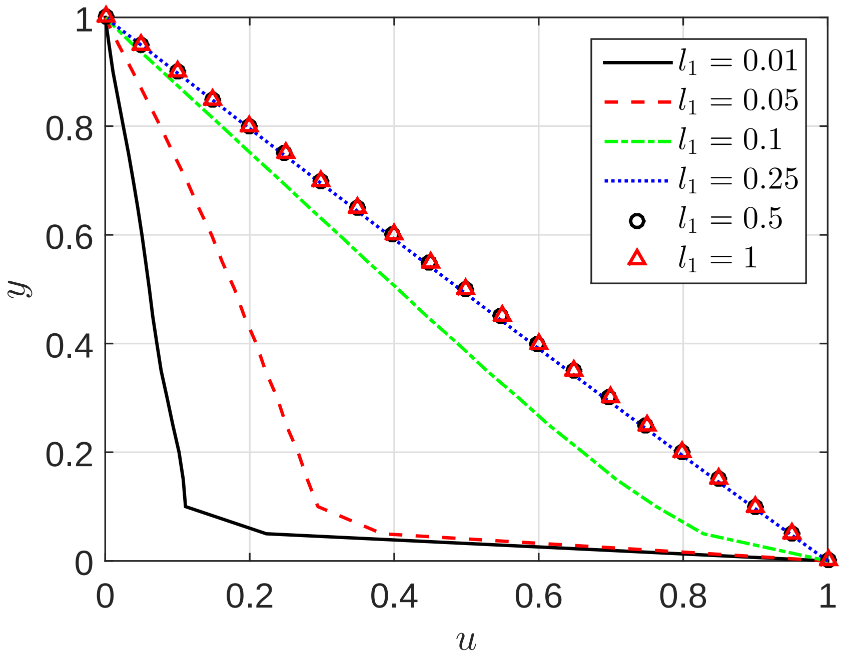

Figure 3.11: The start-up Couette flow of polymer melt using the CB model: The steady velocity profiles of the flow with a range of values of the link tension coefficient $l_1 \in \{0.01, 0.05, 0.1, 0.25, 0.5, 1\}$. Other parameters of the simulation are given in Section 3.7.1 and in Table 3.1.

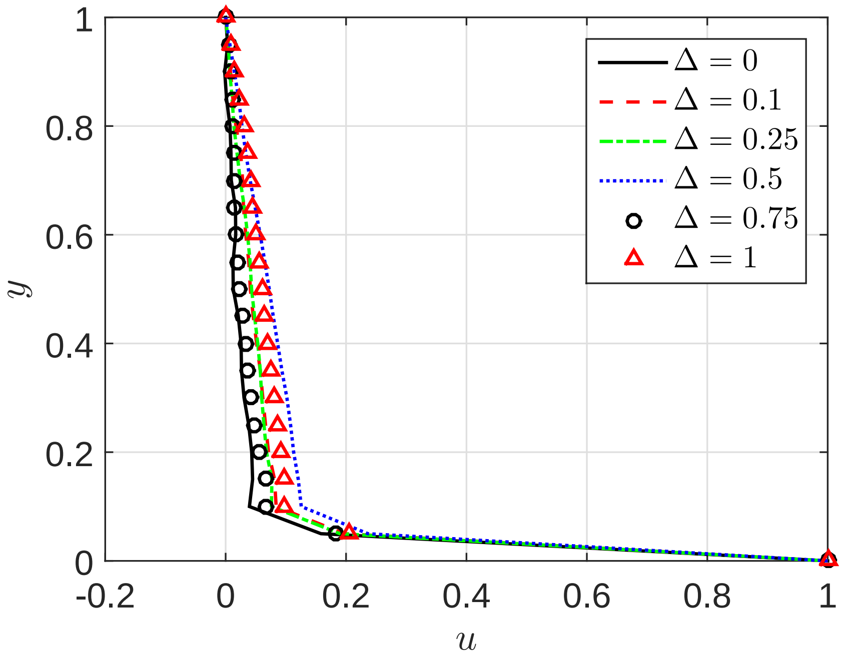

Figure 3.12: The start-up Couette flow of polymer melt using the RR model: The steady velocity profiles of the flow with a range of values of the correlation length parameter $\Delta \in \{0, 0.1, 0.25, 0.5, 0.75, 1\}$ and the link tension coefficient $l_1 = 0.01$. Other parameters of the simulation are given in Section 3.7.1 and in Table 3.1.

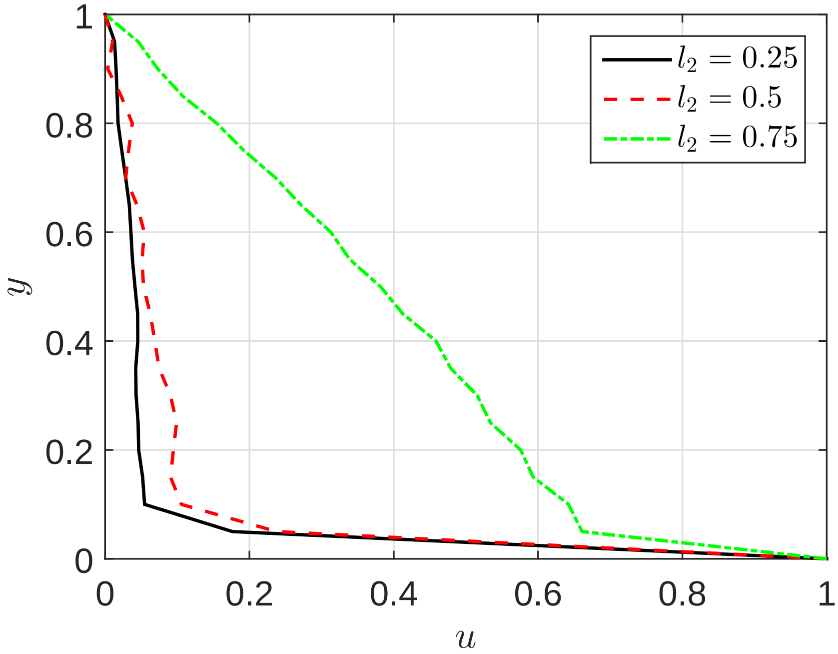

Figure 3.13: The start-up Couette flow of polymer melt using the DR model: The steady velocity profiles of the flow with $l_2 \in \{0.25, 0.5, 1\}$ and $l_1 = l_3 = 0$. Other parameters of the simulation are given in Section 3.7.1 and in Table 3.1.

in the order of the RR, CB, DE and DR models in the low-shear-rate zone. Furthermore, the evolution of velocity at location $y = 0.5$ in the low-shear-rate zone given is also investigated as shown in Fig. 3.14(b). An overshoot is observed in all models at $t \approx 3$ and the velocity profiles then reach a quasi-steady value after $t \approx 20$ for all models.

- The evolution of shear stress (τ_{xy}) and the first normal stress difference (Ψ_1) at location $y = 0.5$ for the four models are shown in Fig. 3.15(a) and Fig. 3.15(b), respectively. Unlike the velocity field, there is not any significant difference between the stresses obtained by the simulation using the four reptation models.

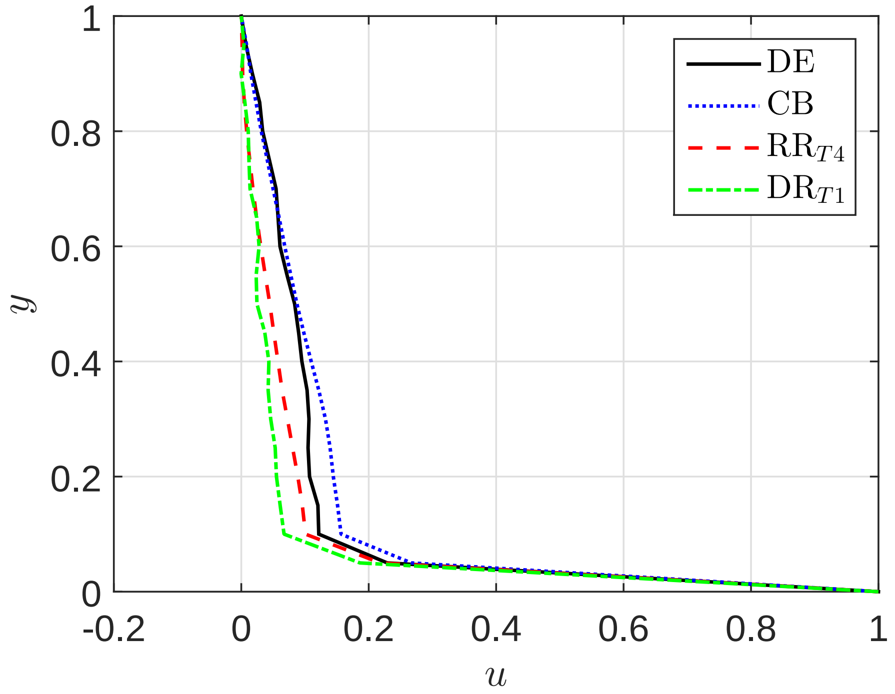

(a)

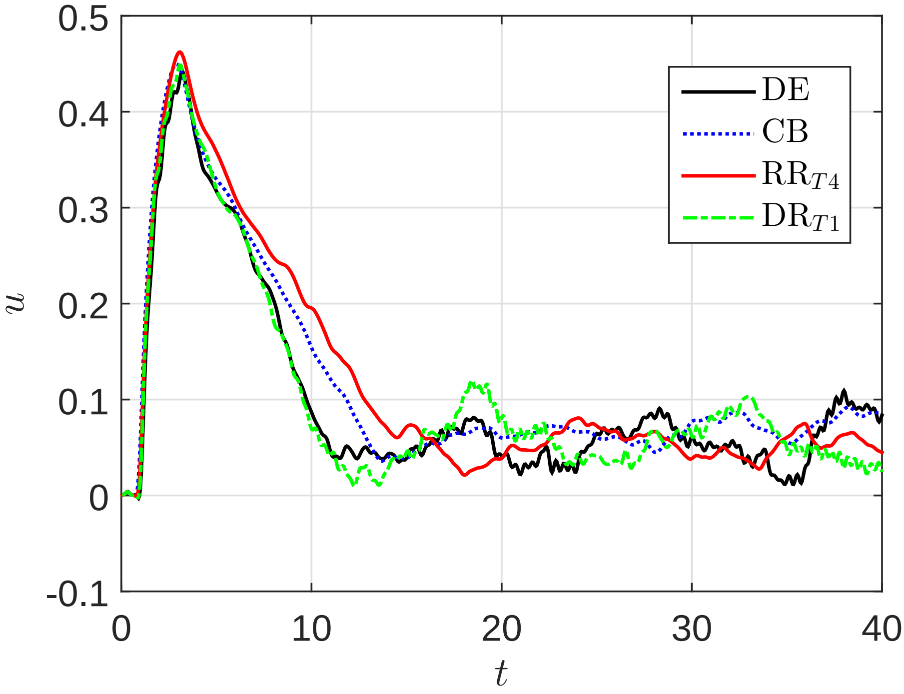

(b)

Figure 3.14: The start-up Couette flow of polymer melt using reptation models: The steady velocity profiles of the flow (figure (a)) and the evolution of the velocity at location $y = 0.5$ (figure (b)) using the DE, CB, RR and DR models.

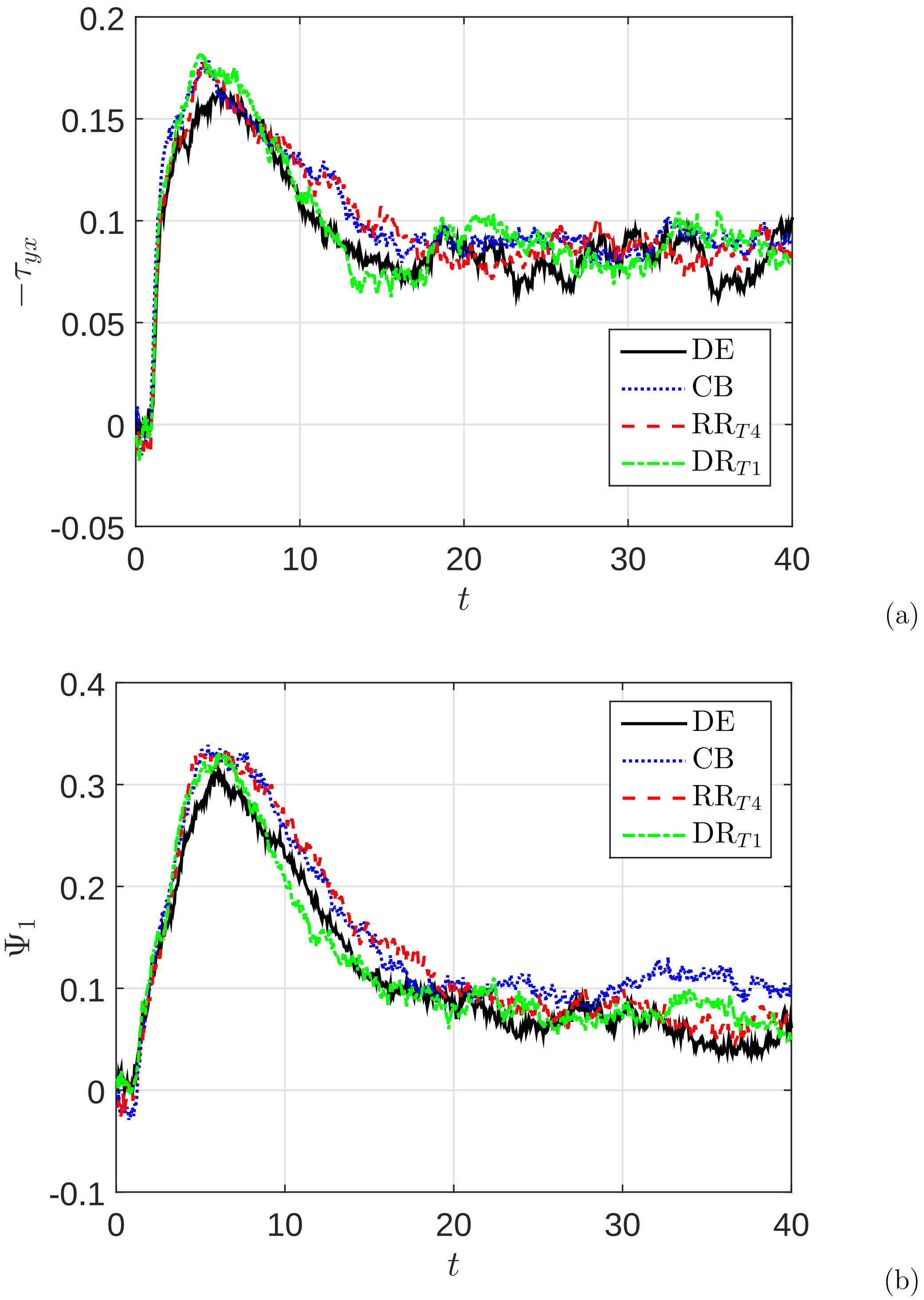

Figure 3.15: The start-up Couette flow of polymer melt using different reptation models: The evolution of the shear stress τ_{xy} (figure (a)) and the first normal stress difference Ψ_1 (figure (b)) at the location $y = 0.5$ using the DE, CB, RR and DR models.

3.7.2 Polymer melt flow past a circular cylinder in a channel using the DE model

The geometry of the flow past a cylinder in a channel is presented in Fig. 3.16 where only half of the flow's domain is considered owing to the geometrical symmetry: $L = 30$ is the total length of the channel; $L_U = 15$ and $L_D = 15$ the upstream and downstream lengths, respectively; $R_c = 1$ the cylinder's radius and $H = 2$ half of the height of the channel. The flow is simulated with the DE model which was studied by Van Heel et al. (1999) using the BCF and finite element method.

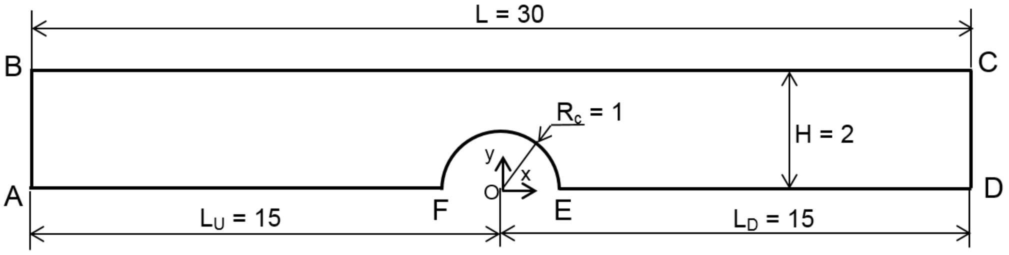

Figure 3.16: The flow past a circular cylinder in a channel: geometrical parameters of the problem.

Governing equations and boundary conditions

The macro-micro governing equations of the problem in 2-D Cartesian coordinates are written as follows.

$$\frac{\partial u}{\partial x} + \frac{\partial v}{\partial y} = 0, \tag{3.35}$$

$$\begin{cases} D_P\left[\left(\frac{\partial^2 u}{\partial x^2}(\mathbf{x},t) + \frac{\partial^2 u}{\partial y^2}(\mathbf{x},t)\right) - \left(\frac{\partial^2 u_0}{\partial x^2}(\mathbf{x},t) + \frac{\partial^2 u_0}{\partial y^2}(\mathbf{x},t)\right)\right] - \frac{\partial p}{\partial x}(\mathbf{x},t) \\ \qquad + \frac{\partial \tau_{p,xx}}{\partial x}(\mathbf{x},t) + \frac{\partial \tau_{p,xy}}{\partial y}(\mathbf{x},t) = 0, \\ D_P\left[\left(\frac{\partial^2 v}{\partial x^2}(\mathbf{x},t) + \frac{\partial^2 v}{\partial y^2}(\mathbf{x},t)\right) - \left(\frac{\partial^2 v_0}{\partial x^2}(\mathbf{x},t) + \frac{\partial^2 v_0}{\partial y^2}(\mathbf{x},t)\right)\right] - \frac{\partial p}{\partial y}(\mathbf{x},t) \\ \qquad + \frac{\partial \tau_{p,xy}}{\partial x}(\mathbf{x},t) + \frac{\partial \tau_{p,yy}}{\partial y}(\mathbf{x},t) = 0, \end{cases} \tag{3.36}$$

$$dS\left(t\right)=\sqrt{\frac{2}{\pi^{2}We}}dW_{1}\left(t\right), \tag{3.37}$$

$$\begin{cases} dP_{x}\left(\mathbf{x},t\right)=\left[\frac{\partial u}{\partial x}\left(\mathbf{x},t\right)P_{x}\left(\mathbf{x},t\right)+\frac{\partial u}{\partial y}\left(\mathbf{x},t\right)P_{y}\left(\mathbf{x},t\right)\right]dt \\ \qquad -\left[u\left(\mathbf{x},t\right)\frac{\partial P_{x}}{\partial x}\left(\mathbf{x},t\right)+v\left(\mathbf{x},t\right)\frac{\partial P_{x}}{\partial y}\left(\mathbf{x},t\right)\right]dt, \\ dP_{y}\left(\mathbf{x},t\right)=\left[\frac{\partial v}{\partial x}\left(\mathbf{x},t\right)P_{x}\left(\mathbf{x},t\right)+\frac{\partial v}{\partial y}\left(\mathbf{x},t\right)P_{y}\left(\mathbf{x},t\right)\right]dt \\ \qquad -\left[u\left(\mathbf{x},t\right)\frac{\partial P_{y}}{\partial x}\left(\mathbf{x},t\right)+v\left(\mathbf{x},t\right)\frac{\partial P_{y}}{\partial y}\left(\mathbf{x},t\right)\right]dt, \\ dP_{z}\left(\mathbf{x},t\right)=-\left[u\left(\mathbf{x},t\right)\frac{\partial P_{z}}{\partial x}\left(\mathbf{x},t\right)+v\left(\mathbf{x},t\right)\frac{\partial P_{z}}{\partial y}\left(\mathbf{x},t\right)\right]dt, \end{cases} \tag{3.38}$$

$$\begin{cases} \tau_{p,xx}=Nn_{p}k_{B}T\left(\frac{1}{3}-\left\langle P_{x}P_{x}\right\rangle\right), \\ \tau_{p,yy}=Nn_{p}k_{B}T\left(\frac{1}{3}-\left\langle P_{y}P_{y}\right\rangle\right), \\ \tau_{p,zz}=Nn_{p}k_{B}T\left(\frac{1}{3}-\left\langle P_{z}P_{z}\right\rangle\right), \\ \tau_{p,xy}=-Nn_{p}k_{B}T\left\langle P_{x}P_{y}\right\rangle, \end{cases} \tag{3.39}$$

where parameters and variables are defined in previous sections. The boundary conditions of the problem are determined correspondingly to ones by Van Heel et al. (1999) as follows.

- At the inlet $\overline{AB}$: A fully developed velocity profile is assigned. The velocity profile is pre-defined by the simulation of the Poiseuille flow through a long channel using the same polymer melt model with a parabolic inlet velocity profile $u=1.5\left(1-\frac{y^{2}}{H^{2}}\right)$ and $v=0$ where u and v are the velocity components along the x and y directions, respectively, and other parameters are defined as before. The boundary condition for pressure is calculated at each time step as presented in Section 3.5.1;

- At the outlet $\overline{DC}$: The fully developed velocity profile u is also set up as for the inlet, $v=0$ and $p=0$;

- On the channel wall $\overline{BC}$ and the cylinder wall $\overline{FE}$: The non-slip boundary condition is imposed: $u=v=0$. The boundary condition of pressure is determined at each time step as presented in Section 3.5.1;

- On the centreline $\overline{AF}$ and $\overline{ED}$: The symmetrical boundary condition of the velocity is applied: $\frac{\partial u}{\partial y}=0$ and $v=0$; and the Neumann boundary condition for pressure is determined at each time step as mentioned in Section 3.5.1.

A pseudo time method combined with the projection technique presented in Section 3.5.1 is used to temporally discretise Eqs (3.36) whereas the explicit time discretisation scheme is applied to Eqs. (3.38). These discretisations yield, respectively

$$\begin{cases} u^{n+1} - D_p\Delta t\left(\frac{\partial^2 u^{n+1}}{\partial x^2} + \frac{\partial^2 u^{n+1}}{\partial y^2}\right) + \Delta t\frac{\partial p^{n+1}}{\partial x} = u^n - \\ \quad D_p\Delta t\left(\frac{\partial^2 u^{n}}{\partial x^2} + \frac{\partial^2 u^{n}}{\partial y^2}\right) + \Delta t\left(\frac{\partial \tau^n_{p,xx}}{\partial x} + \frac{\partial \tau^n_{p,xy}}{\partial y}\right), \\ v^{n+1} - D_p\Delta t\left(\frac{\partial^2 v^{n+1}}{\partial x^2} + \Delta t\frac{\partial^2 v^{n+1}}{\partial y^2}\right) + \frac{\partial p^{n+1}}{\partial y} = v^n - \\ \quad D_p\Delta t\left(\frac{\partial^2 v^{n}}{\partial x^2} + \frac{\partial^2 v^{n}}{\partial y^2}\right) + \Delta t\left(\frac{\partial \tau^n_{p,xy}}{\partial x} + \frac{\partial \tau^n_{p,yy}}{\partial y}\right), \end{cases} \tag{3.40}$$

$$\begin{cases} P_x^{n+1} = P_x^n + \left(\frac{\partial u^{n+1}}{\partial x}P_x^n + \frac{\partial u^{n+1}}{\partial y}P_y^n\right)\Delta t - \left(u^{n+1}\frac{\partial P_x^n}{\partial x} + v^{n+1}\frac{\partial P_x^n}{\partial y}\right)\Delta t, \\ P_y^{n+1} = P_y^n + \left(\frac{\partial v^{n+1}}{\partial x}P_x^n + \frac{\partial v^{n+1}}{\partial y}P_y^n\right)\Delta t - \left(u^{n+1}\frac{\partial P_y^n}{\partial x} + v^{n+1}\frac{\partial P_y^n}{\partial y}\right)\Delta t, \\ P_z^{n+1} = P_z^n - \left(u^{n+1}\frac{\partial P_z^n}{\partial x} + v^{n+1}\frac{\partial P_z^n}{\partial y}\right)\Delta t, \end{cases} \tag{3.41}$$

The velocity and velocity gradient in the micro process governed by Eqs. (3.41) are known and given by the solution of Eqs. (3.40) of the macro process. The time step size is chosen $\Delta t = 0.001$. The parameters of fluid include $N_f = 2000$, $\lambda = 1$, $We = \lambda/\pi^2$, $\eta_0^{DE} = 1$ and the rigidity modulus G and damping parameter D_P for the DE model which are determined, respectively, as follows.

$$G = Nn_pk_BT = \frac{60\eta_0^{DE}}{\lambda} = 60, \quad D_P = \frac{G\Delta t}{\eta_0^{DE}} = 0.06, \tag{3.42}$$

where the parameters are defined as before.

Numerical results and discussion

A grid convergence study is carried out for the case of $\Delta t = 0.001$ with three non-uniform Cartesian grids whose grid parameters are given in Table 3.2 and described in Fig. 3.17. The three meshes are labelled as M1, M2 and M3 where M1 is the coarsest one and M3 is the finest one. Fig. 3.18 shows the convergence of the velocity field reached in the simulation using the three grids.

The convergence of the present scheme for the time step size (Δt) is studied for the case of grid M3 and $\Delta t = \{0.005, 0.002, 0.001\}$. The convergence measure of

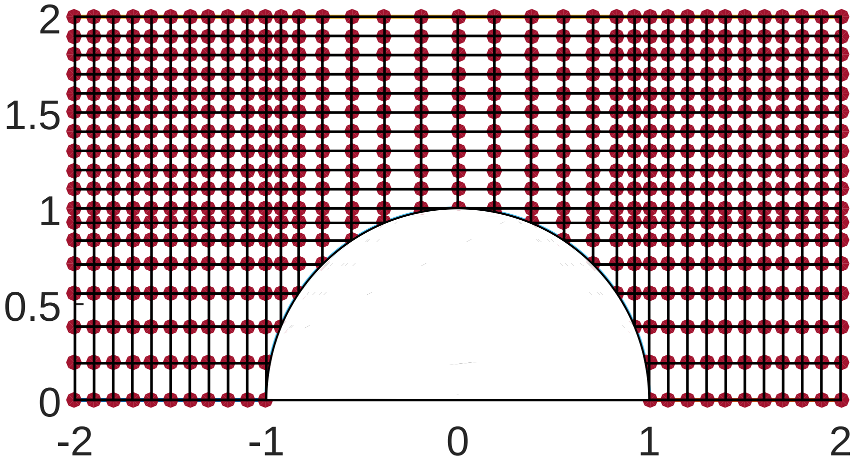

(a) Mesh M1

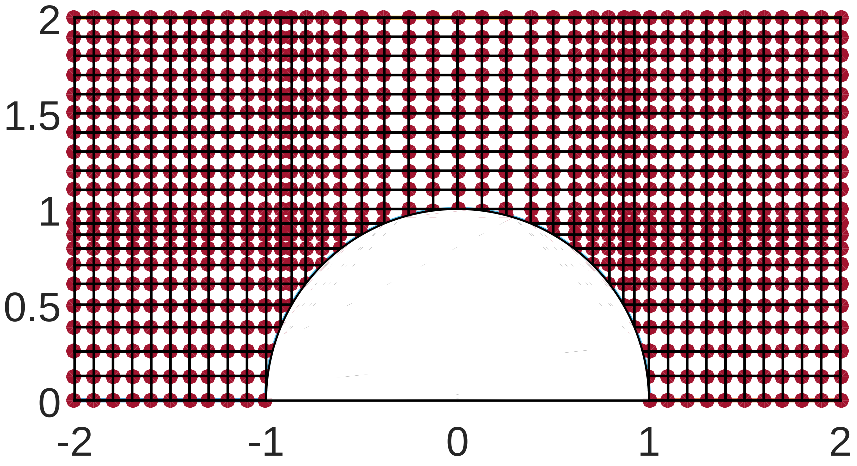

(b) Mesh M2

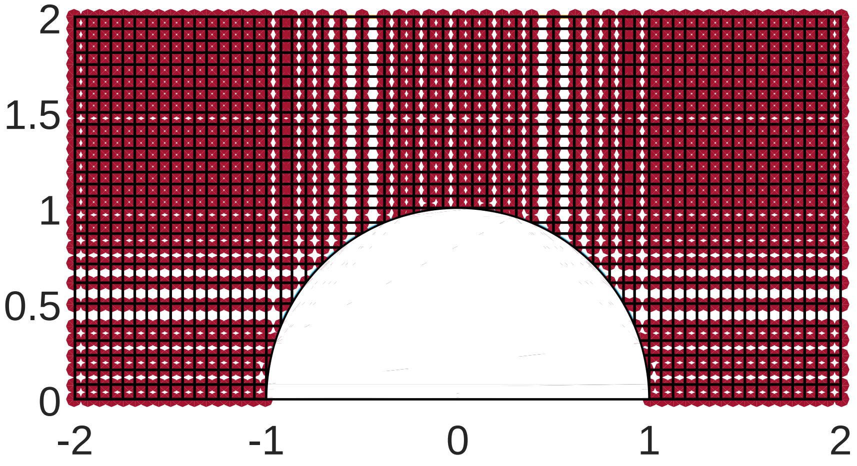

(c) Mesh M3

Figure 3.17: The non-uniform Cartesian grids at the region around the cylinder.

Table 3.2: The flow past a circular cylinder in a channel. The parameters of the three grids M1, M2 and M3. Δx_1: the grid spacing in x-direction $\forall x \in [-15,-5] \bigcup [5,15]$, Δx_2 $\forall x \in [-5,-2] \bigcup [2,5]$, Δx_3 $\forall x \in [-2,-1] \bigcup [1,2]$; Δy: the grid spacing in y-direction; N_{cyn}: the number of collocation points on the cylinder's surface and N: the number of collocation points on the whole domain.

Grid	Δx_1	Δx_2	Δx_3	Δy	N_{cyn}	N
M1	0.5	0.3	0.1	0.1	17	1649
M2	0.5	0.3	0.1	0.1	25	1991
M3	0.4	0.2	0.0625	0.0625	33	3761

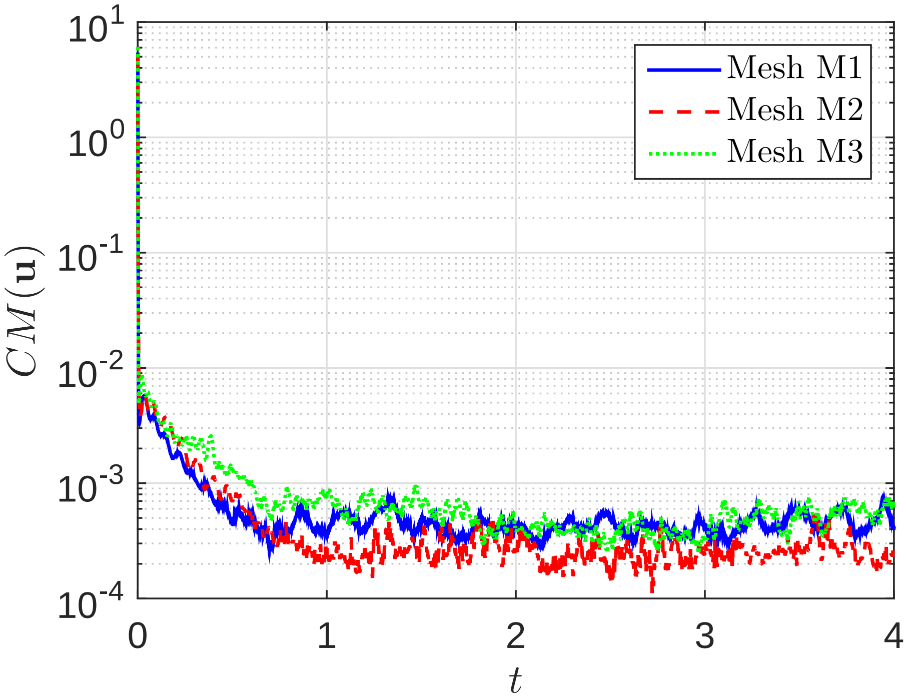

Figure 3.18: The flow past a circular cylinder in a channel: The convergence measure of the velocity field with grid refinement.

the velocity field ($CM(\mathbf{u})$) and the velocity profile in the gap between the wall and the cylinder are introduced in Figs. 3.19 and 3.20, respectively. Results show that the divergence of the velocity field's solution appears after $t \approx 1.6$ for the case of $\Delta t = 0.005$ (Fig. 3.19) while there is mostly no difference between the velocity's solutions for $\Delta t = 0.002$ and $\Delta t = 0.001$ (Fig. 3.20). Therefore, $\Delta t = 0.001$ is chosen as the time step size for this problem.

The results by the present method confirm a very good agreement with those by Van Heel et al. (1999) using 564 elements and the same time step ($\Delta t = 0.001$). Details are presented as follows.

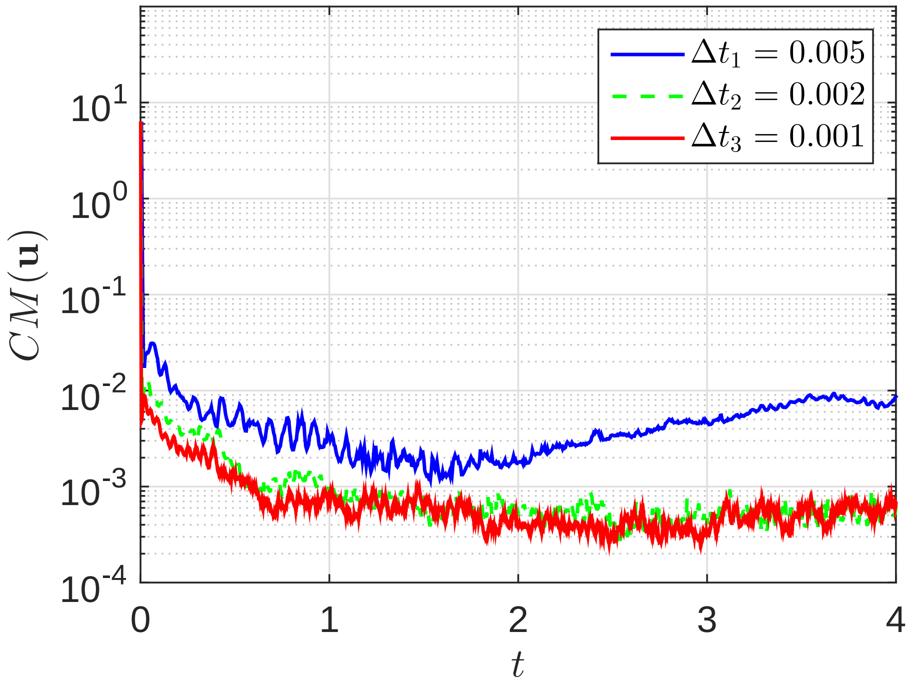

Figure 3.19: The flow past a cylinder in a channel using grid M3: the convergence measure (CM) of the velocity field ($\mathbf{u}$) for different time steps $\Delta t = \{0.005, 0.002, 0.001\}$.

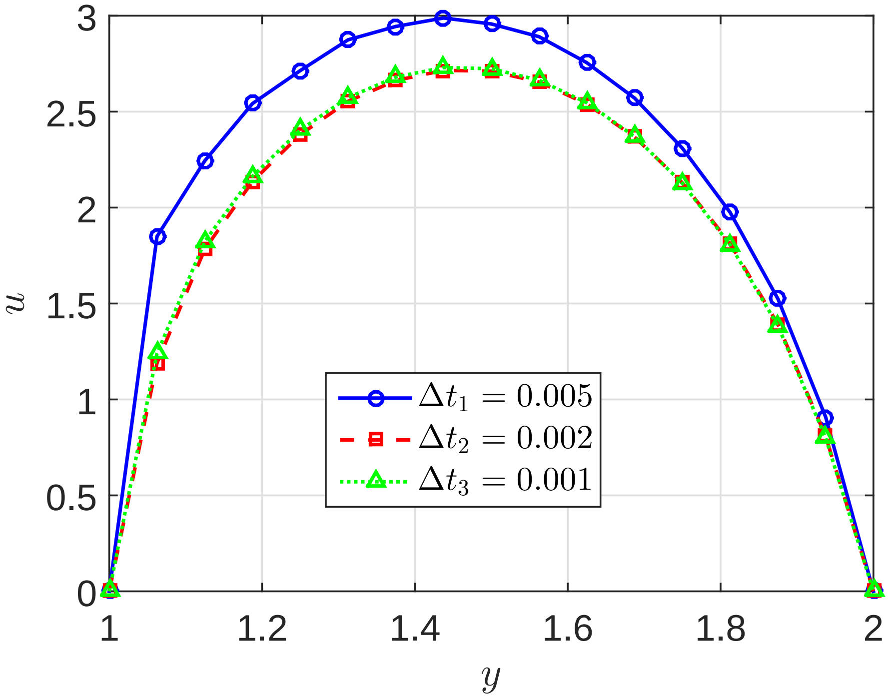

Figure 3.20: The flow past a cylinder in a channel using grid M3: the velocity profile in the gap between the wall ($y = 2$) and the cylinder (y=1) for different time steps $\Delta t = \{0.005, 0.002, 0.001\}$.

- The velocity profile in the gap between the wall and the cylinder is shown in Fig. 3.21. The numerical result for a Newtonian fluid included in the figure shows the difference between polymer melt and Newtonian flows. A nearly symmetrical parabolic shape is for the Newtonian profile whereas an asymmetrical bell-shaped profile is observed in the simulation of polymer melt flows. Indeed, the velocity gradient at the region near the cylinder wall ($y = 1$) is steeper than one near the channel wall ($y = 2$) for the polymer melt flows as observed in Fig. 3.22 whereas it is nearly linear for the Newtonian fluid. Furthermore, the maximum values of the velocity profiles at the middle point of the gap are approximate 2.9 and 2.7 for the Newtonian and the polymer melt flows, respectively, using mesh M3. The obtained results are in excellent agreement with those described in Figs. 6 and 7 of Van Heel et al. (1999).

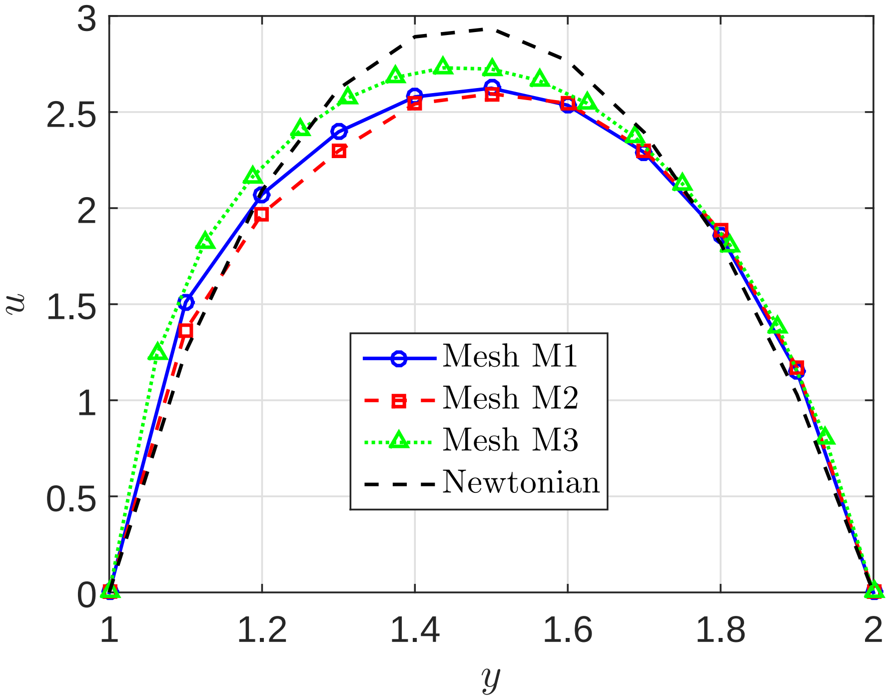

Figure 3.21: The flow past a cylinder in a channel: The velocity profile in the gap between the wall ($y = 2$) and the cylinder ($y = 1$).

Furthermore, the velocity field, described by contours and vectors in the domain, is presented in Figs. 3.23. The results depict a smooth change of the velocity components u, v around the cylinder in Figs. 3.23a, 3.23b and 3.23c.

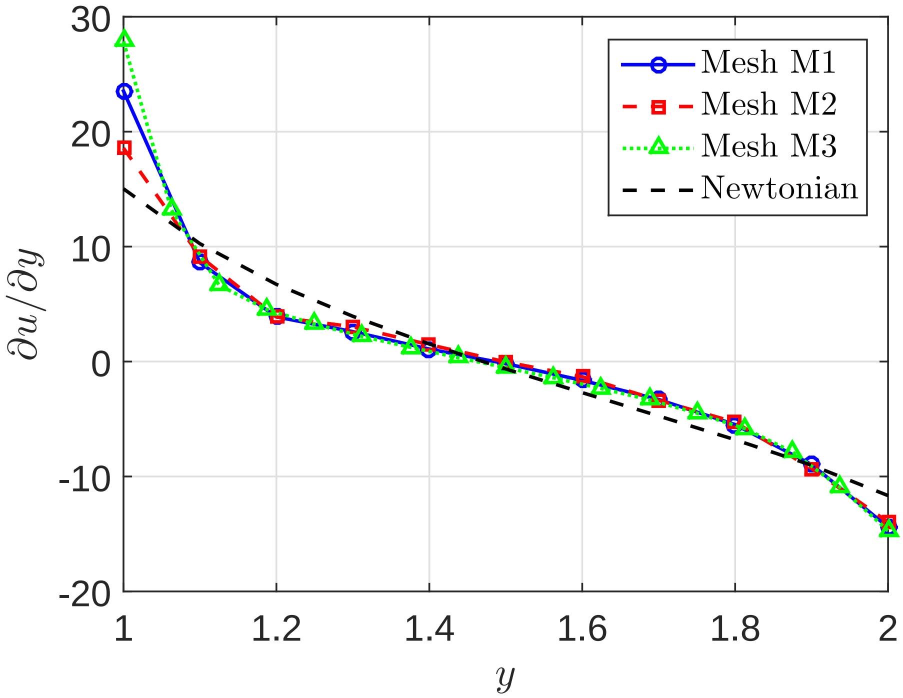

Figure 3.22: The flow past a cylinder in a channel: The velocity gradient $\partial u/\partial y$ in the gap between the wall ($y = 2$) and the cylinder ($y = 1$).

- The stress field is a function of the orientation tensor $\langle \mathbf{PP} \rangle$ via Eqs. (3.39). Thus, the distribution of the components of $\langle \mathbf{PP} \rangle$ along the centreline and the cylinder's surface is studied and shown in Figs. 3.24, 3.25 and 3.26 for $\langle P_x P_x \rangle$, $\langle P_x P_y \rangle$ and $\langle P_y P_y \rangle$, respectively, with the three different meshes. It is worth noting that the surface of the cylinder covers on the range of $x \in [-1, 1]$. The results are in strong agreement with those presented in Van Heel et al. (1999) using the BCF-finite element method.

  Furthermore, the contours with 20 levels of the $\langle P_x P_x \rangle$, $\langle P_x P_y \rangle$, and $\langle P_y P_y \rangle$ components around the cylinder are presented in Figs. 3.27a, 3.27b and 3.27c, respectively. The only contours reported by Van Heel et al. (1999) (their Fig. 8) are $\langle P_x P_x \rangle$ ones which are in very good agreement with results described in Fig. 3.27a of this work.

- Fig. 3.28 describes the pressure distribution on the cylinder's surface with three different meshes M1, M2 and M3. The results show that the pressure gradually increases from the starting point E ($\theta = 0$) to the end point F ($\theta = \pi$) of the cylinder where θ is the angle determining the position of

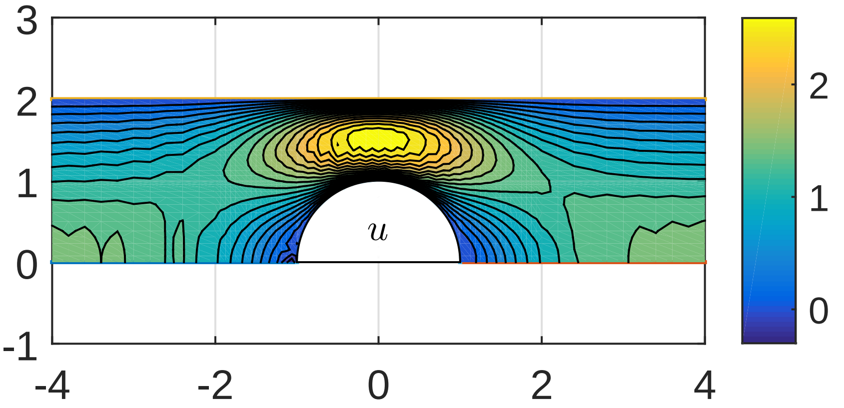

(a) The contour value of u

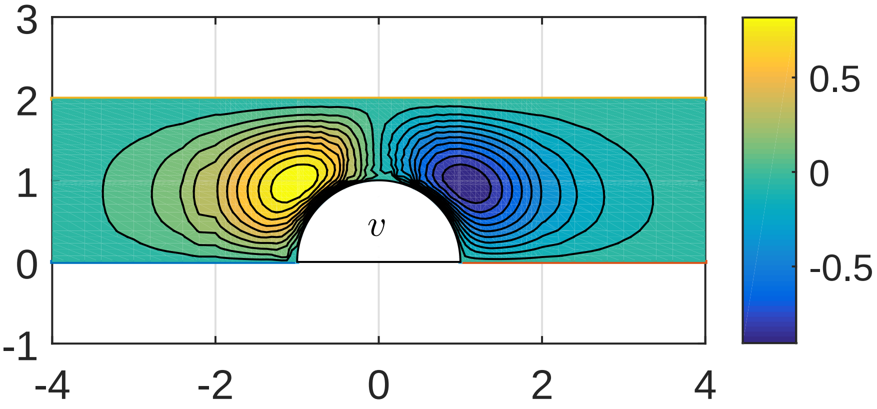

(b) The contour value of v

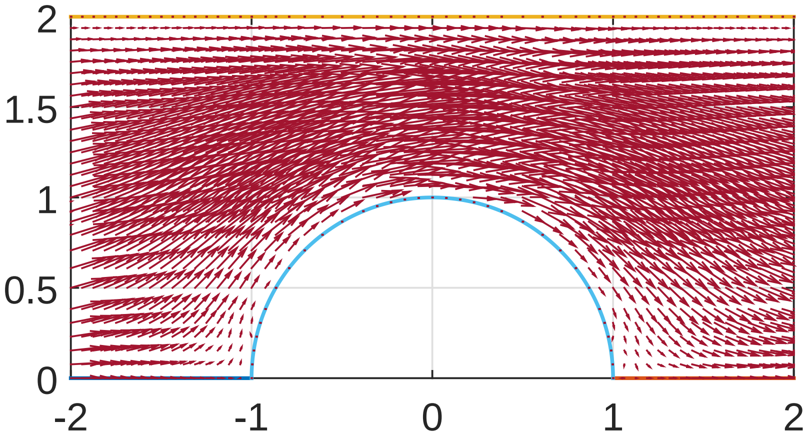

(c) The distribution of the velocity around the cylinder

Figure 3.23: The flow past a circular cylinder in a channel using Mesh M3: The velocity field around the cylinder.

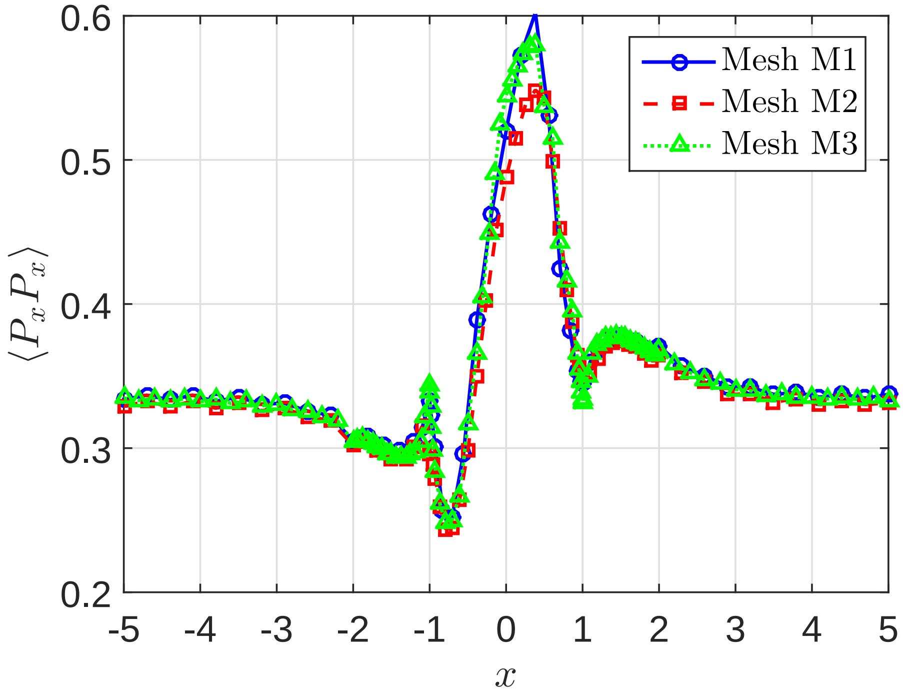

Figure 3.24: The flow past a cylinder in a channel. The distribution of $\langle P_x P_x \rangle$ of the orientation tensor $\langle \mathbf{PP} \rangle$ along the centreline $y = 0$ and the cylinder's surface.

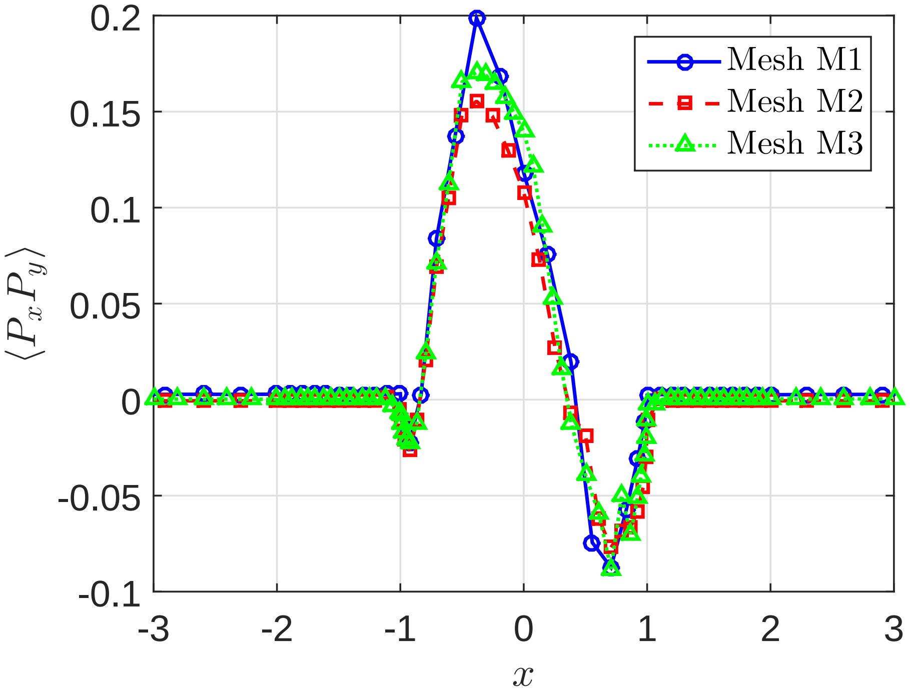

Figure 3.25: The flow past a cylinder in a channel. The distribution of $\langle P_x P_y \rangle$ of the orientation tensor $\langle \mathbf{PP} \rangle$ along the centreline $y = 0$ and the cylinder's surface.

the collocation point on the cylinder's surface (see Fig. 3.16). The pressure distribution corresponding to the Newtonian fluid is also included in the

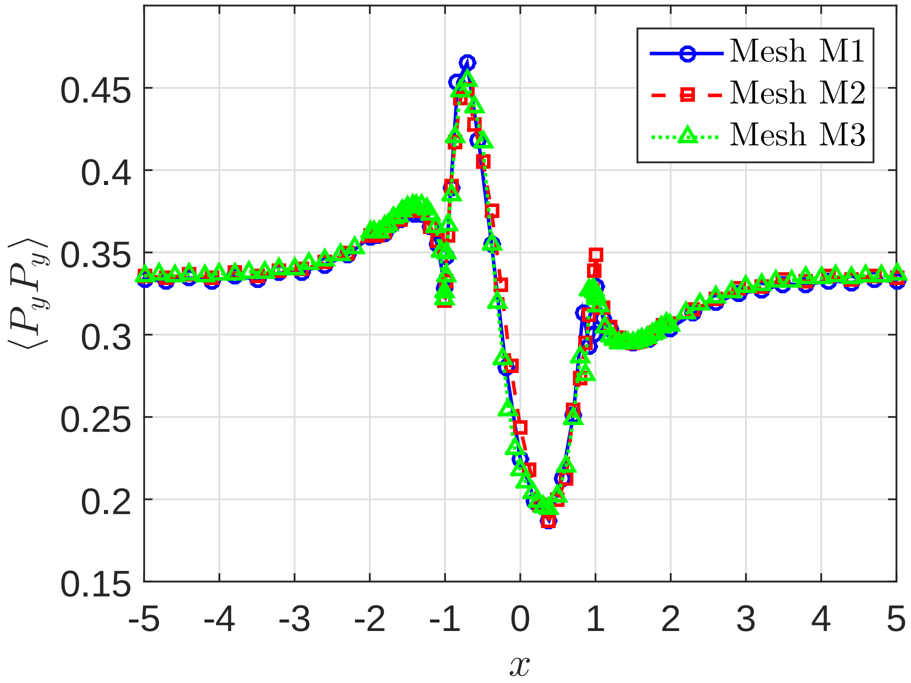

Figure 3.26: The flow past a cylinder in a channel. The distribution of $\big\langle P_y P_y \big\rangle$ of the orientation tensor $\langle \mathbf{PP} \rangle$ along the centreline $y = 0$ and the cylinder's surface.

figure for comparison. Overall, the pressure gradient for the Newtonian fluid is steeper than one for the polymer melt. Indeed, starting from mostly the same pressure $(p \approx 9)$ within $\theta \in \big[0, \pi/4\big]$, the pressure for the Newtonian flow increases faster to reach a maximum value of $p = 59$ versus $p = 49$ for polymer melt flow $\theta = \pi$. A shear-thinning behaviour for polymer melt flow is clearly reflected at the region around the cylinder when an increase of the velocity gradient is followed by a decrease of the pressure (see Fig. 3.22). This observation was also reported in Van Heel et al. (1999).

- While analyzing a fluid flow past a cylinder in a channel, together with pressure, it is desirable to determine the drag force per unit length that the fluid exerts on the cylinder as follows (Phan-Thien and Fan, 1999).

$$F_D = -2 \int_0^{\pi} \Big[\big(-p + \tau_{p,xx} \big) \cos\theta + \tau_{p,xy} \sin\theta \Big]_{r=R} R d\theta. \tag{3.43}$$

The dimensionless drag force per a unit length K is calculated as $K = F_D/\eta_0^{DE} U_c$, where U_c is the characteristic velocity, U_c and η_0^{DE} are chosen

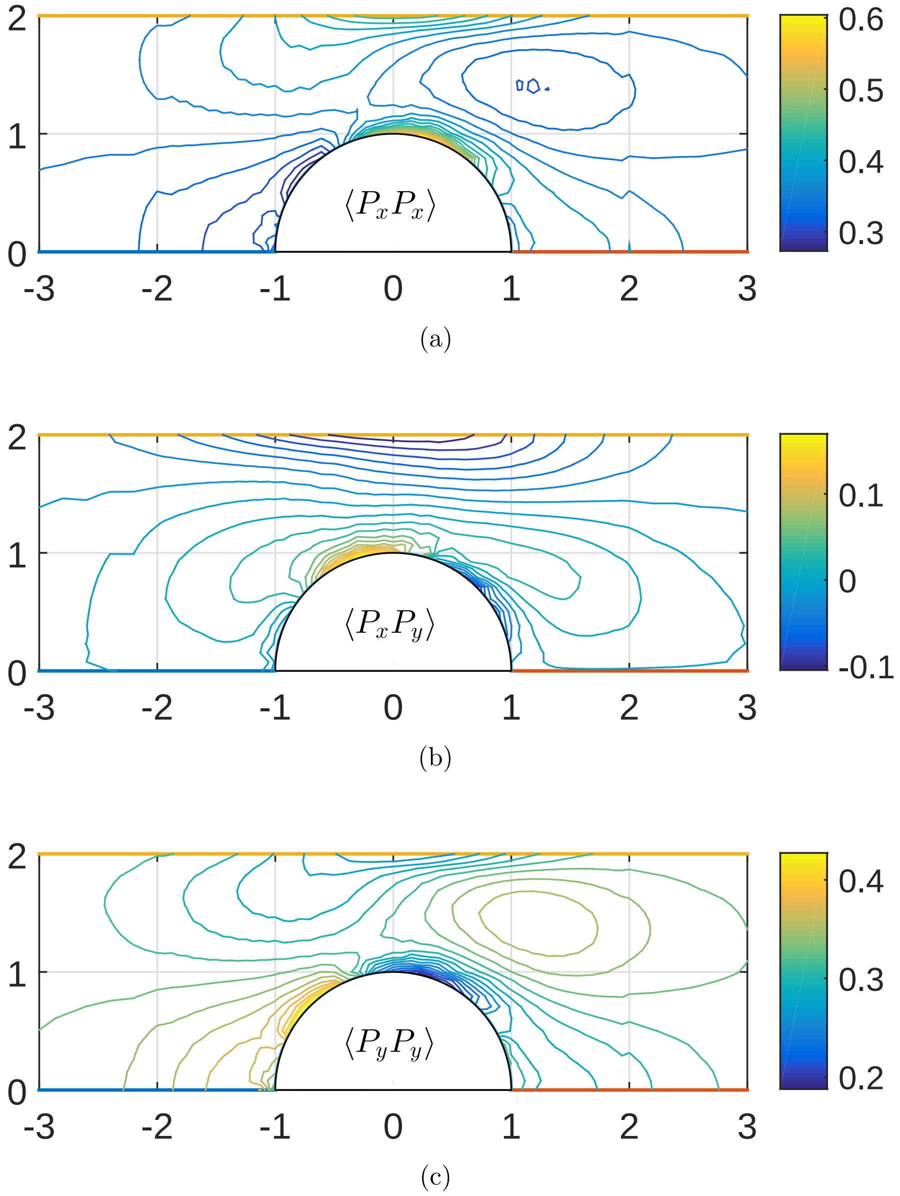

Figure 3.27: The flow past a circular cylinder in a channel using Mesh M3: The contour values of the xx-, xy- and yy-components of the tensor $\langle \mathbf{PP} \rangle$ around the cylinder.

as 1 in the present work. The evolution of K is presented in Fig. 3.29 with three meshes M1, M2 and M3, and is in very good agreement with those by Van Heel et al. (1999) except a small fluctuation observed in the case of mesh M1. The values of K are around 132 and 98 for the corresponding Newtonian fluid and dilute polymer solution flows, respectively (Hulsen et al., 1997), whereas it is about 93 for the polymer melt flow by this work. The decrease of K with an increase of concentration of polymer solutions confirms the shear-thinning behaviour of a viscoelastic fluid (Bird et al.,

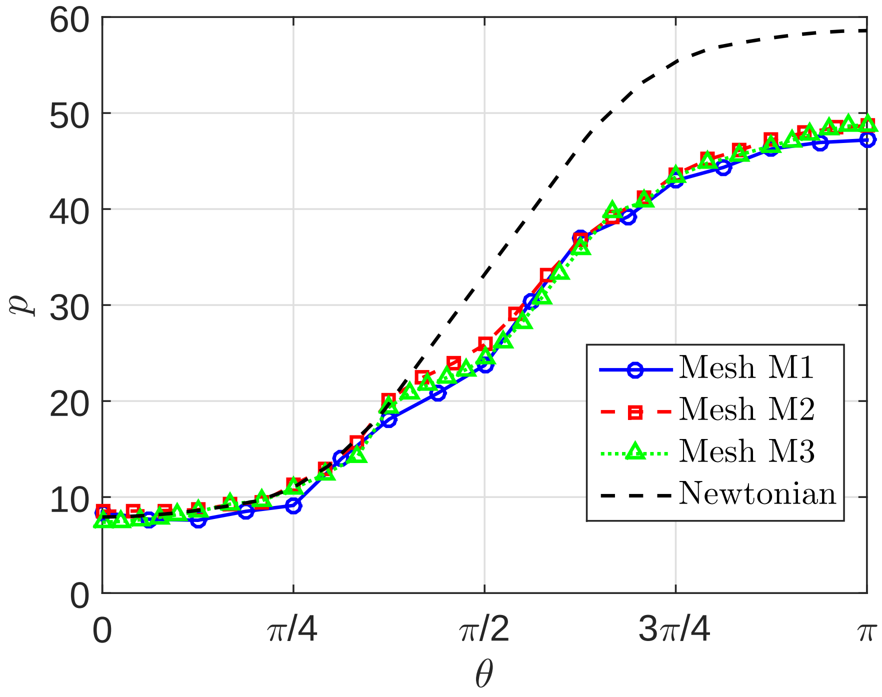

Figure 3.28: The flow past a cylinder in a channel: The distribution of pressure on the cylinder's surface.

1987b).

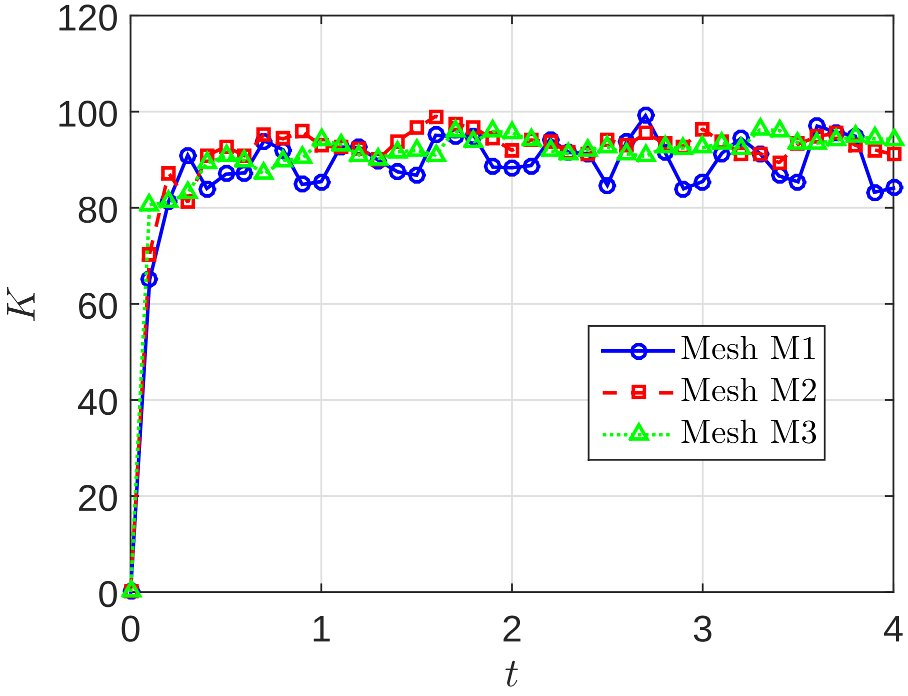

Figure 3.29: The flow past a cylinder in a channel: The evolution of the drag force per unit length exerted on the cylinder using three meshes M1, M2 and M3.

3.8 Concluding remarks

The IRBFN-BCF based coarse-grained method presented in Chapter 2 (Nguyen et al., 2015b) is further developed to simulate polymer melt flows using different reptation models in this chapter (Nguyen et al., 2016a). In the method, the macro conservation equations are solved for the primitive variables including the velocity and pressure using 1D-IRBFN scheme, whereas the BCF based coarse-grained approach is used to determine the polymer stress via stochastic processes associated with a reptation model. Four models (DE, CB, RR and DR) are used in the simulation. The numerical results for the start-up planar Couette flow and the flow over a cylinder in a channel of these model fluids confirm the method efficiency, considering both the enhanced convergence rate of the simulation and the stability of a stochastic process. In the next two chapters some of the techniques developed so far are adapted and augmented with other methods for the simulation of fibre suspension flows.

Chapter 4

A multiscale method based on the fibre configuration field, IRBF and DAVSS for the simulation of dilute fibre suspension flows

In this chapter, a new multiscale simulation technique, which is based on the combination of the integrated radial basis function (IRBF) scheme, the discrete adaptive viscoelastic stress splitting (DAVSS) formulation and the core idea of the Brownian configuration field (BCF) approach, is developed to investigate the rheological properties of dilute fibre suspensions (Nguyen et al., 2015a). In the approach, the evolution of the macroscopic flow and the fibre configurations are captured through two separate computational processes. Indeed, the flow conservation equations, which are expressed in vorticity-stream function formulation, are solved using IRBF-based numerical schemes while the evolution of fibre configuration fields governed by the Jeffery equation is captured using the BCF's principle. The two procedures are coupled together by the Lipscomb expression which is used to determine the fibre stress of dilute fibre suspensions. Owing to advantages of the IRBF scheme and the DAVSS technique, the present method yields a more accurate solution and faster convergence rate. The simulation method is verified and its capability is demonstrated with the fibre suspension flows through two parallel plates, a circular tube and the 4:1 and 4.5:1 axisymmetric contraction geometries which are usually chosen to test a numerical method because of the challenging nature of these problems.

4.1 Introduction

Fibre-reinforced composite materials, e.g. polymer matrices strengthened by glass fibres, are popularly used in many important industrial areas because of their advanced mechanical properties such as high strength and stiffness, and low density (Folkes, 1982). These exceptional properties are mostly dominated by the distribution and orientation of fibres existing inside matrices. Hence, a sufficient understanding of the orientation distribution of fibre configurations in the solvent of a moulding process is very important and needs to be carefully investigated using both experimental and numerical approaches. Indeed, one of the most active research trends in this area is to simulate the flow of fibre suspensions in complex geometries, which has been stimulated by Lipscomb et al. (1988).

In the scope of this research project, we consider rigid cylindrical fibres of the same length and diameter. Fibre suspensions can be classified into three main groups: dilute, semi-dilute and concentrated suspensions based on two basic parameters, the fibre volume fraction ϕ and the aspect ratio a_r of the fibre (length/diameter). Specifically, a suspension is considered as dilute, semi-dilute or concentrated for the case of $\phi a_r^2 < 1$, $1 < \phi a_r^2 < a_r$ or $\phi a_r > 1$, respectively.

Generally, the physical description of flow and the evolution of fibre configurations poses challenges related to the necessity to take into account the fibre-fibre, fibre-fluid, and fibre-boundary interactions, especially for suspension flows through complex geometries (Lipscomb et al., 1988). For dilute suspensions, the fibre-fibre interaction is neglected and the evolution of the fibre configuration is captured by the Jeffery motion equation (Jeffery, 1922). For semi-dilute and concentrated suspensions, the fibre-fibre interaction is significant. Thus, it is necessary to take into consideration this interaction and one possible way is to introduce a diffusion term into Jeffery equation (Folgar and Tucker, 1984).

From the literature, the simulation of a fibre suspension is basically carried out through the following three steps: (i) Introduce a fibre stress component into the momentum conservation equation to include dynamic effects of fibres on the bulk properties of the flow; (ii) Apply an appropriate motion equation to describe the evolution of fibre configuration, as stated above, the Jeffery equation is suitable for dilute suspension whereas the Folgar-Tucker equation is applicable for semi-dilute and concentrated ones; and (iii) Determine the fibre contribution to stress (named fibre stress tensor) using a relevant constitutive equation as a function of the fibres' orientation.

Since the fibre stress tensor is essentially calculated from the fourth-order orientation tensor $\langle \mathbf{PPPP} \rangle$, the basic difference between numerical methods for the simulation of fibre suspensions is the way to handle the fourth-order structure tensor. There are several approaches, reviewed in Section 1.4.2, to process the fourth-order orientation tensor. Among these, the BCF-based approach has emerged as a powerful tool for a stable and accurate solution of fibre suspensions. Following the approach, a high number of fibre configurations is initiated on each computational node/element and the fourth-order tensor is directly calculated from these configurations without using any closure approximations. The approach, in the combination with the DAVSS formulation (Sun et al., 1996) and FEM, has been successfully applied for a range of complex flow problems of fibre suspensions by Fan et al. (1999); Phan-Thien and Fan (1999); Fan et al. (2000) and Lu et al. (2006).

Recently, the macro-micro multiscale methods based on the differentiated and integrated RBF (i.e. DRBF and IRBF) approximations have been developed to simulate successfully a range of dilute polymer solutions (Tran et al., 2009, 2011; Nguyen et al., 2015b). Owing to the advantages of RBF-based high order approximation schemes, the approach achieved high-order convergence rate and accuracy

(Tran et al., 2012a; Nguyen et al., 2015b). In this research, one-dimensional IRBF (1D-IRBF) scheme (Mai-Duy et al., 2008) is employed to discretise the conservation equations using the vorticity-stream function formulation, whereas the fibre configurations governed by Jeffery equation are processed using BCF approach. In addition, the constitutive equation of Lipscomb is exploited to evaluate the fibre stress tensor.

This chapter is organised as follows. The governing equations in the dimensionless form are presented in Section 4.2. Section 4.3 gives a short review of the DAVSS's formulation introduced in the governing momentum equation. The vorticity-stream function approach in planar and axisymmetric flow problems are detailed in Section 4.4, where an implementation of DAVSS technique for the axisymmetric geometry is also described. In Section 4.5, the Euler explicit scheme for temporal discretisation of the equation for fibre configuration fields is presented. The semi-implicit schemes followed by the IRBF-based approximation to the governing flow equations are also described. An algorithm is introduced in detail in Section 4.6. Numerical examples and obtained results are discussed in Section 4.7. Finally, the work is closed by concluding remarks in Section 4.8.

4.2 Dimensionless governing equations for fibre suspension flow

Consider an isothermal and incompressible flow of fibre suspensions in 2-D space. The continuity and momentum equations of the flow are given by (Lu et al., 2006)

$$\nabla \cdot \mathbf{u} = 0, \tag{4.1}$$

$$\frac{\partial \mathbf{u}}{\partial t} + \mathbf{u} \cdot \nabla \mathbf{u} = -\nabla p + \frac{1}{Re} \nabla \cdot \boldsymbol{\tau}_e, \tag{4.2}$$

where t, $\mathbf{u}$, p and $\boldsymbol{\tau}_e$ are the time, velocity field, pressure and extra stress tensor, respectively; and Re the Reynolds number based on the viscosity η_0 of the Newtonian solvent. For fibre suspensions with a Newtonian solvent, the extra stress tensor ($\boldsymbol{\tau}_e$) consists of two components as follows.

$$\boldsymbol{\tau}_e = \boldsymbol{\tau}_s + \boldsymbol{\tau}_f, \tag{4.3}$$

where $\boldsymbol{\tau}_s = 2\mathbf{D}$ and $\boldsymbol{\tau}_f$ are the stress components contributed by the Newtonian solvent and the suspended fibres, respectively; and $\mathbf{D} = \frac{1}{2}\left(\nabla\mathbf{u} + (\nabla\mathbf{u})^T\right)$ the rate of strain tensor.

There are several models used to calculate the stress contributed by suspended fibres, for example, the Lipscomb model (Lipscomb et al., 1988) for dilute suspensions and the Phan-Thien–Graham model (Phan-Thien and Graham, 1991) for semi-dilute and concentrated suspensions. In this chapter, the former one is used to investigate the present method in simulations of dilute fibre suspension flows. The Lipscomb model is given by

$$\boldsymbol{\tau}_f = k_f \mathbf{D} : \langle \mathbf{PPPP} \rangle, \tag{4.4}$$

where $\mathbf{P}$ is the unit vector representing the orientation of a fibre; $\langle \mathbf{PPPP} \rangle$ the fourth-order orientation tensor or structure tensor; and $\left\langle (\cdot) \right\rangle$ the statistical average of $(\cdot)$. The dimensionless quantity k_f is the fibre parameter and defined by

$$k_f = \frac{\phi\mu}{\eta_0}, \tag{4.5}$$

where η_0 is the Newtonian fluid viscosity; ϕ the volume fraction of fibres; μ is the material constant and chosen in the limit of high aspect ratio of fibre as follows (Chiba et al., 2001).

$$\mu = \frac{\eta_0 {a_r}^2}{\ln(a_r)}, \tag{4.6}$$

where a_r is the aspect ratio of fibres. Substituting Eq. (4.6) into Eq. (4.5) yields

$$k_f = \frac{\phi {a_r}^2}{\ln(a_r)}. \tag{4.7}$$

Therefore, the fibre parameter is considered as the only single one in the fibre stress equation (4.4), which describes the impact of suspended fibres on the kinematic behaviour of the flow.

The evolution of fibres' orientation in flow is captured by the Jeffery equation as follows (Lipscomb et al., 1988).

$$\frac{\partial \mathbf{P}}{\partial t} + \mathbf{u} \cdot \nabla \mathbf{P} = \boldsymbol{\Omega} \cdot \mathbf{P} + \lambda \left(\mathbf{D} - \mathbf{D} : \mathbf{PPI} \right) \cdot \mathbf{P}, \tag{4.8}$$

where $\boldsymbol{\Omega} = \frac{1}{2} \left(\left(\nabla \mathbf{u} \right)^T - \nabla \mathbf{u} \right)$ is the vorticity tensor; λ a parameter dependent on the aspect ratio, $\lambda = \frac{a_r^2 - 1}{a_r^2 + 1}$; and $\mathbf{I}$ the identity matrix. As shown in Phan-Thien and Graham (1991), by introducing

$$\mathbf{Q}\left(\mathbf{x}, t\right) = Q \mathbf{P}\left(\mathbf{x}, t\right), \tag{4.9}$$

where Q is the modulus of $\mathbf{Q}$, the Jeffery equation (4.8) is transformed into

$$\frac{\partial \mathbf{Q}}{\partial t} + \mathbf{u} \cdot \nabla \mathbf{Q} = \left(\nabla \mathbf{u} \right)^T \cdot \mathbf{Q} - \zeta \mathbf{D} \cdot \mathbf{Q} \tag{4.10}$$

where $\zeta = 2/(a_r^2 + 1) = 1 - \lambda$.

The fourth-order orientation tensor $\langle \mathbf{PPPP} \rangle$ in Eq. (4.4) can be now defined by

$$\langle \mathbf{PPPP} \rangle = \frac{1}{N_f} \sum_{i=1}^{N_f} \frac{\mathbf{Q}_i}{Q_i} \frac{\mathbf{Q}_i}{Q_i} \frac{\mathbf{Q}_i}{Q_i} \frac{\mathbf{Q}_i}{Q_i}, \tag{4.11}$$

where N_f is the number of fibres. The components of the tensor $\langle \mathbf{PPPP} \rangle$ in a 2-D fibre orientation field are given by (Chiba et al., 2001)

$$\begin{aligned} P_{1111} = \sum_{i=1}^{N_f} \frac{\cos^4 \theta_i}{N_f}, \; P_{1112} = \sum_{i=1}^{N_f} \frac{\cos^3 \theta_i \sin \theta_i}{N_f}, \; P_{1122} = \sum_{i=1}^{N_f} \frac{\cos^2 \theta_i \sin^2 \theta_i}{N_f}, \\ P_{1222} = \sum_{i=1}^{N_f} \frac{\cos \theta_i \sin^3 \theta_i}{N_f}, \; P_{2222} = \sum_{i=1}^{N_f} \frac{\sin^4 \theta_i}{N_f}, \end{aligned} \tag{4.12}$$

where $P_{1111} = \langle P_1 P_1 P_1 P_1 \rangle$, $P_{1112} = \langle P_1 P_1 P_1 P_2 \rangle$, $P_{1122} = \langle P_1 P_1 P_2 P_2 \rangle$, $P_{1222} = \langle P_1 P_2 P_2 P_2 \rangle$, $P_{2222} = \langle P_2 P_2 P_2 P_2 \rangle$; and θ_i is the angle between the x-axis and the axis of fibre i.

4.3 The discrete adaptive viscoelastic stress splitting (DAVSS) formulation

The DAVSS scheme has been widely used in numerical methods to maintain the numerical stability for simulations of viscoelastic fluids (Sun et al., 1996, 1999) and fibre suspensions (Fan et al., 1999; Lu et al., 2006). The DAVSS transformation is introduced into the original momentum equation (4.2) as follows (Fan et al., 1999; Lu et al., 2006).

$$\begin{aligned} \frac{\partial \mathbf{u}}{\partial t} + \mathbf{u}\cdot\nabla\mathbf{u} - \frac{1}{Re}\nabla\cdot\left[\eta_a\left(\nabla\mathbf{u}+(\nabla\mathbf{u})^T\right)\right] &= -\nabla p \\ &\quad -\frac{2}{Re}\nabla\cdot\left[\left(\eta_a-1\right)\mathbf{D}\right]+\frac{1}{Re}\nabla\cdot\boldsymbol{\tau}_f, \end{aligned} \tag{4.13}$$

where η_a is the adaptive viscosity. For the dilute fibre suspension using Lipscomb model, the adaptive viscosity is a function of fibre stress and given by (Lu et al., 2006)

$$\eta_a = k_f + \frac{1+\sqrt{(1/2)\boldsymbol{\tau}_f:\boldsymbol{\tau}_f}}{1+\sqrt{2\mathbf{D}:\mathbf{D}}}, \tag{4.14}$$

where k_f is the fibre parameter. It is worth noting that there are several differences appearing in the second term of the right-hand side of Eq. (4.13) and in the denominator of the second term in Eq. (4.14) as compared with ones mentioned in Fan et al. (1999) and Lu et al. (2006). These differences happen because the strain rate tensor $\mathbf{D}$ is here defined as $\frac{1}{2}\left(\nabla\mathbf{u}+(\nabla\mathbf{u})^T\right)$, instead of $\left(\nabla\mathbf{u}+(\nabla\mathbf{u})^T\right)$ as presented in the cited papers. Furthermore, in this work, the DAVSS formulation is only applied to simulate fibre suspensions in axisymmetric flows but not in the planar Poiseuille one whose geometry is quite simple.

4.4 Vorticity-stream function formulation for 2-D flows

For 2-D problems considered in this work, it is more convenient to use the vorticity-stream function formulation which offers several numerical benefits as

(i) the continuity equation is automatically satisfied; and (ii) the pressure field disappears in the equation of motion.

4.4.1 Vorticity-stream function formulation in the Cartesian coordinates (x, y)

The relations between velocity (u, v), vorticity ω and stream function Ψ are given by

$$\omega = \frac{1}{2}\left(\frac{\partial u}{\partial y} - \frac{\partial v}{\partial x}\right), \tag{4.15}$$

$$u = \frac{\partial \Psi}{\partial y}, \qquad v = -\frac{\partial \Psi}{\partial x}. \tag{4.16}$$

Substituting the expressions in Eq. (4.16) into Eq. (4.15) yields the following vorticity-stream function formulation

$$\frac{\partial^2 \Psi}{\partial x^2} + \frac{\partial^2 \Psi}{\partial y^2} = 2\omega. \tag{4.17}$$

Taking the curl of Eq. (4.2) and using Eqs. (4.1), (4.3) - (4.15), the vorticity transport equation is written as follows.

$$\begin{aligned} \frac{\partial \omega}{\partial t} + u\frac{\partial \omega}{\partial x} + v\frac{\partial \omega}{\partial y} = \frac{1}{Re}\left(\frac{\partial^2 \omega}{\partial x^2} + \frac{\partial^2 \omega}{\partial y^2}\right) \\ + \frac{1}{2Re}\left(\frac{\partial^2 \tau_f^{xx}}{\partial x \partial y} + \frac{\partial^2 \tau_f^{xy}}{\partial y^2} - \frac{\partial^2 \tau_f^{yx}}{\partial x^2} - \frac{\partial^2 \tau_f^{yy}}{\partial x \partial y}\right), \end{aligned} \tag{4.18}$$

where τ_f^{xx}, τ_f^{xy}, τ_f^{yx} and τ_f^{yy} are the stress components of the symmetric fibre stress tensor $\boldsymbol{\tau}_f$.

4.4.2 Axisymmetric vorticity-stream function formulation in the cylindrical coordinates (r, z)

The considered flow is predominantly in the z-direction and the relations between velocity (u_r, u_z), vorticity ω, and stream function Ψ are given by

$$\omega = \frac{1}{2}\left(\frac{\partial u_z}{\partial r} - \frac{\partial u_r}{\partial z}\right), \tag{4.19}$$

$$u_z = \frac{1}{r}\frac{\partial \Psi}{\partial r}, \qquad u_r = -\frac{1}{r}\frac{\partial \Psi}{\partial z}. \tag{4.20}$$

Following manipulation as done in Section 4.4.1, the vorticity transport and stream function equations are given by

$$\begin{aligned}\frac{\partial \omega}{\partial t} + u_z\frac{\partial \omega}{\partial z} + u_r\frac{\partial \omega}{\partial r} - \frac{u_r}{r}\omega = \frac{1}{Re}\left(\frac{\partial^2 \omega}{\partial z^2} + \frac{\partial^2 \omega}{\partial r^2} + \frac{1}{r}\frac{\partial \omega}{\partial r} - \frac{1}{r^2}\omega\right) + \\ \frac{1}{2Re}\left(\frac{\partial^2 \tau_f^{rz}}{\partial r^2} - \frac{\partial^2 \tau_f^{zr}}{\partial z^2} + \frac{\partial^2 \tau_f^{zz}}{\partial r \partial z} - \frac{\partial^2 \tau_f^{rr}}{\partial z \partial r} + \frac{1}{r}\frac{\partial \tau_f^{rz}}{\partial r} - \frac{1}{r}\frac{\partial \tau_f^{rr}}{\partial z} - \frac{1}{r^2}\tau_f^{rz}\right),\end{aligned} \tag{4.21}$$

$$\frac{1}{r}\frac{\partial^2 \Psi}{\partial z^2} + \frac{1}{r}\frac{\partial^2 \Psi}{\partial r^2} - \frac{1}{r^2}\frac{\partial \Psi}{\partial r} = 2\omega, \tag{4.22}$$

where τ_f^{zz}, τ_f^{zr}, τ_f^{rz} and τ_f^{rr} are the stress components of the fibre stress tensor $\boldsymbol{\tau}_f$.

The vorticity transport equation (4.21) is rewritten with the implementation of DAVSS as follows.

$$\begin{aligned}\frac{\partial \omega}{\partial t} + u_z\frac{\partial \omega}{\partial z} + u_r\frac{\partial \omega}{\partial r} - \frac{u_r}{r}\omega - \frac{\eta_a}{Re}\left(\frac{\partial^2 \omega}{\partial z^2} + \frac{\partial^2 \omega}{\partial r^2}\right) = \\ -\frac{\eta_a - 1}{Re}\cdot\left(\frac{\partial^2 \omega}{\partial z^2} + \frac{\partial^2 \omega}{\partial r^2}\right) + \frac{1}{Re}\left(\frac{1}{r}\frac{\partial \omega}{\partial r} - \frac{1}{r^2}\omega\right) + \\ \frac{1}{2Re}\left(\frac{\partial^2 \tau_f^{rz}}{\partial r^2} - \frac{\partial^2 \tau_f^{zr}}{\partial z^2} + \frac{\partial^2 \tau_f^{zz}}{\partial r \partial z} - \frac{\partial^2 \tau_f^{rr}}{\partial z \partial r} + \frac{1}{r}\frac{\partial \tau_f^{rz}}{\partial r} - \frac{1}{r}\frac{\partial \tau_f^{rr}}{\partial z} - \frac{1}{r^2}\tau_f^{rz}\right),\end{aligned} \tag{4.23}$$

where η_a is the adaptive viscosity and given in Eq. (4.14).

4.5 Numerical method

In this work, the fusion of IRBF and DAVSS is used to simulate fibre suspension flows, in which a semi-implicit scheme is applied to temporally discretise the vorticity transport equations (4.18) and (4.23) while the Euler explicit scheme is used for the equation of fibre configuration fields (4.9). At each time step, the 1D-IRBF scheme is employed to approximate both the field variables of flow and the fibre stress tensor.

4.5.1 Temporal discretisations of governing equations

Consider a time dependent differential equation together with its initial and boundary conditions as follows.

$$\frac{\partial \omega(x,t)}{\partial t} + \mathcal{L}\omega(x,t) = f, \quad (x,t) \in \Gamma \times [0,T], \tag{4.24}$$

$$\omega(x,t) = g, \quad (x,t) \in \Gamma \times \{0\}, \tag{4.25}$$

$$\mathcal{B}\omega(x,t) = h, \quad (x,t) \in \partial\Gamma \times [0,T], \tag{4.26}$$

where Γ and $\partial\Gamma$ are a bounded domain and its boundary, respectively; T a final time; $\mathcal{L}$ a differential operator; $\mathcal{B}$ an operator expressing a boundary condition; and f, g and h known functions. Assume that the time interval [0, T] is partitioned into N_t equal sub-intervals $[t^n, t^{n+1}]$ of length Δt ($\Delta t = T/N_t$) with $t^0 = 0$ and $t^{N_t} = T$. In fully discrete schemes, Eq. (4.24) is discretised with respect to both time and space variables. The discretisation in time is accomplished by a time-stepping scheme, followed by the spatial discretisation based on an IRBFN method. Applying the θ scheme to Eq. (4.24) yields

$$\frac{\omega^{n+1} - \omega^n}{\Delta t} + \theta\mathcal{L}\omega^{n+1} + (1-\theta)\mathcal{L}\omega^n = f, \tag{4.27}$$

where superscripts $(n+1)$ and n indicate the two successive time steps at $t^{n+1} = (n+1)\Delta t$ and $t^n = n\Delta t$, respectively; Δt the size of the time step; and $\omega^n = \omega(x,t^n)$ and $\omega^{n+1} = \omega(x,t^{n+1})$. Equation (4.27) together with the constraint conditions Eq. (4.25) and Eq. (4.26) at time t^{n+1} are then spatially discretised using an IRBF approach described in the next section. The obtained solution is the values of the field variable at the grid points.

It is noted that the θ-formulation (4.27) is the Euler explicit, fully implicit and semi-implicit (Crank-Nicolson) schemes for $\theta = 0$, $\theta = 1$ and $\theta = 0.5$, respectively.

Semi-implicit scheme for temporal discretisation of the vorticity transport equation

For 2-D planar flow problem, the Crank-Nicolson scheme is employed to discretise the vorticity transport equation (4.18) in the Cartesian coordinate system as follows.

$$\begin{aligned}\omega^{n+1} - \frac{\Delta t}{2Re}\left(\frac{\partial^2 \omega^{n+1}}{\partial x^2} + \frac{\partial^2 \omega^{n+1}}{\partial y^2}\right) &= \omega^n + \frac{\Delta t}{2Re}\left(\frac{\partial^2 \omega^{n}}{\partial x^2} + \frac{\partial^2 \omega^{n}}{\partial y^2}\right) \\ &\quad -\Delta t u^n \frac{\partial \omega^n}{\partial x} - \Delta t v^n \frac{\partial \omega^n}{\partial y} + \frac{\Delta t}{2Re}\left(\frac{\partial^2 (\tau_f^{xx})^n}{\partial x \partial y} + \frac{\partial^2 (\tau_f^{xy})^n}{\partial y^2}\right. \\ &\quad \left. - \frac{\partial^2 (\tau_f^{yx})^n}{\partial x^2} - \frac{\partial^2 (\tau_f^{yy})^n}{\partial x \partial y}\right),\end{aligned} \tag{4.28}$$

where superscripts $(n+1)$, n and Δt are defined above. The components of fibre stress tensor τ_f^{xx}, τ_f^{xy}, τ_f^{yx} and τ_f^{yy} on the right-hand side of Eq. (4.28) are known quantities, which are determined from the solution of the fibre configuration fields at the previous time step t^n.

For 2-D axisymmetric flow problems, the vorticity equation (4.23) is temporally discretised as follows.

$$
\begin{aligned}
\omega^{n+1} - \frac{\Delta t}{Re}\eta_a \left(\frac{\partial^2 \omega^{n+1}}{\partial z^2} + \frac{\partial^2 \omega^{n+1}}{\partial r^2} \right) &= \omega^n - \frac{\Delta t}{Re}\left(\eta_a - 1\right)\left(\frac{\partial^2 \omega^{n}}{\partial z^2} + \frac{\partial^2 \omega^{n}}{\partial r^2} \right) \\
&\quad + \frac{\Delta t}{Re}\left(\frac{1}{r}\frac{\partial \omega^n}{\partial r} - \frac{1}{r^2}\omega^n \right) - \Delta t u_z^n \frac{\partial \omega^n}{\partial z} - \Delta t u_r^n \frac{\partial \omega^n}{\partial r} + \Delta t \frac{u_r^n}{r}\omega^n \\
&\quad + \frac{\Delta t}{2Re}\left(\frac{\partial^2 (\tau_f^{rz})^n}{\partial r^2} - \frac{\partial^2 (\tau_f^{zr})^n}{\partial z^2} + \frac{\partial^2 (\tau_f^{zz})^n}{\partial r \partial z} - \frac{\partial^2 (\tau_f^{rr})^n}{\partial z \partial r} + \frac{1}{r}\frac{\partial (\tau_f^{rz})^n}{\partial r} \right. \\
&\quad \left. - \frac{1}{r}\frac{\partial (\tau_f^{rr})^n}{\partial z} - \frac{1}{r^2}(\tau_f^{rz})^n \right),
\end{aligned}
\tag{4.29}
$$

where the adaptive viscosity η_a is defined as before; and τ_f^{zz}, τ_f^{zr}, τ_f^{rz} and τ_f^{rr} are components of fibre stress tensor $\boldsymbol{\tau}_f$.

Euler explicit scheme for temporal discretisation of the equation of fibre configuration fields

As noted in Section 4.2, the motion equation for fibres' direction (4.8) has been converted into the evolution equation (4.10) for the configuration $\mathbf{Q}$ by executing a variable transformation in Eq. (4.9). Thus, the Euler explicit scheme is applied for Eq. (4.10) as follows.

$$
\mathbf{Q}\left(\mathbf{x}, t^{n+1}\right) = \mathbf{Q}\left(\mathbf{x}, t^{n}\right) - \Delta t \mathbf{u}\left(\mathbf{x}, t^{n}\right) \cdot \nabla \mathbf{Q}\left(\mathbf{x}, t^{n}\right) + \Delta t \left(\nabla \mathbf{u}\left(\mathbf{x}, t^{n}\right)\right)^T \cdot \mathbf{Q}\left(\mathbf{x}, t^{n}\right),
\tag{4.30}
$$

where $t^n = n\Delta t$ and $t^{n+1} = (n+1)\Delta t$ are the times at steps n and $(n+1)$, respectively; and Δt the time step size for both micro and macro procedures as stated above.

In Eq. (4.30), the velocity field and its gradient are known and obtained from the macro procedure. Furthermore, in order to ensure the stability of the present method, the high-order upwind scheme (Ferreira et al., 2002) is used to approximate the gradient of configuration fields ($\nabla \mathbf{Q}$).

Since the configuration fields, $\mathbf{Q}_i$'s with $i = \left(1, 2, \cdots, N_f\right)$, are independent from each other, Eq. (4.30) can be solved for each configuration field in parallel. The original fibre configuration fields $\mathbf{P}_i$ are then calculated using Eq. (4.9). The fourth-order orientation tensor and the fibre stress are subsequently determined. Lastly, the gradient of the fibre stress tensor is approximated and introduced into the vorticity transport equation in the macro procedure.

4.5.2 Spatial discretisation of elliptic differential equation

At a time t, Eqs. (4.28) and (4.29) are discretised using the 1D-IRBF approximation scheme which has been detailed in Section 2.5.1. The algorithm of the present multiscale method is detailed in the next section.

4.6 Algorithm of the present method

The algorithm of the present method is presented in this section. The implementation will be then described in several illustrative examples in the next section.

(a) Generate a set of collocation points on the considered domain. The initial and boundary conditions of the velocity field and fibre configurations are correspondingly assigned at each collocation point. The stream function's and vorticity's initial and boundary conditions are then determined using Eqs. (4.15), (4.16) and (4.17) for planar flow problems or Eqs. (4.19), (4.20) and (4.22) for axisymmetric ones. Meanwhile, the initial fibre configurations including a set of randomly oriented unit vectors $\mathbf{P}$'s and the transformed vectors $\mathbf{Q}$'s are defined by Eq. (4.9);

(b) Assign N_f fibres to each collocation point based on the BCF idea. All fibres having the same index constitute a fibre configuration field. Hence, there is an ensemble of N_f fibre configuration fields;

(c) Velocity gradients and the strain rate tensor $\mathbf{D}$ are directly calculated from the current velocity field.

(d) Solve the evolution equation of fibres (4.30) for the new configurations ($\mathbf{Q}$'s). Determine the orientation vectors of fibre configurations using Eq. (4.9) and then calculate the fourth-order orientation tensor $\langle\mathbf{PPPP}\rangle$ and the fibre stress tensor at each collocation point. The gradients of fibre stresses are calculated in advance and will be used in the following step as known quantities in the vorticity transport equation;

(e) Solve the stream function equation for the new solution and then calculate the new velocity field. The new velocity field together with the gradients of the fibre stress components obtained by step (d) are used to solve the vorticity equation;

(f) Terminate the simulation when either the desired time or the convergence measure (CM) for the velocity given by Eq. (2.54) is reached.

(g) Return to step (c) for the next time step until the steady state or a given time is reached.

4.7 Numerical examples

The present method is employed to simulate fibre suspension flows between two parallel plates (a planar channel) and through a circular tube. The capability of the present method is then demonstrated with the simulation of the axisymmetric contraction flow of fibre suspension. The obtained results of the first problem are compared with the results published by Chiba et al. (2001) whereas the solutions to the last problem are compared with those presented in Chiba et al. (1990) and Lipscomb et al. (1988). In order to compare the present results with those cited above, we also choose $\lambda = 1$, and as a result $\zeta = 0$ in Eq. (4.10) as shown in the examples below.

4.7.1 Flow between two parallel plates

This problem was studied by Chiba et al. (2001). The geometry of the problem is given in Fig. 4.1 where $L = 10$ and $H = 1$ are the length and height of the channel, respectively.

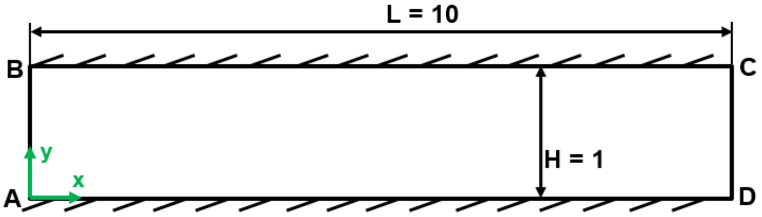

Figure 4.1: Flow through two parallel plates: the geometry of the problem.

Governing equations and boundary conditions

The system of governing equations for this particular problem is obtained from the discussion in sections 4.2 and 4.4 as follows.

$$\begin{aligned}\frac{\partial \omega}{\partial t} + u\frac{\partial \omega}{\partial x} + v\frac{\partial \omega}{\partial y} &= \frac{1}{\mathrm{Re}}\left(\frac{\partial^2 \omega}{\partial x^2} + \frac{\partial^2 \omega}{\partial y^2}\right) \\ &+\frac{1}{2\mathrm{Re}}\left(\frac{\partial^2 \tau_f^{xx}}{\partial x \partial y} + \frac{\partial^2 \tau_f^{xy}}{\partial y^2} - \frac{\partial^2 \tau_f^{yx}}{\partial x^2} - \frac{\partial^2 \tau_f^{yy}}{\partial x \partial y}\right),\end{aligned} \tag{4.31}$$

$$\frac{\partial^2 \Psi}{\partial x^2} + \frac{\partial^2 \Psi}{\partial y^2} = 2\omega, \tag{4.32}$$

$$u = \frac{\partial \Psi}{\partial y}, \qquad v = -\frac{\partial \Psi}{\partial x}, \tag{4.33}$$

$$\frac{\partial \mathbf{Q}}{\partial t} + \mathbf{u}\cdot\nabla\mathbf{Q} = (\nabla\mathbf{u})^T \cdot \mathbf{Q}, \tag{4.34}$$

$$\langle \mathbf{PPPP} \rangle = \left\langle \frac{\mathbf{Q}}{Q}\frac{\mathbf{Q}}{Q}\frac{\mathbf{Q}}{Q}\frac{\mathbf{Q}}{Q} \right\rangle, \tag{4.35}$$

$$\boldsymbol{\tau}_f = k_f \mathbf{D} : \langle \mathbf{PPPP} \rangle . \tag{4.36}$$

In the system of equations (4.31) - (4.36), the first three equations relate to solutions of stream function, vorticity and velocity variables of the flow, while the next two equations are for solutions of the fibre configuration fields $\mathbf{Q}$'s and $\mathbf{P}$'s. The solutions at two different scales are linked together by the last equation, which is to calculate the fibre stress tensor $\boldsymbol{\tau}_f$.

Boundary conditions are applied to the problem as follows.

- At the inlet $\overline{AB}$:
    - A parabolic velocity profile of the Newtonian fluid is applied, i.e. $u = u_{max}\left(1-\left(\frac{2y}{H}-1\right)^2\right)$ and $v=0$, where $u_{max}=1.5$ is the maximum value of the velocity profile;
    - For the fibre configuration field, a set of N_f fibres are generated and assigned at each collocation point on the inlet boundary. A fibre i is defined by its angle $\theta_i = -\frac{\pi}{2}+\frac{\pi(i-1)}{N_f}$, $\big(i=1,...,N_f\big)$;
- On the walls $\overline{BC}$ and $\overline{AD}$:
    - There is no-slip boundary condition for the velocity field, i.e. $u=0$ and $v=0$;
    - The condition of co-linear alignment is used for the fibre configuration fields, i.e. $\theta_i = 0$;
- At the outlet $\overline{DC}$: The flow out condition is applied, i.e. $\frac{\partial u}{\partial x}=0$ and $v=0$.

Discretisation of governing equations and numerical results

Applying the temporal discretisation schemes presented in Section 4.5 to the vorticity transport equation and the evolution equation for fibre configurations in 2-D space yields the following equations

$$\omega^{n+1}-\frac{\Delta t}{2Re}\left(\frac{\partial^2\omega^{n+1}}{\partial x^2}+\frac{\partial^2\omega^{n+1}}{\partial y^2}\right)=\omega^n+\frac{\Delta t}{2Re}\left(\frac{\partial^2\omega^{n}}{\partial x^2}+\frac{\partial^2\omega^{n}}{\partial y^2}\right)-\Delta t u^n\cdot$$
$$\frac{\partial\omega^n}{\partial x}-\Delta t v^n\frac{\partial\omega^n}{\partial y}+\frac{\Delta t}{2Re}\left(\frac{\partial^2(\tau_f^{xx})^n}{\partial x\partial y}+\frac{\partial^2(\tau_f^{xy})^n}{\partial y^2}-\frac{\partial^2(\tau_f^{yx})^n}{\partial x^2}-\frac{\partial^2(\tau_f^{yy})^n}{\partial x\partial y}\right), \tag{4.37}$$

$$Q_x^{n+1}=Q_x^n-\Delta t\left(u^n\frac{\partial Q_x^n}{\partial x}+v^n\frac{\partial Q_x^n}{\partial y}\right)+\Delta t\left(\frac{\partial u^n}{\partial x}Q_x^n+\frac{\partial u^n}{\partial y}Q_y^n\right), \tag{4.38}$$

$$Q_y^{n+1}=Q_y^n-\Delta t\left(u^n\frac{\partial Q_y^n}{\partial x}+v^n\frac{\partial Q_y^n}{\partial y}\right)+\Delta t\left(\frac{\partial v^n}{\partial x}Q_x^n+\frac{\partial v^n}{\partial y}Q_y^n\right), \tag{4.39}$$

where superscripts n and $(n+1)$ indicate the two successive time steps $t_n = n\Delta t$ and $t_{n+1} = (n+1)\Delta t$; and Q_x^{n+1} and Q_y^{n+1} the two components of vector $\mathbf{Q}$ along x and y directions at the time t_{n+1}, respectively. A range of fibre parameters, $k_f \in \{2, 4, 6, 8, 10, 12\}$ is considered. Other parameters of the fluid include the Reynolds number, $Re = 10$ and the number of configuration fields, $N_f = 180$.

A grid convergence study for the flow with $k_f = 12$ and $\Delta t = 0.001$ is done with four different uniform Cartesian grids, whose grid parameters are given in Table 4.1. The four grids are labelled as M1, M2, M3 and M4 where M1 is the coarsest one and M4 is the finest one.

Table 4.1: A grid convergence study for the fibre suspension flow between two parallel plates. Four different grids are used where Δx and Δy are grid spaces in x-direction and y-direction, respectively; and N_x and N_y the number of grid nodes in each direction.

Grid's label	Δx	Δy	$N_x \times N_y$
M1	1/16	1/16	161×17
M2	1/18	1/18	181×19
M3	1/20	1/20	201×21
M4	1/24	1/24	241×25

The convergence of the solutions with four different meshes is confirmed through the convergence measure of the velocity field introduced in Fig. 4.2. Meanwhile, the grid convergence is reflected through the centreline velocity profile and the distribution of the extra shear stress at the outlet in Figs. 4.3.

The effect of the time step size (Δt) on the stability of the present method is also studied for grid M3. A range of simulations with $\Delta t \in \{0.01, 0.005, 0.002, 0.001, 0.0005\}$ and $k_f \in \{2, 4, 6, 8, 10, 12\}$ is done. The convergence measures of the velocity field ($CM(\mathbf{u})$) at $t = 10$ for each and every simulation are given in Table 4.2. Symbol 'X' indicates a divergent measure. It is observed that a sufficiently small time step is required for simulations with high fibre parameters and the $CM(\mathbf{u})$'s decrease with the increase of Δt or k_f. Specifically, the coarsest time step $\Delta t = 0.01$ can be used only in the simulation with $k_f = 2$ while finer time steps $\Delta t = \{0.001, 0.0005\}$ can be used for all values of k_f.

Therefore, grid M3 with $\Delta x = \Delta y = 0.05$ presented in Fig. 4.4 and $\Delta t = 0.001$

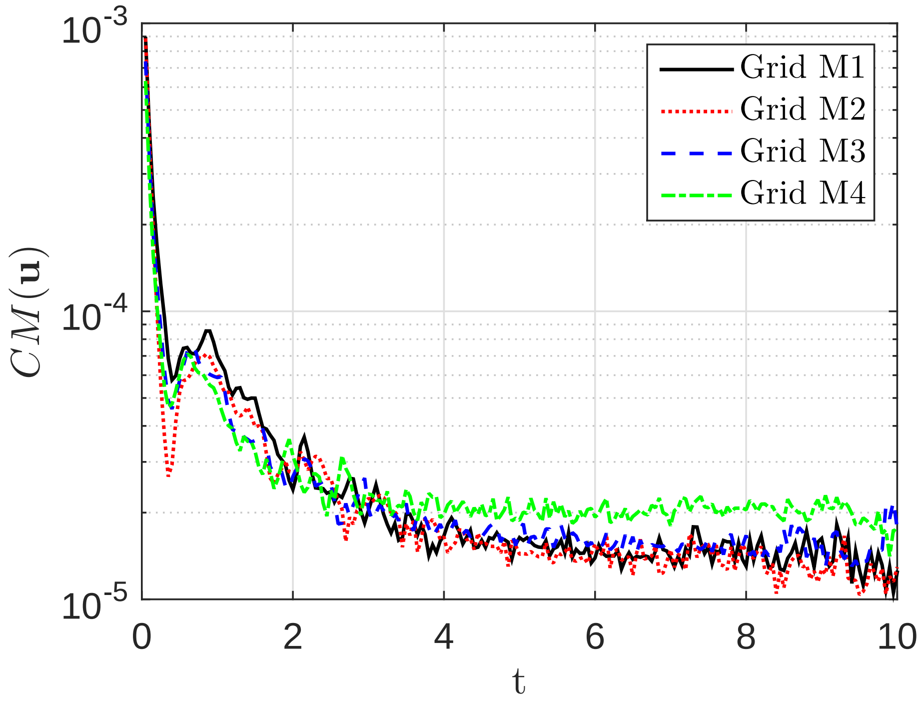

Figure 4.2: A grid convergence study for flow with $k_f = 12$: the convergence measure of the velocity field for grids M1, M2, M3, and M4.

Table 4.2: Fibre suspension flow between two parallel plates. A study for the stability of the present method based on the fibre parameter k_f and the time step size Δt for grid M3. The figures shown in the table are the values of the convergence measure of the velocity field ($CM(\mathbf{u})$) at $t = 10$. 'X' is a divergent measure.

	k_f					
Δt	2	4	6	8	10	12
0.01	2.58E-5	X	X	X	X	X
0.005	6.78E-6	2.11E-5	X	X	X	X
0.002	2.86E-6	1.02E-5	1.84E-5	1.94E-5	X	X
0.001	1.54E-6	3.82E-6	7.77E-6	8.78E-6	1.28E-5	1.76E-5
0.0005	7.45E-7	1.93E-6	3.69E-6	3.95E-6	6.01E-6	7.57E-6

are chosen for all simulation cases in this problem. The numerical results obtained by the present method confirm a very good agreement with those by Chiba et al. (2001) using the finite difference method and the statistical scheme and a much finer mesh of $\Delta x = \Delta y = 0.025$. Several observations are presented as follows.

The orientation of fibres at a position in the flow is illustrated by the ellipse's geometry (Fig. 4.5) whose length and direction of two axes are determined by the eigenvalues and the eigenvectors of the second-order orientation tensor $\langle \mathbf{PP} \rangle$.

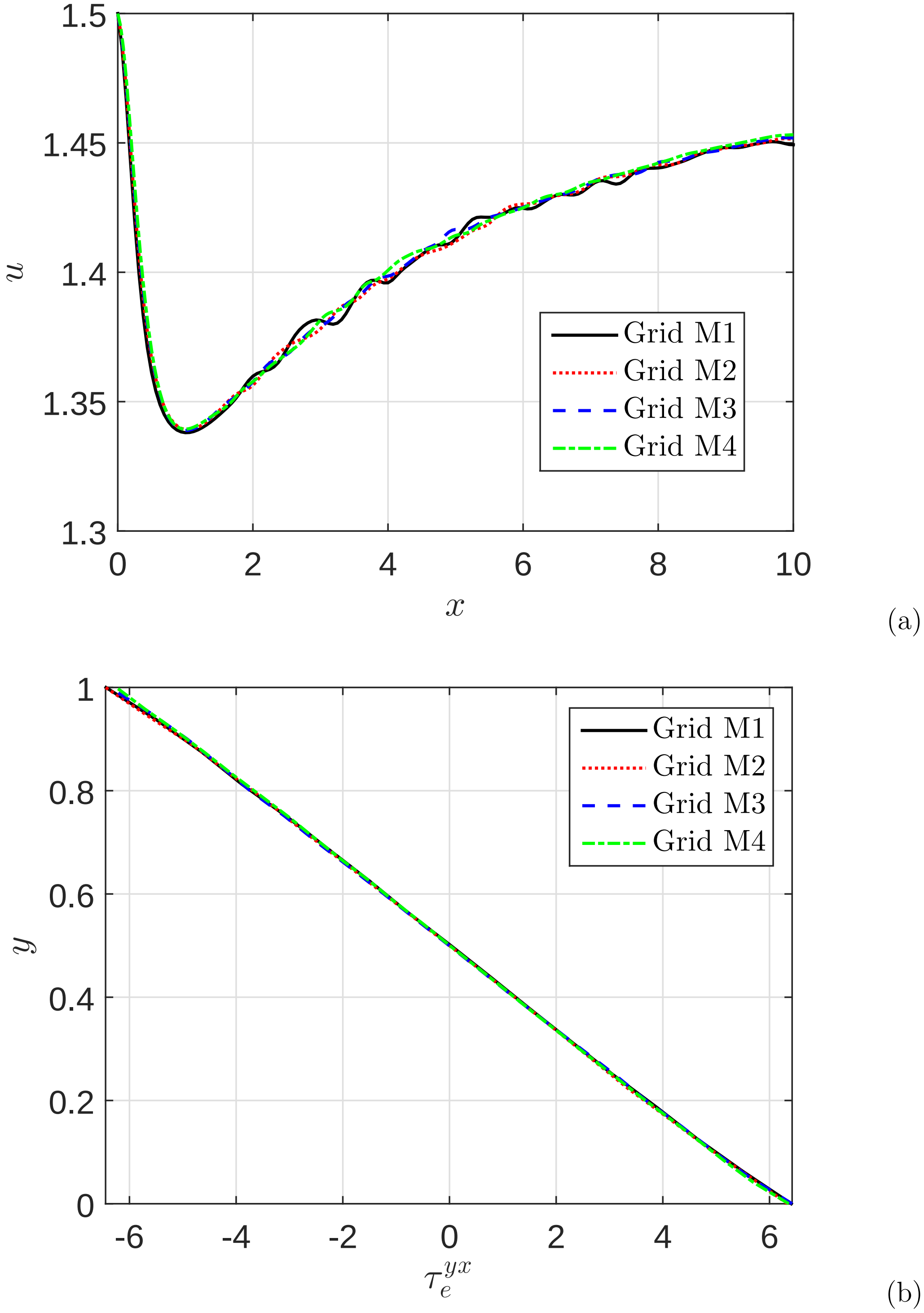

Figure 4.3: A grid convergence study for flow with $k_f = 12$: the axial velocity distribution on the centreline (figure (a)) and the distribution of the extra shear stress at the outlet (figure (b)) for grids M1, M2, M3, and M4.

Thus, there are three cases: a) a circle/circular ellipse indicates an isotropic orientation of fibres at a position; b) an ellipse implies that the predominant direction of fibres is parallel with its major axis and c) a straight line depicts that

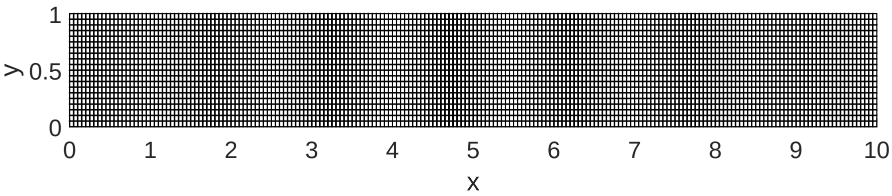

Figure 4.4: Flow through two parallel plates: a uniform Cartesian grid.

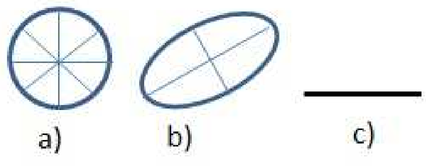

Figure 4.5: Orientation of fibres: a) Circle: the fibres' direction is isotropic; b) Ellipse: the major axis is the predominant direction of fibres and c) Straight line: all fibres completely align with the line.

all fibres completely align with the line.

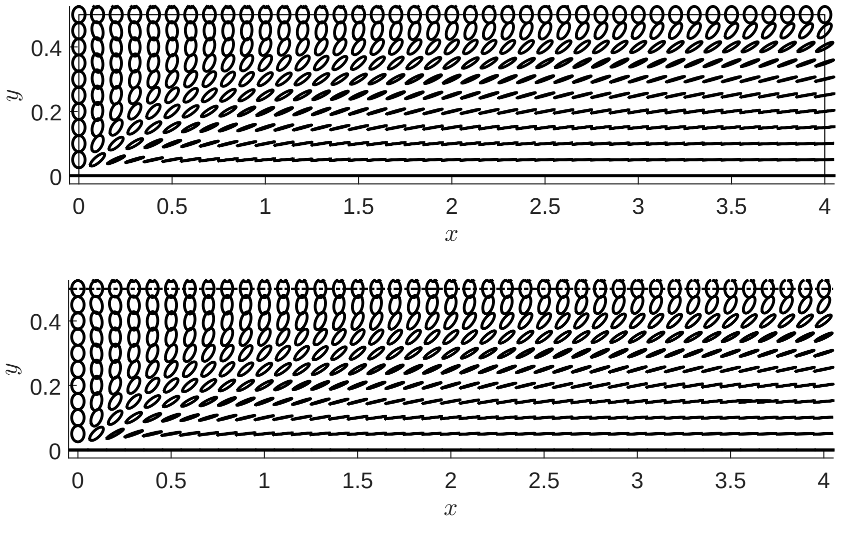

(a)

(b)

Figure 4.6: Fibre suspension flow between two parallel plates: the evolution of fibres' orientation along the channel with $k_f = 2$ (figure (a)) and $k_f = 10$ (figure (b)).

Figs. 4.6 show that the fibres near the channel wall tend to align with the flow direction (x) whereas the fibres' orientation is isotropic at the centreline. The relationship between the shear stress and the fibre's orientation will be discussed later in this section. The results for $k_f = 2$ (Fig. 4.6(a)) and $k_f = 10$ (Fig. 4.6(b)) also show that the fibre parameter does not significantly affect the fibres' orientation in the flow.

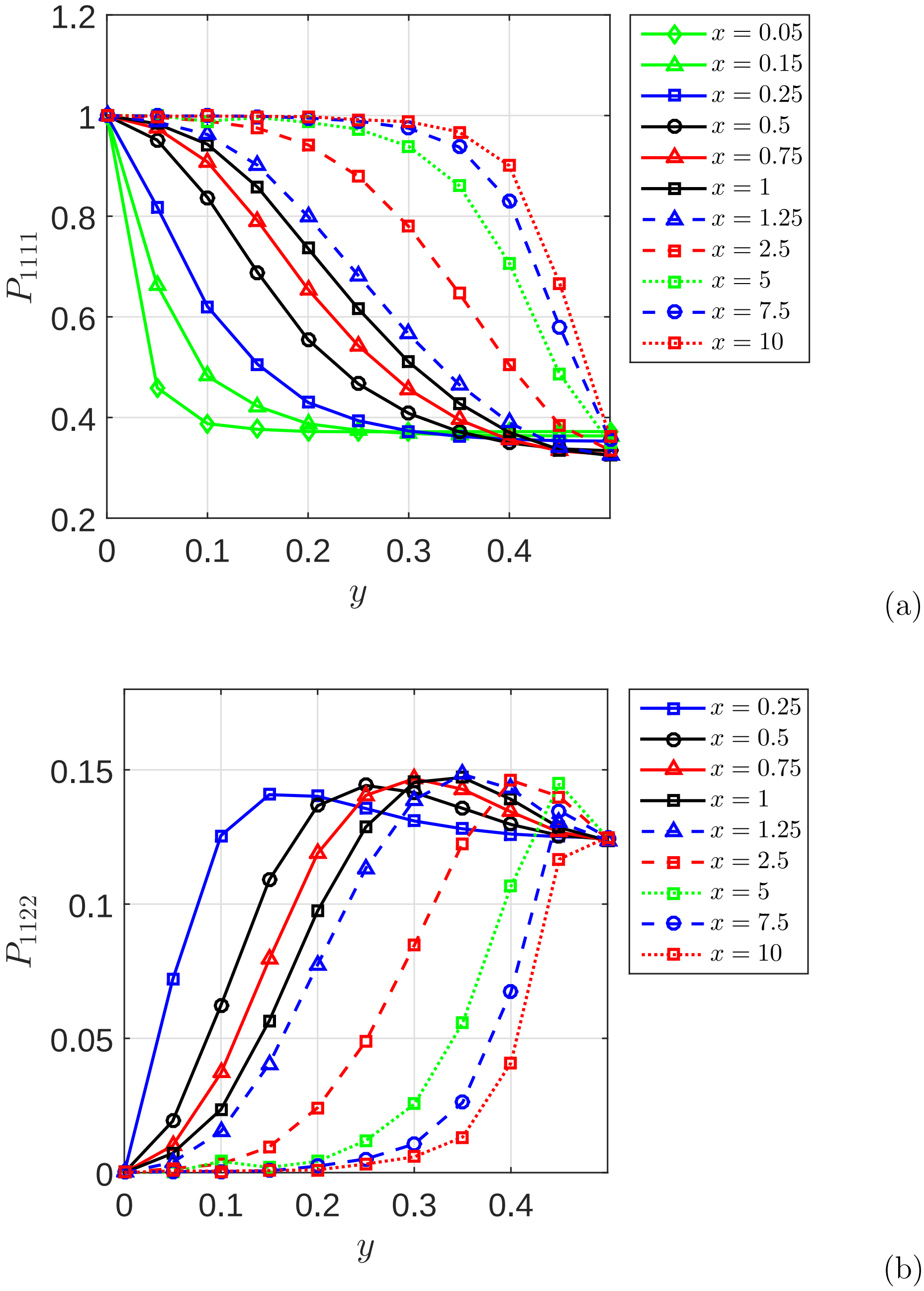

(a)

(b)

Figure 4.7: Fibre suspension flow between two parallel plates: the distribution of components P_{1111} (figure (a)) and P_{1122} (figure (b)) of the fourth-order orientation tensor on several vertical planes ($x_i = \{0.05, 0.15, 0.25, 0.5, 0.75, 1, 1.25, 2.5, 5, 7.5, 10\}$) with respect to y using $k_f = 10$.

Furthermore, Figs. 4.7 present the distribution of the components P_{1111} (Fig. 4.7(a)) and P_{1122} (Fig. 4.7(b)) of the fourth-order tensor $\langle \mathbf{PPPP} \rangle$ on several vertical planes ($x_i \in \{0.05, 0.15, 0.25, 0.5, 0.75, 1, 1.25, 2.5, 5, 7.5, 10\}$) along the channel's length with respect to y (across the channel). The results show that more and more fibres tend to align with the main flow direction (x) as they approach the outlet, especially in the near-wall region.

Fig. 4.8 depicts the development of velocity along the centreline of the channel with a range of fibre parameters $k_f \in \{2, 4, 6, 8, 10, 12\}$. The undershoot is observed in all cases and the undershoot is more pronounced as the fibre parameter increases. The undershoot reflects the effect of the isotropy of fibre configurations at the inlet. The isotropy of fibre configurations resists the development of velocity (u) on the flow direction (x) at the region near the inlet. The velocity then increases along the flow direction to the outlet with a gradual decrease of the isotropy of fibres orientation as described in Fig. 4.6.

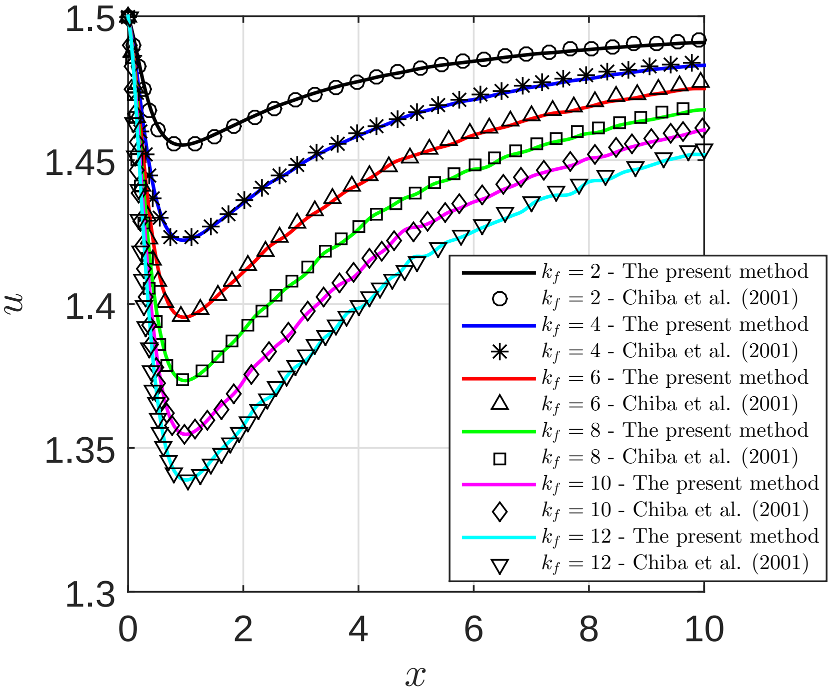

Figure 4.8: Fibre suspension flow between two parallel plates: the centreline velocity profiles for flows with $k_f \in \{2, 4, 6, 8, 10, 12\}$.

Numerical experiments show that the fibre parameter has a considerable effect on the transient velocity field near the inlet (Fig. 4.8). In the downstream direction, as the flow becomes more and more developed, there is an insignificant difference between the velocity profiles at the outlet as shown in Figs. 4.9.

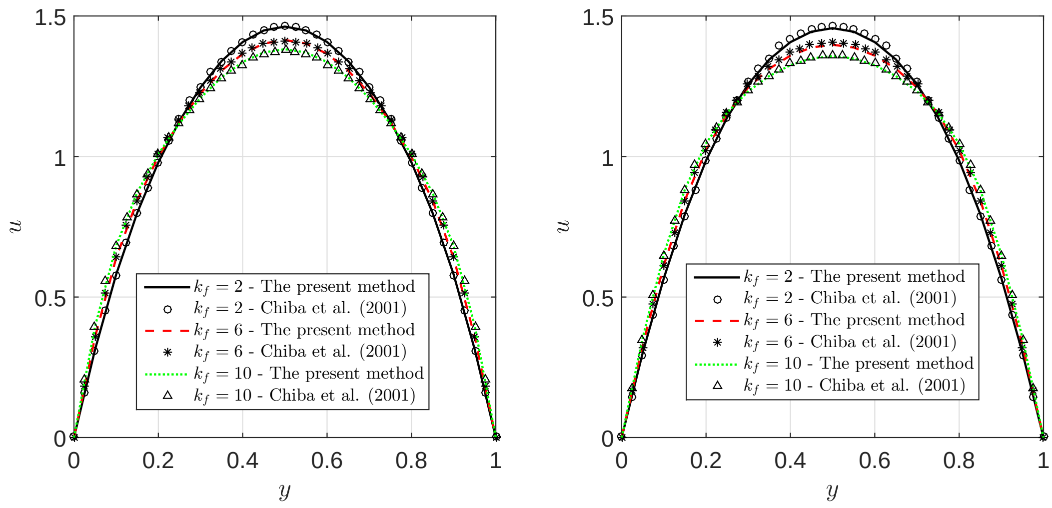

(a) At $x = 0.5$ (b) At $x = 1.25$

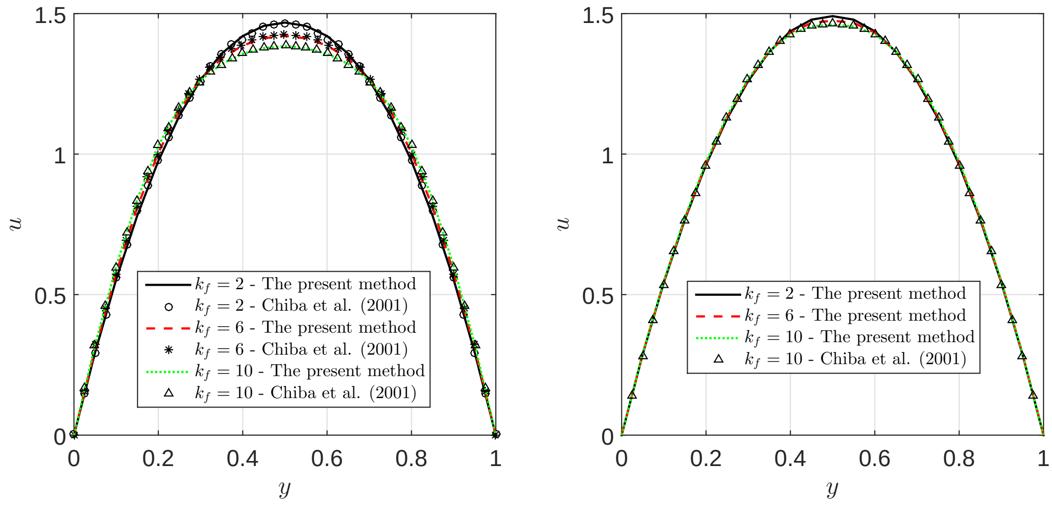

(c) At $x = 2.5$ (d) At $x = 10$

Figure 4.9: Fibre suspension flow between two parallel plates: the effect of the fibre parameter k_f on the axial velocity profiles at several sections $x \in \{0.5, 1.25, 2.5, 10\}$ of the channel.

Finally, the distributions of the shear stress (T_{xy}) and the first normal stress difference ($T_{xx} - T_{yy}$) for the flow with $k_f = 10$ are presented in Figs. 4.10 and 4.11, respectively. In contrast to the Newtonian flow, a high-stress concentration for the shear stress (Fig. 4.10(a)) and the first normal stress difference (Fig. 4.11(a)) appears near the corner between the inlet and the walls in the fibre suspension flow. The reason of the high-stress concentration is the anisotropy of fibres' orientation near the corner (see Figs. 4.6), where there is a steep transition between two extreme states of fibres' orientation, namely the co-linear alignment configuration on the wall and the isotropic configuration at the inlet. The distribution of T_{xy} and $T_{xx} - T_{yy}$ together with their values are in very good agreement with those presented in Chiba et al. (2001).

On the efficiency of the present method, the convergence measures (CM's) of the vorticity, stream function and velocity fields are presented in Fig. 4.12, where the top figure is for $k_f = 2$ and the bottom figure for $k_f = 10$. The convergence in the present method is significantly improved in comparison with one achieved by Chiba et al. (2001). Specifically, with $k_f = 10$ the present method achieves a convergence measure of approximately $3E{-}4$ for vorticity and $2E{-}6$ for stream function (Fig. 4.12(b)) using a much coarser mesh (a factor of 2 in each of the coordinate directions). Furthermore, the results depict that CMs decrease with increasing value of the fibre parameter, for example, $CM(\omega) \approx 3E{-}5$, $CM(\Psi) \approx 2E{-}7$, $CM(V) \approx 1E{-}6$ for $k_f = 2$ and $CM(\omega) \approx 3E{-}4$, $CM(\Psi) \approx 2E{-}6$, $CM(V) \approx 1E{-}5$ for $k_f = 10$. Finally, the efficiency of the present method can also be improved by increasing the number of fibre configuration fields (see Figs. 4.13).

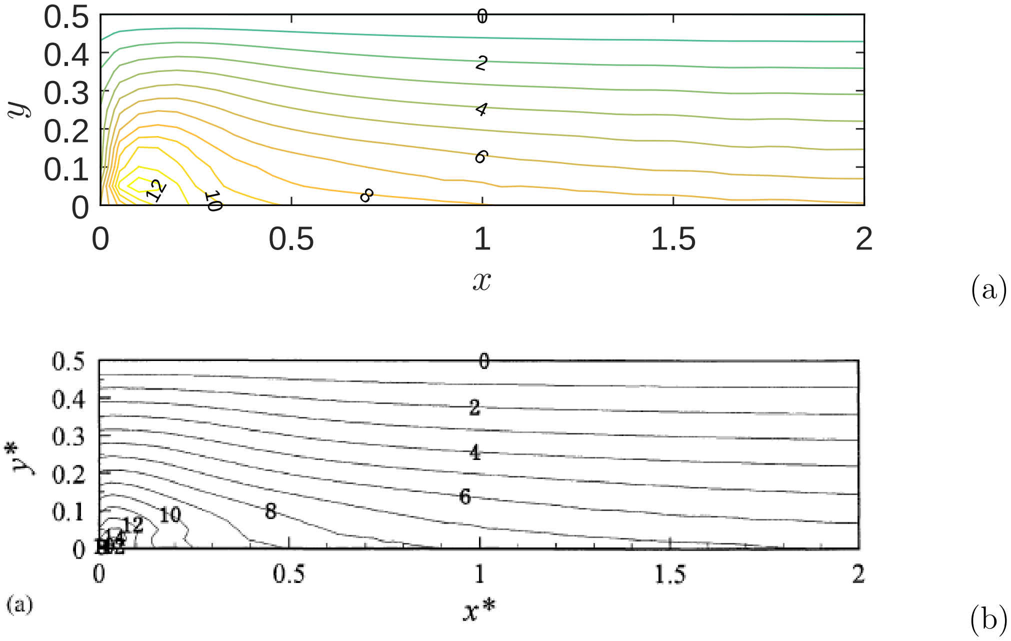

Figure 4.10: Fibre suspension flow between two parallel plates: the distribution of shear stress in the fibre suspension flow with $k_f = 10$ (figure (a)). Figure (b) has been extracted from Fig. 8(a) on page 154 of Chiba et al. (2001) for comparison.

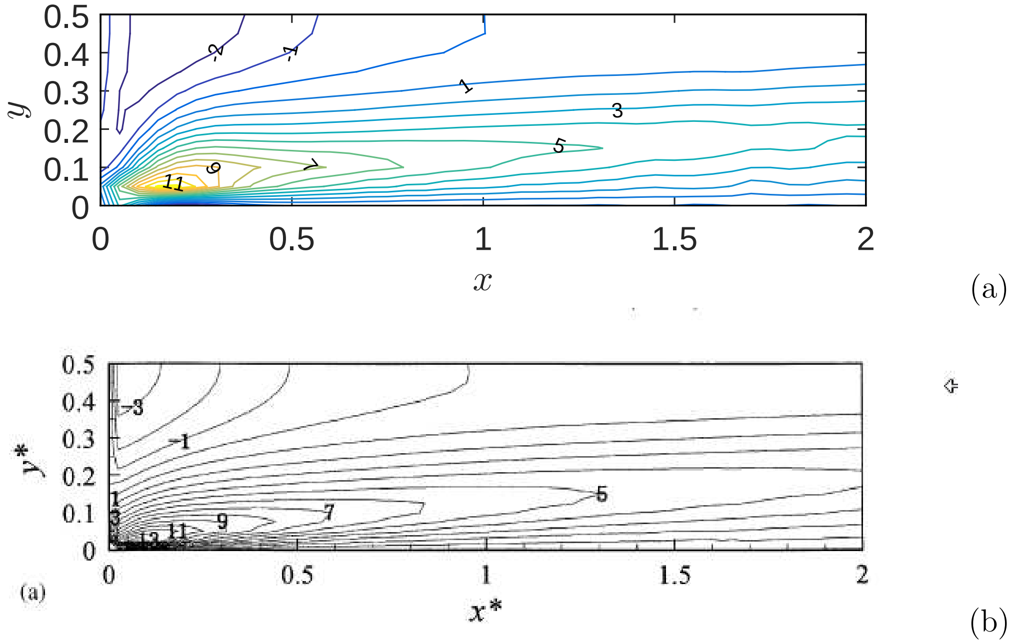

Figure 4.11: Fibre suspension flow between two parallel plates: the distribution of the first normal stress difference (figure (a)) in the fibre suspension flow with $k_f = 10$. Figure (b) has been extracted from Fig. 9(a) on page 155 of Chiba et al. (2001) for comparison.

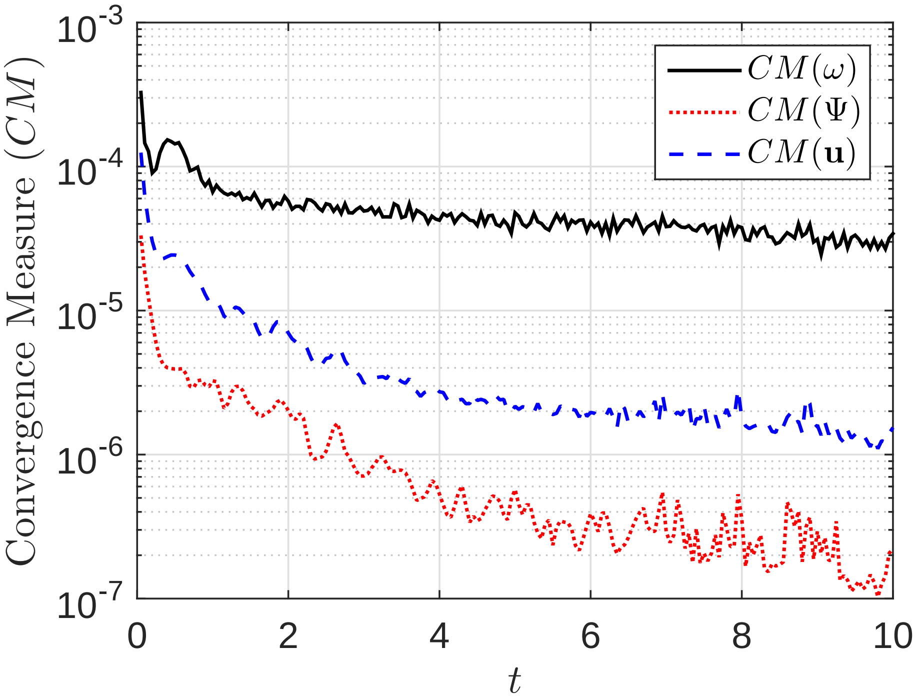

(a)

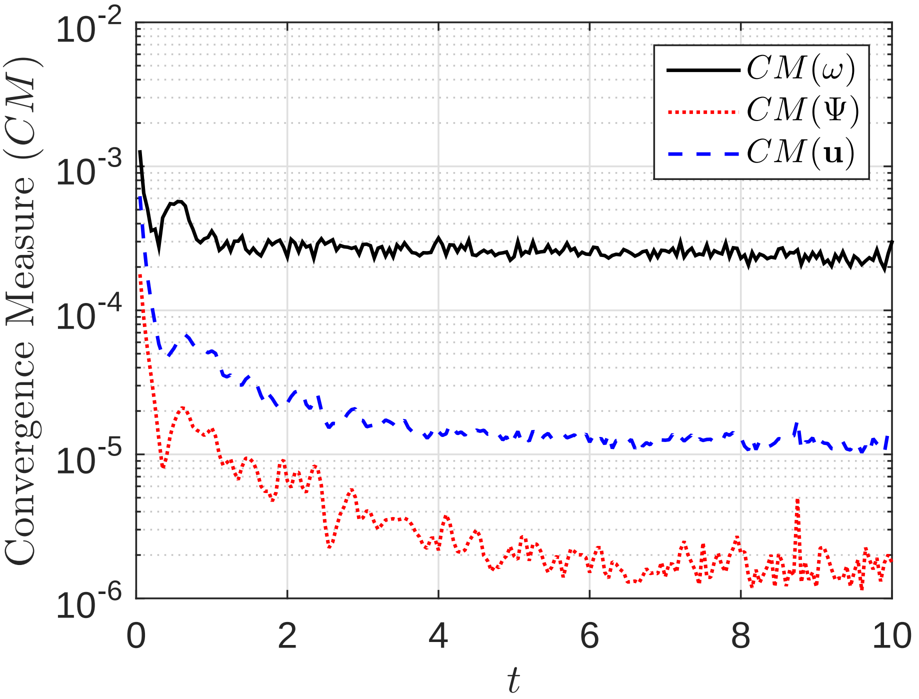

(b)

Figure 4.12: Fibre suspension flow between two parallel plates: the convergence measure for vorticity, stream function and velocity fields of flows with $k_f = 2$ (figure (a)) and $k_f = 10$ (figure (b)).

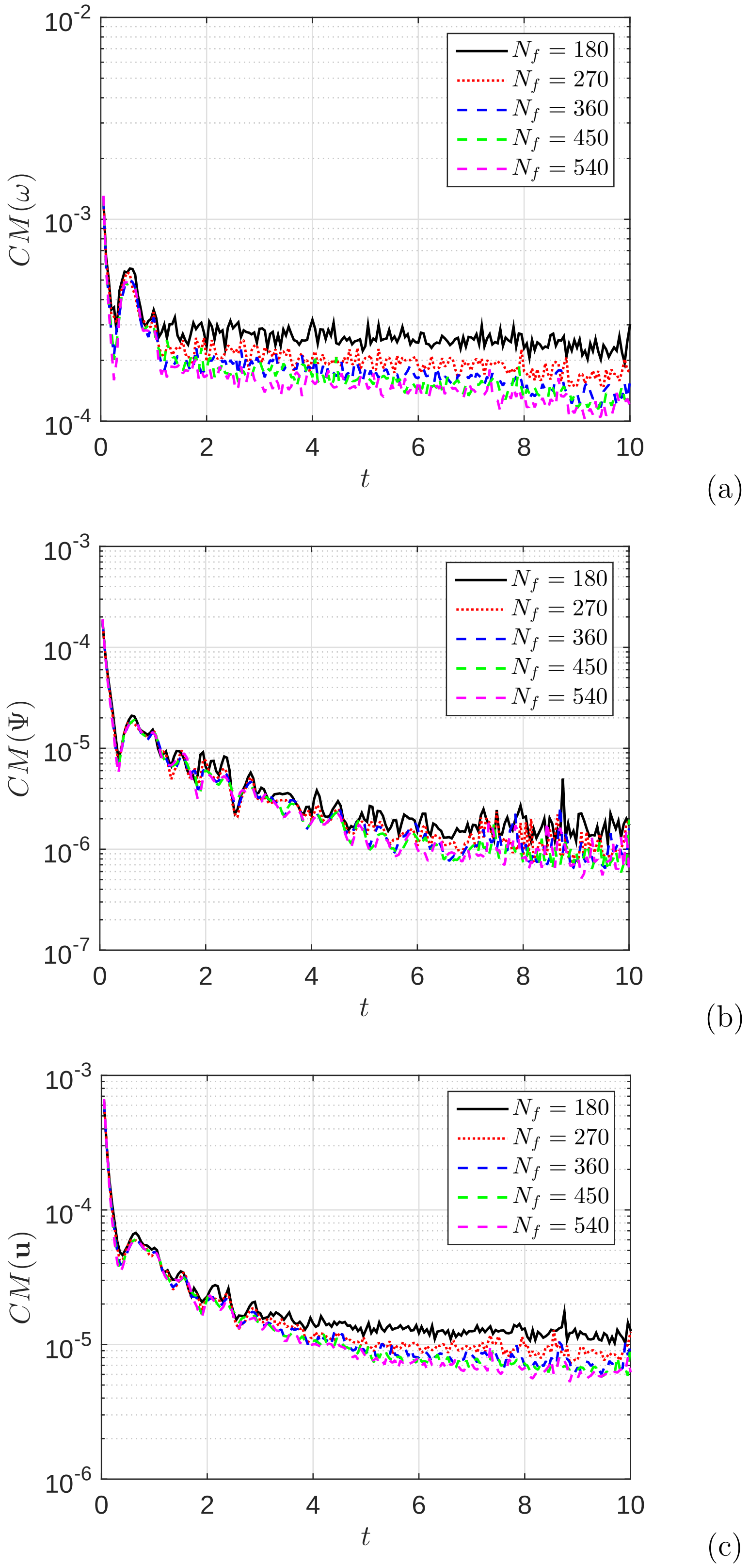

Figure 4.13: Fibre suspension flow between two parallel plates: the convergence measure for vorticity (figure (a)), stream function (figure (b)) and velocity field (figure (c)) of flows using several fibre configuration fields $N_f \in \{180, 270, 360, 450, 540\}$.

4.7.2 Flow through a circular tube

This problem is simulated using the same parameters as described in the fibre suspension flow between two parallel plates. The obtained results are compared with those for fibre suspension flow between two parallel plates. Furthermore, the velocity profile as well as the vorticity and stream function at the outlet will be used to determine several Dirichlet boundary conditions for the fibre suspension flow through an axisymmetric contraction presented in Section 4.7.3.

The flow through a circular tube is an axisymmetric problem, therefore, the investigated domain can be described in Fig. 4.14 where $L = 10$ is the length of the tube and $R = 0.5$ the tube's radius. The other parameters include the Reynolds number $Re = 10$, time step size $\Delta t = 1E{-}3$ and the number of fibre configuration fields $N_f = 180$.

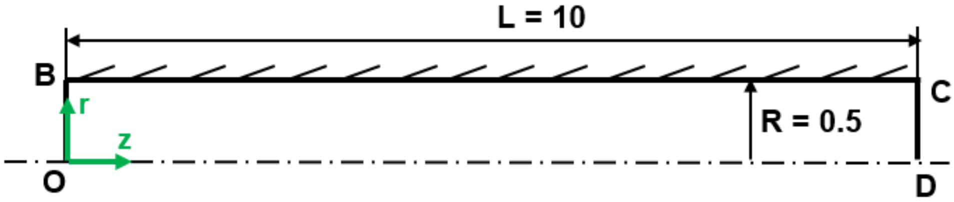

Figure 4.14: Fibre suspension flow through a circular tube: the geometry of the problem.

Governing equations and boundary conditions

The governing equations for this particular problem is obtained from sections 4.2 and 4.4 as follows.

$$\begin{aligned}
&\frac{\partial\omega}{\partial t}+u_z\frac{\partial\omega}{\partial z}+u_r\frac{\partial\omega}{\partial r}-\frac{u_r}{r}\omega-\frac{1}{Re}\eta_a\left(\frac{\partial^2\omega}{\partial z^2}+\frac{\partial^2\omega}{\partial r^2}\right)= \\
&-\frac{1}{Re}\left(\eta_a-1\right)\left(\frac{\partial^2\omega}{\partial z^2}+\frac{\partial^2\omega}{\partial r^2}\right)+\frac{1}{Re}\left(\frac{1}{r}\frac{\partial\omega}{\partial r}-\frac{1}{r^2}\omega\right)+ \\
&\frac{1}{2Re}\left(\frac{\partial^2\tau_f^{rz}}{\partial r^2}-\frac{\partial^2\tau_f^{zr}}{\partial z^2}+\frac{\partial^2\tau_f^{zz}}{\partial r\partial z}-\frac{\partial^2\tau_f^{rr}}{\partial z\partial r}+\frac{1}{r}\frac{\partial\tau_f^{rz}}{\partial r}-\frac{1}{r}\frac{\partial\tau_f^{rr}}{\partial z}-\frac{1}{r^2}\tau_f^{rz}\right),
\end{aligned} \tag{4.40}$$

$$\frac{1}{r}\frac{\partial^2\Psi}{\partial z^2}+\frac{1}{r}\frac{\partial^2\Psi}{\partial r^2}-\frac{1}{r^2}\frac{\partial\Psi}{\partial r}=2\omega, \tag{4.41}$$

$$u_z = \frac{1}{r}\frac{\partial \Psi}{\partial r}, \qquad u_r = -\frac{1}{r}\frac{\partial \Psi}{\partial z}, \tag{4.42}$$

$$\frac{\partial \mathbf{Q}}{\partial t} + \mathbf{u}\cdot\nabla\mathbf{Q} = (\nabla\mathbf{u})^T \cdot \mathbf{Q}, \tag{4.43}$$

$$\langle \mathbf{PPPP} \rangle = \left\langle \frac{\mathbf{Q}}{Q}\frac{\mathbf{Q}}{Q}\frac{\mathbf{Q}}{Q}\frac{\mathbf{Q}}{Q} \right\rangle, \tag{4.44}$$

$$\boldsymbol{\tau}_f = k_f \mathbf{D} : \langle \mathbf{PPPP} \rangle, \tag{4.45}$$

where the parameters in the system (4.40) - (4.45) were presented before. For the numerical stability of the present method, the vorticity transport equation (4.40) is developed using the DAVSS scheme as follows.

$$\begin{aligned}
\omega^{n+1} - \frac{\Delta t}{Re}\eta_a \left(\frac{\partial^2 \omega^{n+1}}{\partial z^2} + \frac{\partial^2 \omega^{n+1}}{\partial r^2} \right) &= \omega^n - \frac{\Delta t}{Re}(\eta_a - 1)\left(\frac{\partial^2 \omega^n}{\partial z^2} + \frac{\partial^2 \omega^n}{\partial r^2} \right) \\
&+ \frac{\Delta t}{Re}\left(\frac{1}{r}\frac{\partial \omega^n}{\partial r} - \frac{1}{r^2}\omega^n \right) - \Delta t u_z^n \frac{\partial \omega^n}{\partial z} - \Delta t u_r^n \frac{\partial \omega^n}{\partial r} + \Delta t \frac{u_r^n}{r}\omega^n \\
&+ \frac{\Delta t}{2Re}\left(\frac{\partial^2 (\tau_f^{rz})^n}{\partial r^2} - \frac{\partial^2 (\tau_f^{zr})^n}{\partial z^2} + \frac{\partial^2 (\tau_f^{zz})^n}{\partial r \partial z} - \frac{\partial^2 (\tau_f^{rr})^n}{\partial z \partial r} + \frac{1}{r}\frac{\partial (\tau_f^{rz})^n}{\partial r} \right. \\
&\qquad \left. - \frac{1}{r}\frac{\partial (\tau_f^{rr})^n}{\partial z} - \frac{1}{r^2}(\tau_f^{rz})^n \right),
\end{aligned} \tag{4.46}$$

Similar to the previous problem, the boundary conditions are given by

- At the inlet $\overline{OB}$:
  - A Newtonian parabolic velocity profile is applied, i.e. $u_z = u_{max}\left(1 - \left(\frac{r}{R}\right)^2\right)$ and $u_r = 0$, where $u_{max} = 1.5$ is the maximum value of the velocity profile;
  - For the fibre configuration field, a set of $N_f = 180$ fibres are generated and assigned at each collocation point on the inlet boundary. A fibre i is defined by the angle $\theta_i = -\frac{\pi}{2} + \frac{\pi(i-1)}{N_f}$, $\left(i = 1, ..., N_f\right)$;
- On the wall $\overline{BC}$:
  - No-slip boundary condition is used, i.e. $u_z = 0$ and $u_r = 0$;
  - For the fibre configuration, the co-linear alignment condition is imposed on the wall, i.e. $\theta_i = 0$;

- At the outlet $\overline{DC}$: A flow out condition is used, i.e. $\frac{\partial u_z}{\partial z} = 0$ and $u_r = 0$;
- On the centreline $\overline{OD}$: The symmetric boundary condition is imposed, i.e. $\frac{\partial u_z}{\partial r} = 0$ and $u_r = 0$.

Discretisation of governing equations

The temporal discretisation of the fibre configuration field $\mathbf{Q}$ is described in the axisymmetric cylindrical coordinates as follows.

$$Q_z^{n+1} = Q_z^n - \Delta t \left(u_z^n \frac{\partial Q_z^n}{\partial z} + u_r^n \frac{\partial Q_z^n}{\partial r} \right) + \Delta t \left(\frac{\partial u_z^n}{\partial z} Q_z^n + \frac{\partial u_z^n}{\partial r} Q_r^n \right), \tag{4.47}$$

$$Q_r^{n+1} = Q_r^n - \Delta t \left(u_z^n \frac{\partial Q_r^n}{\partial z} + u_r^n \frac{\partial Q_r^n}{\partial r} \right) + \Delta t \left(\frac{\partial u_r^n}{\partial z} Q_z^n + \frac{\partial u_r^n}{\partial r} Q_r^n \right), \tag{4.48}$$

where parameters were defined before. A non-uniform grid described in Fig. 4.15 is installed for the simulation with $\Delta z_1 = 0.05, \forall z \in [0, 9.9]$ and $\Delta z_2 = 0.01, \forall z \in [9.9, 10]$; $\Delta r_1 = 0.01, \forall r \in [0, 0.1]$; and $\Delta r_2 = 0.05, \forall r \in [0.1, 0.5]$. Experiences show that finer meshes near the outlet and the centreline are necessary for an accurate solution at these regions.

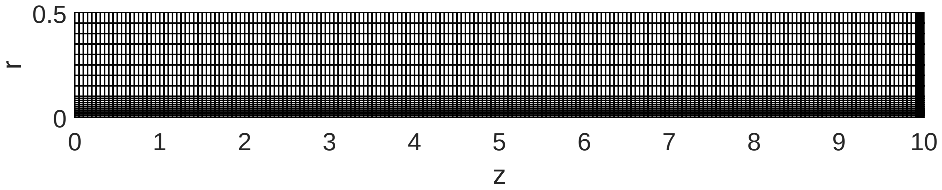

Figure 4.15: Fibre suspension flow through a circular tube: a non-uniform Cartesian grid for the problem.

Results and discussion

Fig. 4.16 depicts the velocity distribution of fibre suspension flows along the centreline of the tube for a range of fibre parameters $k_f \in \{2, 6, 10\}$. An undershoot is also observed in all cases of fibre parameter (solid lines) as in the flow between two parallel plates (dashed lines) but much stronger. Furthermore, the undershoot's positions are closer to the entrance than the ones in the flows between two parallel plates. The undershoot's feature is presented in detail in Table 4.3 for the fibre suspension flows between two parallel plates and a circular tube. The influence of the fibre parameter on the undershoot feature of velocity profiles for both fibre suspension flows is illustrated in Fig. 4.17.

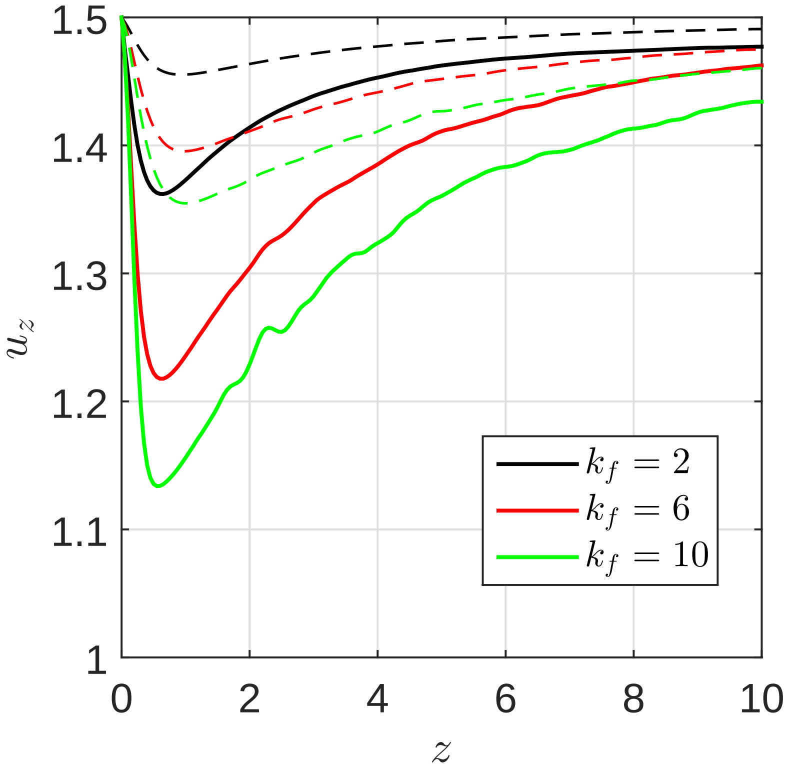

Figure 4.16: Fibre suspension flow through a circular tube: the centreline velocity profiles of flows with $k_f \in \{2, 6, 10\}$ (solid lines). The corresponding results for the fibre suspension flow between two parallel plates presented in Section 4.7.1 are also reproduced in dashed-line form for comparative purpose.

Table 4.3: Fibre suspension flow through a circular tube. Value and distance from the inlet boundary of undershoots appearing in the centreline velocity profiles with $k_f \in \{2, 6, 10\}$. Results for planar flows are included for comparative purpose.

	k_f	Undershoot value	Undershoot's position
Flow through a circular tube	2	1.362	$z = 0.65$
	6	1.2177	$z = 0.65$
	10	1.1338	$z = 0.55$
Flow between two parallel plates	2	1.4552	$x = 0.95$
	6	1.3954	$x = 0.95$
	10	1.3547	$x = 1$

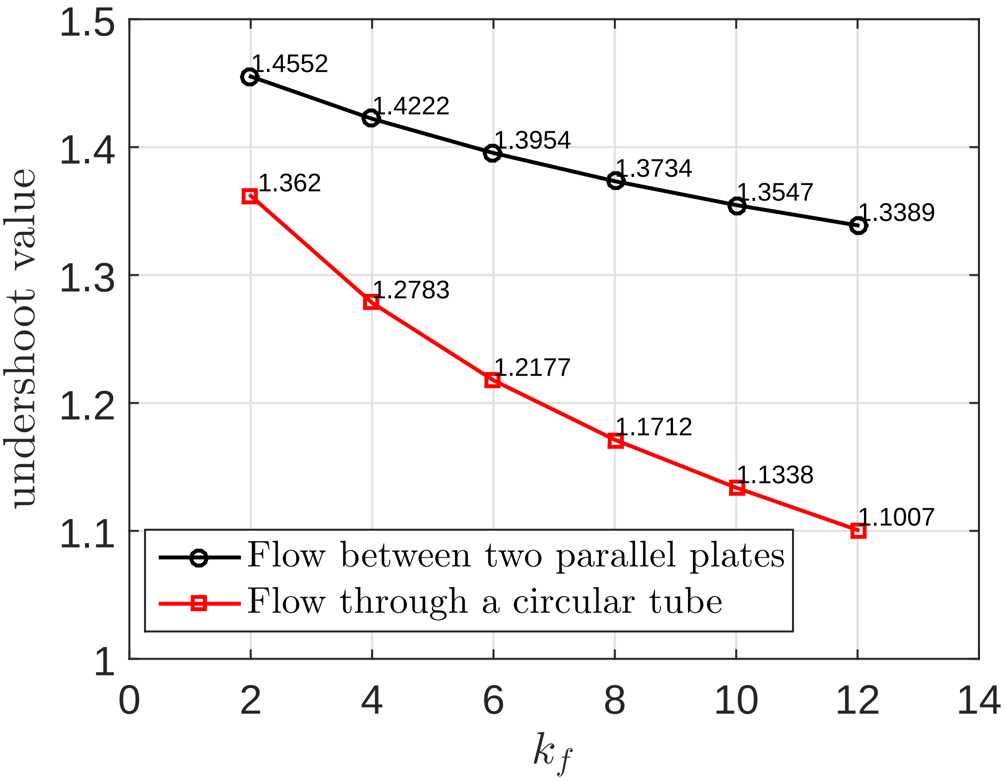

Figure 4.17: Fibre suspension flow through a circular tube: the undershoot value of the centreline velocity profiles for the fibre suspension flows with $k_f \in \{2, 4, 6, 8, 10, 12\}$. The corresponding results of the flow between two parallel plates are also presented here for comparative purpose.

Figs. 4.18 depict the shear stress and the first normal stress difference of the suspension flow through a circular tube with the fibre parameter $k_f = 10$. The distribution of shear stress presented in Fig. 4.18(a) shows that there is no significant difference in comparison with the one by the suspension flow between two parallel plates (Fig. 4.10(a)) . Furthermore, a maximum shear stress of 12 was also observed near the corner of the inlet and the wall boundaries. Meanwhile there is only a small difference in the first normal stress difference distribution between the two suspension flows: a distribution of the first normal stress difference $[-3, 13]$ (Fig. 4.18(b)) for the flow through a circular tube versus $[-2, 11]$ (Fig. 4.11(a)) for the flow between two parallel plates.

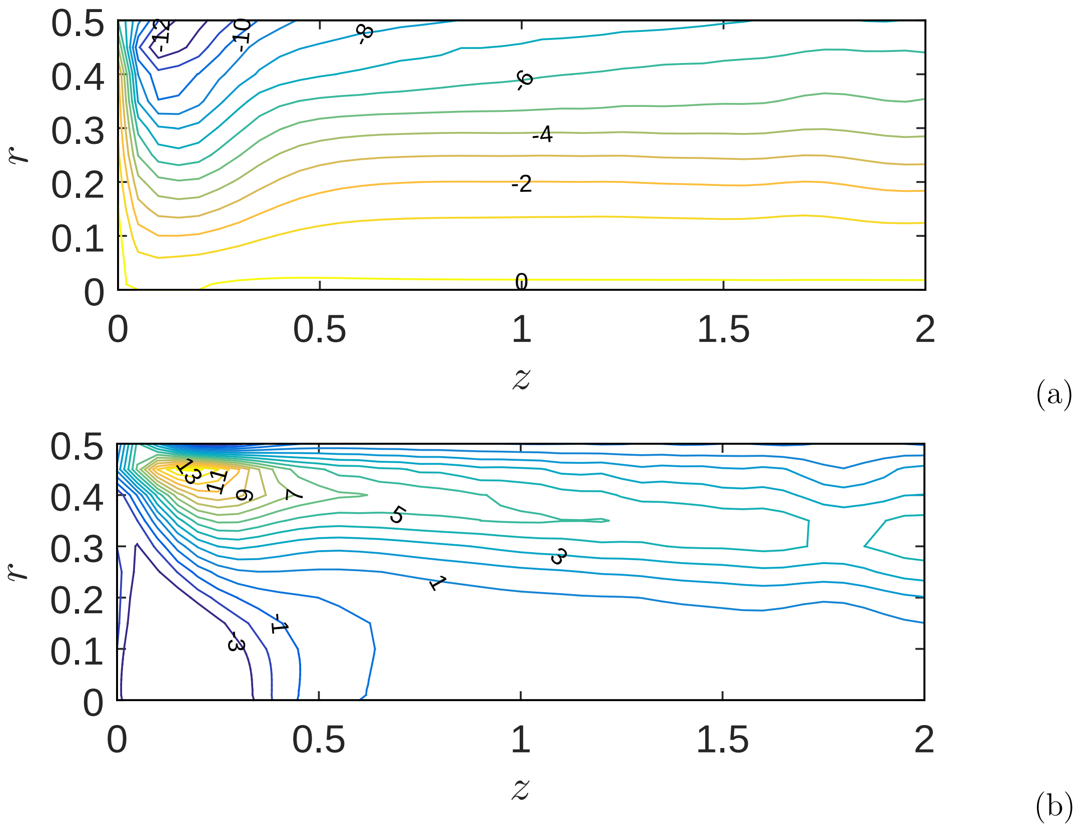

Figure 4.18: Fibre suspension flow through a circular tube: the distribution of shear stress (figure (a)) and the first normal stress difference (figure (b)) for the case of fibre parameter $k_f = 10$.

4.7.3 Flow through 4:1 and 4.5:1 axisymmetric contractions

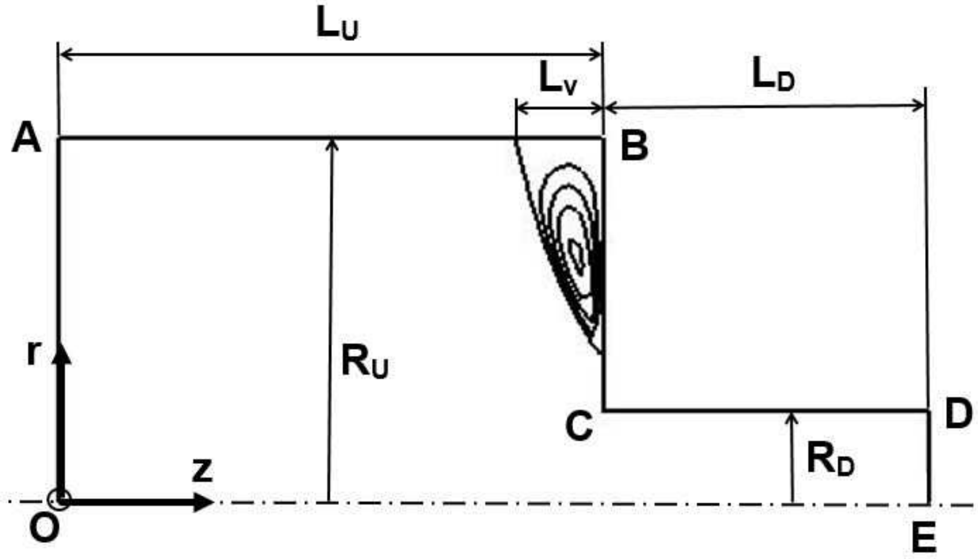

Figure 4.19: Fibre suspension flow through an axisymmetric contraction: A schematic geometry for the 4:1 and 4.5:1 axisymmetric contraction flows.

The geometry of the axisymmetric contraction problem presented in Fig. 4.19 was considered by Chiba et al. (1990) where $L_U = 5$ and $R_U = 1$ are the length and radius of the upstream tube; $L_D = 3$ and $R_D = 0.25$ the length and radius of the downstream tube and L_v the vortex length at the upstream corner. For the 4.5:1 contraction flow, the radius of the upstream tube is increased to $R_U = 1.125$ while the other geometry parameters are the same.

The contraction ratio β and the dimensionless vortex length L_v^* of the problem are defined, respectively, as follows.

$$\beta = \frac{R_U}{R_D}, \qquad L_v^* = \frac{L_v}{2R_U}. \tag{4.49}$$

A non-uniform grid used in the simulation is described in Fig. 4.20. A finer grid are generated to capture sufficiently the values of field variables in the contraction area where the variable gradients are very steep. Furthermore, the axial velocity in the area close to the centreline cannot be calculated using $u_z = \frac{1}{r}\frac{\partial \Psi}{\partial r}$ because of the singularity. In order to avoid this issue, u_z is approximated as $\lim_{r\to 0}\frac{1}{r}\frac{\partial \Psi}{\partial r} = \frac{\partial^2 \Psi}{\partial r^2}$ (L'Hospital rule) on the centreline. Therefore, a finer mesh is installed near the centreline. A detailed cartesian grid is generated as follows. $\Delta z_1 = 0.05, \forall z \in [4,6]$ and $\Delta z_2 = 0.1, \forall z < 4 \bigcup z > 6$; and $\Delta r_1 = 0.01, \forall r \in [0, 0.1]$ and $\Delta r_2 = 0.025, \forall r > 0.1$. The time step size is chosen as $5E{-}4$.

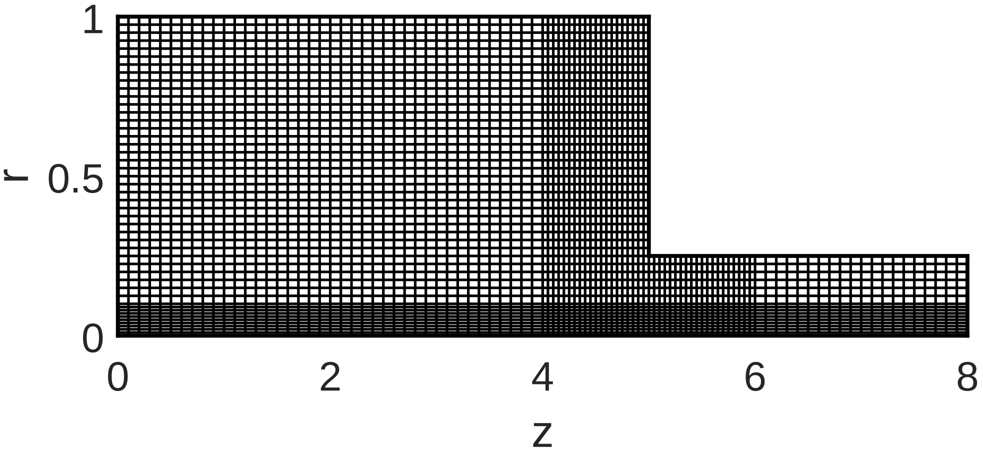

Figure 4.20: Fibre suspension flow through an axisymmetric contraction: a non-uniform Cartesian grid for the 4:1 axisymmetric contraction flow.

Governing equations and boundary conditions

The fibre suspension flow through an axisymmetric contraction is governed by Eqs. (4.40) - (4.48) with the following boundary conditions (see Fig. 4.19).

- At the inlet $\overline{OA}$: The velocity profile and the corresponding stream function and vorticity at the inlet are obtained from the solution of the fibre suspension flow through circular tube with the same parameters of the fluid as presented in Section 4.7.2 (We use a length to diameter ratio of 30 to obtain a fully developed velocity profile). Furthermore, $\frac{\partial \Psi}{\partial z} = 0$ is also imposed;
- At the outlet $\overline{DE}$: The flow-out boundary condition is defined by $\frac{\partial u_z}{\partial z} = 0$ and $u_r = 0$; $\frac{\partial \Psi}{\partial z} = 0$; and $\frac{\partial \omega}{\partial z} = 0$;
- On the walls $\overline{AB}$, $\overline{CD}$ and $\overline{BC}$: The non-slip boundary condition is imposed for the velocity: $u_z = 0$ and $u_r = 0$. Hence, the corresponding boundary conditions for the stream function and the vorticity on the walls are given as follows.

  - On the wall $\overline{AB}$: $\Psi = 0$, $\frac{\partial \Psi}{\partial r} = 0$; and $\omega = \omega_{w_1}$;
  - On the wall $\overline{CD}$: $\Psi = 0$, $\frac{\partial \Psi}{\partial r} = 0$; and $\omega = \omega_{w_3}$;
  - On the wall $\overline{BC}$: $\Psi = 0$, $\frac{\partial \Psi}{\partial z} = 0$; and $\omega = \omega_{w_2}$, where ω_{w_1}, ω_{w_2} and ω_{w_3} are determined and updated using Eq. (4.41) with the known stream function at each time step;

- On the centreline $\overline{OE}$:
  - The symmetric boundary condition of the velocity field is applied, i.e. $\frac{\partial u_z}{\partial r} = 0$ and $u_r = 0$;
  - The corresponding boundary conditions for the stream function and the vorticity are given by $\Psi = \Psi_c$, $\frac{\partial \Psi}{\partial r} = 0$; and $\omega = 0$, where Ψ_c is determined by Eq. (4.42) using the inlet boundary condition of the velocity.

Results and discussion

A range of fibre parameters and Reynolds numbers is used to simulate the two challenging 4:1 and 4.5:1 axisymmetric contraction flow problems by the present method. The number of fibre configuration fields used in all cases is $N_f = 1000$. Results obtained by the present method are in very good agreement with those of Chiba et al. (1990) or Lipscomb et al. (1988). Results are detailed and discussed as follows.

The 4:1 contraction flow is simulated with a range of fibre parameters $k_f \in \{0, 1, \ldots, 11, 12\}$ for $Re = 0$ (the creeping flow); $k_f \in \{0, 1, \ldots, 7, 8\}$ for $Re = 1$; and $k_f = 6$ for $Re = 2$ and $Re = 5$. Fig. 4.21 presents the effect of the fibre parameter (k_f) on the vortex length for the flows with $Re = 0$ and $Re = 1$. Results showed insignificant differences on the vortex length by the present method and the publication in Chiba et al. (1990). For example, for the creeping fibre suspension flow ($Re = 0$), while the vortex length is 0.170 by the experiment mentioned in (Chiba et al., 1990), it is approximately 0.160 and 0.175 by (Chiba et al., 1990) using the Finite Different Method and the present method, respectively. Furthermore, the vortex lengths by our present method are slightly higher for $k_f < 5$ but a bit lower for $k_f > 5$ than those of Chiba et al. (1990) for creeping fibre suspension flows, whereas the obtained results by the present work and from Chiba et al. (1990) are nearly the same for the flows with $Re = 1$.

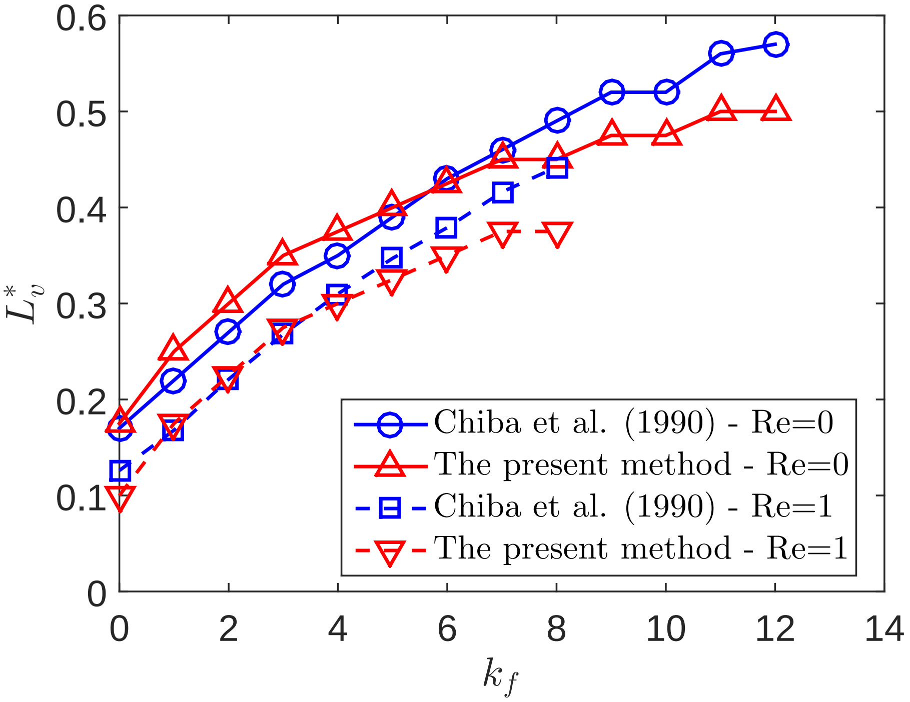

Figure 4.21: The axisymmetric 4:1 contraction flows of fibre suspensions: the effect of the fibre parameter on the vortex length (L_v^*) with a range of $k_f \in \{0, 1, \ldots, 11, 12\}$ for the flows with $Re = 0$ and $k_f \in \{0, 1, \ldots, 7, 8\}$ for the flows with $Re = 1$.

Effect of the fibre suspension on the development of the salient corner vortex is clearly reflected in Fig. 4.22. As compared with the Newtonian fluid flow ($k_f = 0$ - Fig. 4.22(a)) the size of the salient corner vortex of fibre suspension flows gradually grows with increasing fibre parameter. Furthermore, due to the impact by the growing vortex, the gradient of streamlines close to the contraction area reduces with increasing fibre parameter. Results shown in Figs. 4.22 by the present work are in very good agreement with those of Chiba et al. (1990). However, a minor difference has been found in our present work in comparison with others (Chiba et al., 1990; Lipscomb et al., 1988; Lu et al., 2006) in the form of a small secondary vortex at the upstream corner of the contraction as shown in Figs. 4.22. This result may indicate that the present method is capable of capturing such fine details.

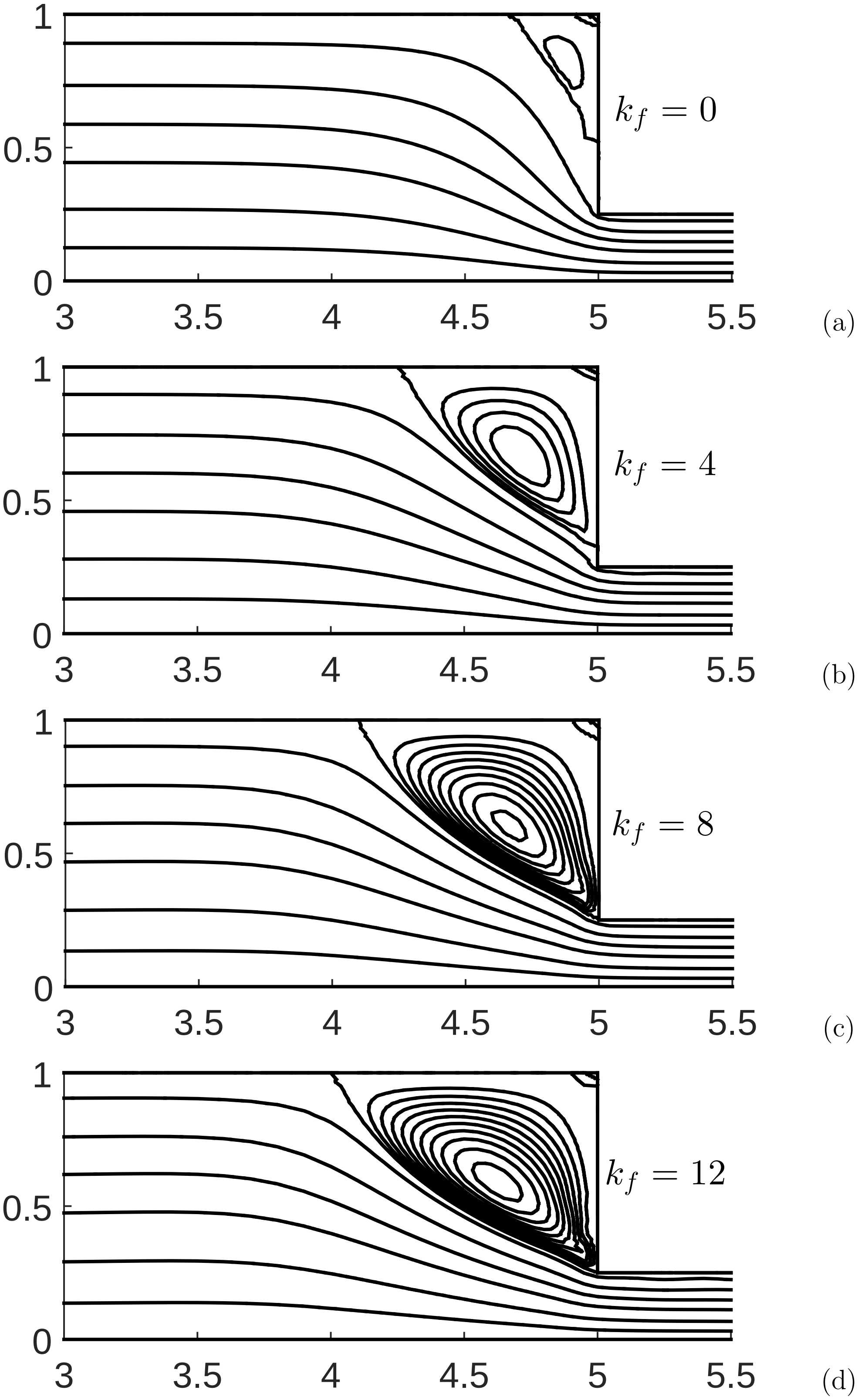

Figure 4.22: The axisymmetric 4:1 contraction flows of fibre suspensions: the effect of the fibre parameter on the streamlines and the vortex of the velocity field for the flows with $Re = 0$ and a range of $k_f \in \{0, 4, 8, 12\}$.

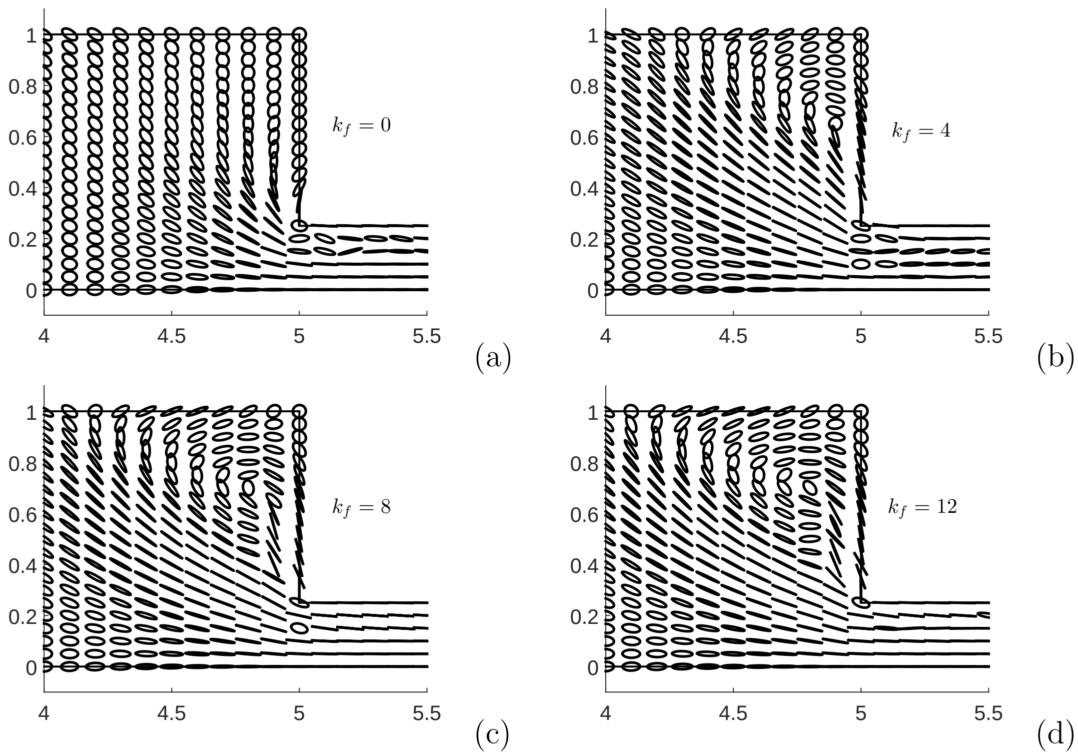

Figure 4.23: The axisymmetric 4:1 contraction flows of fibre suspensions: the distribution of the fibres' orientation around the contraction area for the flows with $Re = 0$ and a range of $k_f \in \{0, 4, 8, 12\}$.

Figs. 4.23 depict the effect of the fibre parameter on the fibres orientation around the contraction area. It can be recognised that fibres tend to align with the flow direction when approaching the contraction region. The fibres are mostly parallel with the flow direction in the downstream due to the impact of the elongation of the fluid. This tendency is more pronounced with increasing fibre parameter.

The effect of Reynolds number on the contraction flow of fibre suspensions was also investigated and presented in Figs. 4.24 with a range of $Re \in \{0, 1, 2, 5\}$ with $k_f = 6$. In contrast to the effect of the fibre parameter (Figs. 4.22), the salient corner vortex diminishes in size as the Reynolds number increases as stated and explained by Chiba et al. (1990).

Fig. 4.25 describes the axial velocity profile along the centreline of fibre suspension flows with a range of $k_f \in \{0, 4, 8, 12\}$ and $Re = 0$. Unlike the case of a viscoelastic fluid, where an overshoot of the velocity profile on the centreline appears near the contraction area (Marchal and Crochet, 1987), it was not observed

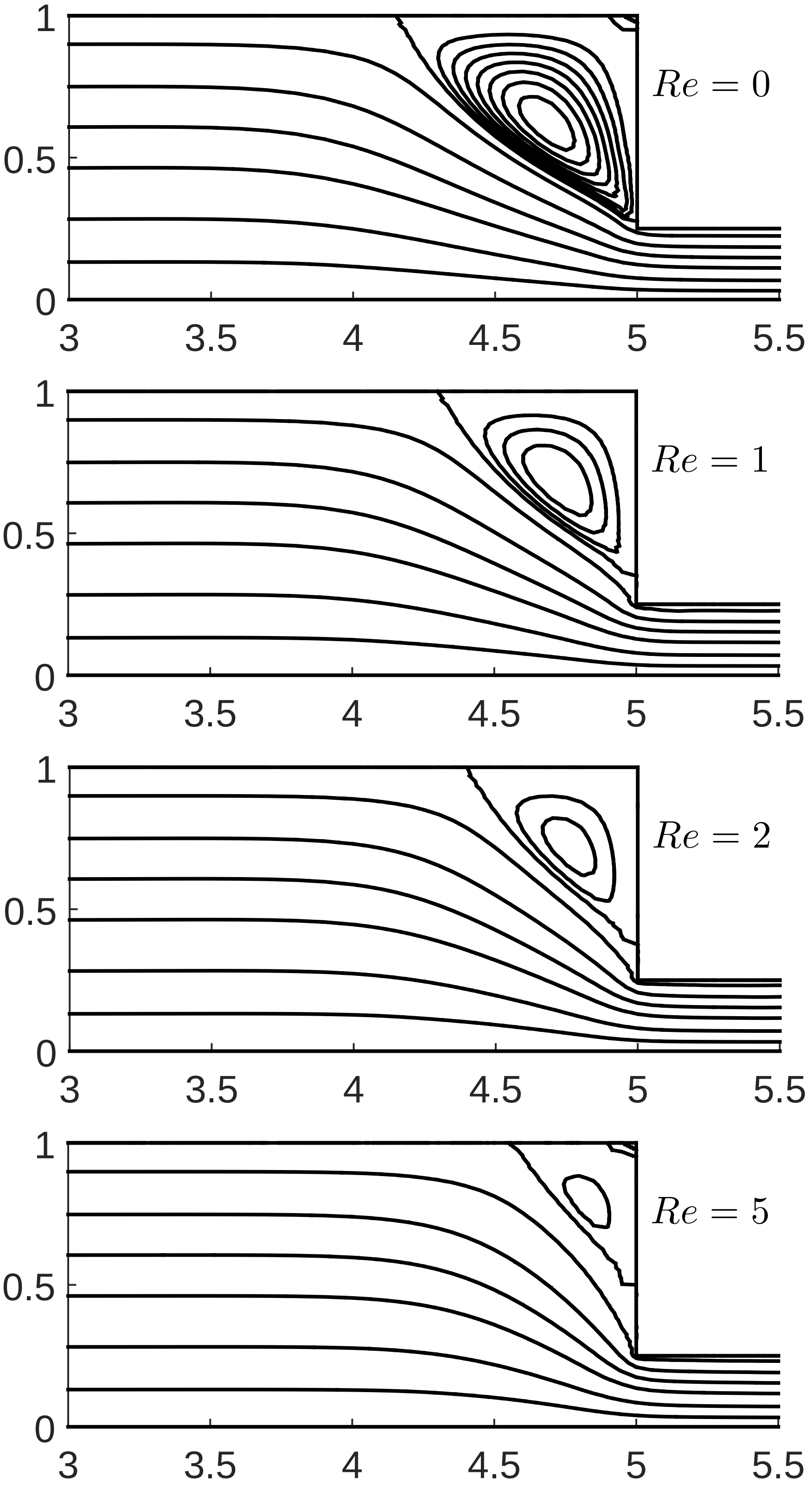

(a)

(b)

(c)

(d)

Figure 4.24: The axisymmetric 4:1 contraction flows of fibre suspensions: the effect of Reynolds number on the streamlines and vortices of the velocity field for a range of $Re \in \{0, 1, 2, 5\}$ and $k_f = 6$.

in the fibre suspension flows. This result was previously confirmed by Chiba et al. (1990); Baloch and Webster (1995). Furthermore, results presented in Fig. 4.25 showed that the axial velocity at the far upstream and far downstream of the flow does not significantly change with the fibre parameter while the velocity gradient increases, with the decrease of the fibre parameter, around the contraction region (Fig. 4.26). This increment of the velocity gradient reaches a maximum peak value (65) with the case of Newtonian fluid ($k_f = 0$).

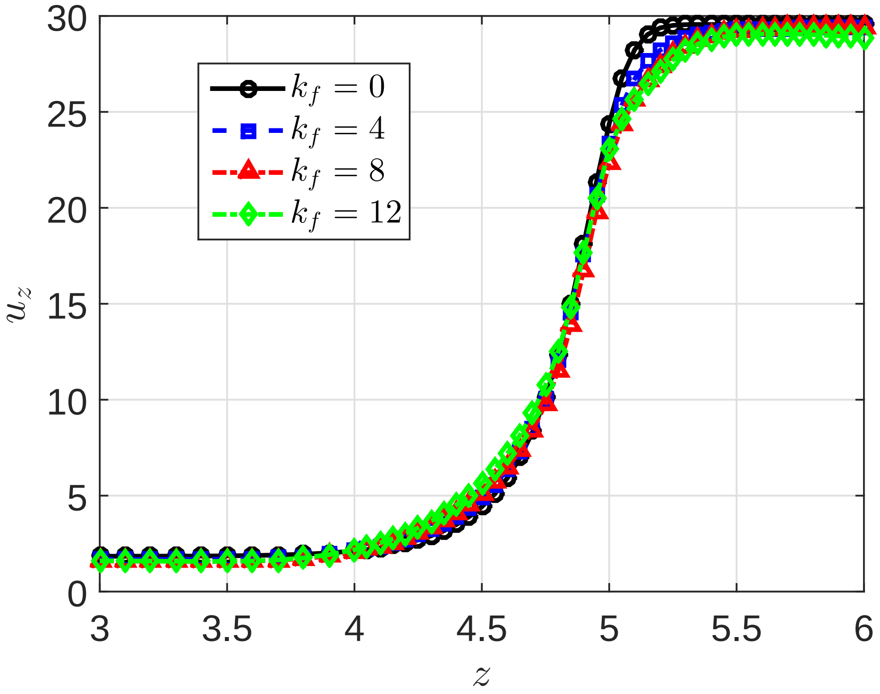

Figure 4.25: The axisymmetric 4:1 contraction flows of fibre suspensions: The axial velocity profile on the centreline for a range of $k_f \in \{0, 4, 8, 12\}$ and $Re = 0$.

The first normal stress difference ($\tau_e^{zz} - \tau_e^{rr}$) of the fibre suspension flow on the centreline is finally determined by the following expression of Chiba et al. (1990)

$$\tau_e^{zz} - \tau_e^{rr} = 2(\frac{\partial u_z}{\partial z} - \frac{\partial u_r}{\partial r}) + k_f \frac{\partial u_z}{\partial z}, \tag{4.50}$$

where the first and second terms on the right-hand side are the Newtonian solvent contribution and the fibre stress contribution to the first normal stress difference of the fibre suspension flow, respectively. Fig. 4.27 depicts the first normal stress difference which gradually increases and reaches a peak value at the position just before the contraction region of the upstream. Furthermore, the first normal

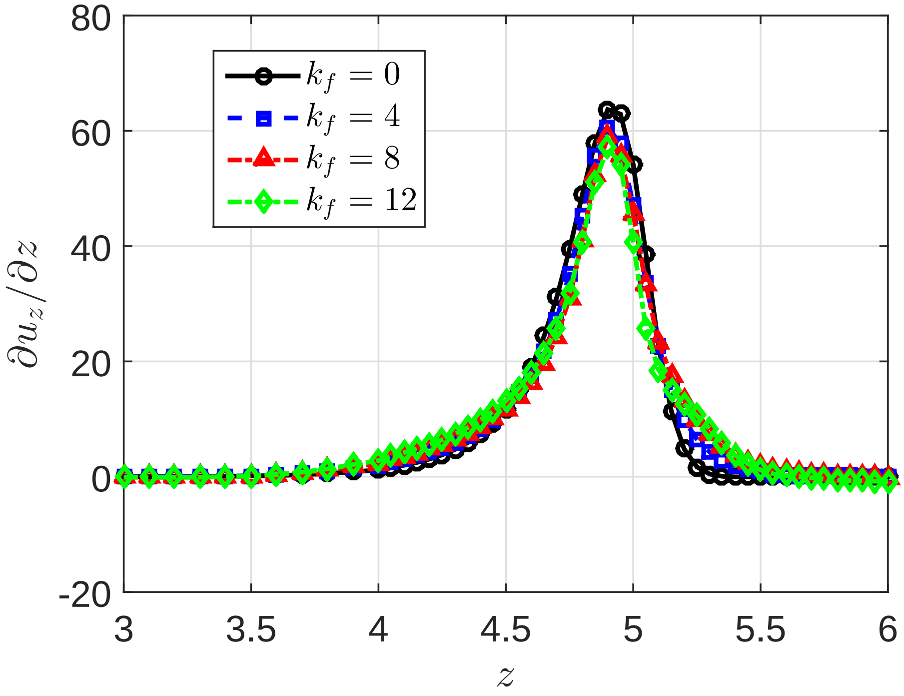

Figure 4.26: The axisymmetric 4:1 contraction flows of fibre suspensions: The velocity gradient profile on the centreline for a range of $k_f \in \{0, 4, 8, 12\}$ and $Re = 0$.

stress difference together with its peak value increase with increasing fibre parameter. In other words, the first normal stress difference along the centreline is smallest for the Newtonian fluid where fibre stress contribution is non-existent (black line, Fig. 4.27).

Finally, the 4.5:1 contraction flow of fibre suspensions is simulated with range of $k_f \in \{0, 1, \ldots, 7, 8\}$ and $Re = 0$. The problem was previously investigated by both experiment and the finite element method in Lipscomb et al. (1988). Fig. 4.28 describes the effect of the fibre parameter on the length of the vortex at the contraction corner. The figure shows that the results by the present method are comparable with the experimental ones and in very good agreement with the numerical ones presented by Lipscomb et al. (1988).

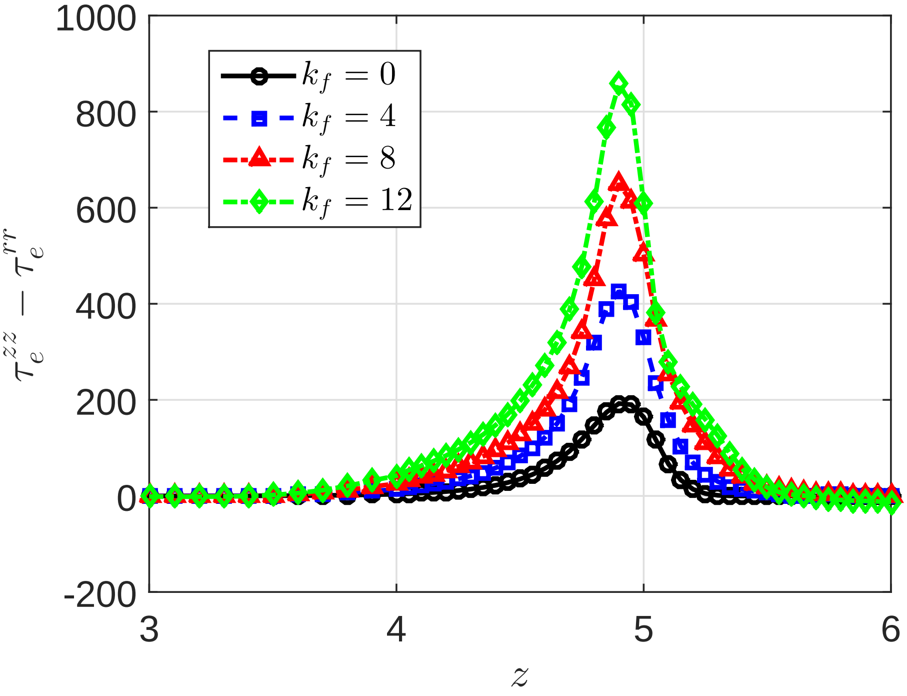

Figure 4.27: The axisymmetric 4:1 contraction flows of fibre suspensions: The first normal stress difference on the centreline for a range of $k_f \in \{0, 4, 8, 12\}$ and $Re = 0$.

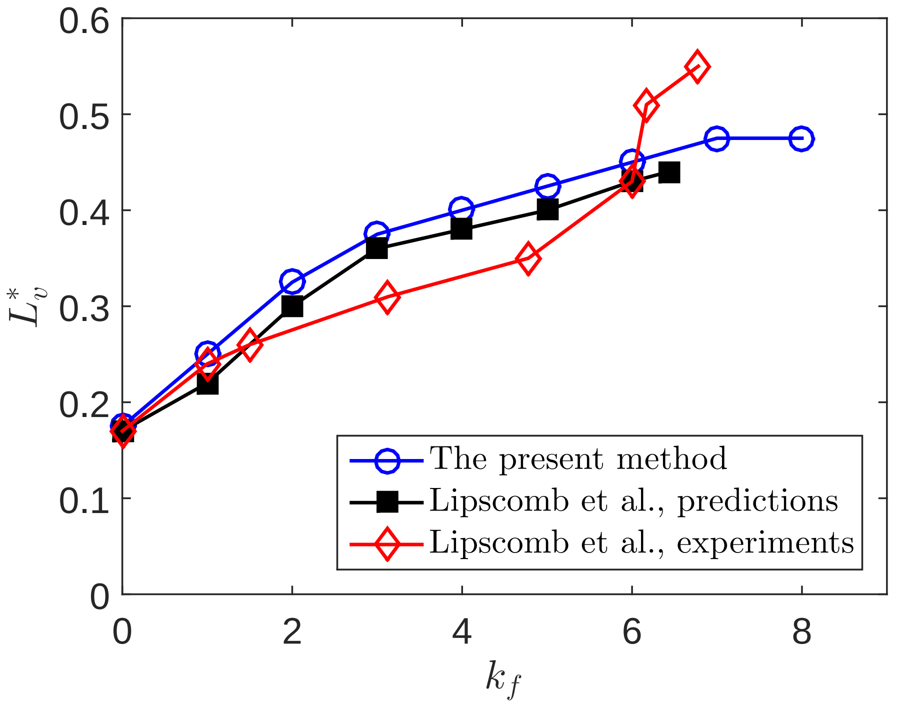

Figure 4.28: The axisymmetric 4.5:1 contraction flows of fibre suspensions: the effect of the fibre parameter on the vortex length (L_v^*) for a range of $k_f \in \{0, 1, \ldots, 7, 8\}$ and $Re = 0$.

4.8 Conclusions

This chapter reports the use of a multiscale method based on the fibre configuration field, the 1D-IRBF scheme and the DAVSS technique to simulate dilute fibre suspension flows. In this new approach, at each time step, the governing differential equations, including the stream function and vorticity transport equations, are spatially discretised using the 1D-IRBF method. Meanwhile, the evolution of fibre configurations governed by Jeffery equation is approximated using the BCF principle. The two scales are linked together by the Lipscomb's model, which is applied to calculate the fibre stress tensor for dilute suspensions. In addition, the adoption of the DAVSS enhances the numerical stability of the 1D-IRBF based scheme in simulating fibre suspension flow problems. As a result, the efficiency of the present approach is significantly increased as stated in Section 4.7. Indeed, the obtained results of the simulation of fibre suspension flows through the challenging 4:1 and 4.5:1 axisymmetric contraction geometries may indicate that the present approach is capable of capturing such fine details as secondary vortices in the corners. An extension of the method for simulations of non-dilute fibre suspensions will be presented in the next chapter.

Chapter 5

Stochastic multiscale simulation of non-dilute fibre suspensions

The multiscale simulation method based on the combination of the Brownian configuration field (BCF), the integrated radial basis function (IRBF) approximation and the discrete adaptive viscoelastic stress splitting (DAVSS) for dilute fibre suspensions reported in Chapter 4 (Nguyen et al., 2015a), is further developed to simulate non-dilute fibre suspension flows. The macro and micro processes are serially proceeded at each time step and then linked together via a fibre-contributed stress formula associated with the kinetic model used. Since the interaction between fibres in non-dilute fibre suspensions is significant, this random interaction is introduced into the evolution equation for the determination of fibre configurations (Folgar and Tucker, 1984) by the BCF method. The fibre stresses are then determined based on the fibre configuration fields using the Phan-Thien–Graham model (Phan-Thien and Graham, 1991). The efficiency of the simulation method is demonstrated with the analysis of the circular Poiseuille flow and the challenging axisymmetric contraction and expansion flows, for a range of fibre concentration from semi-dilute to concentrated regimes.

5.1 Introduction

Generally, fibre suspension flows can be classified into dilute, semi-dilute and concentrated regimes based on two basic parameters: the volume fraction ϕ and the aspect ratio a_r. Specifically, a suspension flow is considered as dilute, semi-dilute or concentrated for the cases of $\phi a_r^2 < 1$, $1 \leq \phi a_r^2 < a_r$ or $\phi a_r^2 \geq a_r$, respectively. For dilute suspension flows, the interaction between fibres can be neglected and the evolution of fibres can be captured by the Jeffery equation (Jeffery, 1922). For the semi-dilute and concentrated suspensions, the physical description of the flow and the evolution of fibre configurations poses a challenge due to the necessity to take into account fibre-fibre interactions. In this work, we modify the high-order IRBF-BCF based stochastic multiscale method described in Chapter 4 (Nguyen et al., 2015a) for dilute suspensions by introducing a diffusion term into the Jeffery equation (Folgar and Tucker, 1984) to obtain the Folgar-Tucker equation for capturing fibre-fibre interaction in non-dilute suspensions. The high-order IRBF scheme is employed to discretise the conservation equations whereas the fibre configurations governed by the Folgar-Tucker equation are advanced using the BCF approach. The two macro-micro processes are coupled using the Phan-Thien–Graham model (Phan-Thien and Graham, 1991) for the fibre stress.

The chapter is organised as follows. The governing equations in the dimensionless form are presented in Section 5.2. Section 5.3 presents macro-micro equations including an introduction of the DAVSS technique into the conservation equations. A coupled macro-micro system of governing equations is presented in Section 5.4, followed by a short review of the present numerical method together with its algorithm. Numerical examples and obtained results are discussed in Section 5.5. Finally, the work is closed by concluding remarks in Section 5.6.

5.2 Governing equations for semi-dilute and concentrated suspension flows

The dimensionless conservation equations for a flow of fibre suspensions is given by (Lu et al., 2006)

$$\nabla \cdot \mathbf{u} = 0, \tag{5.1}$$

$$\frac{\partial \mathbf{u}}{\partial t} + \mathbf{u} \cdot \nabla \mathbf{u} = -\nabla p + \frac{1}{Re} \nabla \cdot \left(\boldsymbol{\tau}_s + \boldsymbol{\tau}_f \right), \tag{5.2}$$

where t, $\mathbf{u}$ and p are the time, velocity and pressure, respectively; $Re = \rho UL/\eta_0$ the Reynolds number where ρ is the fluid density, η_0 the Newtonian solvent viscosity, and U and L the characteristic velocity and length, respectively; $\boldsymbol{\tau}_s = 2\mathbf{D}$ the stress contribution of the Newtonian solvent, $\mathbf{D} = \frac{1}{2}\left(\nabla \mathbf{u} + (\nabla \mathbf{u})^T\right)$ the rate of strain tensor; and $\boldsymbol{\tau}_f$ the stress component contributed by the suspended fibres.

In the present work, the fibre stress $\boldsymbol{\tau}_f$ for semi-dilute and concentrated suspensions is determined using the modified Phan-Thien–Graham model as follows (Fan et al., 1999; Phan-Thien and Graham, 1991).

$$\boldsymbol{\tau}_f = f(\phi) \left(A\mathbf{D} : \langle \mathbf{PPPP} \rangle + 2D_r F \langle \mathbf{PP} \rangle \right), \tag{5.3}$$

where $\mathbf{P}$ is the unit direction vector of fibres; $\langle \mathbf{PP} \rangle$ and $\langle \mathbf{PPPP} \rangle$ the second- and the fourth-order orientation tensors, respectively; $\big\langle (*) \big\rangle$ the statistical average of $(*)$; and D_r the diffusion coefficient. $f(\phi)$, A and F are the fluid parameters which are defined as functions of the volume fraction ϕ and the aspect ratio a_r of the suspended fibres as follows (Fan et al., 1999).

$$f(\phi) = \frac{\phi \left(2 - \phi/\phi_m\right)}{2\left(1 - \phi/\phi_m\right)^2}, \qquad A = \frac{a_r^2}{\ln 2a_r - 1.5}, \qquad F = \frac{3a_r^2}{\ln 2a_r - 0.5}, \tag{5.4}$$

where ϕ_m is the maximum volume packing and empirically determined as a linear function of the aspect ratio by Kitano et al. (1981) as

$$\phi_m = 0.53 - 0.013a_r, \qquad 5 < a_r < 30. \tag{5.5}$$

The evolution of fibres' orientation in non-dilute suspensions is captured by the Folgar-Tucker equation as follows (Folgar and Tucker, 1984).

$$\frac{D\mathbf{P}}{Dt} = \boldsymbol{L} \cdot \mathbf{P} - \boldsymbol{L} : \mathbf{PPP} + (\mathbf{I} - \mathbf{PP}) \cdot \mathbf{F}^{(b)}(t), \tag{5.6}$$

where $\frac{D}{Dt}(\cdot)$ is the material time derivative of $(\cdot)$; and $\mathbf{I}$ the identity tensor. $\boldsymbol{L}$ is the effective velocity gradient tensor and given by

$$\boldsymbol{L} = (\nabla\mathbf{u})^T - \zeta\mathbf{D} \qquad \text{with} \qquad \zeta = \frac{2}{a_r^2 + 1}. \tag{5.7}$$

It should be noted that the fibres' interaction is considered as random collisions by the Brownian force $\mathbf{F}^{(b)}(t)$ with the properties:

$$\langle \mathbf{F}^{(b)}(t) \rangle = 0,$$

$$\langle \mathbf{F}^{(b)}(t+s)\, \mathbf{F}^{(b)}(t) \rangle = 2D_r\delta(s)\mathbf{I},$$

where $\delta(s)$ is the Dirac delta function; $D_r = C_i\dot{\gamma}$ the diffusion coefficient (Folgar and Tucker, 1984), $\dot{\gamma} = \sqrt{2(\mathbf{D} : \mathbf{D})}$ the general strain rate; and C_i the interaction coefficient. In this research, for simplicity, C_i is chosen as a constant as done in Fan et al. (1999); Lu et al. (2006).

By introducing $\mathbf{Q}(\mathbf{x}, t) = Q\mathbf{P}(\mathbf{x}, t)$, Eq. (5.6) is transformed into (Phan-Thien and Fan, 1999)

$$\frac{\partial\mathbf{Q}}{\partial t} + \mathbf{u} \cdot \nabla\mathbf{Q} = \boldsymbol{L} \cdot \mathbf{Q} + Q\mathbf{F}^{(b)}(t), \tag{5.8}$$

where Q is the modulus of $\mathbf{Q}$ and the Brownian force can be written in relation to the Wiener process $\mathbf{W}$ as follows.

$$\mathbf{F}^{(b)}(t) = \sqrt{2C_i\dot{\gamma}}\frac{d\mathbf{W}}{dt}. \tag{5.9}$$

Substituting Eq. (5.9) into Eq. (5.8) yields

$$\frac{\partial \mathbf{Q}}{\partial t} + \mathbf{u} \cdot \nabla \mathbf{Q} = \boldsymbol{L} \cdot \mathbf{Q} + \sqrt{2C_i \dot{\gamma}} Q \frac{d\mathbf{W}}{dt}. \tag{5.10}$$

The second- and fourth-order orientation tensors, $\langle \mathbf{PP} \rangle$ and $\langle \mathbf{PPPP} \rangle$, can now be defined by

$$\langle \mathbf{PP} \rangle = \frac{1}{N_f} \sum_{i=1}^{N_f} \frac{\mathbf{Q}_i}{Q_i} \frac{\mathbf{Q}_i}{Q_i}, \tag{5.11}$$

$$\langle \mathbf{PPPP} \rangle = \frac{1}{N_f} \sum_{i=1}^{N_f} \frac{\mathbf{Q}_i}{Q_i} \frac{\mathbf{Q}_i}{Q_i} \frac{\mathbf{Q}_i}{Q_i} \frac{\mathbf{Q}_i}{Q_i}, \tag{5.12}$$

where N_f is the number of fibre configuration fields.

5.3 Macro-micro governing equations in the cylindrical coordinates (r, z)

5.3.1 Axisymmetric vorticity-stream function formulation with DAVSS technique

For 2-D problems considered in this chapter, the axisymmetric vorticity-stream function formulation in the cylindrical coordinates (r, z) is used for several numerical benefits: (i) the pressure disappears in the equation of motion; and (ii) the continuity equation is automatically satisfied. The relations between velocity (u_r, u_z), vorticity ω, and stream function Ψ are given by

$$\omega = \frac{1}{2}\left(\frac{\partial u_z}{\partial r} - \frac{\partial u_r}{\partial z} \right), \tag{5.13}$$

$$u_z = \frac{1}{r}\frac{\partial \Psi}{\partial r}, \qquad u_r = -\frac{1}{r}\frac{\partial \Psi}{\partial z}. \tag{5.14}$$

After some mathematical manipulations, the stream function and vorticity transport equations can be derived from Eqs. (5.1)-(5.2) as follows.

$$\frac{1}{r}\frac{\partial^2\Psi}{\partial z^2}+\frac{1}{r}\frac{\partial^2\Psi}{\partial r^2}-\frac{1}{r^2}\frac{\partial\Psi}{\partial r}=2\omega. \tag{5.15}$$

$$\begin{aligned}Re\left(\frac{\partial\omega}{\partial t}+u_z\frac{\partial\omega}{\partial z}+u_r\frac{\partial\omega}{\partial r}-\frac{u_r}{r}\omega\right)&=\left(\frac{\partial^2\omega}{\partial z^2}+\frac{\partial^2\omega}{\partial r^2}+\frac{1}{r}\frac{\partial\omega}{\partial r}-\frac{1}{r^2}\omega\right)+\\ \frac{1}{2}\left(\frac{\partial^2\tau_f^{rz}}{\partial r^2}-\frac{\partial^2\tau_f^{zr}}{\partial z^2}+\frac{\partial^2\tau_f^{zz}}{\partial r\partial z}-\frac{\partial^2\tau_f^{rr}}{\partial z\partial r}+\frac{1}{r}\frac{\partial\tau_f^{rz}}{\partial r}-\frac{1}{r}\frac{\partial\tau_f^{rr}}{\partial z}-\frac{1}{r^2}\tau_f^{rz}\right),\end{aligned} \tag{5.16}$$

where τ_f^{zz}, τ_f^{zr}, τ_f^{rz} and τ_f^{rr} are the components of the fibre stress tensor $\boldsymbol{\tau}_f$.

The introduction of the DAVSS technique into Eq. (5.16) yields (Nguyen et al., 2015a)

$$\begin{aligned}Re\left(\frac{\partial\omega}{\partial t}+u_z\frac{\partial\omega}{\partial z}+u_r\frac{\partial\omega}{\partial r}-\frac{u_r}{r}\omega\right)-\eta_a\left(\frac{\partial^2\omega}{\partial z^2}+\frac{\partial^2\omega}{\partial r^2}\right)&=\\ -(\eta_a-1)\left(\frac{\partial^2\omega}{\partial z^2}+\frac{\partial^2\omega}{\partial r^2}\right)+\left(\frac{1}{r}\frac{\partial\omega}{\partial r}-\frac{1}{r^2}\omega\right)&\\ +\frac{1}{2}\left(\frac{\partial^2\tau_f^{rz}}{\partial r^2}-\frac{\partial^2\tau_f^{zr}}{\partial z^2}+\frac{\partial^2\tau_f^{zz}}{\partial r\partial z}-\frac{\partial^2\tau_f^{rr}}{\partial z\partial r}+\frac{1}{r}\frac{\partial\tau_f^{rz}}{\partial r}-\frac{1}{r}\frac{\partial\tau_f^{rr}}{\partial z}-\frac{1}{r^2}\tau_f^{rz}\right),&\end{aligned} \tag{5.17}$$

where η_a is the adaptive viscosity and defined by (Lu et al., 2006)

$$\eta_a=Af(\phi)+\frac{1+\sqrt{(1/2)\boldsymbol{\tau}_f:\boldsymbol{\tau}_f}}{1+\sqrt{(1/2)\mathbf{G}:\mathbf{G}}}, \tag{5.18}$$

where $\mathbf{G}=\nabla\mathbf{u}+(\nabla\mathbf{u})^T$ is twice the strain rate tensor.

5.3.2 Evolution equation for fibre configurations in 2-D axisymmetric coordinates

The effective velocity gradient $\boldsymbol{L}$ is developed in 2-D axisymmetric coordinate (z, r) as follows.

$$\mathbf{L}=\begin{bmatrix}(1-\zeta)\frac{\partial u_z}{\partial z} & \frac{\partial u_z}{\partial r}-\frac{\zeta}{2}(\frac{\partial u_z}{\partial r}+\frac{\partial u_r}{\partial z})\\ \frac{\partial u_r}{\partial z}-\frac{\zeta}{2}(\frac{\partial u_z}{\partial r}+\frac{\partial u_r}{\partial z}) & (1-\zeta)\frac{\partial u_r}{\partial r}\end{bmatrix} \tag{5.19}$$

With the use of Eq. (5.19), the evolution equation (5.10) is expressed in z- and r-directions as

$$\begin{split}\frac{\partial Q_z}{\partial t} + u_z \frac{\partial Q_z}{\partial z} + u_r \frac{\partial Q_z}{\partial r} = (1-\zeta)\frac{\partial u_z}{\partial z} Q_z \\ + \left[\frac{\partial u_z}{\partial r} - \frac{\zeta}{2}\left(\frac{\partial u_z}{\partial r} + \frac{\partial u_r}{\partial z}\right)\right] Q_r + \sqrt{2C_i \dot{\gamma}} Q dW_z,\end{split} \tag{5.20a}$$

$$\begin{split}\frac{\partial Q_r}{\partial t} + u_z \frac{\partial Q_r}{\partial z} + u_r \frac{\partial Q_r}{\partial r} = (1-\zeta)\frac{\partial u_r}{\partial r} Q_r + \\ \left[\frac{\partial u_r}{\partial z} - \frac{\zeta}{2}\left(\frac{\partial u_z}{\partial r} + \frac{\partial u_r}{\partial z}\right)\right] Q_z + \sqrt{2C_i \dot{\gamma}} Q dW_r.\end{split} \tag{5.20b}$$

Developing the fibre stress tensor in Eq. (5.3) in the coordinates (z, r) yields

$$\begin{split}\tau_f^{zz} = f(\phi) A \left[\frac{\partial u_z}{\partial z}\langle P_z P_z P_z P_z\rangle + \left(\frac{\partial u_z}{\partial r} + \frac{\partial u_r}{\partial z}\right)\langle P_z P_z P_z P_r\rangle + \right. \\ \left. \frac{\partial u_r}{\partial r}\langle P_z P_z P_r P_r\rangle\right] + 2 f(\phi) D_r F \langle P_z P_z\rangle,\end{split} \tag{5.21a}$$

$$\begin{split}\tau_f^{rr} = f(\phi) A \left[\frac{\partial u_z}{\partial z}\langle P_z P_z P_r P_r\rangle + \left(\frac{\partial u_z}{\partial r} + \frac{\partial u_r}{\partial z}\right)\langle P_z P_r P_r P_r\rangle + \right. \\ \left. \frac{\partial u_r}{\partial r}\langle P_r P_r P_r P_r\rangle\right] + 2 f(\phi) D_r F \langle P_r P_r\rangle,\end{split} \tag{5.21b}$$

$$\begin{split}\tau_f^{zr} = \tau_f^{rz} = f(\phi) A \left[\frac{\partial u_z}{\partial z}\langle P_z P_z P_z P_r\rangle + \left(\frac{\partial u_z}{\partial r} + \frac{\partial u_r}{\partial z}\right)\langle P_z P_z P_r P_r\rangle + \right. \\ \left. \frac{\partial u_r}{\partial r}\langle P_z P_r P_r P_r\rangle\right] + 2 f(\phi) D_r F \langle P_z P_r\rangle.\end{split} \tag{5.21c}$$

5.4 Numerical method for non-dilute fibre suspension flows

5.4.1 A coupled macro-micro multiscale system

Collecting the macro-micro governing equations and the stress formula, as described above, yields a multiscale system in 2-D axisymmetric coordinates as follows.

$$\frac{1}{r}\frac{\partial^2\Psi}{\partial z^2}+\frac{1}{r}\frac{\partial^2\Psi}{\partial r^2}-\frac{1}{r^2}\frac{\partial\Psi}{\partial r}=2\omega, \tag{5.22a}$$

$$\begin{aligned}Re\left(\frac{\partial\omega}{\partial t}+u_z\frac{\partial\omega}{\partial z}+u_r\frac{\partial\omega}{\partial r}-\frac{u_r}{r}\omega\right)-\eta_a\left(\frac{\partial^2\omega}{\partial z^2}+\frac{\partial^2\omega}{\partial r^2}\right)&=-\left(\eta_a-1\right)\\ \left(\frac{\partial^2\omega}{\partial z^2}+\frac{\partial^2\omega}{\partial r^2}\right)+\left(\frac{1}{r}\frac{\partial\omega}{\partial r}-\frac{1}{r^2}\omega\right)+\frac{1}{2}&\left(\frac{\partial^2\tau_f^{rz}}{\partial r^2}-\frac{\partial^2\tau_f^{zr}}{\partial z^2}+\frac{\partial^2\tau_f^{zz}}{\partial r\partial z}\right.\\ &\left.-\frac{\partial^2\tau_f^{rr}}{\partial z\partial r}+\frac{1}{r}\frac{\partial\tau_f^{rz}}{\partial r}-\frac{1}{r}\frac{\partial\tau_f^{rr}}{\partial z}-\frac{1}{r^2}\tau_f^{rz}\right),\end{aligned} \tag{5.22b}$$

$$\begin{aligned}\frac{\partial Q_z}{\partial t}+u_z\frac{\partial Q_z}{\partial z}+u_r\frac{\partial Q_z}{\partial r}&=\left(1-\zeta\right)\frac{\partial u_z}{\partial z}Q_z\\ +\left[\frac{\partial u_z}{\partial r}-\frac{\zeta}{2}\left(\frac{\partial u_z}{\partial r}+\frac{\partial u_r}{\partial z}\right)\right]&Q_r+\sqrt{2C_i\dot{\gamma}}QdW_z,\end{aligned} \tag{5.23a}$$

$$\begin{aligned}\frac{\partial Q_r}{\partial t}+u_z\frac{\partial Q_r}{\partial z}+u_r\frac{\partial Q_r}{\partial r}&=\left(1-\zeta\right)\frac{\partial u_r}{\partial r}Q_r\\ +\left[\frac{\partial u_r}{\partial z}-\frac{\zeta}{2}\left(\frac{\partial u_z}{\partial r}+\frac{\partial u_r}{\partial z}\right)\right]&Q_z+\sqrt{2C_i\dot{\gamma}}QdW_r.\end{aligned} \tag{5.23b}$$

$$\begin{aligned}\tau_f^{zz}=f(\phi)A&\left[\frac{\partial u_z}{\partial z}\left\langle P_zP_zP_zP_z\right\rangle+\left(\frac{\partial u_z}{\partial r}+\frac{\partial u_r}{\partial z}\right)\left\langle P_zP_zP_zP_r\right\rangle\right.\\ &\left.+\frac{\partial u_r}{\partial r}\left\langle P_zP_zP_rP_r\right\rangle\right]+2f(\phi)D_rF\left\langle P_zP_z\right\rangle,\end{aligned} \tag{5.24a}$$

$$\begin{aligned}\tau_f^{rr}=f(\phi)A&\left[\frac{\partial u_z}{\partial z}\left\langle P_zP_zP_rP_r\right\rangle+\left(\frac{\partial u_z}{\partial r}+\frac{\partial u_r}{\partial z}\right)\left\langle P_zP_rP_rP_r\right\rangle\right.\\ &\left.+\frac{\partial u_r}{\partial r}\left\langle P_rP_rP_rP_r\right\rangle\right]+2f(\phi)D_rF\left\langle P_rP_r\right\rangle,\end{aligned} \tag{5.24b}$$

$$\begin{aligned}\tau_f^{zr}=\tau_f^{rz}=f(\phi)A&\left[\frac{\partial u_z}{\partial z}\left\langle P_zP_zP_zP_r\right\rangle+\left(\frac{\partial u_z}{\partial r}+\frac{\partial u_r}{\partial z}\right)\left\langle P_zP_zP_rP_r\right\rangle\right.\\ &\left.+\frac{\partial u_r}{\partial r}\left\langle P_zP_rP_rP_r\right\rangle\right]+2f(\phi)D_rF\left\langle P_zP_r\right\rangle.\end{aligned} \tag{5.24c}$$

5.4.2 Numerical procedure

The IRBF-DAVSS-BCF based multiscale method, which is presented in Chapter 4 (Nguyen et al., 2015a), is applied to solve the equation system (5.22)-(5.24). The vorticity transport equation (5.22b) is temporally discretised using the semi-implicit scheme as follows.

$$\begin{aligned}
&\omega^{n+1} - \frac{\Delta t}{Re}\eta_a\left(\frac{\partial^2\omega^{n+1}}{\partial z^2} + \frac{\partial^2\omega^{n+1}}{\partial r^2}\right) = \omega^n - \frac{\Delta t}{Re}\left(\eta_a - 1\right)\left(\frac{\partial^2\omega^n}{\partial z^2} + \right.\\
&\left.\frac{\partial^2\omega^n}{\partial r^2}\right) + \frac{\Delta t}{Re}\left(\frac{1}{r}\frac{\partial\omega^n}{\partial r} - \frac{1}{r^2}\omega^n\right) - \Delta t\left(u_z^n\frac{\partial\omega^n}{\partial z} - u_r^n\frac{\partial\omega^n}{\partial r} + \frac{u_r^n}{r}\omega^n\right)\\
&+\frac{\Delta t}{2Re}\left(\frac{\partial^2(\tau_f^{rz})^n}{\partial r^2} - \frac{\partial^2(\tau_f^{zr})^n}{\partial z^2} + \frac{\partial^2(\tau_f^{zz})^n}{\partial r\partial z} - \frac{\partial^2(\tau_f^{rr})^n}{\partial z\partial r} + \frac{1}{r}\frac{\partial(\tau_f^{rz})^n}{\partial r}\right.\\
&\qquad\qquad\left.-\frac{1}{r}\frac{\partial(\tau_f^{rr})^n}{\partial z} - \frac{1}{r^2}(\tau_f^{rz})^n\right),
\end{aligned} \tag{5.25}$$

The evolution equations (5.23a,b) are explicitly discretised by the Euler-Maruyama method as

$$\begin{aligned}
Q_z^{n+1} = Q_z^n &- \left(u_z\frac{\partial Q_z^n}{\partial z} + u_r\frac{\partial Q_z^n}{\partial r}\right)\Delta t + (1-\zeta)\frac{\partial u_z}{\partial z}Q_z^n\Delta t\\
&+\left[\frac{\partial u_z}{\partial r} - \frac{\zeta}{2}\left(\frac{\partial u_z}{\partial r} + \frac{\partial u_r}{\partial z}\right)\right]Q_r^n\Delta t + \sqrt{2C_i\dot{\gamma}\Delta t}QW_z^n,
\end{aligned} \tag{5.26a}$$

$$\begin{aligned}
Q_r^{n+1} = Q_r^n &- \left(u_z\frac{\partial Q_r^n}{\partial z} + u_r\frac{\partial Q_r^n}{\partial r}\right)\Delta t + (1-\zeta)\frac{\partial u_r}{\partial r}Q_r^n\Delta t\\
&+\left[\frac{\partial u_r}{\partial z} - \frac{\zeta}{2}\left(\frac{\partial u_z}{\partial r} + \frac{\partial u_r}{\partial z}\right)\right]Q_z^n\Delta t + \sqrt{2C_i\dot{\gamma}\Delta t}QW_r^n,
\end{aligned} \tag{5.26b}$$

where superscripts $(n+1)$ and n denote the two successive time steps at $t_{n+1} = (n+1)\Delta t$ and $t_n = n\Delta t$, respectively; Δt the time step size.

At each time step, the 1D-IRBF method is used to approximate not only the vorticity/stream function equations but also the first and second derivatives of the field variables including the fibre stresses at collocation points. Details can be found in Nguyen et al. (2015a).

The simulation algorithm can be outlined as follows.

- Calculate the fibre stresses at a time step t_{n+1} from the fibre configuration fields at step t_n (the initial ones for the first step) using Eqs. (5.24a,b,c), and then approximate the derivatives of stresses using the 1D-IRBF scheme;
- Solve Eqs. (5.25) and (5.22a) for the vorticity and stream function, respec-

tively. Then, calculate the velocity of the current step using Eq. (5.14);

- Calculate the effective velocity gradient $\boldsymbol{L}$ using Eq. (5.19);
- Solve Eqs. (5.26a,b) for the fibre configuration fields $\mathbf{Q}$'s using the Euler-Maruyama method;
- Calculate the fibre stress tensor at step t_{n+1} use Eqs. (5.24a,b,c);
- The routine is repeated until either the desired time or the convergence measure (CM) for the velocity, which is evaluated by Eq. (2.54), is reached.

5.5 Numerical examples

This section is to present the simulation of three challenging non-dilute fibre suspension flows using the present simulation method: (i) flow through a circular tube; (ii) flows through 4:1 axisymmetric contraction; and (iii) flows through 1:4 axisymmetric expansion for a range of fibre parameters and several Reynolds numbers. The fibre parameters for cases ranging from semi-dilute to concentrated suspensions are presented in Table 5.1.

Besides bulk properties of a flow, the orientation of fibres in the flow is also considered. At a position in the flow, the fibres' orientation is illustrated by an ellipse's geometry with three cases (Fig. 5.1): (i) a circle/circular ellipse, (ii) an ellipse or (iii) a straight line as presented in Nguyen et al. (2015a). Based on the grid convergence study in the work just cited, the finest discretisations are adapted for the present work.

5.5.1 Flow through a circular tube

The flow through a circular tube of non-dilute fibre suspensions is first investigated. Then, the velocity profile as well as the vorticity and stream function at the outlet will be used as the boundary conditions at the inlet of the fibre suspension flow through an axisymmetric contraction presented in Section 5.5.2.

Table 5.1: Fibre suspension flow through a circular tube. States of fibre suspension fluids: dilute ($\phi a_r^2 < 1$), semi-dilute ($1 \leq \phi a_r^2 < a_r$) and concentrated ($\phi a_r^2 \geq a_r$). a_r: the aspect ratio of fibre, ϕ: the volume fraction, and $(\cdot)^*$: the value of $(\cdot)$ associated with $a_r = 20$.

a_r	ϕ	ϕa_r^2	State of fibre suspension
10	0.01	1	semi-dilute
10	0.02	2	semi-dilute
10	0.05	5	semi-dilute
10	0.08	8	semi-dilute
10	0.10	10	concentrated
10	0.12	12	concentrated
10	0.15	15	concentrated
10	0.18	18	concentrated
10	0.20	20	concentrated
20	0.01	4	semi-dilute
20	0.02	8^*	semi-dilute
20	0.05	20^*	concentrated
20	0.08	32	concentrated
20	0.10	40	concentrated

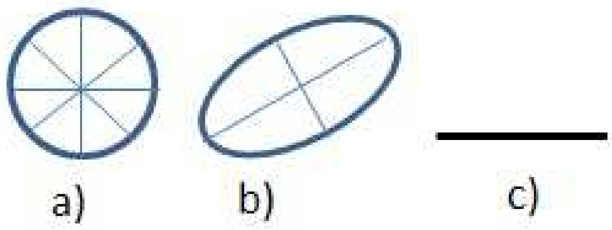

Figure 5.1: Orientation of fibres: a) Circle: the isotropic fibres' direction; b) Ellipse: the major axis is the predominant direction of fibres and c) Straight line: all fibres completely align with the line. This figure is from Chapter 4.

The geometry of the flow through a circular tube is described in Fig. 5.2 where $L = 10$ and $R = 0.5$ are the length and radius of the tube, respectively. Unless otherwise stated, we present the results with $Re = 0$ and $N_f = 1000$. A non-uniform grid described in Fig. 5.3 is used with $\Delta z_1 = 0.05, \forall z \in [0, 9.9]$ and $\Delta z_2 = 0.01, \forall z \in [9.9, 10]$; $\Delta r_1 = 0.01, \forall r \in [0, 0.1]$; and $\Delta r_2 = 0.05, \forall r \in [0.1, 0.5]$. The choice of Δt is discussed shortly. Experiences show that finer meshes near

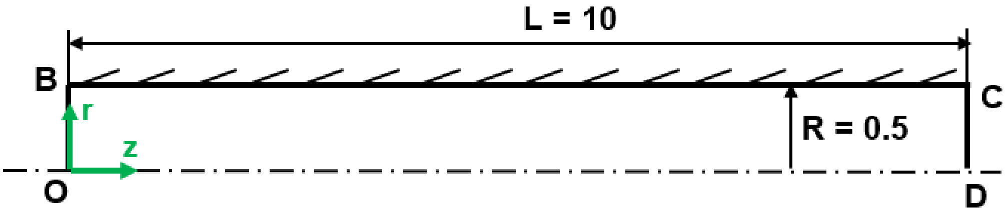

Figure 5.2: Non-dilute fibre suspension flow through a circular tube: the geometry.

the outlet and the centreline are necessary for higher solution accuracy at these regions.

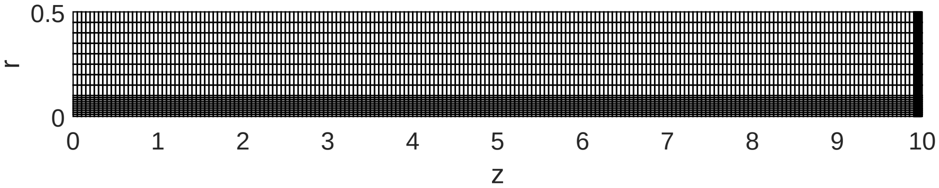

Figure 5.3: Non-dilute fibre suspension flow through a circular tube: the non-uniform Cartesian grid discretisation.

The boundary conditions of this problem are given as follows.

- At the inlet $\overline{OB}$: Newtonian parabolic velocity profile is applied, i.e. $u_z = u_{max}\left(1-\left(\frac{r}{R}\right)^2\right)$ and $u_r = 0$, where $u_{max} = 1.5$ is the maximum value of the velocity profile. For the fibre configuration field, a set of N_f fibres is randomly generated and assigned at each collocation point;

- On the wall $\overline{BC}$: non-slip boundary condition is used, i.e. $u_z = 0$ and $u_r = 0$;

- At the outlet $\overline{DC}$: flow out condition is used, i.e. $\frac{\partial u_z}{\partial z} = 0$ and $u_r = 0$;

- On the centreline $\overline{OD}$: the symmetric boundary condition is set up, i.e. $\frac{\partial u_z}{\partial r} = 0$ and $u_r = 0$.

Together with the non-uniform grid described in Fig. 5.3, the stability of the present method is investigated with a range of time steps $\Delta t = \{0.01, 0.005, 0.002, 0.001\}$. For each value of Δt, the simulation is carried out with a set of values of the fibre parameters $\phi a_r^2 = \{5, 10, 15, 20, 40\}$. The convergence measures of the velocity field ($CM(\mathbf{u})$) at $t = 10$ for the range of time steps are presented in Table 5.2. Symbol 'X' means a divergence measure. The study shows that the simulation is always convergent with $CM(\mathbf{u}) < 1.5E - 4$ using $\Delta t = 0.001$ over the range of fibre parameters. Thus, $\Delta t = 0.001$ is chosen as the time step for the present method to simulate this problem.

Table 5.2: Fibre suspension flow through a circular tube: A study for the stability of the present method with respect to time step size using the non-uniform grid described in Fig. 5.3. Convergence measures of the velocity field ($CM(\mathbf{u})$) at $t = 10$ for different Δt's and fibre parameters (ϕa_r^2). 'X' means a divergence measure.

	ϕa_r^2				
Δt	5	10	15	20	40
0.010	6.93E-4	1.12E-3	X	X	X
0.005	6.90E-5	1.21E-4	3.86E-3	X	X
0.002	8.11E-5	1.51E-4	1.07E-3	X	X
0.001	1.85E-5	4.78E-5	1.33E-4	2.58E-4	1.31E-4

The non-dilute fibre suspension flow is simulated for a range of ϕa_r^2 in order to investigate the role of fibre parameters in the dynamic behaviours of the flow. A discussion of the obtained results and a comparison with others are as follows.

- Fig. 5.4 describes the distribution of the axial velocity u_z along the centreline of the tube for a range of $\phi a_r^2 \in \{1, 5, 8, 10, 15, 20\}$ whose corresponding volume fractions (ϕ) and aspect ratios (a_r) are given in Table 5.1. An undershoot is observed in all cases of ϕa_r^2 at positions near the entrance ($z \in (0.41, 0.74)$). Furthermore, the undershoot is more pronounced with increasing ϕa_r^2.

  The appearance of undershoots reflects the effect of the isotropic configuration of fibres at the inlet. The isotropy of fibre configurations resists the development of the velocity (u_z) at the region near the inlet. The velocity then increases towards the outlet with a gradual decrease of the isotropy of fibres' orientation.

  Results in Fig. 5.4 also show that the u_z velocity on the centreline at the steady state reduces as ϕ and/or a_r increases. It is very interesting to note that the velocity reaches a steady state relatively quickly (at $z \approx 4$

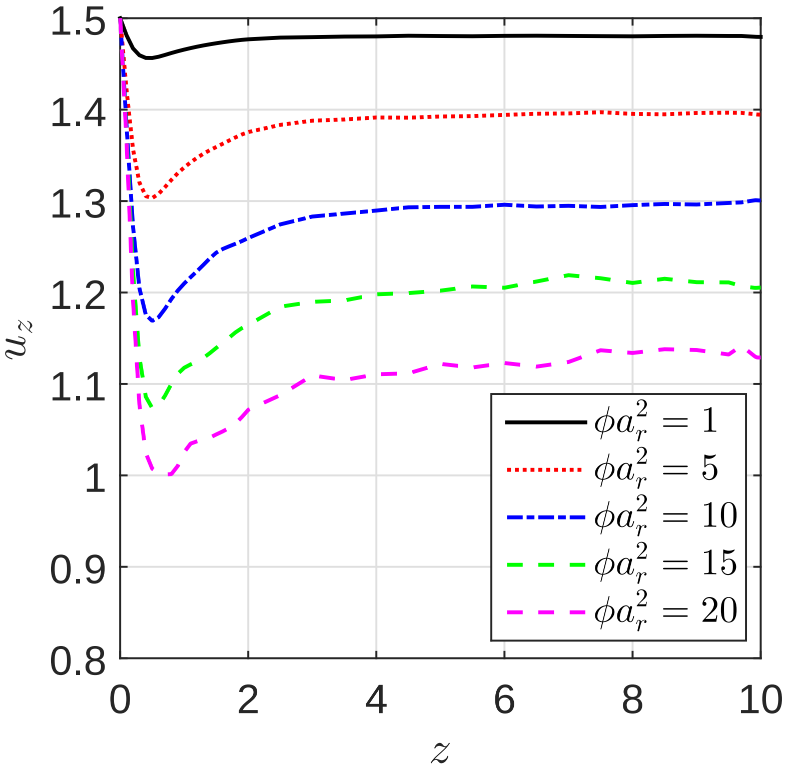

Figure 5.4: Non-dilute fibre suspension flow through a circular tube: the u_z velocity profile along the centreline of flows with $\phi a_r^2 \in \{1, 5, 10, 15, 20\}$.

downstream) in contrast to the dilute fibre suspension flow where the flow is not well developed until much further downstream as reported in Chapter 4, Fig. 4.16 (at $z \approx 10$).

- Fig. 5.5 depicts the effect of ϕ and a_r on the axial velocity profile (u_z) at several sections ($z \in \{0, 0.5, 1, 2, 4, 10\}$) with $\phi a_r^2 = 1$ (semi-dilute) (figure (a)), $\phi a_r^2 = 10$ (concentrated) (figure (b)) and $\phi a_r^2 = 20$ (concentrated) (figure (c)). Numerical experiments show that the velocity profile becomes more plug-like with increasing ϕ and/or a_r. The outlet velocity profile of flows for a range of $\phi a_r^2 = \{1, 5, 10, 15, 20\}$ presented in Fig. 5.6 also shows that the velocity profiles are more plug-like for higher values of a_r and/or ϕ.

- Fig. 5.7 presents the streamlines for the Newtonian flow (figure (a)), semi-dilute fibre suspension flow with $\phi a_r^2 = 5$ (figure (b)) and concentrated fibre suspension flow with $\phi a_r^2 = 20$ (figure (c)). The results show that the streamlines for the fibre suspension flows are significantly different from

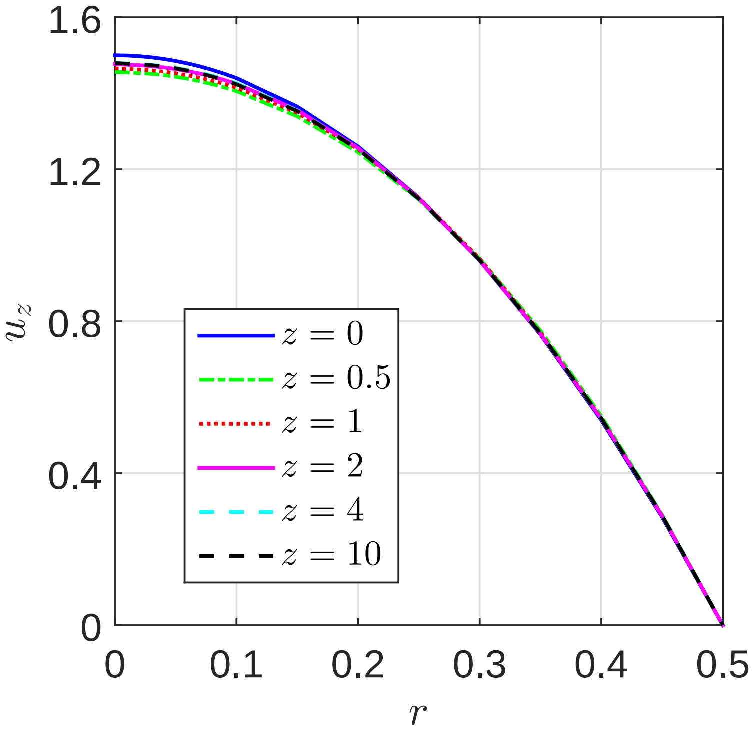

(a)

those for the Newtonian flow in the region near the inlet. Indeed, the streamlines for the fibre suspension are convex while they are straight lines along the channel wall for the Newtonian flow. Furthermore, the streamlines are more convex with increasing of ϕa_r^2.

- The contour of the fibre shear stress and the first normal stress difference for the semi-dilute ($\phi a_r^2 = 5$) and concentrated suspension ($\phi a_r^2 = 20$) flows are presented in Figs. 5.8 and 5.9, respectively. Numerical experiments show that the fibre stresses increase with higher values of ϕa_r^2. For example, the shear stress covers $[-7, 0]$ for the semi-dilute fibre suspension flow and $[-22, 0]$ for the concentrated one. In addition, the shear stress is zero (minimum value) at the centreline and reach maximum value on the wall (Fig. 5.8 - figure (a)) or near the wall (see Fig. 5.8 - figure (b)). Both the first normal stress difference and the shear stress settle down to the steady state downstream from the inlet where the transient behaviour is apparent.

- Finally, the influence of ϕa_r^2 on the convergence measure (CM) for the velocity, stream function and vorticity are reported in Fig. 5.10. Results show a significant influence of ϕa_r^2 on the convergence of the method, where

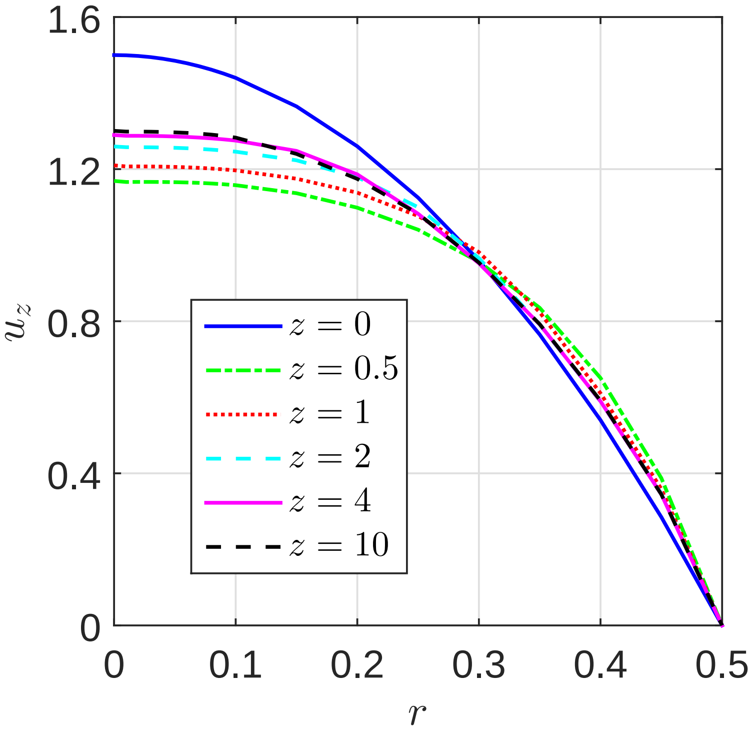

(b)

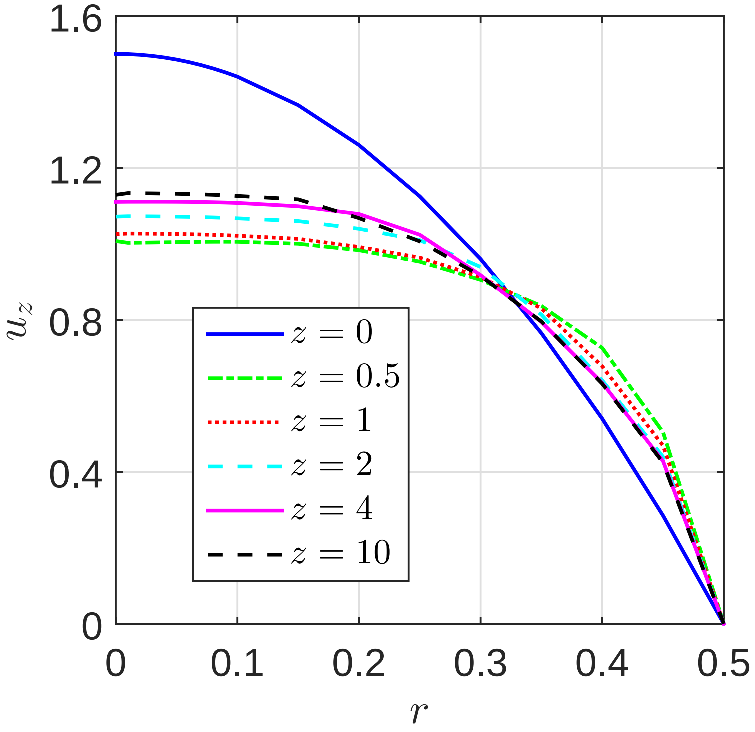

(c)

(b)

Figure 5.5: Non-dilute fibre suspension flow through a circular tube: the effect of fibre parameters on the velocity profile along the fibre direction with $\phi a_r^2 = 1$ (figure (a)); $\phi a_r^2 = 10$ (figure (b)); and $\phi a_r^2 = 20$ (figure (c)).

the CM generally degenerates with increasing level of fibre concentration and/or aspect ratio.

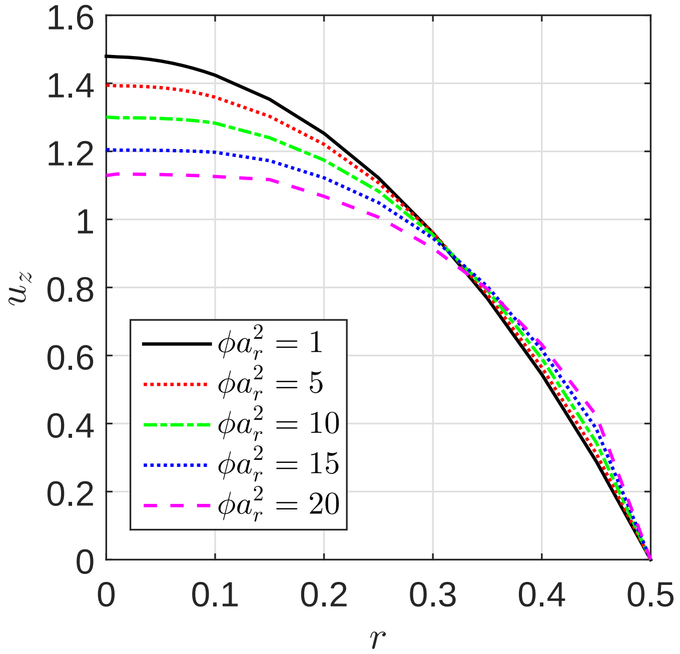

Figure 5.6: Non-dilute fibre suspension flow through a circular tube: the velocity profiles at the outlet of the channel for flows with $\phi a_r^2 \in \{1, 5, 10, 15, 20\}$.

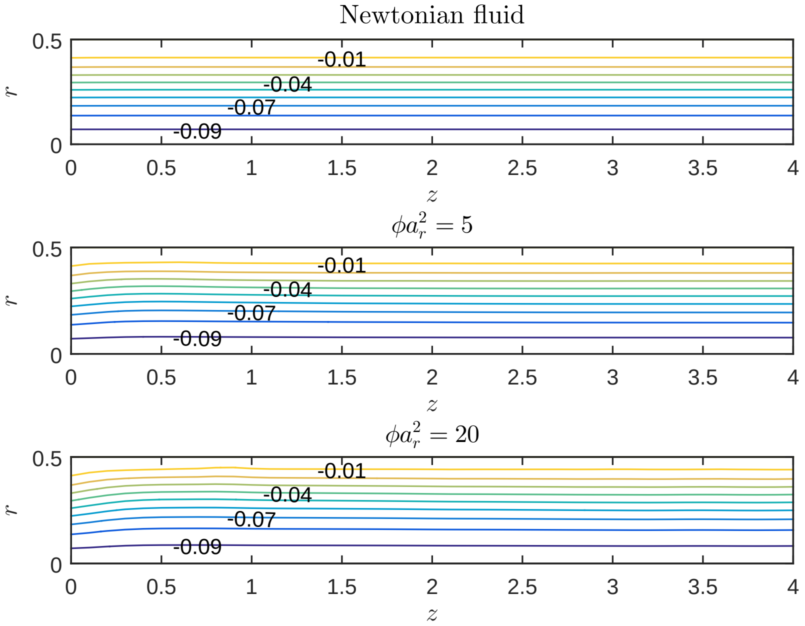

Figure 5.7: Non-dilute fibre suspension flow through a circular tube: the streamlines for the cases of Newtonian fluid (figure (a)), fibre suspensions with $\phi a_r^2 = 5$ (figure (b)) and $\phi a_r^2 = 20$ (figure (c)) in the domain $z \in [0, 4]$.

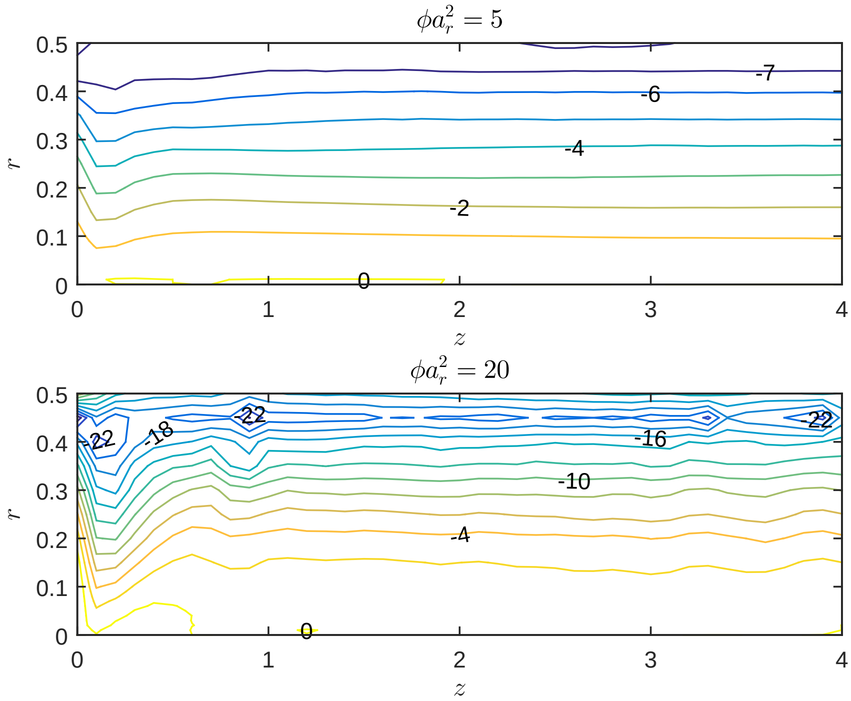

Figure 5.8: Non-dilute fibre suspension flow through a circular tube: the contour of the extra shear stress (τ_e^{zr}) for the flows with $\phi a_r^2 = 5$ (figure (a)) and $\phi a_r^2 = 20$ (figure (b)) in the domain $z \in [0, 4]$.

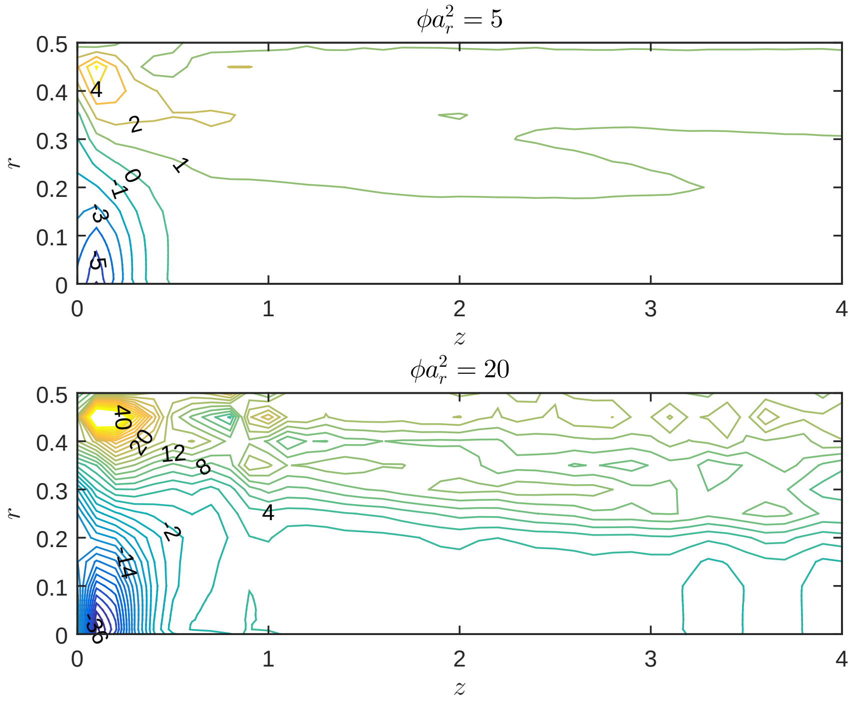

Figure 5.9: Non-dilute fibre suspension flow through a circular tube: the contour of the first normal stress difference ($\tau_e^{zz} - \tau_e^{rr}$) for the flows with $\phi a_r^2 = 5$ (figure (a)) and $\phi a_r^2 = 20$ (figure (b)) in the domain $z \in [0, 4]$.

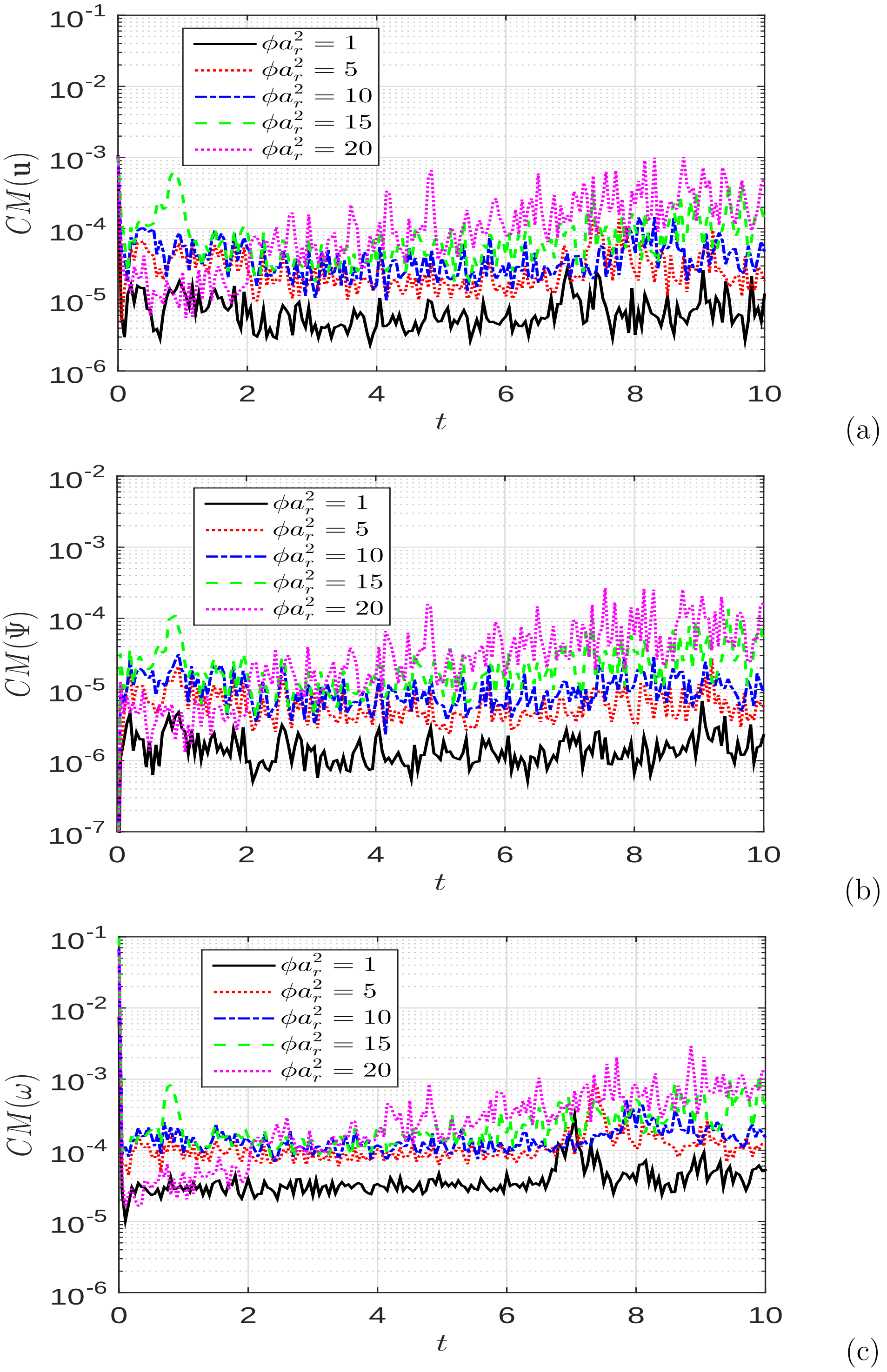

Figure 5.10: Non-dilute fibre suspension flow through a circular tube: the convergence measure for velocity (figure (a)), stream function (figure (b)) and vorticity (figure (c)) of flows with $\phi a_r^2 \in \{1, 5, 10, 15, 20\}$.

5.5.2 The 4:1 axisymmetric contraction flows

A schematic geometry of the 4:1 axisymmetric contraction flow is presented in Fig. 5.11 where L_U and R_U are the length and radius of the upstream tube, respectively; L_D and R_D the length and radius of the downstream tube; and L_v the length of the salient vortex. The contraction ratio (β) and the dimensionless vortex length (L_v^*) are given by

$$\beta = \frac{R_U}{R_D}, \qquad L_v^* = \frac{L_v}{2R_U}. \tag{5.27}$$

The boundary conditions for this problem are as follows.

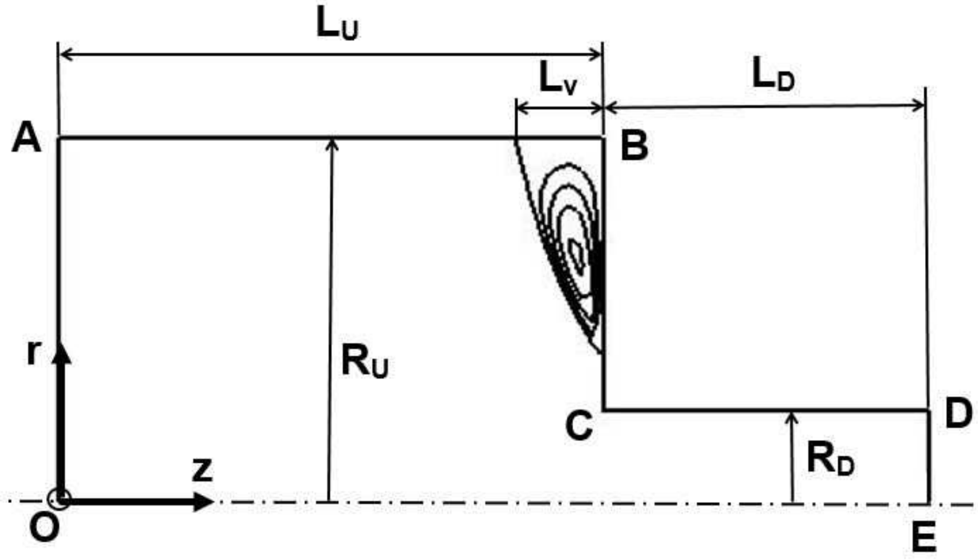

Figure 5.11: A schematic geometry for the axisymmetric contraction flow.

- At the inlet $\overline{OA}$: the velocity, the stream function and the vorticity are taken from the values at the outlet of the circular Poiseuille flows investigated in the previous section. In addition, $\frac{\partial \Psi}{\partial z} = 0$ is also assigned;
- At the outlet $\overline{DE}$: flow-out conditions are defined as $\frac{\partial u_z}{\partial z} = 0$, $u_r = 0$; $\frac{\partial \Psi}{\partial z} = 0$; and $\frac{\partial \omega}{\partial z} = 0$;
- On the walls $\overline{AB}$, $\overline{CD}$ and $\overline{BC}$: non-slip boundary condition is set up for the velocity, i.e. $u_z = 0$ and $u_r = 0$. The corresponding boundary conditions for the stream function and the vorticity are determined by

  - On the wall $\overline{AB}$: $\Psi = 0$, $\frac{\partial \Psi}{\partial r} = 0$; $\omega = \omega_{w_1}$;
  - On the wall $\overline{BC}$: $\Psi = 0$, $\frac{\partial \Psi}{\partial z} = 0$; $\omega = \omega_{w_2}$,
  - On the wall $\overline{CD}$: $\Psi = 0$, $\frac{\partial \Psi}{\partial r} = 0$; $\omega = \omega_{w_3}$;

  where ω_{w_1}, ω_{w_2} and ω_{w_3} are determined and updated using Eq. (5.22a) with the known stream function at each time step;

- On the centreline $\overline{OE}$: symmetric boundary condition for the velocity, i.e. $\frac{\partial u_z}{\partial r} = 0$ and $u_r = 0$; The corresponding boundary conditions for the stream function and vorticity are $\Psi = \Psi_c$, $\frac{\partial \Psi}{\partial r} = 0$ and $\omega = 0$ where Ψ_c is determined by Eq. (5.14).

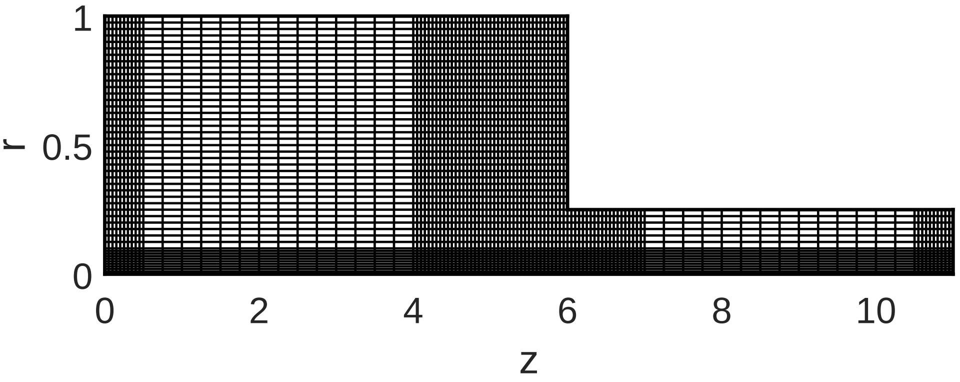

Figure 5.12: A non-uniform Cartesian grid for the 4:1 axisymmetric contraction flow.

The non-uniform grid designed in Nguyen et al. (2015a) is used for the simulation of this problem as follows. $\Delta z_1 = 0.05$ $\forall z \in [0, 0.5] \bigcup [4, 7] \bigcup [10.5, 11]$; $\Delta z_2 = 0.1$ $\forall z \in [0.5, 4] \bigcup [7, 10.5]$; $\Delta r_1 = 0.01$ $\forall r \in [0, 0.1]$; and $\Delta r_2 = 0.025$ $\forall r \in [0.1, 1]$.

The simulation is carried out using $N_f = 1000$ and the time step size $\Delta t = 1E{-}3$. However, in several cases of highly concentrated suspensions, a finer time step is used at the initial time for the numerical stability of the method. Unless otherwise stated, the simulation is carried out for the 4:1 contraction flow with $L_U = 6$, $R_U = 1$, $L_D = 5$ and $R_D = 0.25$ and $Re = 0$.

Firstly, the impact of the fibre aspect ratio (a_r) and volume fraction (ϕ) on the flow pattern and fibres' orientation is investigated. A discussion of the present results and a comparison with those by Lu et al. (2006) using the BCF-finite element method are described next.

- Fig. 5.13 presents the effect of the fibre parameters (ϕ, a_r) on the vortex length (L_v^*) for two cases of fibre suspension as follows.
  - $a_r = 10$ with a range of $\phi \in \{0.01, 0.02, 0.05, 0.08, 0.10, 0.12, 0.15, 0.18, 0.20\}$;
  - $a_r = 20$ with a range of $\phi \in \{0.01, 0.02, 0.05, 0.08, 0.10\}$.

  Numerical experiments show that the vortex length is more pronounced with increasing ϕ or/and a_r. This trend was also reported in Lu et al. (2006) but larger vortices are observed in the present results.

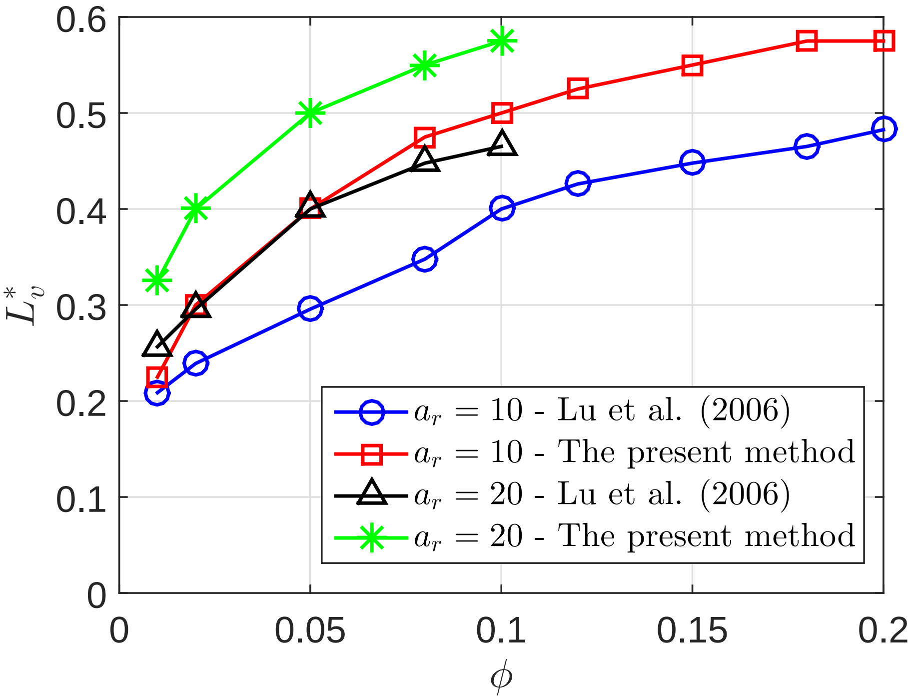

Figure 5.13: The 4:1 axisymmetric contraction flows of non-dilute fibre suspensions: the effect of fibre parameters on the vortex length (L_v^*) with $a_r = 10$ and a range of $\phi \in \{0.01, 0.02, 0.05, 0.08, 0.10, 0.12, 0.15, 0.18, 0.20\}$; and $a_r = 20$ and a range of $\phi \in \{0.01, 0.02, 0.05, 0.08, 0.10\}$.

- Fig. 5.14 describes the effect of fibre parameters on the shape and length of the vortex at the salient corner for a range of $\phi a_r^2 \in \{1, 5, 10, 15, 20\}$. The salient vortex's size is more pronounced with increasing of ϕa_r^2 as presented in the figure. In addition, the present numerical results also depict that, unlike the Newtonian flow where the vortex boundary is concave, it is slightly convex for fibre suspension flows as reported in Lipscomb et al. (1988); Chiba et al. (1990); Lu et al. (2006).

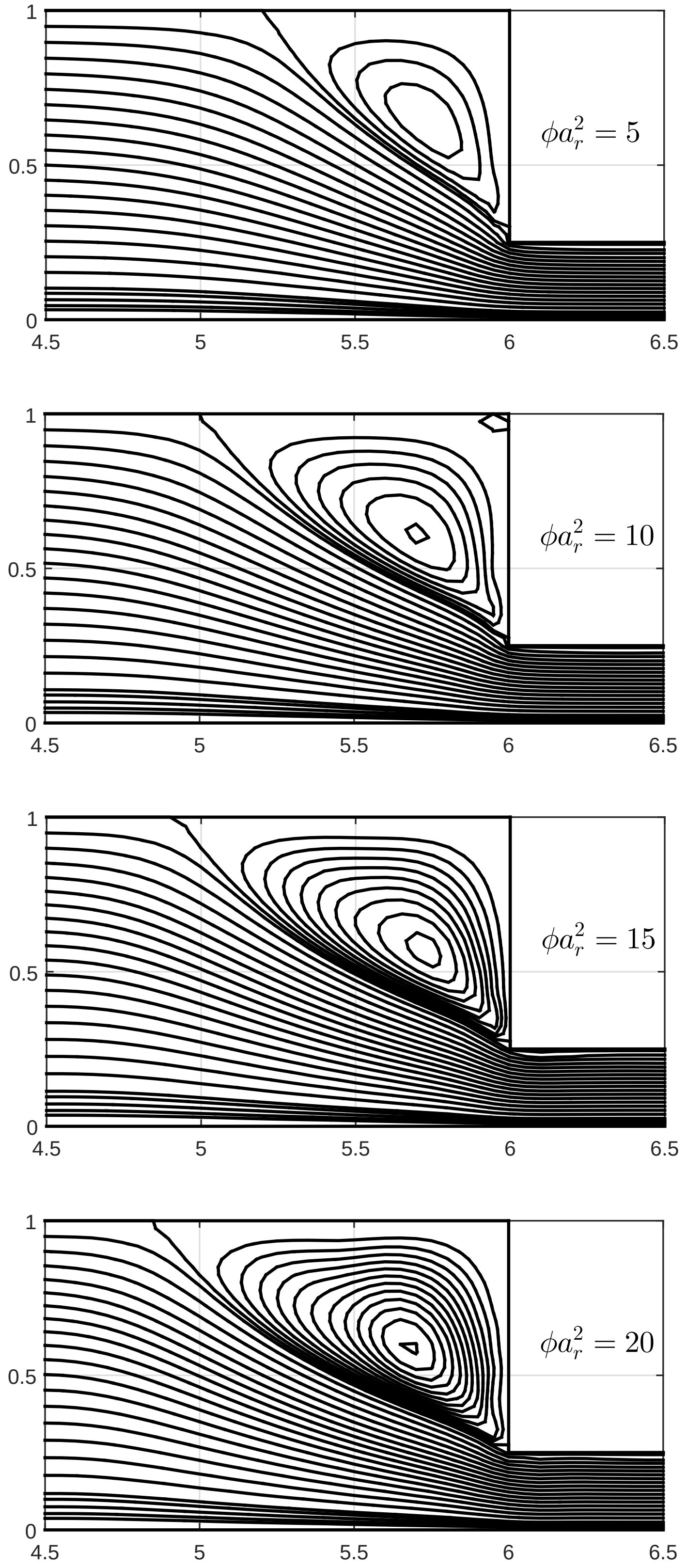

(a)

(b)

(c)

(d)

Figure 5.14: The 4:1 axisymmetric contraction flows of non-dilute fibre suspensions: the effect of ϕa_r^2 on the salient corner vortex size for $\phi a_r^2 = \{5, 10, 15, 20\}$.

- The influence of ϕa_r^2 on the orientation of fibres around the abrupt contraction is reported in Fig. 5.15 by a blue ellipse/line/circle (see Fig. 5.1) at a position whereas the black dashed lines are for the streamlines for four cases of $\phi a_r^2 \in \{5, 10, 15, 20\}$. Several notable points are discussed as follows.
  - Fibres distribution in the main area of the flow tends to be less anisotropic with increasing ϕa_r^2. Fig. 5.15 shows that the region dominated by anisotropic fibres distribution is gradually shrinking from Fig. 5.15(a) ($\phi a_r^2 = 5$: semi-dilute) to Fig. 5.15(d) ($\phi a_r^2 = 20$: concentrated). This is caused by the random interaction between fibres in a non-dilute suspension. This interaction, which is stronger with increasing ϕa_r^2, reduces the influence of the flow velocity on the fibres' orientation.
  - The fibres distribution is more isotropic towards the centre of the vortex.

The effect of *Re* on the vortex size is also studied by the present method for $\phi a_r^2 = 12$. Numerical experiments show that the length of vortex slightly reduces with increasing *Re* as presented in Fig. 5.16 for a range of $Re \in \{0, 1, 2, 5\}$. This observation is similar to one in dilute fibre suspension flows (Nguyen et al., 2015a; Abdul-Karem et al., 1993).

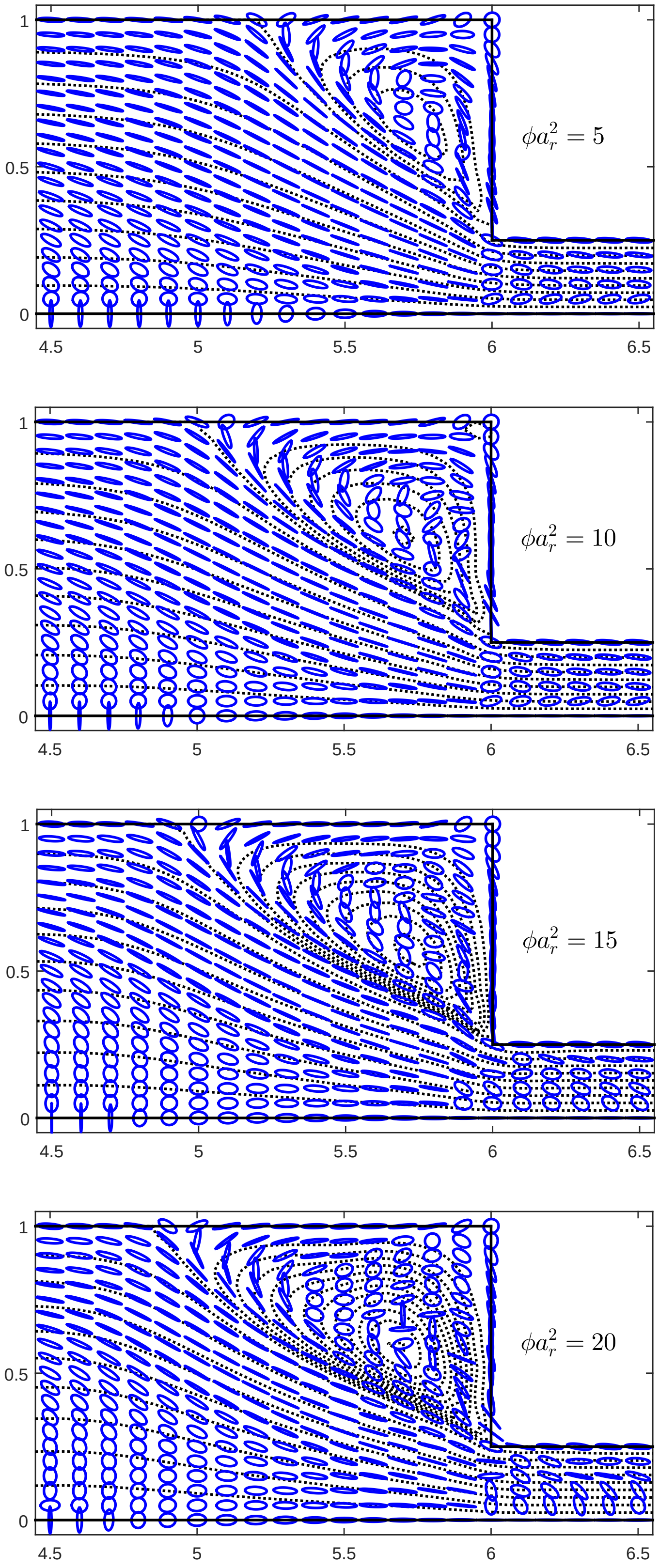

(a)

(b)

(c)

(d)

Figure 5.15: The 4:1 axisymmetric contraction flows of non-dilute fibre suspensions: the orientation of fibres around the contraction area for $\phi a_r^2 \{5, 10, 15, 20\}$.

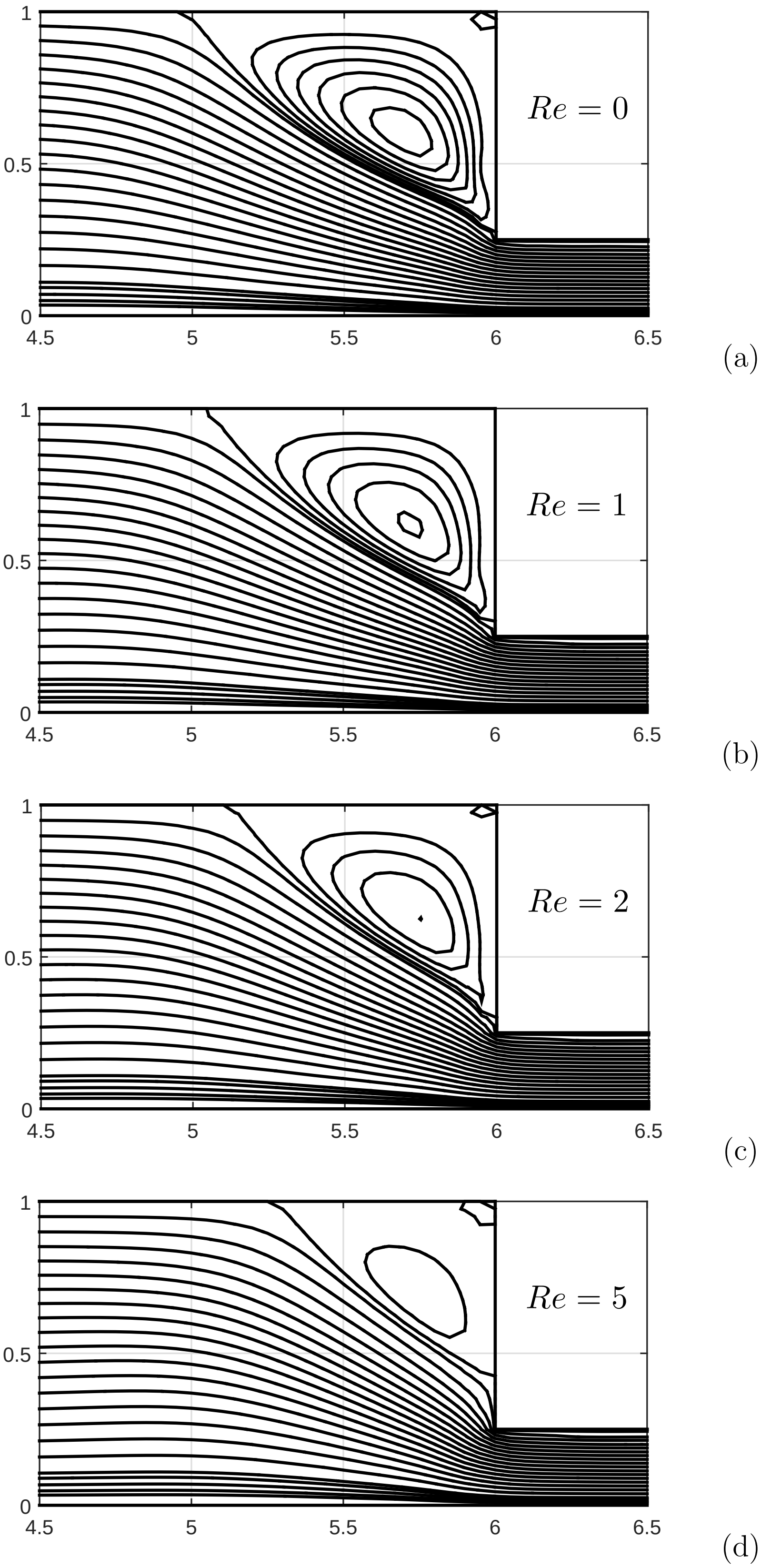

Figure 5.16: The 4:1 axisymmetric contraction flows of non-dilute fibre suspensions: the effect of Reynolds number (Re) on the salient corner vortex for $\phi a_r^2 = 12$.

5.5.3 The 1:4 axisymmetric expansion flow

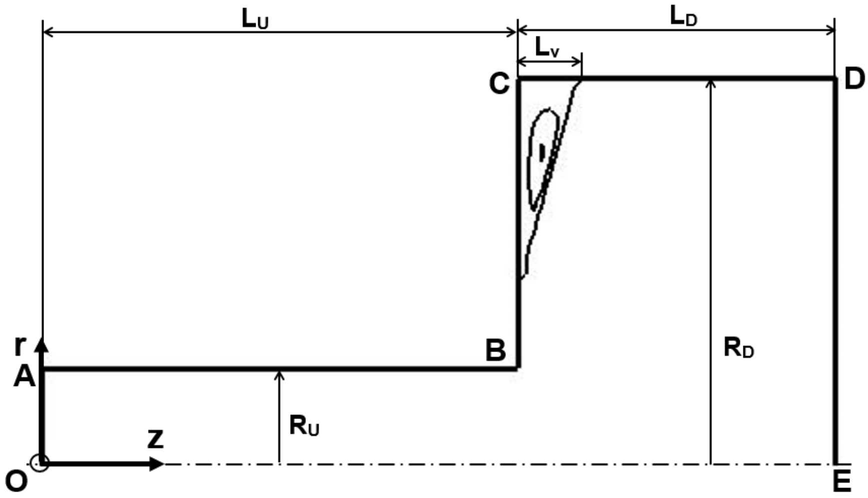

Figure 5.17: A schematic geometry for the 1:4 axisymmetric expansion flow.

A schematic geometry of the 1:4 axisymmetric expansion flow is presented in Fig. 5.17 where $L_U = 6$ and $R_U = 0.25$ are the length and radius of the upstream tube, respectively; $L_D = 4$ and $R_D = 1$ the length and radius of the downstream tube; and L_v the vortex length. The expansion ratio (β) and the dimensionless vortex length (L_v^*) are similarly defined as in Eq. (5.27) but for the expansion flow. The problem was studied by Lu et al. (2006) using the BCF – finite element method.

The boundary conditions of this problem are given as follows.

- At the inlet $\overline{OA}$: the velocity, the stream function and the vorticity are taken from the values at the outlet of the axisymmetric contraction flow investigated in Section 5.5.2. $\frac{\partial \Psi}{\partial z} = 0$;
- At the outlet $\overline{DE}$: the velocity, the stream function and the vorticity at the inlet of the axisymmetric contraction problem are used as the Dirichlet boundary conditions of this problem. $\frac{\partial \Psi}{\partial z} = 0$;
- On the walls $\overline{AB}$, $\overline{CD}$ and $\overline{BC}$: non-slip boundary condition is set up for the velocity: $u_z = 0$ and $u_r = 0$. Hence, the corresponding boundary conditions for the stream function and the vorticity on the walls are given as follows.

  - On the wall $\overline{AB}$: $\Psi = 0$, $\frac{\partial \Psi}{\partial r} = 0$; and $\omega = \omega_{w_1}$;
  - On the wall $\overline{BC}$: $\Psi = 0$, $\frac{\partial \Psi}{\partial z} = 0$; $\omega = \omega_{w_2}$;
  - On the wall $\overline{CD}$: $\Psi = 0$, $\frac{\partial \Psi}{\partial r} = 0$; and $\omega = \omega_{w_3}$;

  where ω_{w_1}, ω_{w_2} and ω_{w_3} are determined using Eq. (5.22a) with the known stream function at each time step;

- On the centreline $\overline{OE}$: the symmetric boundary condition of the velocity is applied, i.e. $\frac{\partial u_z}{\partial r} = 0$ and $u_r = 0$. The corresponding boundary conditions for the stream function and the vorticity are given by $\Psi = \Psi_c$, $\frac{\partial \Psi}{\partial r} = 0$ and $\omega = 0$ where Ψ_c is determined by Eq. (5.14) using the inlet boundary condition of the velocity.

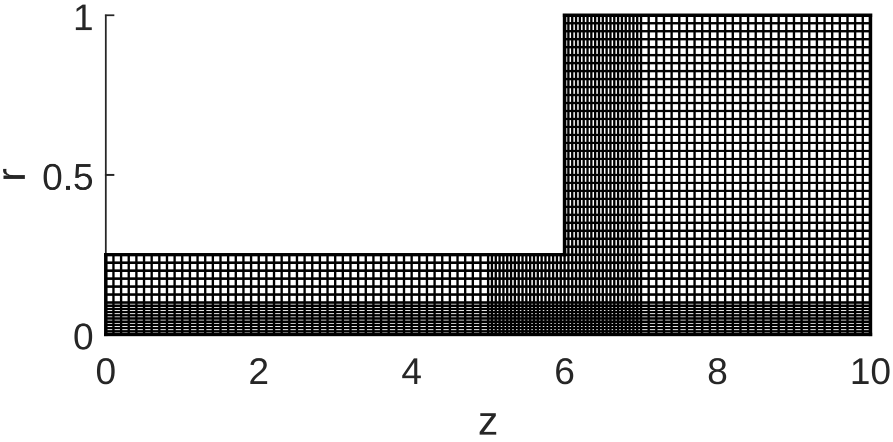

Figure 5.18: A non-uniform Cartesian grid for the 1:4 axisymmetric expansion flow.

A non-uniform Cartesian grid used to simulate the flow. Finer grids in regions near the outlet and inlet and around the abrupt expansion and the centreline are necessary to produce accurate solutions. A detailed Cartesian grid is designed as follows: $\Delta z_1 = 0.05$ $\forall z \in [5, 7]$; $\Delta z_2 = 0.1$ $\forall z \in [0, 5] \bigcup [7, 10]$; $\Delta r_1 = 0.01$ $\forall r \in [0, 0.1]$; and $\Delta r_2 = 0.025$ $\forall r \in [0.1, 1]$. A schematic non-uniform grid is described in Fig. 5.18. As in the contraction flow problem, the time step size $\Delta t = 1E{-}3$ is used in the simulation, however, a smaller time step is used at the initial time for the simulation of flows of highly concentrated suspensions. A discussion of the present results and a comparison with those by Lu et al. (2006) and others are as follows.

Fig. 5.19 presents the effect of fibre parameters (ϕ, a_r) on the vortex length (L_v^*) of the 1:4 expansion flow for the following two cases of fibre suspensions:

- $a_r = 10$ with a range of $\phi \in \{0.01, 0.02, 0.05, 0.08, 0.10, 0.12, 0.15, 0.18, 0.20\}$;
- $a_r = 20$ with a range of $\phi \in \{0.01, 0.02, 0.05, 0.08, 0.10\}$.

The present results are in very good agreement with those by Lu et al. (2006). Indeed, in the contraction flows, the vortex length is more pronounced with increasing ϕ and/or a_r (Fig. 5.13), while it changes insignificantly in the expansion flows ($L_v^* \approx 0.175 \ldots 0.27$) (Fig. 5.19). In addition, the vortex lengths in the expansion flows are smaller than those in the contraction flows with the same fibre parameters. However, while the vortex length is nearly unchanged, a small lip vortex appears near the re-entrant corner with a sufficiently large value of ϕa_r^2 as seen in Fig. 5.20 for a range of $\phi a_r^2 \in \{5, 10, 15, 20\}$. This is notable because lip vortex has been reported only for the Newtonian and viscoelastic expansion flows with high expansion ratio and Weissenberg number (Baloch et al., 1995, 1996) but not in any report on fibre suspension flows.

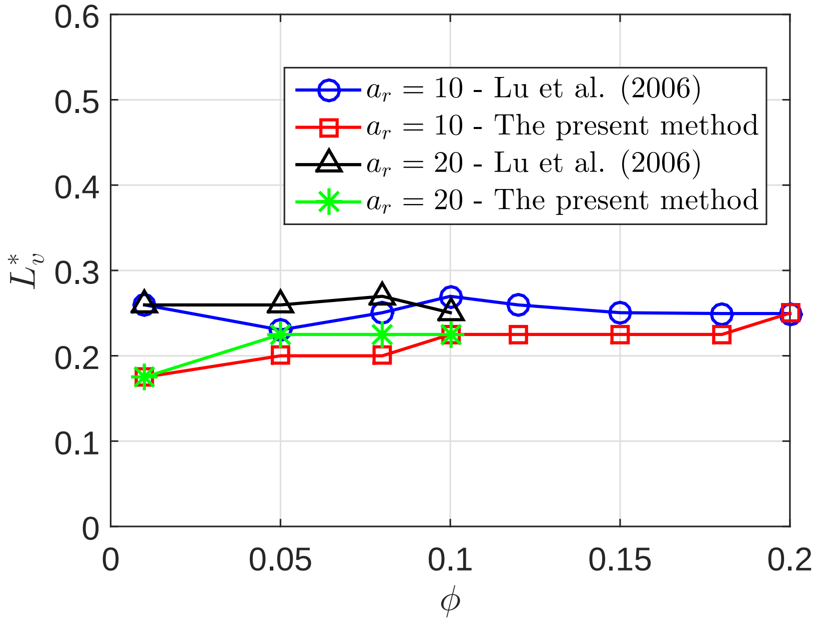

Figure 5.19: The 1:4 axisymmetric expansion flows of non-dilute fibre suspensions: the effect of fibre parameters on the vortex length (L_v^*) for $a_r = 10$ and a range of $\phi \in \{0.01, 0.02, 0.05, 0.08, 0.10, 0.12, 0.15, 0.18, 0.20\}$; and $a_r = 20$ and a range of $\phi \in \{0.01, 0.02, 0.05, 0.08, 0.10\}$.

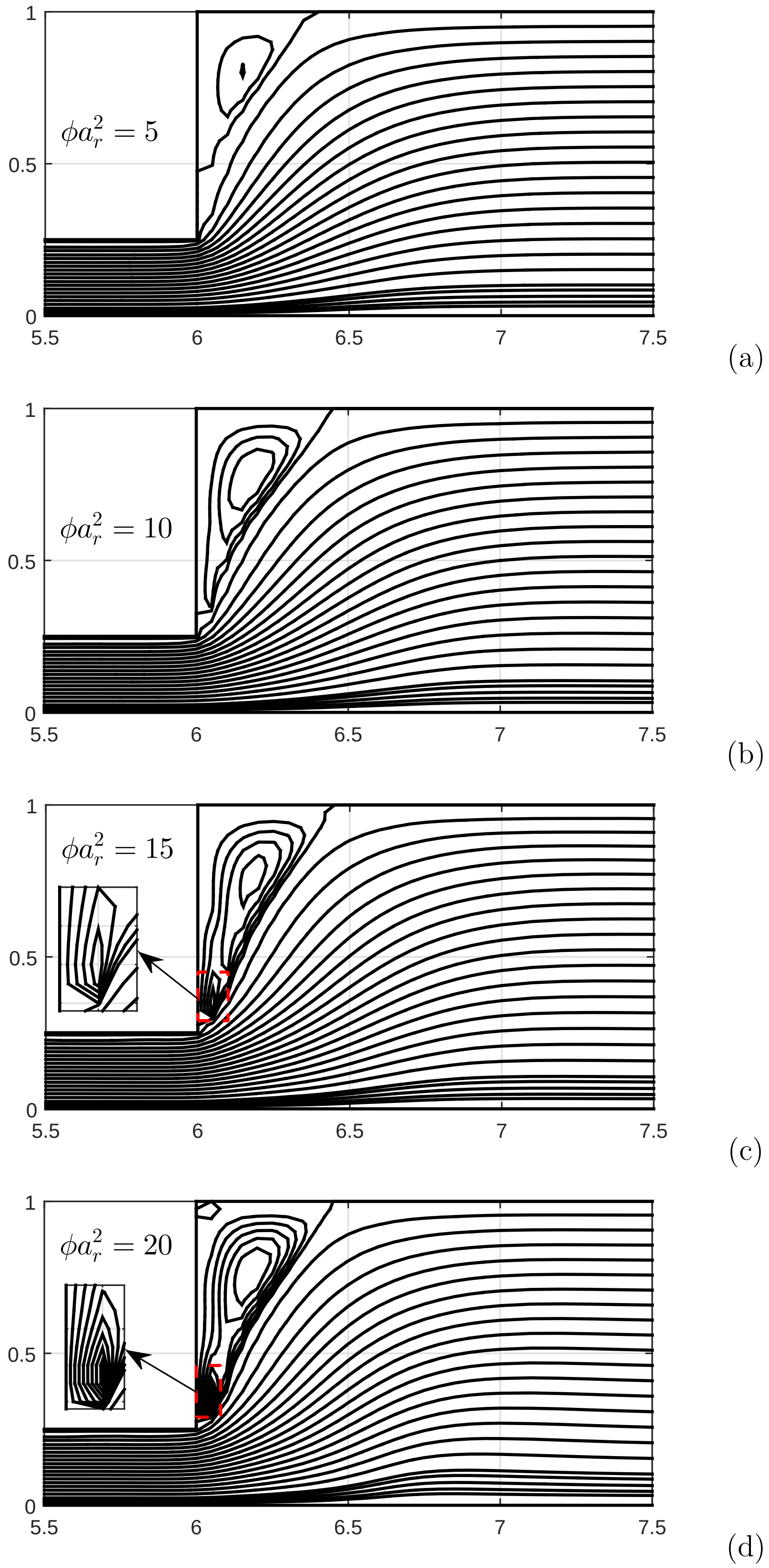

Figure 5.20: The 1:4 axisymmetric expansion flows of non-dilute fibre suspensions: the effect of ϕr_a^2 on the salient vortex pattern for $\phi a_r^2 \in \{5, 10, 15, 20\}$. A lip vortex appears for higher values of ϕa_r^2.

Fig. 5.21 presents the orientation of fibres together with streamlines (black dashed lines) around the expansion area for a range of $\phi a_r^2 \in \{5, 10, 15, 20\}$. Numerical experiments show that most fibres, except ones on the centreline, tend to align with the flow direction in the upstream region whereas fibres' direction becomes more random along the streamline in the downstream region. As a result, fibres are not tangential to streamlines near the vortex boundary, which is in contrast to the observation in the contraction flow. These observations are in very good agreement with those by several experimental and numerical studies (Abdul-Karem et al., 1993; Chiba and Nakamura, 1998; Verweyst and Tucker, 2002). The present numerical experiments also show that inertia has a strong influence on the vortex size as evidenced by the fast growing vortex with increasing $Re \in \{0, 1, 2, 5\}$ as seen in Fig. 5.22 and reported in experimental works by Abdul-Karem et al. (1993); Townsend and Walters (1994). In addition, the boundary is convex for the creeping flow ($Re = 0$) but becomes more and more concave for the flows at higher Re.

A simulation of the 1:2 expansion flow of non-dilute fibre suspensions with the fibre's aspect ratio $a_r = 10$ and volume fraction $\phi = 0.15$ using a range of the numbers of fibre configuration fields $N_f \in \{500, 1000, 2000\}$ is also carried out in order to compare the results of fibre stress with those by Lu et al. (2006). The profiles of shear stress (τ_f^{zr}), normal stresses (τ_f^{zz} and τ_f^{rr}) and the first normal stress difference ($\tau_f^{rr} - \tau_f^{zz}$) at the location $(z, r) = (5.75, 0.5)$ are presented in Fig. 5.23. The present numerical experiments indicate that while τ_f^{rr} and τ_f^{zr}, about 10 (Fig. 5.23(a)) and 57 (Fig. 5.23(c)) for $N_f = 1000$, respectively, are in good agreement with those by Lu et al. (2006), τ_f^{zz} and $\tau_f^{rr} - \tau_f^{zz}$ reported in Figs. 5.23(b) and 5.23(d) are smaller than those of the same authors. Furthermore, the smoothness of fibre stresses, especially τ_f^{zz}, is enhanced with increasing number of fibre configuration fields as described in the figure.

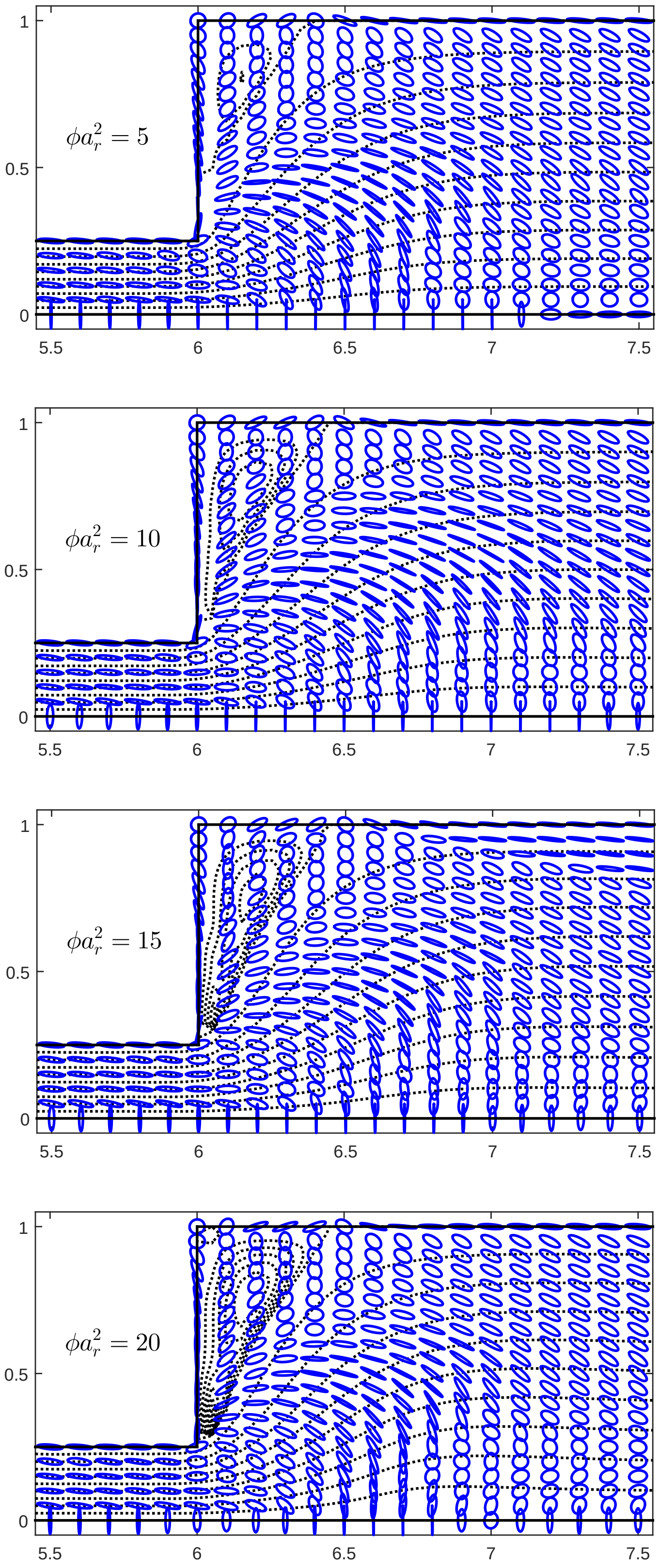

(a)

(b)

(c)

(d)

Figure 5.21: The 1:4 axisymmetric expansion flows of non-dilute fibre suspensions: the fibre orientation distribution around the expansion area for $a_r = 10$ and $\phi \in \{0.05, 0.10, 0.15, 0.20\}$.

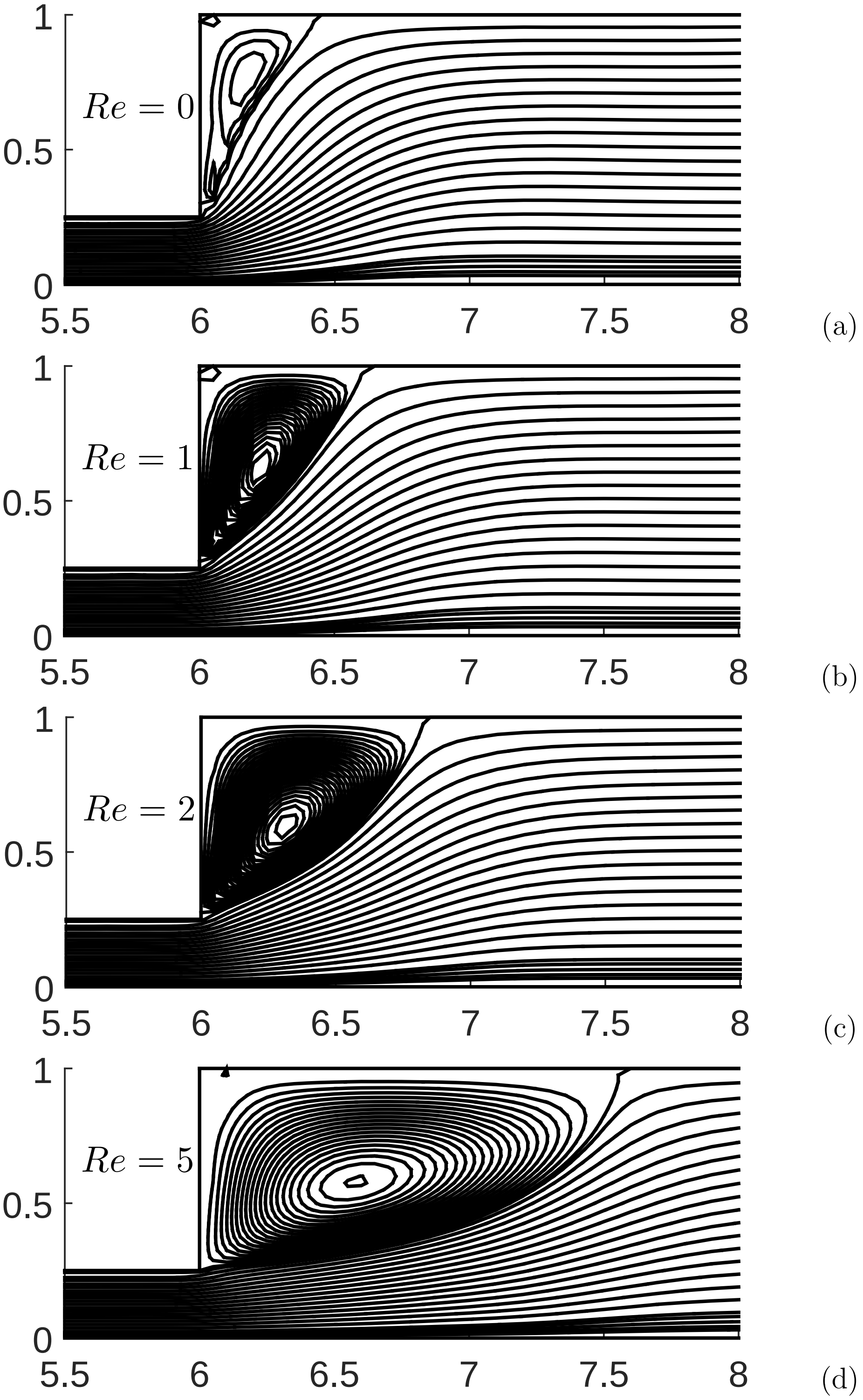

Figure 5.22: The 1:4 axisymmetric expansion flows of non-dilute fibre suspensions: the effect of the Reynolds number on the salient corner vortex for $a_r = 10$ and $\phi = 0.12$.

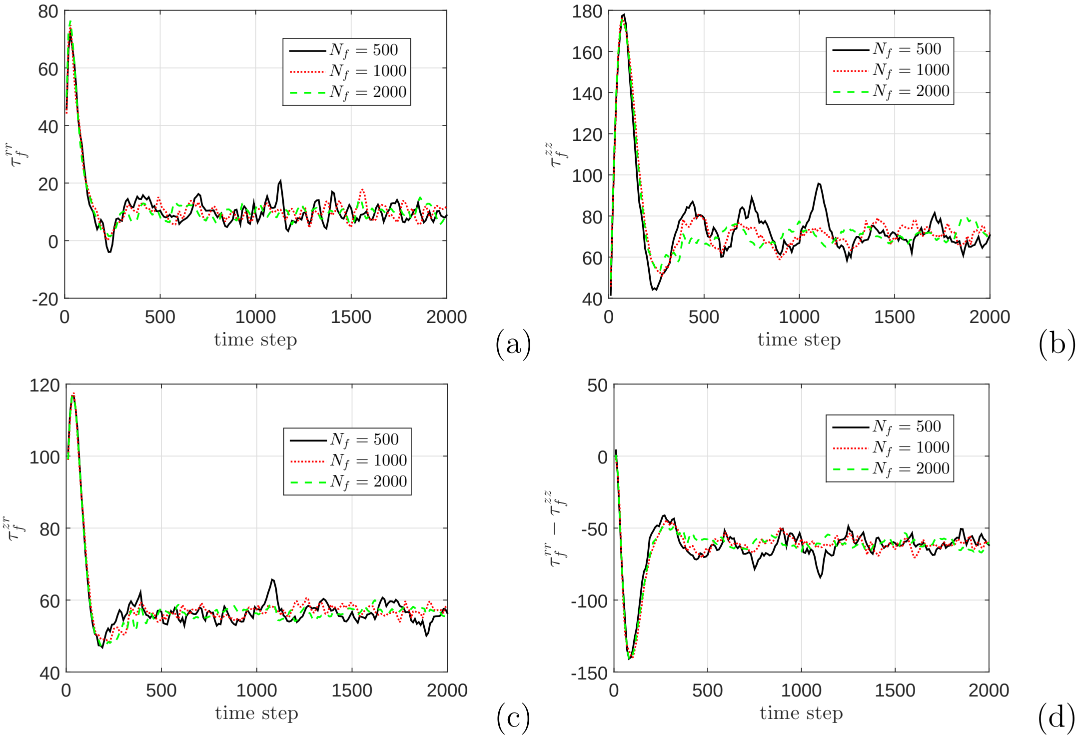

Figure 5.23: The 1:2 axisymmetric expansion flows of non-dilute fibre suspensions for $a_r = 10$ and $\phi = 0.15$: the evolution of fibre stresses including shear stress (τ_f^{zr}), normal stresses (τ_f^{zz} and τ_f^{rr}) and the first normal stress difference ($\tau_f^{rr} - \tau_f^{zz}$) at position $z = 5.75$ and $r = 0.5$.

5.6 Conclusions

The multiscale simulation method based on the fusion of high-order IRBF approximation, BCF idea and DAVSS technique for dilute fibre suspensions by Nguyen et al. (2015a) is further developed for non-dilute fibre suspensions in this chapter. The work is to simulate semi-dilute and concentrated fibre suspension flows where the evolution of fibre configurations governed by the Folgar-Tucker equation are determined using the BCF method and the fibre stress is approximated by the Phan-Thien–Graham model. The efficiency of the present method for the simulation of non-dilute fibre suspension flows is based on both the stability of the stochastic process and the accuracy of the method. As an illustration of the method, the Poiseuille flow through a circular tube and two challenging flows; the 4:1 axisymmetric contraction and 1:4 axisymmetric expansion flows are examined for a range of fibre parameters from semi-dilute to concentrated regimes. Results by the present method are in very good agreement with those by Lu et al. (2006). In addition, several dynamic behaviours of fluid flows from the present numerical experiments including the fibres' orientation are similar to experimental observations reported by Abdul-Karem et al. (1993); Baloch and Webster (1995); Verweyst and Tucker (2002). Finally, the present work discovers the existence of a lip vortex in the 1:4 expansion flows of more concentrated fibre suspensions.

Chapter 6

A numerical solution based on the Fokker-Planck equation for dilute polymer solutions using high-order RBF methods

As an alternative to the BCF-based approach discussed in previous chapters, this chapter presents a numerical method for the Fokker-Planck equation (FPE) based mesoscopic modelling of dilute polymer solutions using radial basis function (RBF) approaches (Nguyen et al., 2014). The stress is determined by the solution of an FPE while the velocity field is locally calculated via the solution of conservation partial differential equations (PDEs) (Bird et al., 1987a; Chauviere and Lozinski, 2004b). The FPE and PDEs are approximated separately by two different IRBF methods. Indeed, the time implicit discretisation of both FPE and PDEs is carried out using collocation methods where the high-order RBF approximants improve significantly the accuracy of the numerical solutions and the convergence rate (Ottinger, 1996; Hulsen et al., 1997). As an illustration of the method, the evolution of a start-up planar Couette flow is studied for the Hookean and finitely extensible nonlinear elastic (FENE) dumbbell models.

6.1 Introduction

For polymer flow calculation, mesoscopic multiscale approaches are recently regarded as more realistic than the closed-form counterparts but the computational involved requires much more work (Bird et al., 1987a; Ottinger, 1996). These methods can be mathematically expressed in two equivalent forms (i) stochastic differential equations (SDE) or (ii) the deterministic Fokker-Planck equations (FPE) (Bird et al., 1987a; Chauviere and Lozinski, 2004b; Ottinger, 1996). Since the SDE-based approaches usually yield noisy numerical approximation (Chauviere and Lozinski, 2004b; Ottinger, 1996; Tran-Canh and Tran-Cong, 2004) and require large computation time, the simulation of the flow of polymer liquids using of the FPE has attracted significant attention in spite of their computational complexity. Recently, radial basis function networks (RBFNs) are recognised as a potentially powerful tool in numerical analysis. The application of RBFNs for the numerical discretisation of differential equations has received a great deal of attention over the past two decades (Fasshauer, 2007). More recently, an alternative approach based on the integrated RBF (IRBF) expressions for the interpolation of functions and the solution of differential equations was proposed (Mai-Duy and Tran-Cong, 2001). It was found that the IRBF approach outperforms the differentiated RBFs (DRBFs) approach regarding accuracy and convergence rate over a wide range of the RBF width. In this work, we introduce the IRBF-based numerical method for the FPE-based mesoscopic models for viscoelastic flow calculations. The method is used to numerically discretise not only the macro-scale conservation equations but also the FPE for the distribution of probability density of polymer molecules. The present method yields a higher accuracy of the approximate solutions by avoiding the deterioration of accuracy caused by differentiation, and reducing noises in the approximation processes.

6.2 The FPE-based simulation method for some non-Newtonian fluids

Consider the complete system of equations consisting of momentum and mass conservation at the macroscopic scale, the FPE for the distribution of dumbbells (or end-to-end vector **r**) and the coupling equation (Kramers formula) for stress in dimensionless form as follows (Chauviere and Lozinski, 2004b; Tran et al., 2012b).

$$Re\frac{\partial \mathbf{u}}{\partial t} + Re\,(\mathbf{u}\cdot\nabla\mathbf{u}) - (1-\varepsilon)\Delta\mathbf{u} + \nabla p = \nabla\cdot\boldsymbol{\tau}_p, \tag{6.1}$$

$$\nabla\cdot\mathbf{u} = 0, \tag{6.2}$$

$$\begin{aligned}\frac{\partial\psi}{\partial t}(t,\mathbf{x},\mathbf{r}) + \mathbf{u}(t,\mathbf{x})\cdot\nabla\psi(t,\mathbf{x},\mathbf{r}) = -\nabla_{\mathbf{r}}\cdot\Bigg[\bigg(\nabla\mathbf{u}\,(t,\mathbf{x})\cdot\mathbf{r}\\ -\frac{1}{2We}\mathbf{F}\,(\mathbf{r})\bigg)\,\psi\,(t,\mathbf{x},\mathbf{r})\Bigg] + \frac{1}{2We}\Delta_{\mathbf{r}}\psi\,(t,\mathbf{x},\mathbf{r})\,,\end{aligned} \tag{6.3}$$

$$\boldsymbol{\tau}_p(t,\mathbf{x}) = \frac{\epsilon}{We}\left(\int\big(\mathbf{r}\otimes\mathbf{F}(\mathbf{r})\psi(t,\mathbf{x},\mathbf{r})\big)\,d\mathbf{r} - \mathbf{I}d\right), \tag{6.4}$$

where $\mathbf{u}$ is the velocity; p the pressure arisen due to the incompressibility constraint; $\boldsymbol{\tau}_p$ the polymer-contributed stress; $\psi(t,\mathbf{x},\mathbf{r})$ the probability density function of dumbbells $\mathbf{r}$; $Re = \frac{\rho UL}{\eta_o}$ the Reynolds number with ρ the density; $We = \frac{\lambda_H U}{L}$ Weissenberg number; $\eta_p = n_d k_B T\lambda_H$ the viscosity associated with the polymers; $\lambda_H = \zeta/4H$ the relaxation time of the polymer chains with H and ζ a spring constant and the friction coefficient between the dumbbell and the solvent, repectively; η_s the viscosity of solvent; η_o ($\eta_o = \eta_s + \eta_p$) the total viscosity of the solution; n_d dumbbell density; k_B Boltzmann constant; T the absolute temperature; and $\varepsilon = \frac{\eta_p}{\eta_o}$.

$L = \sqrt{\frac{k_B T}{H}}$ is the characteristic length; U the characteristic velocity; and b non-dimensional parameter related to the maximal polymer length (Ottinger, 1996; Tran et al., 2009, 2011). **F** is the dumbbell internal force and given in dimensionless form for the Hookean and FENE dumbbell models, respectively as follows.

$$\mathbf{F}(\mathbf{r}) = \mathbf{r}, \qquad \mathbf{F}(\mathbf{r}) = \frac{\mathbf{r}}{1-\frac{\|\mathbf{r}\|^2}{b}} \tag{6.5}$$

In this research, the Gaussian-IRBF (G-IRBF) based scheme is employed for solving the FPE (Eq. (6.3)) and then determining the probability density function $\psi(t, \mathbf{x}, \mathbf{r})$ of $\mathbf{r}$, which is used to calculate the polymer stress via the Kramers formula (Eq. (6.4)). The discretisation of the macro-scale governing equations (Eq. (6.1)-(6.2)) is carried out using an MQ-IRBF method. These two processes are serially performed and connected together via the coupling equation in which the field variables solutions obtained by one process is considered as the known in the other.

6.3 Solving the FPE based multiscale model with an IRBF method

Recently, Tran et al. (2012b) solved the FPE using the IRBFN approach. Since mathematically, the FPE is a second-order parabolic partial differential equation (Risken, 1989), the IRBF based computational techniques are described for the numerical solution of parabolic PDEs, i.e. the numerical solutions of both PDEs (6.1)-(6.2), and FPE (6.3). Consider a parabolic differential equation together with its initial and boundary conditions as follows.

$$\frac{\partial u}{\partial t} + \mathcal{L}u = f, \quad (x,t) \in \Omega \times [0,T], \tag{6.6}$$

$$u = g, \quad (x,t) \in \Omega \times \{0\}, \tag{6.7}$$

$$\mathcal{B}u = h, \quad (x,t) \in \partial\Omega \times [0,T], \tag{6.8}$$

where Ω and $\partial\Omega$ are a bounded domain and its boundary, respectively; T a final time; $\mathcal{L}$ a differential operator; $\mathcal{B}$ an operator expressing a boundary condition; and f, g and h known functions.

Assume that the time interval $[0,T]$ is partitioned into N_t equal subintervals $[t_n, t_{n+1}]$ of length $\Delta t = T/N_t$ with $t_0 = 0$ and $t_{N_t} = T$. In fully discrete schemes, Eq. (6.6) is discretised with respect to both time and space variables. The discretisation in time is accomplished by a time-stepping scheme, followed by the spatial discretisation based on the 1D-IRBFN method.

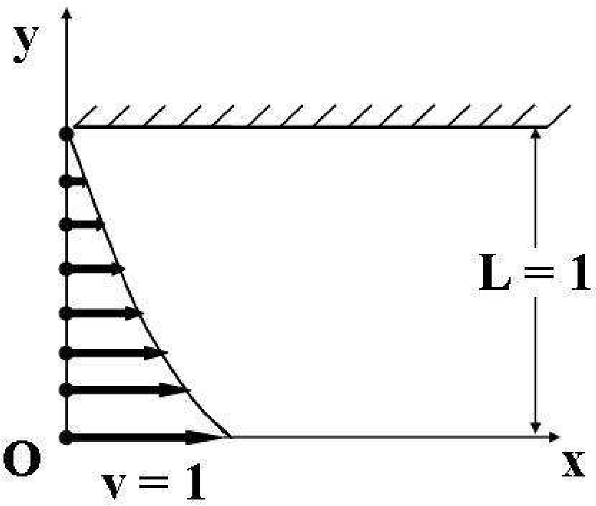

Figure 6.1: Start-up planar Couette flow problem: the bottom plate moves with a constant velocity $V = 1$, the top plate is fixed; no slip boundary conditions apply at the fluid-solid interfaces. The collocation point distribution is only schematic.

Applying the θ-scheme to Eq. (6.6) yields

$$\frac{u^{n+1} - u^n}{\Delta t} + \theta \mathcal{L} u^{n+1} + (1 - \theta) \mathcal{L} u^n = f, , \tag{6.9}$$

where $t_{n+1} = t_n + \Delta t$, $u^{n+1} = u(x, t_{n+1})$. Eq. (6.9) together with the constraints Eqs. (6.7)-(6.8) at a time t_{n+1} are then spatially discretised using the 1D-IRBF approach described in Section 2.5.1. The obtained solution is the values of the field variable at the grid points.

6.4 Numerical example

The present method is verified with the simulation of the start-up planar Couette flow using Hookean and FENE dumbbell model fluids. This problem was earlier studied by Le Bris and Lelievre (2009); Laso and Ottinger (1993) and Tran et al. (2011) for the Hookean and FENE dumbbell models. The problem is defined in Fig. 6.1. For time $t < 0$, the fluid is at rest. At $t = 0$, the lower plate starts to move with a constant velocity $V = 1$.

From the characteristics of the start up Couette flow of a dumbbell model fluid, the system of macro-micro equations (6.1)-(6.3) is rewritten as follows.

$$Re\frac{\partial u}{\partial t}(t,y) - (1-\varepsilon)\frac{\partial^2 u}{\partial y^2}(t,y) = \frac{\partial \tau_p}{\partial y}(t,y), \tag{6.10}$$

$$\begin{aligned}\frac{\partial \psi}{\partial \mathrm{t}}(t,y,X,Y) = -\frac{\partial}{\partial X}\left[\left(\frac{\partial u}{\partial y}(t,y)Y - \frac{1}{2We}F\left(X,Y\right)\right)\psi(t,y,X,Y)\right] + \\ \frac{\partial}{\partial Y}\left(\frac{1}{2We}Y\psi(t,y,X,Y)\right) + \frac{1}{2We}\left(\frac{\partial^2}{\partial X^2}+\frac{\partial^2}{\partial Y^2}\right)\psi(t,y,X,Y),\end{aligned} \tag{6.11}$$

where u and τ_p are the x-component of the velocity and the shear stress of the flow, respectively; $(X,\, Y)$ the components of the end-to-end vector $\mathbf{r}$ of a dumbbell at a location y.

6.4.1 Start-up planar Couette flow with the Hookean dumbbell model

The fluid parameters of the flow include Weissenberg number $We = 0.5$, Reynolds number $Re = 0.1$ and the ratio $\varepsilon = 0.9$ as done in Laso and Ottinger (1993); Le Bris and Lelievre (2009), and Tran et al. (2011) using different BCF based methods. In this research, the discretisation of Eqs. (6.10)-(6.11) are carried out through two interlaced processes of different scale as follows.

Discretisation of the FPE in configuration space

Let ϕ be a new function defined as $\phi = \psi/\psi_{eq}$ where $\psi_{eq}\left(X,Y\right)$ is the equilibrium solution of Eq. (6.11) for $u=0$ and given by

$$\psi_{eq}\left(X,Y\right) = \frac{1}{2\pi}\exp\left(-\frac{X^2+Y^2}{2}\right).$$

The FPE (6.11) with $F(X,Y) = \mathbf{r}$ for the Hookean dumbbell model is rewritten as

$$\begin{aligned}\psi_{eq}\frac{\partial \phi}{\partial \mathrm{t}}(t,X,Y) = -\frac{\partial}{\partial X}\left(\frac{\partial u}{\partial y}Y\psi_{eq}\phi\right) + \\ \frac{1}{2We}\frac{\partial}{\partial Y}\left(\psi_{eq}\frac{\partial \phi}{\partial X}\right) + \frac{1}{2We}\frac{\partial}{\partial Y}\left(\psi_{eq}\frac{\partial \phi}{\partial Y}\right),\end{aligned} \tag{6.12}$$

with $\phi(0, X, Y) = 1$. The time discretisation of the FPE (6.12) using the semi implicit method yields

$$\begin{aligned}\psi_{eq}\frac{\phi^{n+1}-\phi^{n}}{\Delta t} &= -\frac{\partial}{\partial X}\left(\frac{\partial u}{\partial y}Y\psi_{eq}\phi^{n}\right)+\\ \frac{1}{2We}\frac{\partial}{\partial X}\left(\psi_{eq}\frac{\partial \phi^{n+1}}{\partial X}\right)&+\frac{1}{2We}\frac{\partial}{\partial Y}\left(\psi_{eq}\frac{\partial \phi^{n+1}}{\partial Y}\right).\end{aligned} \tag{6.13}$$

It is noted that $\frac{\partial \psi_{eq}}{\partial i} = -i\psi_{eq},\ i = \{X, Y\}$. Developing Eq. (6.13) yields

$$\begin{aligned}\gamma\left(\frac{\partial^2\phi^{n+1}}{\partial X^2}+\frac{\partial^2\phi^{n+1}}{\partial Y^2}\right)-\gamma\left(X\frac{\partial \phi^{n+1}}{\partial X}+Y\frac{\partial \phi^{n+1}}{\partial Y}\right)-\phi^{n+1} &=\\ X\frac{\partial u^{n}}{\partial y}\frac{\partial \phi^{n}}{\partial X}\Delta t+\left(XY\frac{\partial u^{n}}{\partial y}\Delta t+1\right)\phi^{n},&\end{aligned} \tag{6.14}$$

where $\gamma = \frac{\Delta t}{2We}$. Using a uniform Cartesian grid of 25 × 25 collocation points for a bounded configuration domain (bi-periodic domain in the configuration space). This corresponds to 625 dumbbells ($\mathbf{r}_i,\ i = 1, \cdots, 625$) selected in the bounded configuration domain (Fig. 6.2).

Eq. (6.14) is dicretised using the 1D-RBFN scheme as presented in Section 2.5.1 and the ψ values at grid points are then calculated as above $\psi = \phi\psi_{eq}$.

The stress $\boldsymbol{\tau}_p$ is determined using Eq. (6.4). The stresses $(\tau_p)_{i,j}$ at the time t_i and collocation points y_j are employed in the RHS of Eq. (6.15) for the discretisation of the macro process as described in the next section.

Discretisation of the macroscopic equation

Applying the full implicit method for time discretisation of the macroscopic governing equation (6.10) yields

$$Re\frac{u^{n+1}-u^{n}}{\Delta t}-(1-\varepsilon)\frac{\partial^2 u^{n+1}}{\partial y^2}=\frac{\partial(\tau_p^n)}{\partial y},$$

or

$$-\alpha\frac{\partial^2 u^{n+1}}{\partial y^2}+\beta u^{n+1}=\frac{\partial(\tau_p^n)}{\partial y}+\beta u^{n}, \tag{6.15}$$

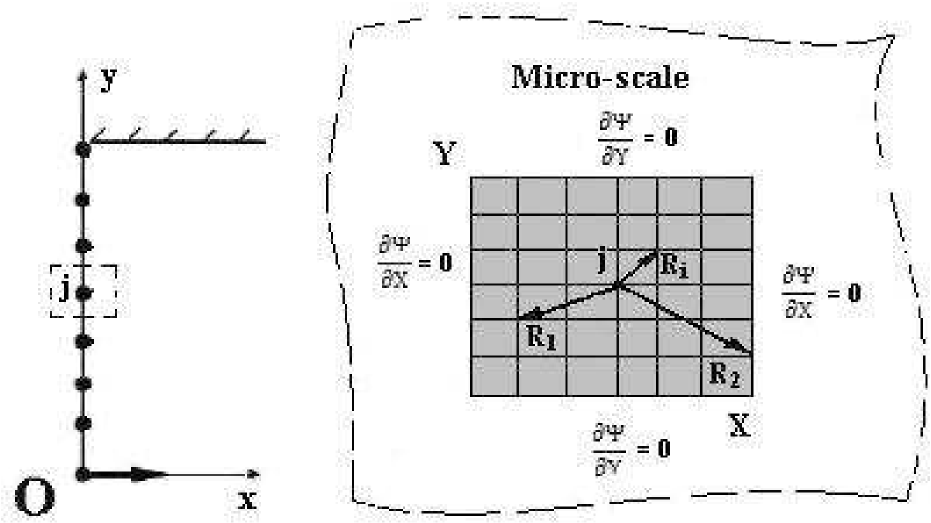

Figure 6.2: Start-up planar Couette flow using a Hookean dumbbell model fluid: Discretisation of a 2-D bounded domain (bi-periodic domain) of the micro configuration space $\{X, Y\}$ developed at a location point y_j of the Couette flow problem. The collocation point distribution is only schematic.

where Δt is uniform time step; $\beta = Re/\Delta t$; $\alpha = 1 - \varepsilon$; and $u^{n+1} = u(y, t_{n+1})$ with $u_0 = u(y, 0)$. The time discrete equation (6.15) is then spatially discretised (see Section 2.5.1) using N_y uniform collocation points. T is the final time when the flow has reached its steady state.

The macroscopic governing equation (6.15) together with initial and boundary conditions are similarly solved using the 1D-IRBFs collocation method in which $(\tau_p)_{n,j}$ are known at the time t_n and obtained from the micro-scale process.

Results and discussion

Using a time step of $\Delta t = 0.01$ for both macro and micro processes, a coarse spatial discretisation $\Delta y = 0.05$ ($N_y = 21$), the solution obtained by the present method is in very good agreement with ones using the IRBF-BCF multiscale method with a similar discretisation for the macro-scale component and 1000 dumbbells for the micro configuration space by Tran et al. (2011). Several observations are presented as follows.

Fig. 6.3 depicts evolutions of the velocity at four locations $y \in \{0.2, 0.4, 0.6, 0.8\}$.

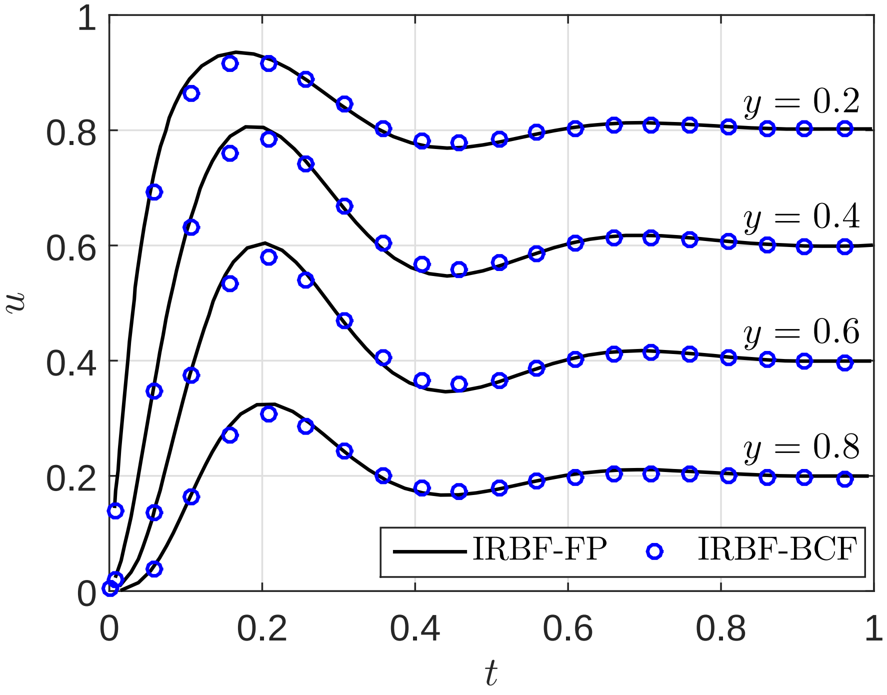

Figure 6.3: Start-up planar Couette flow using a Hookean dumbbell model fluid: the parameters of the problem are number of dumbbells $N = 625$, number of collocation points $N_y = 21$, $\Delta t = 0.01$, Weissenberg Number $We = 0.5$, Reynolds number $Re = 0.1$ and the ratio $\varepsilon = 0.9$. The evolution of the velocity at locations $y \in \{0.2, 0.4, 0.6, 0.8\}$ in comparison with the results of the IRBF-BCF multiscale method by Tran et al. (2011).

The results show a very small difference between the present results and those obtained from the IRBF-BCF method in the unsteady period of the flow.

Fig. 6.4 presents the shear stress at four locations $y \in \{0.2, 0.4, 0.6, 0.8\}$. The results show a significant decrease of noise in the approximation of the stress in comparison with the results by the BCF based method as presented in Fig. 6.5.

Using a coarser distribution of collocation points $(N_y = 15, \Delta t = 0.01)$ and $(N_y = 17, \Delta t = 0.01)$, numerical experiments depict that the present method is able to produce a very high degree of accuracy using a relatively coarse grid.

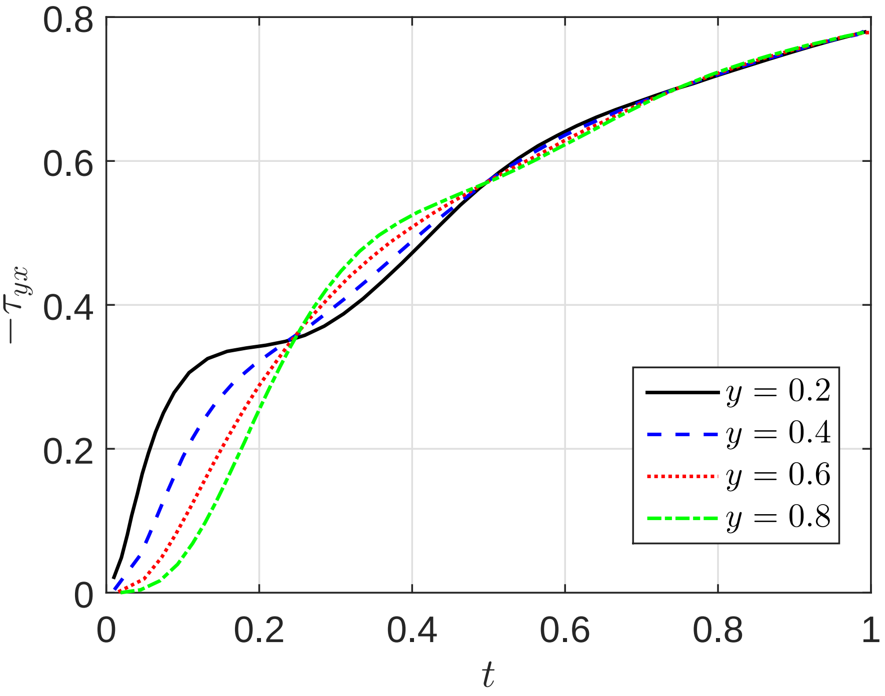

Figure 6.4: Start-up planar Couette flow using a Hookean dumbbell model fluid: the parameters are shown in Fig. 6.1 and the caption of Fig. 6.3. The evolution of shear stress at the locations $y \in \{0.2, 0.4, 0.6, 0.8\}$.

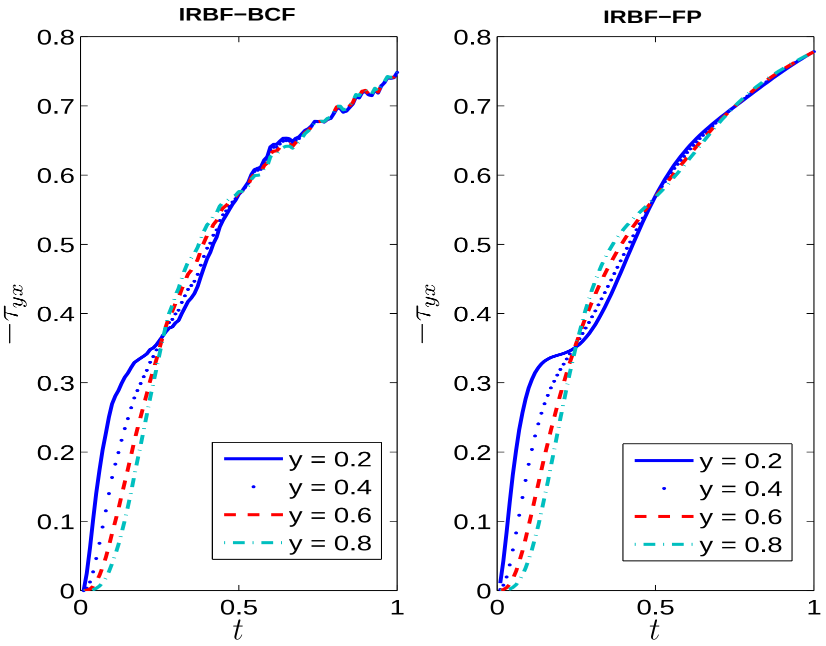

Figure 6.5: Start-up planar Couette flow using a Hookean dumbbell model fluid: the parameters are shown in Fig. 6.1 and the caption of Fig. 6.3. The evolution of shear stress at the locations $y \in \{0.2, 0.4, 0.6, 0.8\}$ in comparison with the results of the IRBF-BCF multiscale method by Tran et al. (2011).

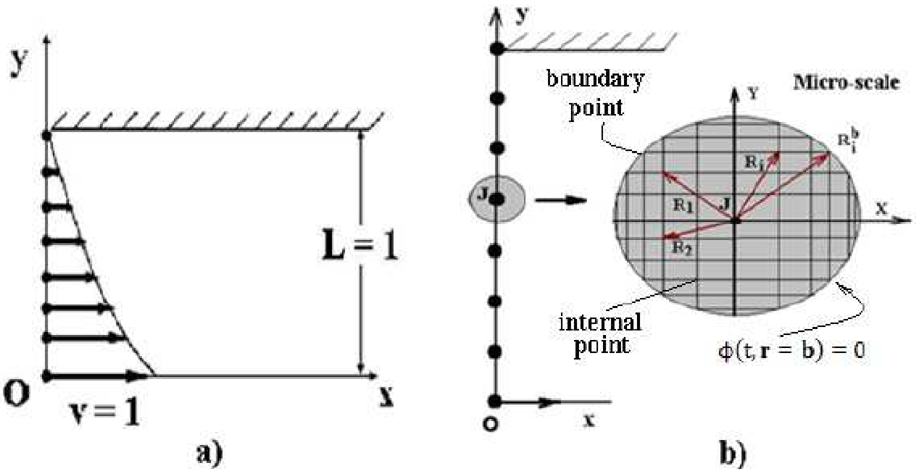

Figure 6.6: a) Start-up planar Couette flow problem using the FENE dumbbell model; b) Discretisation of a 2-D bounded domain of the micro configuration space X, Y developed at a location point y_j: the collocation point distribution is only schematic..

6.4.2 Start-up planar Couette flow with the FENE dumbbell model

The FENE fluid model is considered with the Weissenberg number $We = 49.62$, Reynolds number $Re = 1.2757$, the ratio $\epsilon = 0.9479$ and $b = 50$ as done in Tran et al. (2009) and Laso and Ottinger (1993).

Following manipulation as done in Section 6.4.1, time discretisation of the FPE (6.12) for the FENE model yields

$$\begin{aligned}\gamma\left(\frac{\partial^2\phi^{n+1}}{\partial X^2}+\frac{\partial^2\phi^{n+1}}{\partial Y^2}\right)-\gamma\left(X\frac{\partial\phi^{n+1}}{\partial X}+Y\frac{\partial\phi^{n+1}}{\partial Y}\right)-\phi^{n+1}=&\\ X\frac{\partial u^n}{\partial y}\frac{\partial\phi^n}{\partial X}\Delta t+\left(XF\frac{\partial u^n}{\partial y}\Delta t+1\right)\phi^n&\end{aligned}\tag{6.16}$$

where $\mathbf{F}=\frac{\mathbf{r}}{1-\frac{\|\mathbf{r}\|^2}{b}}$ is for the FENE dumbbell model (Eq. (6.5)) and $\mathbf{r}^2 = X^2+Y^2$. Other parameters was presented before.

At a collocation point, using a grid of N_m collocation points for a bounded circular domain of radii $r = \sqrt{b}$ (Fig. 6.6,b). The vectors $\mathbf{r}_i$, $(\mathbf{r}_i, i = 1, \cdots, N_m)$ correspond to N_m dumbbells. The initial condition and boundary condition of

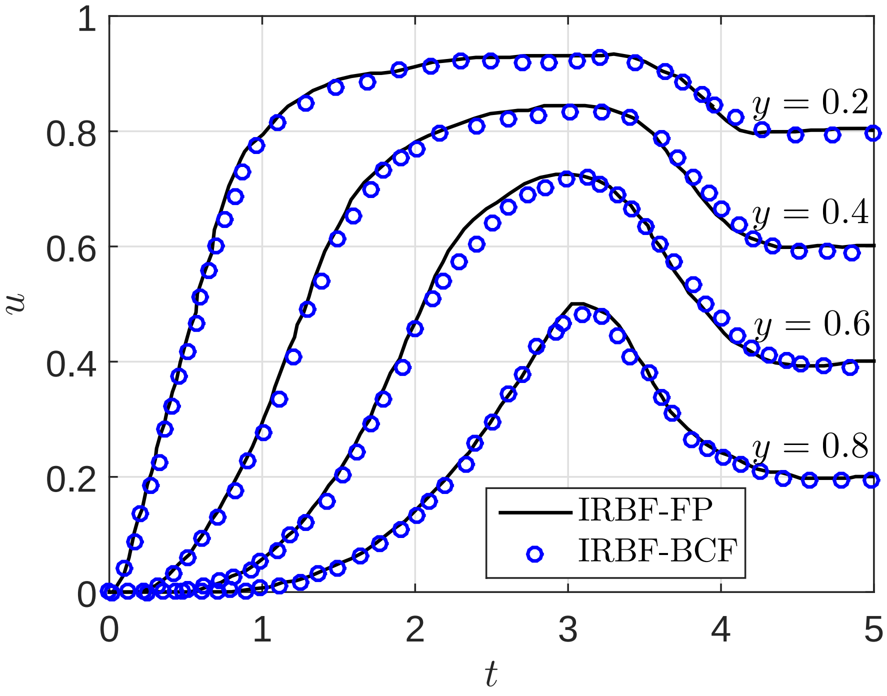

Figure 6.7: Start-up planar Couette flow using FENE dumbbell model fluid: the evolution of velocity at locations $y \in \{0.2, 0.4, 0.6, 0.8\}$.

the density function: $(\phi(0, \mathbf{r}) = 1)$ and $\phi(t, \mathbf{r}) = 0$ $(\|\mathbf{r}\| = \sqrt{b})$.

Following the numerical procedure as presented in Section 6.4.1. Using a time step of $\Delta t = 0.01$ for both macro and micro processes, a coarse spatial discretisation $\Delta y = 0.05$ $(N_y = 21)$ for macro-domain and a grid of $N_m = 341$ collocation points (301 internal points and 40 boundary points) for the configuration domain, the solution obtained by the present method is in good agreement with those by Tran et al. (2011) using the IRBF-BCF approach with a similar discretisation for the macro-scale component and 1000 dumbbells for the micro configuration space. Several observations and typical comparison with others are presented as follows.

Fig. 6.7 depicts evolutions of the velocity and at four locations $y \in \{0.2, 0.4, 0.6, 0.8\}$ and Fig. 6.8 shows the shear stress at the locations $y \in \{0.4, 0.6, 0.8\}$ by the present method. Generally, results are in very good agreement with those by Tran et al. (2011). However, observations show that the evolution of stress approximated by the present method is smoother than those by Tran et al. (2011) using the BCF based scheme with the same parameters.

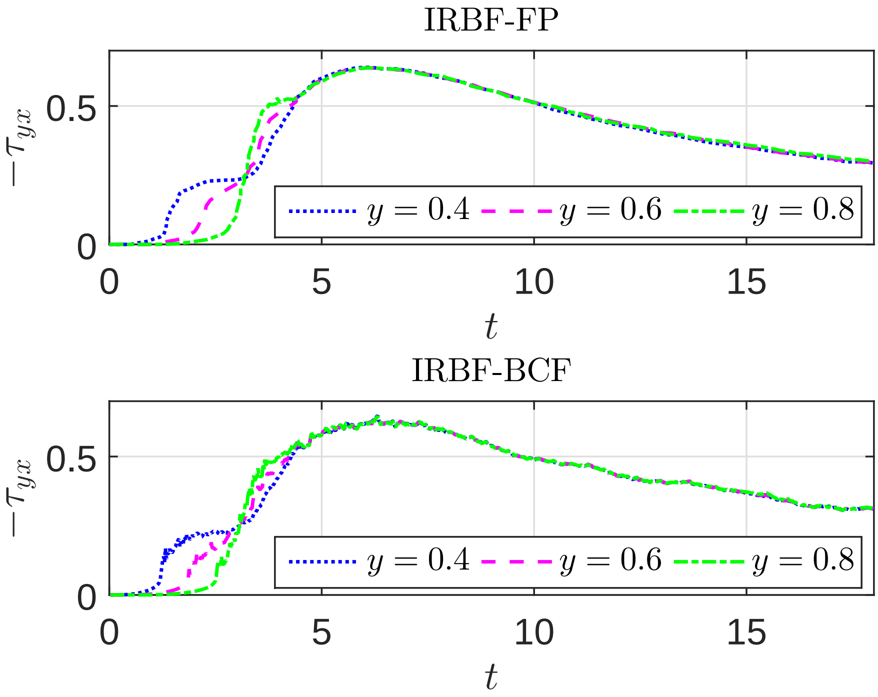

Figure 6.8: Start-up planar Couette flow using FENE dumbbell model fluid: the evolution of shear stress at locations $y \in \{0.4, 0.6, 0.8\}$.

6.5 Conclusions

This chapter reports the use of the 1D-IRBF method to firstly simulate a macro-micro multiscale model of dilute polymer solutions governed by the Fokker-Planck equations and the mass and momentum conservation equations. All governing equations are discretised using the 1D-IRBF collocation method. Although the method requires further investigation, it has several advantages (i) improvement of the approximation accuracy owing to the avoidance of the reduction in convergence rate caused by differentiation; and (ii) significant reduction of noise in the approximation in comparison with the stochastic macro-micro methods via the use of integration as a smoothing operator to construct the approximants.

Chapter 7

Conclusions

This chapter concludes the thesis with a brief summary of the main contributions and achievements of our present research project as well as some suggestions for future works and extensions.

7.1 Research achievements and contributions

Key contributions and achievements of this research project are summarised as follows.

7.1.1 Research contributions

The main contribution of this research project focuses on the further development of IRBF-BCF based multiscale methods for the simulation of complex fluid flows including dilute polymer solution, polymer melt and fibre suspension flows. The contribution is summarised as follows.

- The improvement of the 1D-IRBF-BCF based CG method for the simulation of polymer liquids. For the dilute polymer solutions, the method is investigated through the simulation of complex polymer solutions modelled by the bead spring chains with the presence of the mechanical interactions in polymer chains such as the finitely extensible nonlinear elastic spring force, the hydrodynamic interaction and the excluded volume effects. For polymer melt systems where the stability of numerical methods is a challenge in the simulation, the method efficiency is demonstrated by the successful simulation of polymer melts described by the classical reptation models. These allow the present method to effectively simulate models which are realistic in comparison with experimental results.

- The development of a new multiscale simulation technique based on the fusion of the 1D-IRBFN method, the BCF idea and the DAVSS technique for the simulation of dilute and non-dilute fibre suspensions with a range of $\phi a_r^2 = 1 \div 40$. Numerical experiments confirm the method efficiency evidenced by (i) the enhanced convergence rate of the solution; (ii) the improved stability of the simulation; and (iii) the avoidance of costly meshing processes; only simple Cartesian grids are required to discretise equations.

7.1.2 Research achievements

Details of achievement can be summarised as follows.

A successful enhancement of the 1D-IRBFN-BCF based CG method for the simulation of dilute polymer solutions using the complex nonlinear BSC model

This achievement has been introduced in Chapter 2. Macro conservation equations are temporally discretised with the Crank-Nicolson semi-implicit scheme whereas the Euler explicit is for the SDE. The 1D-IRBFN method is used not only to solve the macro conservation equations but also to approximate the variables and their derivatives (the shear stress and the first normal stress) obtained from the evolution equation for configuration fields. These lead to a significant improvement in the convergence rate and the stability of the method. In addition, the present method efficiently simulate dilute polymer solutions modelled by complex bead-spring chains with the presence of the nonlinear interaction forces

(FENE, HI and EV effects) between beads in the same polymer chain. Thus, the method possesses a capability for the simulation of realistic models of polymers.

A successful simulation of polymer melt systems modelled by the reptation theory using the 1D-IRBFN-BCF multiscale method

This achievement has been presented in Chapter 3. The present CG method has been applied to successfully simulate polymer melt systems described by reptation models including the DE, CB, RR and DR models. Although the stability of numerical methods is always a challenge in the simulation, results by the present multiscale method for the simulation of the start-up planar Couette flow, and the flow past a cylinder in a channel show a very good agreement with those published in the literature. In addition, the simulation of polymer melts with different reptation models allows to investigate the role of several physical interactions of polymers by considering parameters which are introduced in the models.

A successful development of the IRBF-BCF-DAVSS multiscale scheme for the simulation of fibre suspensions

This achievement has been presented in Chapter 4 and Chapter 5 for dilute and non-dilute fibre suspensions, respectively. A new multiscale simulation technique based on the fusion of the 1D-IRBF scheme, the BCF idea and the DAVSS technique has been developed to simulate fibre suspensions in complex flows. In this new approach, the macro differential equations are written in the vorticity-stream function formulation. The resulting vorticity transport equation is then integrated with the DAVSS technique to enhance the stability of the 1D-IRBF approximation method. For the micro procedure while the evolution of fibre configurations is captured by the Jeffery equation for dilute fibre suspensions, the Folgar-Tucker equation is used for non-dilute fibre suspensions. The Lipscomb and the Phan-Thien–Graham models are used to determined the fibre stress tensor for the dilute and non-dilute suspensions, respectively. The efficiency of the present method based on the improved convergence rate and accuracy, and the enhanced stability of the simulation, evidenced by results as stated in these chapters. As an illustration, the stability and accuracy of the method have been verified with several numerical examples including challenging problems such as the 4:1 and 4.5:1 axisymmetric contraction and the 1:4 expansion flows. The obtained results are in very good agreement with ones in the literature. In particular, our numerical experiments discover several interesting dynamic behaviours of fibre solutions flows, for example, the secondary vortex in the 4:1 axisymmetric contraction flow or the lip vortex in the 1:4 axisymmetric expansion flow for the highly concentrated fibre suspension (Chapter 5).

An initial success in the simulation of polymer solutions governed by the FPE using the 1D-IRBF scheme

This achievement has been presented in Chapter 6. The conservation equation and the FPE are temporally discretised using a θ method. At a time step, both of them are then spatially discretised using the 1D-IRBF collocation method. While the MQ-IRBF is used for the conservation equations, the G-IRBF is for the FPE. Although more investigations are necessary, the initial results show that the method benefits (i) the enhanced numerical stability in solving the FPE, and (ii) the increased convergence rate of the method.

7.2 Possible future works

Several possible future works include

- A development of parallel algorithms for both macro and micro procedures based on Domain Decomposition method. The algorithm as expected will help reduce the computational time as well as further improve the stability of the present method.
- A further development of the 1D-IRBFN-based method for the solution of

both the deterministic and stochastic evolution equations of coarse-grained models, especially for the FPE based macro-micro multiscale approach.

- An application of the present multiscale simulation scheme in simulating several real problems in the biology and/or food security.

Appendix A

Radial Basis Functions

A.1 Some well known RBFs

The following are several commonly used RBFs.

- **Gaussian-RBF**

$$g_j(r, b_j) = g_j(\|\mathbf{x} - \mathbf{c}_j\|, a_j) = \exp\left(-\frac{r^2}{(a_j)^2}\right), \tag{A.1}$$

- **Multiquadrics RBF (MQ-RBF)**

$$g_j(r, a_j) = g_j(\|\mathbf{x} - \mathbf{c}_j\|, a_j) = \sqrt{r^2 + (a_j)^2}, \tag{A.2}$$

- **Inverse multiquadrics RBF (IMQ-RBF)**

$$g_j(r, a_j) = g_j(\|\mathbf{x} - \mathbf{c}_j\|, a_j) = \frac{1}{\sqrt{r^2 + (a_j)^2}}, \tag{A.3}$$

- **Thin-plate splines RBF (TPS-RBF)**

$$g_j(r) = g_j(\|\mathbf{x} - \mathbf{c}_j\|) = r^{2s}\log(r), \qquad s = 1, 2, ..., \tag{A.4}$$

- **Compact support RBF (CS-RBF)**

$$g_j(r) = g_j(\|\mathbf{x} - \mathbf{c}_j\|) = (1 - r)_+^l p(r), \qquad l = 1, 2, ..., \tag{A.5}$$

where $\mathbf{x}$ is the field points, $\mathbf{c}_j$ and a_j the centre and width of RBF at the jth node, s the order of TPS-RBF, and $p(r)$ is a polynomial of Wendland CS-RBF (Wendland, 1995, 1998). While the MQ-RBF, TPS-RBF and CS-RBF exhibit a global response, i.e. they increase monotonically with increasing distance from the centre, the Gaussian-RBF and IMQ-RBF have a local response (localised function) (Haykin, 1998; Beatson and Light, 1997). RBFs are multivariate as a function of $\mathbf{x} \in \mathbf{R}^d$, but univariate as a function of r, which should be a tremendous computational advantage if the space dimension is large.

A.2 MQ-RBFs from integration process

For the 1D-IRBF scheme used in this research project, the one-dimensional MQ-RBF has been chosen for the approximate process of the original function and its derivatives and written as

$$G_j^{[2]} = g_j\left(x\right) = \sqrt{(x - c_j)^2 + a_j^2}, \tag{A.6}$$

The new basis functions obtained from integrating the MQ-RBF are as follows.

$$\begin{aligned} G_j^{[1]}\left(x\right) &= \int G_j^{[2]}\left(x\right) dx \\ &= \frac{r}{2} A + \frac{(a_i)^2}{2} B, \end{aligned} \tag{A.7}$$

$$\begin{aligned} G_j^{[0]}(x) &= \int G_j^{[1]}(x)\,dx \\ &= \left(\frac{r^2}{6} - \frac{(a_i)^2}{3}\right) A + \frac{(a_i)^2 r}{2} B, \end{aligned} \tag{A.8}$$

where $r = x - c_i$, $A = \sqrt{r^2 + (a_i)^2}$, and $B = \ln(r + A)$.

Appendix B

Tensor products

B.1 Dyadic products

B.1.1 In 2-D space

Let $\mathbf{a} = \{a_1, a_2\}^T$, $\mathbf{b} = \{b_1, b_2\}^T$, $\mathbf{c} = \{c_1, c_2\}^T$ and $\mathbf{d} = \{d_1, d_2\}^T$ be vectors in 2D space. The dyadic product of two vectors **a** and **a** denoted as **ab** or $\mathbf{a} \otimes \mathbf{b}$ is a second-order tensor and defined as follows.

$$\mathbf{ab} = \left\{ \begin{array}{c} a_1 \\ a_2 \end{array} \right\} \left\{ \begin{array}{c} b_1 \\ b_2 \end{array} \right\} = \begin{bmatrix} a_1 b_1 & a_1 b_2 \\ a_2 b_1 & a_2 b_2 \end{bmatrix} \tag{B.1}$$

The dyadic product of four vectors **abcd** is a fourth-order tensor and given by

$$\begin{aligned} \mathbf{abcd} &= \left\{ \begin{array}{c} a_1 \\ a_2 \end{array} \right\} \left\{ \begin{array}{c} b_1 \\ b_2 \end{array} \right\} \left\{ \begin{array}{c} c_1 \\ c_2 \end{array} \right\} \left\{ \begin{array}{c} d_1 \\ d_2 \end{array} \right\} = \begin{bmatrix} a_1 b_1 & a_1 b_2 \\ a_2 b_1 & a_2 b_2 \end{bmatrix} \begin{bmatrix} c_1 d_1 & c_1 d_2 \\ c_2 d_1 & c_2 d_2 \end{bmatrix} \\ &= \begin{bmatrix} a_1 b_1 c_1 d_1 & a_1 b_1 c_1 d_2 & a_1 b_2 c_1 d_1 & a_1 b_2 c_1 d_2 \\ a_1 b_1 c_2 d_1 & a_1 b_1 c_2 d_2 & a_1 b_2 c_2 d_1 & a_1 b_2 c_2 d_2 \\ a_2 b_1 c_1 d_1 & a_2 b_1 c_1 d_2 & a_2 b_2 c_1 d_1 & a_2 b_2 c_1 d_2 \\ a_2 b_1 c_2 d_1 & a_2 b_1 c_2 d_2 & a_2 b_2 c_2 d_1 & a_2 b_2 c_2 d_2 \end{bmatrix} \end{aligned} \tag{B.2}$$

It is worth noting that the double dot product is only between tensors whose order is two or higher. The double dot product of two second-order tensors is a scalar whereas the product between the second and fourth-order tensors is a second-order tensor.

B.1.2 In 3-D space

Let $\mathbf{a} = \{a_1, a_2, a_3\}^T$, $\mathbf{b} = \{b_1, b_2, b_3\}^T$, $\mathbf{c} = \{c_1, c_2, c_3\}^T$ and $\mathbf{d} = \{d_1, d_2, d_3\}^T$ be vectors in 3-D space, the dyadic products **ab** and **abcd** are written, respectively as follows.

$$\mathbf{ab} = \begin{bmatrix} a_1b_1 & a_1b_2 & a_1b_3 \\ a_2b_1 & a_2b_2 & a_2b_3 \\ a_3b_1 & a_3b_2 & a_3b_3 \end{bmatrix} \tag{B.3}$$

$$
\begin{aligned}
\mathbf{abcd} = & \left[\begin{array}{cccccc}
a_1b_1c_1d_1 & a_1b_1c_1d_2 & a_1b_1c_1d_3 & a_1b_2c_1d_1 & a_1b_2c_1d_2 & a_1b_2c_1d_3 \\
a_1b_1c_2d_1 & a_1b_1c_2d_2 & a_1b_1c_2d_3 & a_1b_2c_2d_1 & a_1b_2c_2d_2 & a_1b_2c_2d_3 \\
a_1b_1c_3d_1 & a_1b_1c_3d_2 & a_1b_1c_3d_3 & a_1b_2c_3d_1 & a_1b_2c_3d_2 & a_1b_2c_3d_3 \\
a_2b_1c_1d_1 & a_2b_1c_1d_2 & a_2b_1c_1d_3 & a_2b_2c_1d_1 & a_2b_2c_1d_2 & a_2b_2c_1d_3 \\
a_2b_1c_2d_1 & a_2b_1c_2d_2 & a_2b_1c_2d_3 & a_2b_2c_2d_1 & a_2b_2c_2d_2 & a_2b_2c_2d_3 \\
a_2b_1c_3d_1 & a_2b_1c_3d_2 & a_2b_1c_3d_3 & a_2b_2c_3d_1 & a_2b_2c_3d_2 & a_2b_2c_3d_3 \\
a_3b_1c_1d_1 & a_3b_1c_1d_2 & a_3b_1c_1d_3 & a_3b_2c_1d_1 & a_3b_2c_1d_2 & a_3b_2c_1d_3 \\
a_3b_1c_2d_1 & a_3b_1c_2d_2 & a_3b_1c_2d_3 & a_3b_2c_2d_1 & a_3b_2c_2d_2 & a_3b_2c_2d_3 \\
a_3b_1c_3d_1 & a_3b_1c_3d_2 & a_3b_1c_3d_3 & a_3b_2c_3d_1 & a_3b_2c_3d_2 & a_3b_2c_3d_3
\end{array}\right. \\
& \qquad \left.\begin{array}{ccc}
a_1b_3c_1d_1 & a_1b_3c_1d_2 & a_1b_3c_1d_3 \\
a_1b_3c_2d_1 & a_1b_3c_2d_2 & a_1b_3c_2d_3 \\
a_1b_3c_3d_1 & a_1b_3c_3d_2 & a_1b_3c_3d_3 \\
a_2b_3c_1d_1 & a_2b_3c_1d_2 & a_2b_3c_1d_3 \\
a_2b_3c_2d_1 & a_2b_3c_2d_2 & a_2b_3c_2d_3 \\
a_2b_3c_3d_1 & a_2b_3c_3d_2 & a_2b_3c_3d_3 \\
a_3b_3c_1d_1 & a_3b_3c_1d_2 & a_3b_3c_1d_3 \\
a_3b_3c_2d_1 & a_3b_3c_2d_2 & a_3b_3c_2d_3 \\
a_3b_3c_3d_1 & a_3b_3c_3d_2 & a_3b_3c_3d_3
\end{array}\right]
\end{aligned}
\tag{B.4}
$$

B.2 Double dot product

Consider two second-order tensors $\mathbf{A}$ and $\mathbf{B}$ and a fourth-order tensor $\boldsymbol{\Omega}$. The products $\mathbf{A} : \mathbf{B}$ and $\boldsymbol{\Omega} : \mathbf{A}$ are explicitly written in 2D and 3D spaces as follows.

B.2.1 In 2-D space

$$\mathbf{A} : \mathbf{B} = A_{11}B_{11} + A_{12}B_{12} + A_{21}B_{21} + A_{22}B_{22}, \tag{B.5}$$

$$\mathbf{E} = \boldsymbol{\Omega} : \mathbf{A} = \begin{bmatrix} E_{11} & E_{12} \\ E_{21} & E_{22} \end{bmatrix}, \tag{B.6}$$

where the components of the tensor $\mathbf{E}$ are defined by

$$\begin{aligned}
E_{11} &= \Omega_{1111}A_{11} + \Omega_{1112}A_{21} + \Omega_{1121}A_{12} + \Omega_{1122}A_{22},\\
E_{12} &= \Omega_{1211}A_{11} + \Omega_{1212}A_{21} + \Omega_{1221}A_{12} + \Omega_{1222}A_{22},\\
E_{21} &= \Omega_{2111}A_{11} + \Omega_{2112}A_{21} + \Omega_{2121}A_{12} + \Omega_{2122}A_{22},\\
E_{22} &= \Omega_{2211}A_{11} + \Omega_{2212}A_{21} + \Omega_{2221}A_{12} + \Omega_{2222}A_{22}.
\end{aligned}$$

B.2.2 In 3-D space

$$\begin{gathered}
\mathbf{A} : \mathbf{B} = A_{11}B_{11} + A_{12}B_{12} + A_{13}B_{13} + A_{21}B_{21} + \\
A_{22}B_{22} + A_{23}B_{23} + A_{31}B_{31} + A_{32}B_{32} + A_{33}B_{33},
\end{gathered} \tag{B.7}$$

$$\mathbf{E} = \boldsymbol{\Omega} : \mathbf{A} = \begin{bmatrix} E_{11} & E_{12} & E_{13} \\ E_{21} & E_{22} & E_{23} \\ E_{31} & E_{32} & E_{33} \end{bmatrix}, \tag{B.8}$$

where the components of the tensor **E** are defined by

$$
\begin{aligned}
E_{11} =& \Omega_{1111}A_{11} + \Omega_{1112}A_{21} + \Omega_{1113}A_{31} + \Omega_{1121}A_{12} + \\
& \Omega_{1122}A_{22} + \Omega_{1123}A_{32} + \Omega_{1131}A_{13} + \Omega_{1132}A_{23} + \Omega_{1133}A_{33}, \\
E_{12} =& \Omega_{1211}A_{11} + \Omega_{1212}A_{21} + \Omega_{1213}A_{31} + \Omega_{1221}A_{12} + \\
& \Omega_{1222}A_{22} + \Omega_{1223}A_{32} + \Omega_{1231}A_{13} + \Omega_{1232}A_{23} + \Omega_{1233}A_{33}, \\
E_{13} =& \Omega_{1311}A_{11} + \Omega_{1312}A_{21} + \Omega_{1313}A_{31} + \Omega_{1321}A_{12} + \\
& \Omega_{1322}A_{22} + \Omega_{1323}A_{32} + \Omega_{1331}A_{13} + \Omega_{1332}A_{23} + \Omega_{1333}A_{33} \\
E_{21} =& \Omega_{2111}A_{11} + \Omega_{2112}A_{21} + \Omega_{2113}A_{31} + \Omega_{2121}A_{12} + \\
& \Omega_{2122}A_{22} + \Omega_{2123}A_{32} + \Omega_{2131}A_{13} + \Omega_{2132}A_{23} + \Omega_{2133}A_{33}, \\
E_{22} =& \Omega_{2211}A_{11} + \Omega_{2212}A_{21} + \Omega_{2213}A_{31} + \Omega_{2221}A_{12} + \\
& \Omega_{2222}A_{22} + \Omega_{2223}A_{32} + \Omega_{2231}A_{13} + \Omega_{2232}A_{23} + \Omega_{2233}A_{33}, \\
E_{23} =& \Omega_{2311}A_{11} + \Omega_{2312}A_{21} + \Omega_{2313}A_{31} + \Omega_{2321}A_{12} + \\
& \Omega_{2322}A_{22} + \Omega_{2323}A_{32} + \Omega_{2331}A_{13} + \Omega_{2332}A_{23} + \Omega_{2333}A_{33}, \\
E_{31} =& \Omega_{3111}A_{11} + \Omega_{3112}A_{21} + \Omega_{3113}A_{31} + \Omega_{3121}A_{12} + \\
& \Omega_{3122}A_{22} + \Omega_{3123}A_{32} + \Omega_{3131}A_{13} + \Omega_{3132}A_{23} + \Omega_{3133}A_{33}, \\
E_{32} =& \Omega_{3211}A_{11} + \Omega_{3212}A_{21} + \Omega_{3213}A_{31} + \Omega_{3221}A_{12} + \\
& \Omega_{3222}A_{22} + \Omega_{3223}A_{32} + \Omega_{3231}A_{13} + \Omega_{3232}A_{23} + \Omega_{3233}A_{33}, \\
E_{33} =& \Omega_{3311}A_{11} + \Omega_{3312}A_{21} + \Omega_{3313}A_{31} + \Omega_{3321}A_{12} + \\
& \Omega_{3322}A_{22} + \Omega_{3323}A_{32} + \Omega_{3331}A_{13} + \Omega_{3332}A_{23} + \Omega_{3333}A_{33}.
\end{aligned}
$$

References

Abdul-Karem, T., Binding, D. M., and Sindelar, M. (1993). Contraction and expansion flows of non-Newtonian fluids. *Composites Manufacturing*, 4(2):109–116.

Advani, S. G. and Tucker III, C. L. (1987). The use of tensors to describe and predict fiber orientation in short fiber composites. *Journal of Rheology*, 31(8):751–784.

Advani, S. G. and Tucker III, C. L. (1990). Closure approximations for three-dimensional structure tensors. *Journal of Rheology*, 34(3):367–386.

Aksel, N. (2002). A brief note from the editor on the "second-order fluid". *Acta Mechanica*, 157(1):235–236.

Ammar, A., Mokdad, B., Chinesta, F., and Keunings, R. (2006). A new family of solvers for some classes of multidimensional partial differential equations encountered in kinetic theory modeling of complex fluids. *Journal of Non-Newtonian Fluid Mechanics*, 139(3):153–176.

Ammar, A., Mokdad, B., Chinesta, F., and Keunings, R. (2007). A new family of solvers for some classes of multidimensional partial differential equations encountered in kinetic theory modelling of complex fluids: Part II: Transient simulation using space-time separated representations. *Journal of Non-Newtonian Fluid Mechanics*, 144(2):98–121.

An-Vo, D. A., Mai-Duy, N., and Tran-Cong, T. (2011). A C2-continuous control-volume technique based on cartesian grids and two-node integrated-RBF elements for second-order elliptic problems. *CMES: Computer Modeling in Engineering & Sciences*, 72(4):299–334.

Avgousti, M., Liu, B., and Beris, A. N. (1993). Spectral methods for the viscoelastic time-dependent flow equations with applications to Taylor-Couette flow. *International Journal for Numerical Methods in Fluids*, 17(1):49–74.

Baaijens, F. P. T. (1998). Mixed finite element methods for viscoelastic flow analysis: a review. *Journal of Non-Newtonian Fluid Mechanics*, 79(2):361–385.

Baloch, A., Townsend, P., and Webster, M. F. (1995). On two- and three-dimensional expansion flows. *Computers & Fluids*, 24(8):863–882.

Baloch, A., Townsend, P., and Webster, M. F. (1996). On vortex development in viscoelastic expansion and contraction flows. *Journal of Non-Newtonian Fluid Mechanics*, 65(2):133–149.

Baloch, A. and Webster, M. F. (1995). A computer simulation of complex flows of fibre suspensions. *Computers & Fluids*, 24(2):135–151.

Barone, M. R. and Tucker, C. L. (1989). *Fundamentals of Computer Modeling for Polymer Processing*. Hanser.

Beatson, R. K. and Light, W. A. (1997). Fast evaluation of radial basis functions: methods for two-dimensional polyharmonic splines. *IMA Journal of Numerical Analysis*, 17(3):343–372.

Bell, T. W., Nyland, G. H., De Pablo, J. J., and Graham, M. D. (1997). Combined Brownian dynamics and spectral simulation of the recovery of polymeric fluids after shear flow. *Macromolecules*, 30(6):1806–1812.

Beris, A. N., Avgousti, M., and Souvaliotis, A. (1992). Spectral calculations of viscoelastic flows: evaluation of the Giesekus constitutive equation in model flow problems. *Journal of Non-Newtonian Fluid Mechanics*, 44:197–228.

Bernal, F. and Kindelan, M. (2007). RBF meshless modeling of non-Newtonian Hele-Shaw flow. *Engineering Analysis with Boundary Elements*, 31(10):863–874.

Bernstein, B., Kearsley, E. A., and Zapas, L. J. (1963). A study of stress relaxation with finite strain. *Transactions of The Society of Rheology*, 7(1):391–410.

Bird, R. B., Armstrong, R. C., and Hassager, O. (1987a). *Dynamics of Polymer Liquids, Volume 1: Fluid mechanics*. New York: John Wiley & Sons.

Bird, R. B., Curtiss, C. F., Armstrong, R. C., and Hassager, O. (1987b). *Dynamics of Polymer Liquids, Volume 2: Kinetic theory*. New York: John Wiley & Sons.

Bird, R. B., Saab, H. H., and Curtiss, C. F. (1982a). A kinetic theory for polymer melts. III. Elongational flows. *The Journal of Physical Chemistry*, 86(7):1102–1106.

Bird, R. B., Saab, H. H., and Curtiss, C. F. (1982b). A kinetic theory for polymer melts. IV. Rheological properties for shear flows. *The Journal of Chemical Physics*, 77:4747–4757.

Brebbia, C. A., Telles, J. C. F., and Wrobel, L. C. (1984). *Boundary Element Techniques: Theory and Applications in Engineering*. Berlin: Springer-Verlag.

Canuto, C., Hussaini, M. Y., Quarteroni, A., and Zang, T. A. (1988). *Spectral Methods in Fluid Dynamics*. Berlin: Springer-Verlag.

Chauviere, C. and Lozinski, A. (2004a). Simulation of complex viscoelastic flows using the Fokker-Planck equation: 3D FENE model. *Journal of Non-Newtonian Fluid Mechanics*, 122(1):201–214.

Chauviere, C. and Lozinski, A. (2004b). Simulation of dilute polymer solutions using a Fokker-Planck equation. *Computers & Fluids*, 33(5):687–696.

Chauviere, C. and Owens, R. G. (2002). A robust spectral element method for simulations of time-dependent viscoelastic flows, derived from the Brownian configuration field method. *Journal of Scientific Computing*, 17(1-4):191–199.

Chiba, K. and Nakamura, K. (1998). Numerical solution of fiber suspension flow through a complex channel. *Journal of Non-Newtonian Fluid Mechanics*, 78(2):167–185.

Chiba, K., Nakamura, K., and Boger, D. V. (1990). A numerical solution for the flow of dilute fiber suspensions through an axisymmetric contraction. *Journal of Non-Newtonian Fluid Mechanics*, 35(1):1–14.

Chiba, K., Yasuda, K., and Nakamura, K. (2001). Numerical solution of fiber suspension flow through a parallel plate channel by coupling flow field with fiber orientation distribution. *Journal of Non-Newtonian Fluid Mechanics*, 99(2):145–157.

Chinesta, F. and Ausias, G. (2015). *Rheology of Non-spherical Particle Suspensions*. Elsevier.

Chung, D. H. and Kwon, T. H. (2001). Improved model of orthotropic closure approximation for flow induced fiber orientation. *Polymer Composites*, 22(5):636–649.

Chung, D. H. and Kwon, T. H. (2002). Invariant-based optimal fitting closure approximation for the numerical prediction of flow-induced fiber orientation. *Journal of Rheology*, 46(1):169–194.

Chung, T. J. (1978). Finite element analysis in fluid dynamics. *NASA STI/Recon Technical Report A*, 78:44102.

Cintra Jr, J. S. and Tucker III, C. L. (1995). Orthotropic closure approximations for flow-induced fiber orientation. *Journal of Rheology*, 39(6):1095–1122.

Crochet, M. J., Davies, A. R., and Walters, K. (1984). *Numerical Simulation of Non-Newtonian Flow*. Amsterdam: Elsevier.

Cruz, C., Chinesta, F., and Regnier, G. (2012). Review on the Brownian Dynamics Simulation of Bead-Rod-Spring Models Encountered in Computational Rheology. *Archives of Computational Methods in Engineering*, 19(2):227–259.

Curtiss, C. F. and Bird, R. B. (1981a). A kinetic theory for polymer melts. I. The equation for the single-link orientational distribution function. *The Journal of Chemical Physics*, 74:2016–2025.

Curtiss, C. F. and Bird, R. B. (1981b). A kinetic theory for polymer melts. II. The stress tensor and the rheological equation of state. *The Journal of Chemical Physics*, 74:2026–2033.

de Gennes, P. G. (1971). Reptation of a polymer chain in the presence of fixed obstacles. *The Journal of Chemical Physics*, 55:572–579.

des Cloizeaux, J. (1988). Double Reptation vs. Simple Reptation in Polymer Melts. *Europhysics Letters*, 5:437–442.

Dinh, S. M. and Armstrong, R. C. (1984). A rheological equation of state for semiconcentrated fiber suspensions. *Journal of Rheology*, 28:207.

Doi, M. and Edwards, S. F. (1978a). Dynamics of concentrated polymer systems. Part 1. Brownian motion in the equilibrium state. *Journal of the Chemical Society, Faraday Transactions 2*, 74:1789–1801.

Doi, M. and Edwards, S. F. (1978b). Dynamics of concentrated polymer systems. Part 2. Molecular motion under flow. *Journal of the Chemical Society, Faraday Transactions 2: Molecular and Chemical Physics*, 74:1802–1817.

Doi, M. and Edwards, S. F. (1978c). Dynamics of concentrated polymer systems. Part 3. The constitutive equation. *Journal of the Chemical Society, Faraday Transactions 2*, 74:1818–1832.

Dou, H.-S., Khoo, B. C., Phan-Thien, N., Yeo, K. S., and Zheng, R. (2007). Simulations of fibre orientation in dilute suspensions with front moving in the filling process of a rectangular channel using level-set method. *Rheologica Acta*, 46(4):427–447.

Dupret, F., Verleye, V., and Languillier, B. (1997). Numerical prediction of the molding of composite parts. *ASME-PUBLICATIONS-FED*, 243:79–90.

Engquist, B., Lotstedt, P., and Runborg, O. (2009). *Multiscale Modeling and Simulation in Science*, volume 66. Springer Science.

Ericksen, J. L. (1960). Transversely isotropic fluids. *Colloid and Polymer Science*, 173(2):117–122.

Fan, X. J. (2006). *Numerical Study on Some Rheological Problems of Fibre Suspensions*. PhD thesis, The University of Sydney.

Fan, X.-J., Phan-Thien, N., and Zheng, R. (1998). Completed double layer boundary element method for periodic suspensions. *Journal of Applied Mathematics and Physics*, 49(2):167–193.

Fan, X.-J., Phan-Thien, N., and Zheng, R. (1999). Simulation of fibre suspension flows by the Brownian configuration field method. *Journal of Non-Newtonian Fluid Mechanics*, 84(2):257–274.

Fan, X.-J., Phan-Thien, N., and Zheng, R. (2000). Simulation of fibre suspension flow with shear-induced migration. *Journal of Non-Newtonian Fluid Mechanics*, 90(1):47–63.

Fasshauer, G. E. (2007). *Meshfree Approximation Methods with Matlab.* Singapore: World Scientific Publishers.

Ferreira, V. G., Tome, M. F., Mangiavacchi, N., Castelo, A., Cuminato, J. A., Fortuna, A. O., and McKee, S. (2002). High-order upwinding and the hydraulic jump. *International Journal for Numerical Methods in Fluids*, 39(7):549–583.

Folgar, F. and Tucker, C. L. (1984). Orientation behavior of fibers in concentrated suspensions. *Journal of Reinforced Plastics & Composites*, 3(2):98–119.

Folkes, M. J. (1982). *Short Fibre Reinforced Thermoplastics.* New York: Research Studies Press, Wiley.

Franke, R. (1982). Scattered data interpolation: tests of some methods. *Mathematics of Computation*, 38(157):181–200.

Fu, C.-Q., Jiang, H.-M., Yin, H.-J., Su, Y.-C., and Zeng, Y.-M. (2009). Finite volume method for simulation of viscoelastic flow through a expansion channel. *Journal of Hydrodynamics, Ser. B*, 21(3):360–365.

Ganvir, V., Lele, A., Thaokar, R., and Gautham, B. P. (2007). Simulation of viscoelastic flows of polymer solutions in abrupt contractions using an arbitrary Lagrangian Eulerian (ALE) based finite element method. *Journal of Non-Newtonian Fluid Mechanics*, 143(2):157–169.

Gardiner, C. W. (2004). *Handbook of Stochastic Mechanics.* New York: Springer.

Gheorghiu, C. I. (2007). *Spectral Methods for Differential Problems.* Romani: Casa Cartii de Stiinta.

Girault, V. and Raviart, P.-A. (1979). An analysis of a mixed finite element method for the Navier-Stokes equations. *Numerische Mathematik*, 33(3):235–271.

Givler, R. C. (1981). Numerically predicted fiber orientations in dilute suspensions. Technical report, DTIC Document.

Givler, R. C., Crochet, M. J., and Pipes, R. B. (1983). Numerical prediction of fiber orientation in dilute suspensions. *Journal of Composite Materials*, 17(4):330–343.

Goettler, L. A., Lambright, A. J., Leib, R. I., and Dimauro, P. J. (1981). Extrusion-shaping of curved hose reinforced with short cellulose fibers. *Rubber Chemistry and Technology*, 54(2):277–301.

Goettler, L. A., Leib, R. I., and Lambright, A. J. (1979). Short fiber reinforced hose-A new concept in production and performance. *Rubber Chemistry and Technology*, 52(4):838–863.

Griebel, M. and Ruttgers, A. (2014). Multiscale simulations of three-dimensional viscoelastic flows in a square-square contraction. *Journal of Non-Newtonian Fluid Mechanics*, 205:41–63.

Hand, G. L. (1962). A theory of anisotropic fluids. *Journal of Fluid Mechanics*, 13(01):33–46.

Hardy, R. L. (1971). Multiquadric equations of topography and other irregular surfaces. *Journal of Geophysical Research*, 76(8):1905–1915.

Haykin, S. (1998). *Neural Networks: A Comprehensive Foundation*. Prentice Hall PTR.

Henderson, D. and Plaschko, P. (2006). *Stochastic Differential Equations in Science and Engineering*, volume 1. World Scientific Pub.

Herrchen, M. and Ottinger, H. C. (1997). A detailed comparison of various FENE dumbbell models. *Journal of Non-Newtonian Fluid Mechanics*, 68(1):17–42.

Hinch, E. J. and Leal, L. G. (1975). Constitutive equations in suspension mechanics. Part 1. General formulation. *Journal of Fluid Mechanics*, 71(3):481–495.

Hinch, E. J. and Leal, L. G. (1976). Constitutive equations in suspension mechanics. Part 2. Approximate forms for a suspension of rigid particles affected by Brownian rotations. *Journal of Fluid Mechanics*, 76(1):187–208.

Hirsch, C. (2007). *Numerical Computation of Internal and External Flows: The Fundamentals of Computational Fluid Dynamics*, volume 1. Butterworth-Heinemann.

Ho-Minh, D., Mai-Duy, N., and Tran-Cong, T. (2010). Galerkin/collocation methods based on 1D-integrated-RBFNs for viscoelastic flows. *CMES: Computer Modeling in Engineering & Sciences*, 70(3):217–251.

Hoang-Trieu, T.-T., Mai-Duy, N., and Tran-Cong, T. (2012). Several compact local stencils based on integrated RBFs for fourth-order ODEs and PDEs. *CMES: Computer Modeling in Engineering & Sciences*, 84(2):171–203.

Hua, C. C. and Schieber, J. D. (1996). Application of kinetic theory models in spatiotemporal flows for polymer solutions, liquid crystals and polymer melts using the CONNFFESSIT approach. *Chemical Engineering Science*, 51:1473–1485.

Hua, C. C. and Schieber, J. D. (1998). Viscoelastic flow through fibrous media using the CONNFFESSIT approach. *Journal of Rheology*, 42:477–491.

Hulsen, M. A., Van Heel, A. P. G., and Van Den Brule, B. H. A. A. (1997). Simulation of viscoelastic flows using Brownian configuration fields. *Journal of Non-Newtonian Fluid Mechanics*, 70(1):79–101.

Hunter, P. and Pullan, A. (2001). *FEM/BEM Notes*. Department of Engineering Science, The University of Auckland, New Zeland.

Jack, D. A., Schache, B., and Smith, D. E. (2010). Neural network-based closure for modeling short-fiber suspensions. *Polymer Composites*, 31(7):1125–1141.

Jafari, A. (2011). *Simulation of Time-Dependent Viscoelastic Fluid Flows by Spectral Elements*. PhD thesis, Ecole Polytechnique Federale de Lausanne.

Jeffery, G. B. (1922). The motion of ellipsoidal particles immersed in a viscous fluid. *Proceedings of the Royal Society of London. Series A, Containing papers of a mathematical and physical character*, pages 161–179.

Jongschaap, R. J. J. (1988). *Some Comments on Reptation Theories*, pages 99–102. Springer.

Jongschaap, R. J. J. and Geurts, B. J. (1988). A New Reptation Model for Polymeric Liquids. In Lemstra, P. J. and Kleintjens, L. A., editors, *Integration of Fundamental Polymer Science and Technology*, chapter 69, pages 461–465. Netherlands: Springer.

Jourdain, B., Lelievre, T., and Le Bris, C. (2002). Numerical analysis of micro-macro simulations of polymeric fluid flows: A simple case. *Mathematical Models & Methods in Applied Sciences*, 12(09):1205–1243.

Kansa, E. J. (1990). Multiquadrics–A scattered data approximation scheme with applications to computational fluid dynamics–II: solutions to parabolic, hyperbolic and elliptic partial differential equations. *Computers & Mathematics with Applications*, 19(8):147–161.

Kaye, A. (1962). Non-Newtonian flow in incompressible fluids. Technical report, College of Aeronautics Cranfield.

Keentok, M., Georgescu, A. G., Sherwood, A. A., and Tanner, R. I. (1980). The measurement of the second normal stress difference for some polymer solutions. *Journal of Non-Newtonian Fluid Mechanics*, 6(34):303–324.

Keunings, R. (2004). Micro-macro methods for the multiscale simulation of viscoelastic flow using molecular models of kinetic theory. *Rheology Reviews*, pages 67–98.

Kim, J. and Moin, P. (1985). Application of a fractional-step method to incompressible Navier-Stokes equations. *Journal of Computational Physics*, 59(2):308–323.

Kitano, T., Kataoka, T., and Shirota, T. (1981). An empirical equation of the relative viscosity of polymer melts filled with various inorganic fillers. *Rheologica Acta*, 20(2):207–209.

Kloeden, P. E. and Platen, E. (1992). *Numerical Solution of Stochastic Differential Equations*, volume 23. Springer Verlag.

Koppol, A. P., Sureshkumar, R., and Khomami, B. (2007). An efficient algorithm for multiscale flow simulation of dilute polymeric solutions using bead-spring chains. *Journal of Non-Newtonian Fluid Mechanics*, 141(2):180–192.

Laso, M. and Ottinger, H. C. (1993). Calculation of viscoelastic flow using molecular models: the CONNFFESSIT approach. *Journal of Non-Newtonian Fluid Mechanics*, 47:1–20.

Laso, M., Picasso, M., and Ottinger, H. C. (1997). Two dimensional time dependent viscoelastic flow calculations using CONNFFESSIT. *AIChE Journal*, 43(4):877–892.

Le Bris, C. and Lelievre, T. (2009). *Multiscale Modelling of Complex Fluids: A Mathematical Initiation*, pages 49–137. Springer.

Le Bris, C. and Lelievre, T. (2012). Micro-macro models for viscoelastic fluids: modelling, mathematics and numerics. *Science China Mathematics*, 55(2):353–384.

Le-Cao, K., Mai-Duy, N., Tran, C.-D., and Tran-Cong, T. (2010). Towards an analysis of shear suspension flows using radial basis functions. *CMES: Computer Modeling in Engineering & Sciences*, 67(3):265–294.

Lipscomb, G. G., Denn, M. M., Hur, D. U., and Boger, D. V. (1988). The flow of fiber suspensions in complex geometries. *Journal of Non-Newtonian Fluid Mechanics*, 26(3):297–325.

Liu, S., Liu, X., Guan, X. F., He, P. F., and Yuan, Y. (2013). A Stochastic Multiscale Model for Predicting the Thermal Expansion Coefficient of Early-age Concrete. *CMES: Computer Modeling in Engineering & Sciences*, 92(2):173–191.

Liu, S., Liu, X., Yuan, Y., He, P. F., and Mang, H. A. (2014a). A Stochastic Multi-Scale Model for Prediction of the Autogenous Shrinkage Deformations of Early-age Concrete. *CMC: Computers, Materials & Continua*, 39(2):85–112.

Liu, S., Liu, X., Yuan, Y., Mang, H. A., Zhang, D.-G., Zhou, H.-M., Yang, Q. W., Du, S. G., Liang, C. F., and Yang, L. J. (2014b). Constitutive Modeling of Early-Age Concrete by a Stochastic Multi-scale Method. *CMES: Computer Modeling in Engineering & Sciences*, 100(3):157–200.

Lopez-Gomez, I. D., Estrada, O., and Osswald, T. (2007). Modeling and simulation of polymer processing using the radial functions method. *Wak Zeitschrift Kunststofftechnik*, 3(2).

Lozinski, A. and Chauviere, C. (2003). A fast solver for Fokker-Planck equation applied to viscoelastic flows calculations: 2D FENE model. *Journal of Computational Physics*, 189(2):607–625.

Lozinski, A., Owens, R. G., and Phillips, T. N. (2011). The Langevin and Fokker-Planck equations in polymer rheology. *Handbook of Numerical Analysis*, 16:211–303.

Lozinski, A., Owens, R. G., and Quarteroni, A. (2002). On the simulation of unsteady flow of an Oldroyd-B fluid by spectral methods. *Journal of Scientific Computing*, 17(1):375–383.

Lu, Z., Khoo, B. C., Dou, H.-S., Phan-Thien, N., and Seng Yeo, K. (2006). Numerical simulation of fibre suspension flow through an axisymmetric contraction and expansion passages by Brownian configuration field method. *Chemical Engineering Science*, 61(15):4998–5009.

Magda, J. J., Larson, R. G., and Mackay, M. E. (1988). Deformation-dependent hydrodynamic interaction in flows of dilute polymer solutions. *The Journal of Chemical Physics*, 89(4):2504–2513.

Mai-Duy, N. (2005). Solving high order ordinary differential equations with radial basis function networks. *International Journal for Numerical Methods in Engineering*, 62(6):824–852.

Mai-Duy, N., Le-Cao, K., and Tran-Cong, T. (2008). A Cartesian grid technique based on one-dimensional integrated radial basis function networks for natural convection in concentric annuli. *International Journal for Numerical Methods in Fluids*, 57(12):1709–1730.

Mai-Duy, N. and Tanner, R. I. (2005). Computing non-Newtonian fluid flow with radial basis function networks. *International Journal for Numerical Methods in Fluids*, 48(12):1309–1336.

Mai-Duy, N. and Tanner, R. I. (2007). A collocation method based on one-dimensional RBF interpolation scheme for solving PDEs. *International Journal of Numerical Methods for Heat & Fluid Flow*, 17(2):165–186.

Mai-Duy, N. and Tran-Cong, T. (2001). Numerical solution of differential equations using multiquadric radial basis function networks. *Neural Networks*, 14:185–199.

Mai-Duy, N. and Tran-Cong, T. (2003). Approximation of function and its derivatives using radial basis function networks. *Applied Mathematical Modelling*, 27(3):197–220.

Mai-Duy, N. and Tran-Cong, T. (2005). An efficient indirect RBFN-based method for numerical solution of PDEs. *Numerical Methods for Partial Differential Equations*, 21(4):770–790.

Mai-Duy, N. and Tran-Cong, T. (2009a). A Cartesian-grid discretisation scheme based on local integrated RBFNs for two-dimensional elliptic problems. *CMES: Computer Modeling in Engineering & Sciences*, 51(3):213–238.

Mai-Duy, N. and Tran-Cong, T. (2009b). Integrated radial-basis-function networks for computing Newtonian and non-Newtonian fluid flows. *Computers & Structures*, 87(11):642–650.

Mai-Duy, N. and Tran-Cong, T. (2011). Compact local integrated-RBF approximations for second-order elliptic differential problems. *Journal of Computational Physics*, 230(12):4772–4794.

Malkus, D. S., Nohel, J. A., and Plohr, B. J. (1990). Dynamics of shear flow of a non-Newtonian fluid. *Journal of Computational Physics*, 87(2):464–487.

Marchal, J. M. and Crochet, M. J. (1987). A new mixed finite element for calculating viscoelastic flow. *Journal of Non-Newtonian Fluid Mechanics*, 26(1):77–114.

Masubuchi, Y. (2014). Simulating the flow of entangled polymers. *Annual Review of Chemical and Biomolecular Engineering*, 5:11–33.

McLeish, T. C. B. and Ball, R. C. (1986). A molecular approach to the spurt effect in polymer melt flow. *Journal of Polymer Science Part B: Polymer Physics*, 24(8):1735–1745.

McLeish, T. C. B. and Larson, R. G. (1998). Molecular constitutive equations for a class of branched polymers: The pom-pom polymer. *Journal of Rheology*, 42(1):81–110.

Mochimaru, Y. (1983). Unsteady-state development of plane Couette flow for viscoelastic fluids. *Journal of Non-Newtonian Fluid Mechanics*, 12(2):135–152.

Mompean, G. and Deville, M. (1997). Unsteady finite volume simulation of Oldroyd-B fluid through a three-dimensional planar contraction. *Journal of Non-Newtonian Fluid Mechanics*, 72(2):253–279.

Mu, Y., Zhao, G., Zhang, C., Chen, A., and Li, H. (2010). Three-dimensional simulation of planar contraction viscoelastic flow by penalty finite element method. *International Journal for Numerical Methods in Fluids*, 63(7):811–827.

Ngo-Cong, D., Mai-Duy, N., Karunasena, W., and Tran-Cong, T. (2012). Local moving least square-one-dimensional integrated radial basis function networks technique for incompressible viscous flows. *International Journal for Numerical Methods in Fluids*, 70(11):1443–1474.

Nguyen, H. Q., Tran, C. D., Pham-Sy, N., and Tran-Cong, T. (2014). A Numerical Solution Based on the Fokker-Planck Equation for Dilute Polymer Solutions Using High Order RBF Methods. *Applied Mechanics and Materials*, 553:187–192.

Nguyen, H. Q., Tran, C. D., and Tran-Cong, T. (2015a). A multiscale method based on the fiber configuration field, IRBF and DAVSS for the simulation of fiber suspension flows. *CMES: Computer Modeling in Engineering & Sciences*, 109-110(4):361–403.

Nguyen, H. Q., Tran, C. D., and Tran-Cong, T. (2015b). RBFN stochastic coarse-grained simulation method: Part I - Dilute polymer solutions using Bead-Spring Chain models. *CMES: Computer Modeling in Engineering & Sciences*, 105(5):339–439.

Nguyen, H. Q., Tran, C. D., and Tran-Cong, T. (2015c). Simulation of flow of fibre suspensions using an IRBF-BCF based multiscale approach. In *Proceeeding of the 11th International Conference on CFD in the Minerals and Process Industries*, pages 1–6. The Commonwealth Scientific and Industrial Research Organisation (CSIRO), Australia.

Nguyen, H. Q., Tran, C. D., and Tran-Cong, T. (2016a). RBFN stochastic coarse-grained simulation method: Part II - Polymer melt simulation using reptation models (Under review). *CMES: Computer Modeling in Engineering & Sciences.*

Nguyen, H. Q., Tran, C. D., and Tran-Cong, T. (2016b). Simulation of non-dilute fibre suspension flows using the high-order IRBF-BCF based multiscale method (In press). *CMES: Computer Modeling in Engineering & Sciences.*

Oldroyd, J. G. (1950). On the formulation of rheological equations of state. In *Proceedings of the Royal Society of London A: Mathematical, Physical and Engineering Sciences*, volume 200, pages 523–541. The Royal Society.

Olsson, F. (1994). A solver for time-dependent viscoelastic fluid flows. *Journal of Non-Newtonian Fluid Mechanics*, 51(3):309–340.

Osswald, T. A. and Gramann, P. J. (2001). Polymer processing simulations trends. *Society for the Advancement of Material and Process Engineers.*

Ottinger, H. C. (1987a). A model of dilute polymer solutions with hydrodynamic interaction and finite extensibility. I. Basic equations and series expansions. *Journal of Non-Newtonian Fluid Mechanics*, 26(2):207–246.

Ottinger, H. C. (1987b). Generalized Zimm model for dilute polymer solutions under theta conditions. *The Journal of Chemical Physics*, 86(6):3731–3749.

Ottinger, H. C. (1989a). Computer simulation of reptation theories. I. Doi-Edwards and Curtiss-Bird models. *The Journal of Chemical Physics*, 91:6455–6462.

Ottinger, H. C. (1989b). Gaussian approximation for Rouse chains with hydrodynamic interaction. *The Journal of Chemical Physics*, 90(1):463–473.

Ottinger, H. C. (1990). Computer simulation of reptation theories. II. Reptating-rope model. *The Journal of Chemical Physics*, 92:4540–4547.

Ottinger, H. C. (1996). *Stochastic Processes in Polymeric Fluids: Tools and Examples for Developing Simulation Algorithms.* Berlin: Springer.

Ottinger, H. C. and Laso, M. (1992). Smart polymers in finite element calculation. *Theoretical and Applied Rheology*, 1:286–288.

Ottinger, H. C. and Laso, M. (1995). Bridging the gap between molecular models and viscoelastic flow calculations. In *Technical Papers of the Annual Technical Conference*, pages 2604–2618. Society of Plastics Engineers Incorporated.

Ottinger, H. C., Van den Brule, B. H. A. A., and Hulsen, M. A. (1997). Brownian configuration fields and variance reduced CONNFFESSIT. *Journal of Non-Newtonian Fluid Mechanics*, 70:255–261.

Owens, R. G. and Phillips, T. N. (2002). *Computational Rheology*, volume 2. World Scientific.

Patera, A. T. (1984). A spectral element method for fluid dynamics: Laminar flow in a channel expansion. *Journal of Computational Physics*, 54(3):468–488.

Perera, M. G. N. and Walters, K. (1977). Long-range memory effects in flows involving abrupt changes in geometry: Part I: flows associated with I-shaped and T-shaped geometries. *Journal of Non-Newtonian Fluid Mechanics*, 2(1):49–81.

Pham-Sy, N., Tran, C.-D., Hoang-Trieu, T.-T., Mai-Duy, N., and Tran-Cong, T. (2013). Compact local IRBF and domain decomposition method for solving PDEs using a distributed termination detection based parallel algorithm. *CMES: Computer Modeling in Engineering & Sciences*, 92(1):1–31.

Phan-Thien, N. (1978). A nonlinear network viscoelastic model. *Journal of Rheology*, 22(3):259–283.

Phan-Thien, N. (2012). *Understanding Viscoelasticity: An Introduction to Rheology*. Berlin: Springer-Verlag.

Phan-Thien, N. and Fan, X.-J. (1999). Pressure drop created by a sphere settling in a tube containing a fiber suspension. *Journal of Rheology*, 43:1.

Phan-Thien, N. and Graham, A. L. (1991). A new constitutive model for fibre suspensions: flow past a sphere. *Rheologica Acta*, 30(1):44–57.

Phan-Thien, N., Sugeng, F., and Tanner, R. I. (1987a). The squeeze-film flow of a viscoelastic fluid. *Journal of Non-Newtonian Fluid Mechanics*, 24(1):97–119.

Phan-Thien, N. and Tanner, R. I. (1977). A new constitutive equation derived from network theory. *Journal of Non-Newtonian Fluid Mechanics*, 2(4):353–365.

Phan-Thien, N., Tran-Cong, T., and Ramia, M. (1987b). A boundary-element analysis of flagellar propulsion. *Journal of Fluid Mechanics*, 184:533–549.

Phan-Thien, N., Zheng, R., and Graham, A. L. (1991). The flow of a model suspension fluid past a sphere. *Journal of Statistical Physics*, 62(5-6):1173–1195.

Prabhakar, R. and Prakash, J. R. (2004). Multiplicative separation of the influences of excluded volume, hydrodynamic interactions and finite extensibility on the rheological properties of dilute polymer solutions. *Journal of Non-Newtonian Fluid Mechanics*, 116(2):163–183.

Prakash, J. R. (2001). Rouse chains with excluded volume interactions: linear viscoelasticity. *Macromolecules*, 34(10):3396–3411.

Prakash, J. R. (2002). Rouse chains with excluded volume interactions in steady simple shear flow. *Journal of Rheology*, 46(6):1353–1380.

Risken, H. (1989). *The Fokker-Planck equation: method of solution and applications*. Berlin: Springer.

Rotne, J. and Prager, S. (1969). Variational treatment of hydrodynamic interaction in polymers. *The Journal of Chemical Physics*, 50:4831–4837.

Rouse, J. and Prince, E. (1953). A theory of the linear viscoelastic properties of dilute solutions of coiling polymers. *The Journal of Chemical Physics*, 21(7):1272–1280.

Sahin, M. and Wilson, H. J. (2008). A parallel adaptive unstructured finite volume method for linear stability (normal mode) analysis of viscoelastic fluid flows. *Journal of Non-Newtonian Fluid Mechanics*, 155(1):1–14.

Sandri, D. (2004). Numerical study of a new finite element method for the approximation of viscoelastic fluid flow problems. *Journal of Non-Newtonian Fluid Mechanics*, 118(2):103–120.

Sun, J., Phan-Thien, N., and Tanner, R. I. (1996). An adaptive viscoelastic stress splitting scheme and its applications: AVSS/SI and AVSS/SUPG. *Journal of Non-Newtonian Fluid Mechanics*, 65(1):75–91.

Sun, J., Smith, M. D., Armstrong, R. C., and Brown, R. A. (1999). Finite element method for viscoelastic flows based on the discrete adaptive viscoelastic stress splitting and the discontinuous Galerkin method: DAVSS-G/DG. *Journal of Non-Newtonian Fluid Mechanics*, 86(3):281–307.

Sunthar, P. and Prakash, J. R. (2005). Parameter-free prediction of DNA conformations in elongational flow by successive fine graining. *Macromolecules*, 38(2):617–640.

Sureshkumar, R. and Beris, A. N. (1995). Effect of artificial stress diffusivity on the stability of numerical calculations and the flow dynamics of time-dependent viscoelastic flows. *Journal of Non-Newtonian Fluid Mechanics*, 60(1):53–80.

Tanner, R. I. (1988). From A to (BK) Z in constitutive relations. *Journal of Rheology*, 32:673.

Tanner, R. I. and Xue, S. C. (2002). Computing transient flows with high elasticity. *Korea-Australia Rheology Journal*, 14(4):143–159.

Temam, R. (1977). *Navier-Stokes Equation: Theory and Numerical Analysis*, volume 2. North-Holland.

Thai-Quang, N., Le-Cao, K., Mai-Duy, N., and Tran-Cong, T. (2012). A high-order compact local integrated-RBF scheme for steady-state incompressible viscous flows in the primitive variables. *CMES: Computer Modeling in Engineering & Sciences*, 84(6):528–557.

Tien, C. M. T., Thai-Quang, N., Mai-Duy, N., Tran, C.-D., and Tran-Cong, T. (2015). High-order fully coupled scheme based on compact integrated RBF approximation for viscous flows in regular and irregular domains. *CMES: Computer Modeling in Engineering & Sciences*, 105(4):301–340.

Townsend, P. and Walters, K. (1994). Expansion flows on non-Newtonian liquids. *Chemical Engineering Science*, 49(5):748–763.

Tran, C. D., An-Vo, D. A., Mai-Duy, N., and Tran-Cong, T. (2011). An integrated RBFN-based macro-micro multi-scale method for computation of visco-elastic fluid flows. *CMES: Computer Modeling in Engineering & Sciences*, 82(2):137–162.

Tran, C. D., Mai-Duy, N., Le-Cao, K., and Tran-Cong, T. (2012a). A continuum-microscopic method based on IRBFs and control volume scheme for viscoelastic fluid flows. *CMES: Computer Modeling in Engineering & Sciences*, 85(6):499–519.

Tran, C.-D., Mai-Duy, N., and Tran-Cong, T. (2012b). Computation of a Fokker-Planck-equation-based multi-scale model for complex flows using the IRBFN method. In *Proceedings of the 6th European Congress on Computational Methods in Applied Sciences and Engineering (ECCOMAS 2012)*, pages 8821–8834. Vienna University of Technology.

Tran, C. D., Phillips, D. G., and Tran-Cong, T. (2009). Computation of dilute polymer solution flows using BCF-RBFN based method and domain decomposition technique. *Korea-Australia Rheology Journal*, 21(1):1–12.

Tran-Canh, D. and Tran-Cong, T. (2002a). BEM-NN computation of generalised Newtonian flows. *Engineering Analysis with Boundary Elements*, 26(1):15–28.

Tran-Canh, D. and Tran-Cong, T. (2002b). Computation of viscoelastic flow using neural networks and stochastic simulation. *Korea-Australia Rheology Journal*, 14(4):161–174.

Tran-Canh, D. and Tran-Cong, T. (2004). Element-free simulation of dilute polymeric flows using Brownian Configuration Fields. *Korea-Australia Rheology Journal*, 16(1):1–15.

Tran-Cong, T., Mai-Duy, N., and Phan-Thien, N. (2001). BEM-RBF approach for viscoelastic flow analysis. *Boundary Elements XXIII*, 10:329–338.

Tran-Cong, T. and Phan-Thien, N. (1988). Three-dimensional study of extrusion processes by Boundary Element Method. *Rheologica Acta*, 27(1):21–30.

Tran-Cong, T. and Phan-Thien, N. (1989). Stokes problems of multiparticle systems: A numerical method for arbitrary flows. *Physics of Fluids A: Fluid Dynamics*, 1:453.

Tran-Cong, T., Phan-Thien, N., and Graham, A. L. (1990). Stokes problems of multiparticle systems: Periodic arrays. *Physics of Fluids A: Fluid Dynamics*, 2(5):666–673.

Turner, M. J., Clough, R. W., Martin, H. C., and Topp, L. P. (1956). Stiffness and deflection analysis of complex structures. *Journal of the Aeronautical Society*, 23:805.

Van den Brule, B. (1993). Browian dynamics simulation of finitely extensible bead-spring chains. *Journal of Non-Newtonian Fluid Mechanics*, 47:357–378.

Van Heel, A. P. G., Hulsen, M. A., and Van den Brule, B. H. A. A. (1999). Simulation of the Doi-Edwards model in complex flow. *Journal of Rheology*, 43:1239–1260.

Van Os, R. G. M. and Phillips, T. N. (2004). The prediction of complex flows of polymer melts using spectral elements. *Journal of Non-Newtonian Fluid Mechanics*, 122(1):287–301.

Van Os, R. G. M. and Phillips, T. N. (2005). Efficient and stable spectral element methods for predicting the flow of an XPP fluid past a cylinder. *Journal of Non-Newtonian Fluid Mechanics*, 129(3):143–162.

Verdier, P. H. and Stockmayer, W. H. (1962). Monte Carlo calculations on the dynamics of polymers in dilute solution. *The Journal of Chemical Physics*, 36(1):227–235.

Verleye, V., Couniot, A., and Dupret, F. (1993). Prediction of fiber orientation in complex injection molded parts. In *Proceedings of the 9th International Conference on Composite Materials*, volume 3, pages 642–650.

Verweyst, B. E. and Tucker, C. L. (2002). Fiber Suspensions in Complex Geometries: Flow/Orientation Coupling. *The Canadian Journal of Chemical Engineering*, 80(6):1093–1106.

Wachs, A. and Clermont, J.-R. (2000). Non-isothermal viscoelastic flow computations in an axisymmetric contraction at high Weissenberg numbers by a finite volume method. *Journal of Non-Newtonian Fluid Mechanics*, 95(2):147–184.

Wedgewood, L. E., Ostrov, D. N., and Bird, R. B. (1991). Kinetic theory and rheology of dilute suspensions of finitely extendible dumbbells. *Journal of Non-Newtonian Fluid Mechanics*, 40(1):119–139.

Weinan, E. and Engquist, B. (2003). Multiscale modeling and computation. *Notices of the American Mathematical Society*, 50:1062–1070.

Wendland, H. (1995). Piecewise polynomial, positive definite and compactly supported radial functions of minimal degree. *Advances in Computational Mathematics*, 4(1):389–396.

Wendland, H. (1998). Error estimates for interpolation by compactly supported radial basis functions of minimal degree. *Journal of Approximation Theory*, 93(2):258–272.

Wiest, J. M. and Tanner, R. I. (1989). Rheology of bead-nonlinear spring chain macromolecules. *Journal of Rheology*, 33(2):281–316.

Xue, S.-C., Phan-Thien, N., and Tanner, R. I. (1998). Three dimensional numerical simulations of viscoelastic flows through planar contractions. *Journal of Non-Newtonian Fluid Mechanics*, 74(1):195–245.

Yamakawa, H. (1971). *Modern Theory of Polymer Solutions*. New York: Happer and Row.

Zimm, B. H. (1956). Dynamics of polymer molecules in dilute solution: viscoelasticity, flow birefringence and dielectric loss. *The Journal of Chemical Physics*, 24:269–278.

Zylka, W. (1991). Gaussian approximation and Brownian dynamics simulations for Rouse chains with hydrodynamic interaction undergoing simple shear flow. *The Journal of Chemical Physics*, 94(1):4628.